Cooperative control of an active magnetic bearing and sensorless drive system

GL Kruger

orcid.org/0000-0002-5716-9160

Thesis submitted in fulfilment of the requirements for the degree *Doctor of Philosophy in Computer and Electronic Engineering* at the North-West University

Promoter:	Prof G van Schoor
Co-Promoter:	Prof PA van Vuuren

Graduation ceremony: May 2019

Student number: 13039210

Abstract

Keywords: Vibration control; Sensorless vector control; Magnetic bearing, Runout identification, Unbalanced magnetic pull

This thesis presents the cooperative control of an active magnetic bearing (AMB) and sensorless drive system. Traditionally, these two systems are considered as independent modular components within a larger system. The control of both systems requires angular speed information. Principally, the speed is required in the unbalance control of the AMB and the speed control of the drive. Furthermore, the speed is also required in both systems to compute cross-coupling terms for feedforward cancellation.

Historically, the speed is estimable in both systems, but only above a threshold speed. The speed estimation in the AMB relied on the orbit generated due to unbalance. The speed estimation of the sensorless drive (of a surface mounted PMSM) relied upon the generated back-emf. This resulted in the sensorless drive system requiring an open-loop start-up procedure.

It has been found by utilizing a novel method which relies on the disturbance force on the rotor, due to unbalanced magnetic pull, that it is possible for the AMB system to estimate the angular position of the rotor from standstill up to an upper limit in speed. Sharing this estimated angular position with the drive system, it is possible to skip the open-loop start-up of the drive and start it in vector controlled mode. The drive is switched to sensorless drive mode before the angular position accuracy upper limit is reached. After this switchover, the estimated angle by the sensorless vector control is in turn shared with the AMB system for unbalance control. The sensorless drive control algorithm has been reorganized to integrate in such a manner with the AMB's estimated angular position so that a smooth bumpless transfer results during the switchover.

The main contributions of this work are the disturbance force model identification by the AMB system for estimation of the angular position and the supervisory coordination of the two controlled systems to act cooperatively. The key structure proposed for consolidation of the shared state information between the two systems is by integration into a phase-locked loop (PLL).

“2 *Aan U, o God, kom ’n lofsang toe in Sion: geloftes moet betaal word* 3 *aan U wat die gebed verhoor. Na U toe sal alle mense kom* 4 *om hulle skuld te bely. Ons sondes het ons ingehaal, maar U maak ons daarvan vry.* 5 *Dit gaan goed met die mens vir wie U uitkies en laat naderkom om in u tempel te bly. Laat ons die goeie dinge in u huis in oorvloed geniet, die goeie dinge in u heilige woning.”* Psalm 65: 2-5

“2 *Praise awaits you, our God, in Zion; to you our vows will be fulfilled.* 3 *You who answer prayer, to you all people will come.* 4 *When we were overwhelmed by sins, you forgave our transgressions.* 5 *Blessed are those you choose and bring near to live in your courts! We are filled with the good things of your house, of your holy temple.”* Psalm 65: 2-5

Acknowledgement

I would like to thank my advisors, Prof. George, and Prof. Pieter, for their encouragement and support during the course of this study. They sacrificed many hours to listen and perturb my thoughts with meaningful questions. Thank you for your patience and financial support.

I would like to thank my friends for their encouragement, those in the McTronX research group and those outside, most of whom have already moved on to other walks of life. I would like to especially thank: Rikus, Melvin, DB, Gerhard, CJ, SW, Jan & Angelique, André & Leenta, Henri, Kenny, Gawie, Fabian, Oom Trümpelmann and Goden.

I would like to thank the friends at the "Dampad" dining hall.

Everyone at church, the weekly Bible study, and everyone else who prayed for me, thank you!

I would also like to thank the NRF[1] and the North-West University for financial support.

Lastly, I would like to thank my family and especially my parents. Thank you for your love and support. Your kind words are written somewhere where it can never be erased.

[1]This work is based on the research supported wholly or in part by the National Research Foundation (NRF) of South Africa (Grant numbers 82117). Opinions expressed and conclusions arrived at are those of the authors and are not necessarily to be attributed to the NRF.

Contents

List of Figures

List of Tables

Nomenclature

Acronyms

ADC	Analogue-to-Digital Converter
DSP	Digital Signal Processor
FOC	Field Oriented Control
PD controller	Proportional and derivative controller
PI controller	Proportional and integral controller
V/f Control	Volt/frequency Control
VSI	Voltage source inverter
AC	Alternating Current
AMB	Active Magnetic Bearing
DC	Direct Current
emf	Electromotive force [V]
FESS	Flywheel Energy Storage System
IGBT	Insulated Gate Bipolar Transistor
LUT	Look-up table
PM	Permanent Magnet
PMSM	Permanent Magnet Synchronous Machine
pu	Per Unit
r/min	revolutions per minute
rms	root-mean-square
S/N	Signal-to-noise ratio

SiC	Silicon carbide
SM	Synchronous Machine
DPLL	Digital phase-locked loop
FOC	Field oriented control
GaN	Gallium nitride
HEMT	High-electron-mobility transistor

Symbols

R_s	Stator phase resistance [Ω]
i_d	Instantaneous d-axis current [A]
$\boldsymbol{i}_{dq0}$	Instantaneous current vector in dq0 reference frame [A]
$\boldsymbol{v}_{dq0}$	Instantaneous voltage vector in dq0 reference frame [V]
ω_m	Rotor mechanical frequency [rad/s]
ω_r	Rotor electrical frequency [rad/s]
ω_s	Stator electrical frequency [rad/s]
i_a, i_b, i_c	Instantaneous a, b and c phase current [A]
i_q	Instantaneous q-axis current [A]
P	Power [W]
v_a, v_b, v_c	Instantaneous a, b and c phase voltage [V]
v_{DC}	Instantaneous DC bus voltage [V]
v_d	Instantaneous d-axis voltage [V]
v_q	Instantaneous q-axis voltage [V]
T_c	Inverter switching/carrier period [s]
T_s	Controller sample period [s]
λ_p	Stator flux linkage due to rotor permanent magnet [Wb.turns]
L_s	Stator phase inductance [H]
z_p	Number of pole pairs
B	Viscous friction loss [N.m.s/rad]
J	Rotor polar moment of inertia [N.m.s^2/rad]

Chapter 1

Introduction

1.1 Background

This thesis considers an active magnetic bearing (AMB) system combined with a synchronous permanent magnet machine (PMSM) in the form of a flywheel system. The inner components of such a system are depicted in Fig 1.1 with the outer supporting structure not shown. The rotor structure is levitated within the air-gap of the AMB stator by applying suitable counteracting forces which are generated by electromagnets. The required suitable forces are computed by an electronic control system, based on the position sensor signals which sense the rotor position within the air-gap. The flywheel system is spun up by the PMSM in order to store kinetic energy. The energy is recovered by the same PMSM acting as a generator when needed.

The AMB and PMSM combination is used in other systems besides the flywheel, such as centrifuges, turbo-machines, and pumps.

1.1.1 Vibration control background

An active magnetic bearing faces a set of problems, which, when solved successfully, counts (ironically) as one of the advantages of an AMB. This set of problems is broadly categorised under vibration. A vibration classification scheme is presented in Fig. 1.2. The classification of the "Groups" are attributable to [1]. "Group A" methods are concerned with lowering bearing currents, e.g. allowing the rotor to rotate about its inertial axis. "Group B" methods are concerned with the high precision rotation of the rotor about its geometric centre.

The root cause of vibration is because all manufactured components exhibit a degree of mass unbalance. Mass unbalance occurs when a planar rigid body's centre of mass does not coincide with its geometrical centre. When considering a three dimensional rigid body as in Fig. 1.1, the centre of mass may also have a non-zero Z component. Even if the

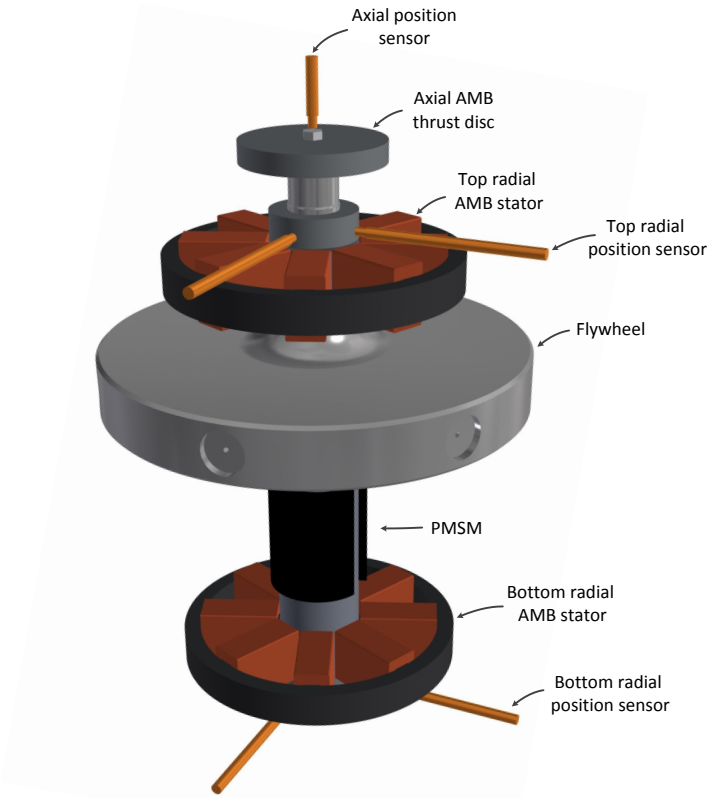

Figure 1.1: Rigid rotor free body diagram with AMBs and PMSM.

machining process may satisfy extreme geometrical tolerances, the constructed rotor may still have mass unbalance due to inhomogeneous material density. Referring back to Fig. 1.1 the unbalance causes the rigid body's principal axis of inertia and the Z-axis to be non-collocated.

If the Z component of the centre of mass is zero, then the Z-axis and the principal axis of inertia of the rotor are parallel, in which case the unbalance is known as static imbalance. In the case of a non-zero Z component of the centre of mass, an additional angle exists between the Z-axis and principal axis of inertia.

At standstill, the mass unbalance in itself is not a problem. Only when the rotor has an angular velocity, Ω, does a conventional proportional and derivative (PD) controller[1] have a problem to generate the centripetal force required to reject the sinusoidal disturbance caused by the mass unbalance. The magnitude of the required centripetal force is proportional to the mass unbalance and the square of the angular velocity as shown in (1.1):

$$F_{cen\,d} \propto m_e \omega_r^2 \,. \tag{1.1}$$

The PD controller cannot reject the relative high-frequency sinusoidal disturbance due to

[1] Assuming the controller's objective is to rotate the rotor about the geometric centre.

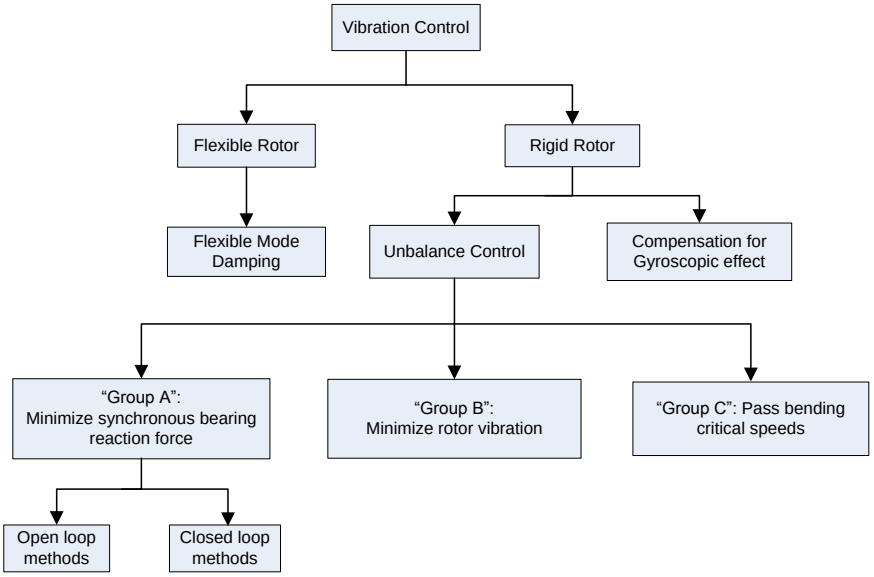

Figure 1.2: Breakdown of vibration control categories ([1, 2]).

the correction force always lagging the sinusoidal disturbance.

One proposed method of addressing this phase lag is to transform the measured rotor position to a reference frame which is synchronous to the angular velocity of the rotor. Relative to this new reference frame the sinusoidal disturbance appears as a 0 Hz disturbance, such that an integrator term added in this reference frame and transformed back to the stationary reference frame would result in successful cancellation of the synchronous disturbance. The control in the rotating reference frame has been proposed and tested by De Miras and Charara [5, 6, 7]. Cancelling the rotor vibration by the AMBs would result in large forces being transmitted to the AMB housing in which the rotor sensors reside. This, in turn, could result in housing resonant mode excitation as well as erroneous sensor measurement resulting in positive feedback. Also, the forces generated by this method are large and may saturate the AMB, hence the AMB has to be designed with large dynamic load capacity.

Another option is to ignore the synchronous part of the position measurement via notch filters. This would allow the rotor to spin about its principal axis of inertia [8]. As long as the distance between the centre of mass and the geometric centre is smaller than the clearance between the magnetic centre and the back-up bearing, the rotor will be able to spin without run-out against the back-up bearing. This method results in a small AMB current ripple. In the case of permanent magnet biased AMBs this result in significantly increased efficiency due to copper loss savings.

The notch filter approach is an open-loop unbalance compensation technique and does not present a stability problem for weakly gyroscopic rotors [8]. The gyroscopic effect is

also a synchronous disturbance and needs to be compensated, which would be ignored by the notch filter. As shown by [9] the gyroscopic effect is a destabilizing disturbance but does not make the system unstable, some extra destabilizing mechanism is required for the system to become unstable.

A notch filter implementation based on the rotating coordinate transformation is presented by Zheng and Feng [10], which is related to the work presented by De Miras and Charara, but establishes the equivalence between the rotating coordinate transformations and the two-step modulator notch filter.

Observers or adaptive controllers are able to estimate the rotor unbalance and generate an injection signal accordingly. They fall under the category of closed-loop methods. The proponents of open-loop methods point out that the observers are of a high order. Microprocessor/controllers have improved since the proposal of the closed-loop methods.

Also, the stability bounds of the closed-loop method have to be determined. For example, an adaptive autocentering control is proposed by [11], which is a closed-loop method. At certain angular velocities the estimator has to be turned off and the controller uses the held estimator outputs for cancelling the synchronous disturbance, allowing the rotor to spin about its inertial axis. After crossing the unstable frequency the estimator is allowed to turn back on. They note that the method is applicable to the dynamic imbalance case as well, but it is not usable for systems with flexible modes. Another problem with this method is that it requires the angular speed measurement. Also a drift in the speed measurement during the period that the estimator has to be turned off would result in an erroneous synchronous force generated, which could destabilize the system. Low-frequency drift in the speed estimation could be countered if the method used an angular position input instead.

A unification between the open-loop and closed-loop method has been proposed by [8], known as a "generalized notch filter", since all unbalance compensation methods have a possible "black-box" representation [1].

Other important developments have been done by Tamisier *et al.* [2], who managed to combine a closed-loop unbalance compensation scheme with flexible mode damping ("Group C"), which was a problem with previous methods, such as the method by [11] mentioned earlier. They also showed that their method can be combined with other existing vibration control techniques. Tamisier also proposed to extend his previous method to cancel the cross-coupling term due to the gyroscopic effect [12]. He also recognized and addressed the stability problem of closed-loop vibration control methods.

1.1.2 Sensorless vector control background

The most basic "sensorless controller" is scalar control or V/f control [13]. Sensorless vector control has a much higher dynamic response, but for the surface mounted permanent

magnet synchronous machines the speed and angle at stand-still and low speed are not estimable [14]. This implies the requirement of an open-loop start-up method which requires parameter tuning [4]. High-speed machines operate over a broad frequency range and the parameters may need to be modelled as a function of frequency. Also, the high frequency operation entails that the ADC, control loop execution and PWM update cycle delays are not negligible and need to be accounted for during the control design and compensated during control implementation.

1.2 Areas of possible contribution

All of the unbalance compensation schemes considered thus far require at least an angular speed signal input. In order to alleviate this necessity, an extension of the unbalance estimator has been proposed by Lee *et al.* [15] such that the speed signal may be extracted from the AMB position signals themselves. This showed that there was indeed a need for the AMB control to be independent of the speed sensor. Herzog *et al.* [8] also reported on methods which are independent of a speed sensor input, i.e. the angular velocity is estimated using phase-locked loop methods using signals internal to the notch filter. Whether this method of removing the speed sensor actually increases the system reliability still needs to be investigated [8]. Lee *et al.* [15] also recognized that if an electrical machine is present, then this could be used instead to derive an angular speed estimation. In fact, Lee *et al.* were able to use the estimated speed from the AMB vibration control as an input for an induction machine drive, although they admitted that the system had slow speed variation, i.e. a low dynamic drive was used.

Nevertheless, these methods rely on a certain amount of unbalance of rotor eccentricity to be present such that the signal-to-noise ratio (S/N) is large enough to accurately estimate the angular velocity, hence they also only work at higher speeds. Lee *et al.* [15] also suggested that their proposed algorithm should be tested in combination with a vector controlled drive (higher dynamics/faster speed variation).

The speed estimation from either the AMB or electrical drive does not work well at low speed. The speed estimation bandwidth of the AMB has not been tested or compared with that of a sensorless electrical drive. Only in one instance in literature [15], did the drive benefit from speed estimation from the unbalance control.

The presented background on the developments of vibration control, especially the last noted shortcomings and suggestions for future research from the literature, has been in preparation for the problem statement presented in the following section.

From a practical implementation viewpoint, computational improvements of the implemented controllers are always welcomed. In the control of high-speed machines, it is especially desirable to improve computational efficiency because it leads to higher possible sample rates. Hence, the control is less influenced by time delay and quantization effects.

Delays can be compensated using static delay compensation [13], but such compensation is only an approximation. The best remedy to compensate delay is to make the delay as small as possible. The prototyping platform for this study is the DS1005 system which employs a single, dated, PowerPC processor, which has the job of performing the AMB *and* the PMSM control. Performing advanced control techniques of just one of these systems on a single processor is a demanding task. Performing the control of both systems on one processor thus demands computational efficiency of the entire system. Seeking to improve the computational efficiency also encourages the discovery of possible instances of sharing state information between both systems resulting in a higher probability of finding ways to make the system cooperative.

1.3 Problem Statement

The speed and angle estimation of the sensorless drive and active magnetic bearing have not been considered in unison, despite the fact that the sensorless drive and AMB reside in the same system. The estimation of the speed and angle have only been considered with respect to the two systems as independent modular units. The development of an algorithmic structure or framework which fuses and consolidates the state estimation of the two systems would be a theoretic advancement with practical value. A second shortcoming of these two systems is in the lack of angular estimation at standstill and low speed. The angular dependent disturbance force presented in the bearingless drives literature may be beneficially exploited to overcome this shortcoming.

1.4 Research aims and objectives

The research aims and objectives of this thesis are:

- Identify previous methods of combining the AMB and drive control in literature.
- Identify problems and weaknesses within the AMB and drive systems that may be alleviated by combining the control into a cooperative control strategy.
- Develop simulation models of the AMB and drive systems of varying fidelity for control system development and accurately representing the non-idealities of each system.
- Investigate and analyse new methods of realizing cooperative control methods.
- Reduce the computational demand of the AMB and sensorless drive control such that it is implementable on a single control platform.
- Perform parameter identification of the developed system models.

- Develop or modify existing hardware to allow the implementation of the developed control algorithms.
- Implement and test the novel algorithms.

1.5 Research methodology

Literature study: Identify previous methods of combining the AMB and drive control. Identify problems and weaknesses within each system that may be alleviated by combining the control into a cooperative control strategy.

Modelling and experimental testing: During the modelling phase, try to discover non-idealities or effects which are usually neglected or unwanted and develop methods to compensate for these and to exploit them for additional control functionality. This is an iterative process which is alternated with testing on the physical system. Discrepancies in the measured system response which deviates from the "standard" system model provide clues for unmodelled non-idealities which may be exploited.

Combine/factorize functional patterns: Determine which control structures in the AMB and drive system are similar such that these structures may be combined or factored into one structure in order to yield a cooperative control and to reduce computational overhead.

Non-ideality parameter identification: Perform parameter identification to obtain the parameters of models for the non-ideality effects which are to be exploited for extra functionality.

Parameter identification of nominal system parameters: Perform parameter identification of the nominal system parameters, i.e. the AMB and the PMSM, which takes into account the influence which the non-idealities would have on the system parameters. In the case of the AMB system parameters, the effect of sensor run-out, air-gap irregularity and the disturbance force due to the permanent magnet of the PMSM have to be accounted for. In the case of the PMSM, the non-ideality due to the inverter non-linearity and three-phase line filter has to be accounted for.

Develop or modify existing hardware: The non-ideality effects which are to be exploited may generate relatively small amplitude signals which may easily be corrupted by measurement noise or other secondary non-ideality effects. Thus, in order to successfully implement the algorithms, the hardware may has to be modified or new hardware has to be developed so that the S/N of the system is sufficient such that the primary[2] non-ideality effects may be exploited and that the secondary[3] non-

[2] An example of a primary non-ideality effect is the angular dependent disturbance force due to the permanent magnet of the PMSM.

[3] An example of a secondary non-ideality effect is that of the inverter non-ideality (e.g. dead-time).

ideality effects may be compensated for. The measurement noise may be remedied by synchronizing the inverter of the drive and all of the switching power amplifiers of the AMB. In addition, shielding, grounding, and EMI-filters may also have to be reviewed.

Implement and test algorithms: Implement the control algorithms of the separate AMB and drive control systems and evaluate the performance of each separate system as a baseline. Implement the cooperative control algorithms where the separate control algorithms become linked and overlapping functional algorithms are refactored into a unified structure. The performance of the cooperative control is compared to the baseline performance.

1.6 Contributions of research

The unique contributions in this work are as follows:

- Development of an empirical model and parameter identification procedure for the characterization of the permanent magnet's force disturbance.
- An algorithmic advancement in the open-loop start-up of the sensorless vector control which allows for a bumpless transition from open-loop to closed-loop operation. The bumpless start-up procedure also reduces the computational complexity of the sensorless vector control.
- Utilization of the permanent magnet's force disturbance to estimate the rotor angular position at standstill and to allow for sensored vector control start-up. The bumpless start-up method is modified to allow for the vector control to start-up with the AMB functioning as the angular position sensor and smoothly transitioning to the drive's estimated angular position.
- The development of a novel inverter non-linearity identification procedure and post-processing algorithm which is able to recover the zero voltage component algebraically and thus decouple the non-linearity so that look-up tables may be generated to compensate for the non-linearity as it originates in each individual phase as a function of the phase current.

Publications

During the course of the thesis, two conference articles were presented:

Control of magnetically suspended rotor combined with motor drive system [16]: This paper presented the start-up of the sensorless drive using an open-loop start-up

strategy. Upon switching to the sensorless control after start-up a current transient would result. The paper presents a method of reinitializing the current controllers upon switchover such that a smaller transient results. At higher speed, a weighted averaging of the sensorless drive's speed and the estimated speed from the unbalance control is considered in order to reduce the speed ripple and subsequent current ripple in the drive.

Pseudo-magnetic centre identification of an active magnetic bearing

for sensorless drive control start-up [17]: The paper presented a method of detecting the runout of the rotor by means of an estimated force disturbance. The true magnetic centre is approximated by a method called the pseudo-magnetic centre identification. During the course of the paper, it was assumed that the angular variation of the estimated pseudo-magnetic centre was only due to the magnetic centre variation. It was noted that the pseudo-magnetic centre variation is influenced by external disturbance force variation. It was thought that the disturbance force causes only a DC offset, but as will be presented in this thesis, the disturbance force variation was responsible for the angular dependence in the estimated magnetic centre. Hence, the pseudo-magnetic centre may be considered as an indirect or model-free method of exploiting the angular dependent disturbance force.

The previous paper presented an indirect method of exploiting the angular dependent disturbance force. In this thesis an angular dependent disturbance force model is presented, which allows for a more rigorous treatment in deriving the estimated angle from the disturbance force. Hence, a journal article will be submitted presenting the model based disturbance force angular estimation of the rotor, along with the cooperative control integration with the drive.

1.7 Thesis overview

The thesis is outlined as follows[4]:

Chapter 2: Literature study As stated in the methodology the literature study consists of a selecting a vibration control method, which will suit the requirement of being able to be combined with the sensorless vector controlled drive. Also, background on the sensorless vector drive control and its own shortcomings need to be presented from literature. Previous methods of codependence between the AMB and the sensorless drive is sought, which are later evaluated and improved upon in this study. Novel methods of codependence and cooperation between the AMB and

[4]Note that no results chapter is included. The results of the designed control presented in each chapter is included at the end of that chapter.

sensorless drive can only be claimed in showing that the new method is absent from literature or that it results from combining existing methods in a new way.

Chapter 3: AMB control The AMB control design consists of the design of the AMB controller in centre-of-gravity coordinates using a feedback linearisation framework. This is followed by the design of the rotor rigid body dynamics observer, since utilization of the estimated disturbance force later on is an important signal to be exploited to obtain cooperative control features. Two different disturbance force models are presented. The first is based on the unbalanced magnetic pull due to the permanent magnet of the PMSM alone. The second model, builds forth on the former model to compensate the disturbance force due to improper force inverse function parameters and compensation of higher order terms in the force function. With the AMB control designed and disturbance forces compensated the unbalance control design and measured results are presented.

Chapter 4: Sensorless vector control The sensorless vector control is well established in the literature and the control design procedure of Kshirsagar *et al.* [4] is followed. The drive used in this thesis has a three-phase line filter. The work presented by Salomäki [18] addresses the sensorless control of drives with filters. Salomäki opts for a full-state observer approach, but due to unwarranted computational complexity the observer presented by Kshirsagar *et al.* is justified and used instead. This comes down to using a reduced order observer. The start-up method of the sensorless vector control is modified to yield a bumpless start-up which is computationally more efficient than a pure open-loop start-up which switches to closed-loop at some predefined threshold speed. The chapter finishes by extending the non-salient fixed parameter observer proposed by Kshirsagar *et al.* to a salient parameter varying observer for the sensorless control.

Chapter 5: Cooperative control integration This chapter presents the estimation of the angular position based on the disturbance force due to the unbalance magnetic pull of the PMSM. The angular estimation of the AMB and the sensorless drive is fused using the modified tracking controller which was originally only used for angle estimation in the sensorless drive. The cooperative control start-up improves upon the open-loop start-up.

Chapter 6: Conclusion and recommendation The outcome of the hypotheses are discussed based on the measurement results in the previous chapter. The discrepancies between the implemented system and the simulation results are discussed. Based on the experience and insights gained during the course of the study, recommendations are made for future research.

Appendix A: Inverter non-ideality compensation The non-ideality compensation consists of a novel method of characterising the inverter non-linearity and decoupling

the distortion to a non-linear function for each phase. The non-linearity/distortion is mainly caused by the dead-time effect and secondarily by non-linear device voltage drops. The DC bus disturbance rejection is also presented with an efficient means of calculating the reciprocal of the DC bus voltage based on the Newton-Raphson method. The appendix finishes off with a method of compensating the distortion due to the quantization noise of the PWM, which is not so much important for control purposes, but is required during the inverter non-linearity characterisation.

Appendix B: PMSM parameter identification The PMSM parameter identification is important to include as the parameter accuracy influences the performance of the speed and angle estimation by the sensorless control. The quality of the estimated speed and angle in turn will influence the performance of any other subsystem which depend on either as an input. It is found that the three-phase filter combined with the PMSM has non-linear parameters, which should either be accounted for via an averaging technique (choose a robust value) or the electrical domain observer has to be extended to be parameter varying.

Appendix C: AMB parameter identification The AMB system parameter identification consists of the rigid rotor plant and AMB force function parameters to be identified. The parameter identification is performed by pulsing each AMB individually and fitting the force function parameters using an off-line method so that the simulated response matches the measured response.

Appendix D: AMB power amplifier design The AMB power amplifier design presents an overview of the chosen topology and the reasoning behind various design choices. Most of the design choices of the power amplifier can be traced back to a requirement of reducing the switching noise within the system. A comparison of the noise on the eddy current sensor signals between the old (commercial) and the newly developed power amplifier is presented as a performance evaluation.

Appendix E: Digital supplement The digital supplement provides some useful simulation models and algorithm code embedded into the pdf version of the thesis.

Chapter 2

Literature study

The literature study serves to provide background on active magnetic bearings and sensorless drives and the control of these systems. Advantages of each technology and the shortcomings or difficulties faced implementing and operating each system are also highlighted. Previous methods of addressing these challenges are reported. Special emphasis is given to previous methods which reported on coupling the control of these two systems.

2.1 AMB introduction

2.1.1 Active magnetic bearing operating principle

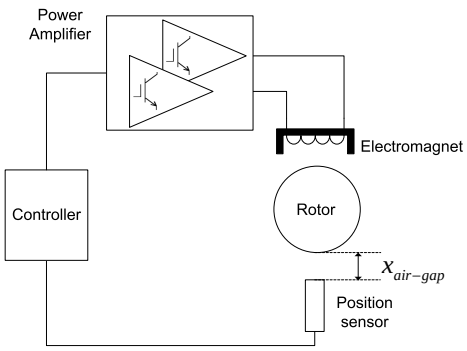

Figure 2.1: Active magnetic bearing system.

An active magnetic bearing (AMB) is an example of a mechatronic system [19]. Its purpose is to provide a magnetic force in order to suspend an object, typically a rotor, such that it can rotate freely. The AMB achieves this objective by incorporating components that originate from diverse engineering disciplines. As shown in Fig. 2.1, the force required to suspend a rotor is generated by electromagnets which may be aided by permanent

magnets to provide bias flux. The required currents in the electromagnets are computed in a controller which take the rotor position measurement as input. The current references generated by the control software are actuated by power amplifiers. The control software needs to continuously update the reference current because the AMB system is inherently unstable [1]. Usually, there is a backup bearing with an inner diameter larger than the rotor in order to catch the rotor in case of an AMB failure.

2.1.2 Advantages of AMBs

It is not difficult to imagine the benefits of using an AMB compared to a conventional bearing. The advantages are (amongst others):

- The system has lower rotational friction losses.
- Very high-speed operation.
- Lubrication-free operation is environmentally friendly and requires less or no maintenance. In fact, some applications demand lubricant-free operation, e.g. the helium heat exchanger of a pebble bed modular reactor [20].
- There is less of a misalignment problem possible between two bearings on the ends of the rotor, i.e. the AMB can tolerate larger misalignment than that of conventional bearings [21].
- Due to lower friction losses and the ability to control vibration, AMBs lend themselves to systems which require higher operating speeds and enabling new applications [22].
- The rotor position signals and the electromagnet currents can be used for fault diagnosis of the AMB and rotor [23, 24, 25, 26].
- The controller signals are also proportional to the bearing forces which may also elucidate operating conditions of the rest of the plant itself. For example, monitoring of the cutting tool condition in a milling machine [27].
- No bearing "run-in" is required [28].
- No current leakage between stator and rotor due to induced common-mode voltages on the rotor by the motor drive, since the AMB air-gap provides galvanic isolation.

Due to the advantages of the AMB, it is typically used in applications such as machine tool spindles [29], vacuum systems, turbo-machinery, flywheel energy storage [30] and inertial wheel systems used for attitude control of satellites [1]. Other future applications AMBs have been considered, such as AMB applied to jet engines [31].

2.1.3 Disadvantages of AMBs

AMBs, however, have their own drawbacks, such as:

- Higher initial capital cost. An AMB may have a lower cost if the payback period of the AMB is shorter than the system lifetime. More importantly, depending on the application, better performance outweighs the higher cost [29].
- Limited load capacity due to magnetic saturation, limited coil current and a minimum required air-gap [32, 33].
- Larger size and weight. Despite AMBs having a larger size, it has been shown that AMBs can replace conventional bearings on some existing systems (retrofitted) [34, 19].
- Increased complexity and more sources of possible failure.
- AMB systems require specialist knowledge to design, commission and maintain [28].

Despite the disadvantages, certain applications demand AMBs to be used. The advantages often outweigh the disadvantages, depending on the intended application.

2.2 AMB control

2.2.1 Brief overview

The complexity of the control algorithms used to generate the currents within the AMB's electromagnet has developed alongside the development of the electronic processing units. Initially, AMB controllers were simple analogue PID controllers. The AMB control was based on decentralized control, i.e. the control signal was originally derived from the position signal of that particular axis [35]. With the advent of digital electronics, the control could be realized digitally and a centralized control scheme could be implemented which accounted for the coupling of position signals of different ends of the rotor into a centralized control law.

Originally, the control law was designed using a linearisation of the plant and actuator, but also due to digital electronics, a non-linear control law could be realized [36]. As processing capacity increased higher and higher order controllers could be realized on a single processing unit [37].

Another control advancement made possible due to increased computational capacity is the compensation of other disturbances such as unbalance control and compensation of the rotor gyroscopic effect, which is presented next.

2.2.2 Disturbance compensation

2.2.2.1 Unbalance control

All rotors have a certain degree of mechanical unbalance. Unbalance is the condition that a rotor's inertial axis of rotation does not coincide with the geometrical centre. This is caused by machining inaccuracy and non-uniform material density.

Unbalance is corrected, up to a certain specification, by measuring the vibration caused by a rotating rotor and removing or adding mass on the rotor so as to cancel the unbalance. Even after balancing some unbalance remains within the tolerated limit allowed for by the balance specification. In applications requiring the rotor to accurately spin about its geometric centre a stringent unbalance specification is given and/or the AMBs are designed to operate at higher bearing load forces and power amplifiers are designed to operate at higher bearing load currents.

Active magnetic bearings have the ability to allow the rotor to rotate about its centre of mass due to the extra degree of freedom allowed for by the air-gap between the rotor and the electromagnet pole tips of the AMB. In certain applications, it is preferable to rotate the rotor about its centre of mass. The unbalance explanation is further aided by Fig. 2.2. The centrifugal force, $\boldsymbol{F}$, required for the rotor to rotate about its geometric centre whilst sustaining a mass unbalance is given by [38]:

$$\boldsymbol{F} = \boldsymbol{r}_\epsilon M \Omega^2 \,, \tag{2.1}$$

where $\boldsymbol{r}_\epsilon$, is called the mass eccentricity of the rotor, with mass M. The eccentricity is the displacement of the centre of mass, point C, from the geometric centre, point G. The rotor is assumed spinning with a velocity of Ω. By controlling the AMB in order to allow the rotor to spin about its centre of mass the AMB does not have to generate this centrifugal force.

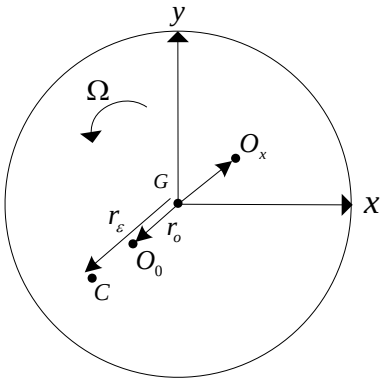

Figure 2.2: Rotor unbalance and eccentricity.

Unbalance control is achieved by "ignoring" or filtering the deviations of the position sensor

signals which are synchronous to the rotation of the rotor [39, 40]. By not generating a reactive force in response to the synchronous deviations of the position signals a force-free control is achieved. It is thus as if the rotor is spinning in free space. With unbalance control the AMBs only have to stabilize the rotor and account for other disturbance forces such as gravity.

Various unbalance control techniques have been presented in the literature, but they can be broadly classified as open-loop and closed-loop techniques. Open-loop techniques are able to cancel the synchronous disturbance of the position signal by *a priori* knowledge of the unbalance and a signal may be generated given the rotor angle as an input to cancel the disturbance signal. Closed-loop methods determine the unbalance disturbance magnitude, phase and frequency from the synchronous disturbance signal in order to generate a signal which is used to cancel the synchronous disturbance which is fed into the control.

The most common example of a closed-loop method is that of the notch-filter. The notch-filter requires the speed of the rotor as a parameter input in order for the notch centre frequency to correspond to the rotor frequency. The notch filter introduced into the control-loop has an effect on the overall closed-loop dynamics and thus need to be accounted for in the control design in order to ensure stability. The design of a generalized notch-filter presented by [8] takes the sensitivity function into account in the design process in order to arrive at a stable unbalance control law.

The position signal disturbance, due to unbalance, may be modelled as:

$$r_{\epsilon x} = |\boldsymbol{r}_\epsilon| \cos(\Omega t + \phi) \tag{2.2}$$

$$r_{\epsilon y} = |\boldsymbol{r}_\epsilon| \sin(\Omega t + \phi) \ . \tag{2.3}$$

Usually, the unbalance control algorithm requires the rotor frequency, Ω, as an external input and the unbalance control only determines the magnitude and phase of the unbalance. An alternative, but equivalent expression of the unbalance disturbance signal is given by:

$$r_{\epsilon x} = A_x \cos(\Omega t) + B_x \sin(\Omega t) \tag{2.4}$$

$$r_{\epsilon y} = A_y \cos(\Omega t) + B_y \sin(\Omega t) \ , \tag{2.5}$$

which accounts for the phase offset, ϕ, of the unbalance with the trigonometric sum of *sine* and *cosine* terms. The unbalance control thus operates by determining the truncated Fourier series coefficients, A_x, B_x, A_y, B_y, online. From these coefficients, a reference signal is generated which cancels the synchronous disturbance from the measured signal.

The unbalance control is depicted in block diagram form in Fig. 2.3. The notch filter reproduces an estimate of the eccentricity disturbance, $\hat{y}_d$, depicted as an output measurement error, y_d. The disturbance estimate is subtracted from the sensor signal and is no longer present in the input signal, $u(t)$, to the control.

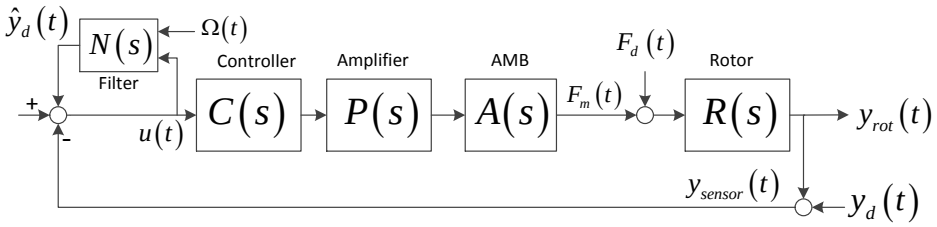

Figure 2.3: Unbalance control block diagram (adapted from [3]).

It has been shown that the unbalance control may also estimate the rotor frequency from the disturbance in the position signal [41, 15, 42, 43, 44]. This is done in order to make the unbalance control independent of the requirement of speed or angular position signal inputs. Herzog *et al.* mentioned that it may increase the system robustness to do away with reliance on the position signal for unbalance control, but further investigation was required. Indeed, Hutterer [44] showed that estimation of the rotor angle included in the unbalance observer may be used as a back-up to the estimated angle from the sensorless drive in case the drive should fail.

2.2.2.2 Geometric centre control

In applications requiring the rotor to spin precisely about the geometric centre, the disturbance rejection problem is formulated differently. Unlike the unbalance control which aimed at reducing the control effort in the AMB reference currents, the geometric centre control instead enhances the control effort such that the position variation due to the force disturbance is cancelled. It has been noted by Jiang *et al.* [3] that the geometric centre control may be obtained by switching the pickup and insertion points of the unbalance control. The insertion point may also be inserted at other possible points further forward in the signal path.

The geometric centre control is thus depicted as in Fig. 2.4. Instead of modelling the unbalance as a measurement error it may also be modelled as a disturbance force, F_d. By providing an estimate of the force disturbance, $\hat{F}_d$, which matches the centrifugal force required to keep the rotor spinning about the geometric centre no position disturbance results due to the unbalance. Jiang *et al.* [3] showed that the *same* notch filter algorithm (based on online identification of the Fourier coefficients) may be used for either unbalance or geometric centre control, by switching the pickup points. Information of the rotor speed is required in both the unbalance and geometric centre control.

An example of an application requiring the geometric centre control is that of an AMB supported spindle used for micro-milling [27]. Besides compensation of the unbalance force another non-ideality is that due to runout of the sensor ring on which the AMB position sensor measures the rotor position. Runout is due to the non-circularity of the sensor ring. Left uncompensated the runout will affect the quality and precision of the machined part.

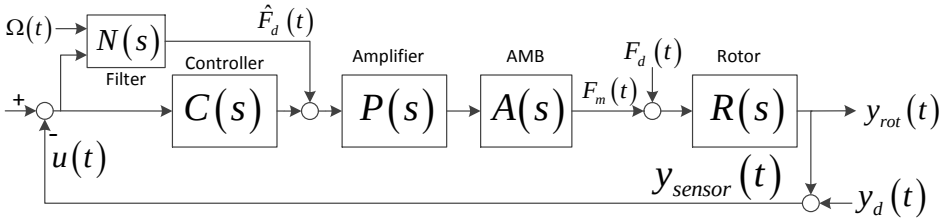

Figure 2.4: Geometric centre control block diagram (adapted from [3]).

The runout is a function of the angular position and may be determined offline or online and subsequently subtracted from the measured rotor position given that the rotor angle is known or estimated. Blom [27] presented an online estimation of the runout, modelled as a truncated Fourier series, given noisy angular position signals and extended the method to also estimate the rotor angular position if no such angle information is available.

2.2.2.3 Compensation of the gyroscopic effect

Although not a disturbance in itself, the gyroscopic effect is excited by disturbances, such as unbalance, and tends to exacerbate the response to disturbances. The control stability of a rigid rotor is analysed by Dimond *et al.* using a nondimensionalized model with different values for the ratio of polar inertia to transverse inertia, $P = \frac{J_p}{J_t}$ [9]. For the linearised force model, the rotor is asymptotically stable but tends towards marginal stability as the inertia ratio of the rotor increases. A rotor with a high inertia ratio is called a highly gyroscopic rotor. The gyroscopic effect alone does not cause the rotor to become unstable but in the presence of other destabilizing mechanisms, such as delays, the control may become unstable. It has been shown in the analyses performed by Mohamed and Emad [45] that the nonlinear model of the AMB in conjunction with the gyroscopic effect is sufficient to cause a Hopf bifurcation, i.e. the control is not stable in an equilibrium point but a limit cycle results.

Due to the destabilizing gyroscopic effect of the rotor the control gains have to be designed as speed dependent or another option is to use a model-based compensation of the gyroscopic effect via a feed-forward compensation. Feed-forward compensation of the gyroscopic effect also requires the rotor speed as an input, as pointed out by [40] (and implemented by others, e.g. [46]) and more recently revisited by Hutterer *et al.* [47, 48]. The system's sensitivity function and hence the system eigenvalues are demonstrated to be speed independent after feed-forward compensation of the gyroscopic effect. Another reason why the speed independent eigenvalues due to feed-forward compensation of the gyroscopic effect are desirable is that it simplifies the design of the unbalance control which has to take into account the sensitivity function in order to guarantee stability [8]. Hutterer *et al.* [49] demonstrated such an unbalance control including gyroscopic compensation in. The unbalance observer that they presented included estimation of the rotor

speed which in turn was utilized by the gyroscopic compensation.

2.3 Sensorless drive control

2.3.1 Basic types of sensorless control

The type of drive considered in this thesis is the three-phase permanent magnet synchronous machine (PMSM). The most basic form of sensorless control of the PMSM is by generating an open-loop voltage which is proportional to the angular speed of the rotor. This is the so called V/f or scalar control [13]. A small voltage surplus is added in order to overcome the resistive and inductive voltage drop of the stator windings and inverter non-ideality [50]. The stator current causes a magnetic field such that the rotor experiences a torque due to its permanent magnet which tends to align, but lag that of the stator. The angular difference between the revolving stator and rotor magnetic fields thus ensures the continued production of torque.

For higher efficiency and improved dynamic control of the torque, the stator current is controlled in order to independently manipulate the magnitude and phase of the current. This results in the so-called vector or field oriented control (FOC). In order to ensure that the angle of the stator's magnetic field is aligned 90° ahead of the rotor's magnetic field during motoring mode (or lagging during generating mode) the rotor angle is required, which may be obtained from an angular position sensor or may be estimated from the voltage and current measurements of the drive using an observer.

Angle and speed estimation are mainly accomplished by two possible means. The first is the estimation of the back-emf, i.e. the voltage induced in the stator due to the rotation of the rotor. The other is by the exploitation of saliency, i.e. measuring the angular dependent inductance of the machine by means of current injection and capturing the corresponding response to estimate the inductance and infer the angle from the inductance variation.

2.3.2 Sensorless drive start-up

At standstill, the rotor angle is unobservable using back-emf based methods since no back-emf is generated [51]. At low operating speeds, the back-emf magnitude is small or in the same order of magnitude as that of the voltage distortion due to inverter non-linearities. As the rotor speed increases the S/N of the estimated speed, based on back-emf methods, improves. For machines with saliency, the rotor angle may still be estimated at stand-still and low speed. One such saliency-based method is known as INFORM [52].

Yang and Hsu [53] demonstrated the combined control of a saliency and back-emf based sensorless drive. The saliency based angle estimation is used for the drive start-up and

a gradual transition to the back-emf based sensorless control is performed as the speed increases. A smooth transition is achieved by using a speed-dependent weighting function for the saliency and back-emf feedback signals used as inputs to a single phase-locked loop used for the speed and angle estimation. Previous methods relied on two separate observers. The control switched over from the saliency-based estimate to the back-emf based estimate at a threshold speed which caused an unwanted transient during the switchover. By utilizing a single observer and phase-locked loop a smooth (bumpless) transition is achieved with no current spike during the transition.

The surface mounted permanent magnet machine has little saliency and observation of the initial angle and speed is problematic. A lot of research has been done to improve the initial angle estimation accuracy and to increase the speed range for which a usable estimate may be obtained.

Wu *et al.* [54] have found that the initial angle may be determined by inducing saturation in the stator back-iron by applying square voltage pulses and measuring the resulting current. If the stator magnetic field is additive to the rotor magnetic field the inductance saturates easier and a larger current pulse results. In the case that the fields are opposing the stator inductance remains large and the current does not increase as much. By applying the voltage pulses to the various phases and measuring the response the initial rotor angle may be estimated. The authors did not account for the possible risk of demagnetization of the permanent magnets. In the case that the stator back-iron is sufficiently large a very high saturation current would be required which may endanger the permanent magnets.

By accurately accounting for the variation of the stator phase resistance the observer usable speed range may be increased, but at standstill, the rotor angle (and thus speed) is still unobservable [55]. Jansson *et al.* [56] presented an observer for non-salient machines and focused on improving the synchronization at start-up. They modified the current control law such that $i_d = \frac{i_q}{\lambda_s}$, which according to them causes the sensitivity to stator resistance variation to "vanish", at least analytically. Their start-up algorithm does not include an open-loop phase on purpose in order to show that the estimator still converges after the haphazard start-up characterized by large disturbances in the drive current and estimated states.

In the speed range that the angle is unobservable, an open-loop start-up strategy is required. Fatu *et al.* [57] have proposed a current based open-loop start-up and named it $\mathrm{I} - f$ control. The advantage of the current based start-up over that of a V/f start-up is that the current controllers inherently compensates for the inverter non-ideality and stator resistance. Hence, the so-called boost voltage does not have to be manually configured. Their method uses a low pass filter to switch from the open-loop generated angle to the back-emf based estimated angle. Although the authors claim little transient upon transitioning it is significant enough that this technique may not be called bumpless.

Special attention to improving the reliability of the rotor start-up is presented by Arafa

et al. [58]. They also overcame the start-up problem by employing a current controlled open-loop start-up.

Other means of improving the usable speed range over standard observers is with the use of advanced filtering and control techniques in order to try to overcome the effect of noise. One such method is the Rao-Blackwellized particle filter implemented on an FPGA presented by Šmídl *et al.* [59]. The filter is realized by implementing a Kalman filter on the linear part of the model and a sequential Monte Carlo run is performed only on the non-linear part of the model which improves computational efficiency.

2.4 Towards cooperation between AMB and drive

2.4.1 Similarities in development

2.4.1.1 Benefits due to increase in real-time processing capability

The AMB and sensorless drive controllers have both benefited by the increase in processing capability of digital controllers. This has allowed the implementation of complex, non-linear controllers and compensation of non-idealities in order to improve performance and to reduce cost. Compensation of non-idealities such as unbalance in AMBs or torque ripple reduction in drives result in a direct performance improvement and has an implicit cost saving as a result. For instance, the balancing specification does not have to be as stringent resulting in fewer iterations of the balancing procedures. Compensation of torque ripple in the control may result in less vibration which in turn may increase the service life of the machine.

2.4.1.2 Reduction in sensor count

Another means by which more complex controllers result in cost savings is that it aids the reduction of the number of sensors required. For AMB systems the eddy current sensors are costly and extensive research has been done in the field of self-sensing [60]. Self-sensing entails that the AMB actuator itself may be used to infer the rotor position. Self-sensing relies on the variation of the inductance of the AMB actuator which is a function of the air-gap between the electromagnet pole tip and the rotor. Self-sensing may either reduce the system cost by replacing the sensors or increasing the system reliability by acting as a redundant sensor.

The estimation of the angular position and speed from the unbalance observer proposed by Hutterer *et al.* [49] is also in the spirit of reducing the sensor count as implied by the use of the term “self-sensing” in their paper title.

In sensorless drives, the most obvious means of reducing the system cost is by replacing the angular position sensor with an angular position observer. Removing the physical

sensor entails a cost saving of more than the cost of the sensor itself. The increased cost of designing the system to make room for the sensor and its connections to the controller is also saved. In harsh operating environments removing the physical sensor also increases the system robustness.

Several secondary sensors in sensorless drive systems may also be removed in order to reduce the sensor count and hence the cost of the system. In the compensation of the inverter non-linearity, some of the earliest used methods were to directly measure (and filter) the output voltage of the drive for sensorless control. With the improvement in switching transistors, faster switching is possible with less dead-time required. Inverter non-ideality compensation algorithms also improved. The result is that voltage sensors may be removed and the inverter non-ideality may instead be compensated by feed-forward means made possible by increased processing capability.

The number of current sensors required for the drive has also decreased. The most obvious method of reducing the sensor count is by doing away with the rotor angular speed or position sensor and replacing it with a sensorless control algorithm. Examples of the position sensor may be an accurate encoder or a low-resolution hall-effect sensor. The sensorless control algorithm requires a drive current measurement. One means of reducing the current sensor count is to measure only the DC link current and from the switch state inferred from the PWM pulse pattern, the phase current may be reconstructed. This has been proposed by Blaabjerg and Pedersen [61] (or even earlier by others). The phase current reconstruction accuracy has increased over time along with the algorithm complexity made possible by increased processing capability [62]. Initially, the sensorless algorithm also required phase voltage measurement, but another means of reducing the number of sensors in the drive is to remove the phase voltage measurement and use the reference voltage in the sensorless control instead. The inverter output voltage non-linearity is compensated via feed-forward terms instead of feedback using voltage measurement [63].

The trend in increased processing capability and continuous improvement in system performance and cost reduction of the AMB and drive systems has lead to instances of interdependence between the AMB and drive systems. Lee *et al.* [15] used the speed estimate from the AMB unbalance control as a speed sensor for the induction machine drive. It was also noted that the estimated speed signal from the drive may also be used as the frequency input required for the unbalance controller. Hence, it has been shown that the drive and AMB in the same system may be used as a speed sensor required by the other system. Use of the estimated signal in one system which originated from the other system was done as an option which was serendipitously available without purposeful intent during the system design.

2.4.2 Interdependence between AMB and drive systems

The easiest form of interdependence to recognize between the AMB and drive systems is when the physical boundary between the two systems are removed. With a physical merging of the AMB and drive system the so-called self-bearing motor or bearingless drive results [28]. The stators of the AMB and drive are fused with the current in the joint stator coils controlled to yield a torque producing current and a levitation force current. The study of this thesis is the focus of cooperation between the *control* of a physically separate AMB and drive system. Many of the concepts still carry over to the case when the two systems are physically merged.

It has been suggested in the literature that the estimated speed and angle of the drive may be used in the unbalance control and gyroscopic feed-forward compensation [8]. Later it was further investigated by Hutterer *et al.* [49, 44] whom also developed a speed observer using signals internal to the unbalance control itself as a redundant speed signal source in the event of a drive fault. Without the speed and angle for unbalance control and gyroscopic feed-forward compensation, the rotor may become unstable. Unfortunately, the performance of the unbalance observer was only demonstrated during steady-state and not for rotor acceleration and that at only one particular speed.

In the case that the angle and speed estimates are generated from signals internal to the unbalance estimator itself the speed estimator bandwidth has to be higher than that of the unbalance estimator. This condition is satisfied by decreasing the unbalance estimator bandwidth. Stated differently, the unbalance estimator bandwidth could be increased if it had an independent angular position input. The reduction of the unbalance estimator bandwidth causes concern during acceleration of the rotor as it may not be fast enough to track the unbalance. As noted by Herzog *et al.* [8] the convergence of the unbalance estimator has to be fast enough to follow the peak angular acceleration, but slow enough in order to limit the bandwidth to reject noise and interference with the first bending mode.

During the literature study, as the number of examples of interdependence grew, it became apparent that a classification scheme for the interdependence between the AMB and drive systems would be useful. Such a classification scheme is proposed with the aid of Fig. 2.5. The nodes, “AMB Control” and “Sensorless drive Control”, denote vertices of a graph. The node, “CM”, denotes a condition monitoring system. The edges, **E** and **G**, denote data flows to the condition monitoring system and edges, **F** and **H**, denote potential data flows back to the respective systems in the form of alarms. The self-loops in the graph, **A** and **B**, denote instances where a non-ideality or disturbance in a system has been compensated such that the system itself benefits due to its compensation. Instances, where the primary compensation mechanism results in useful information and has been used in the accompanying system by the authors, are denoted by edges, **C** and **D**. Instances where useful information resulted from the compensation which *could* have been used or

may be used in the future are denoted with edges, **C'** and **D'**. Examples of the type of scenario in each category follow:

A Compensation of the unbalance and eccentricity due to runout with unbalance control or geometric centre control.

B Utilization of the back-emf for speed and angle estimation of the rotor.

C, C' If the compensation in **A**, such as unbalance control in the *AMB*, resulted in the estimation of the angular frequency which is in turn used in the *drive's* speed control loop.

D, D' If the estimation of the angular speed and position in **B** is used by the AMB unbalance control.

G Stator current signals, estimated back-emf, frequency, and angle.

E Rotor position within the air-gaps, estimated frequency, and angle.

H Drive safety shutdown command, speed limit reference.

F Switching over to a redundant AMB upon a failure detected by the condition monitoring. Upon condition monitoring fault detection the AMB control may reconfigure the control to use the appropriate matrix transformation for inverse force actuation. For example, the method presented by [64]. Another type of fault is the rub of the rotor against the back-up bearing, upon detection the control may enter a subroutine to recover rotor position following contact, e.g. [65].

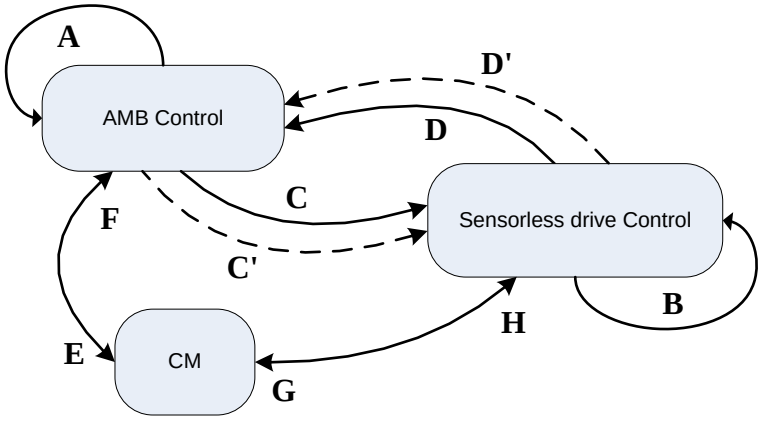

Figure 2.5: AMB and sensorless drive interdependence classification.

Corne *et al.* [66] have used an AMB test rig as a means of emulating mass unbalance and misalignment between two rotating shafts. Frequency domain signatures in the drive's

stator current were characterized which serve as a means to detect and prevent faults in mechanical bearings. It is important to note that the eccentricity detected is that within the plane of the stator of the motor. If a rigid rotor is assumed it may further be assumed that a direct correlation exists between the eccentricities of the rotor within the drive and AMB stators. If the rotor is flexible the two eccentricities may be uncorrelated but still have a dynamical relationship.

An eccentricity fault diagnosis is also presented by Ebrahimi and Faiz [67, 68, 69]. Instead of generating the fault signatures with a specialised test rig, the authors present an analytical approach with parameters obtained from FEM simulations. The generated signatures are also in the frequency domain.

Han *et al.* [70] studied the forces experienced by the rotor due to an eccentricity within the motor's stator. This force is typically named the unbalanced magnetic pull. The force experienced by the rotor in a PMSM is a function of the d-axis current. In high-speed machines, the drive usually has a relatively large current control bandwidth. Thus, the possibility exists to use the drive's stator as an extra control plain in flexible rotors to help pass the first bending mode frequency.

In self-bearing motors, the required force and torque may be quite non-linear and are both functions of the angular position and stator currents. The force and torque are modelled as polynomials of the rotor angular position and current by Manninen *et al.* [71]. The physically separated AMB and drive may beneficially borrow these type of models to suppress the disturbance force due to unbalances magnetic pull. This requires communication of the current and angular position from the drive control to the AMB control (type **D** interdependence).

Other works of note which included models of the disturbance force are that of Mukherjee *et al.* [72] and Zhao *et al.* [73], which are from the self-bearing literature. The reason that these works are of interest is that the speed and angle estimation is performed using back-emf or saliency-based methods, but they show that the radial disturbance force is also a function of the angular position. Estimation of the rotor angle from the *radial disturbance force* could not be found in the literature by the author.

Table 2.1, presents a summary of the literature in which interdependence between the drive and AMB have been identified by applying the proposed classification scheme to each instance.

Table 2.1: Previous interdependence and cooperative control uses in literature.

Authors	Reference	A	B	C	C'	D	D'	E,F	G,H
Lee *et al.*	[15]	✓		✓					
Lee *et al.*	[74]	✓			✓				
Shafai *et al.*	[75, 42]	✓			✓				
Hutterer *et al.*	[49, **?**]	✓	✓		✓	✓			
Jiang *et al.*	[3]		✓						
Corne *et al.*	[66]						✓		✓
Ebrahimi and Faiz	[67, 68, 69]						✓		✓
Manninen *et al.*	[71]					✓			
Blom	[27]	✓			✓				
Abulrub *et al.*	[65]							✓	
Raggl *et al.*	[76]		✓	✓		✓			
Meeker	[64]							✓	

2.5 Cooperative control

This chapter concludes with the proposal of the need for cooperative control between the AMB and the sensorless drive systems. The previous instances found in the literature were only of general interdependence between the AMB and drive system. Cooperation is a specialised instance of interdependence in which both systems benefit due to interaction and sharing of resources to achieve a shared goal. Referring back to Fig. 2.5, cooperation would typically be an instance in which actions denoted by edges **C** and **D,** are simultaneously present. From table 2.1, it can be observed that little attention has been given to such instances, but that there is an indication towards such cooperative control. Even if edges **C** and **D** were present, it would not necessarily constitute a cooperative control, since each system may benefit from the other *without* a common goal or a synergistic effect resulting.

The sensorless control of a bearingless pump presented by Raggl *et al.* [76] may be an instance of cooperative control between the AMB and drive. The bearingless pump has an initial angle uncertainty. The rotor angle is required in order to produce the correct levitation force on the rotor which is initially in contact with the stator. An alignment step is not allowed due to the requirement of the bearingless pump to not cause any abrasion. The initial rotor angle is determined from the radial position sensors. Thus, the drive obtained information from the AMB which is a type **B** and **C** data flow. The polarity of the rotor magnet is detected by first assuming the polarity and applying the levitation force. If it was correctly assumed the rotor will levitate and it will be confirmed by the radial position sensors. If it was erroneously assumed the rotor will not levitate (or rotate) and the assumption is corrected and the procedure is repeated. During the sensorless control of the drive, the estimated rotor angle is shared with the AMB, a type **D** data flow, in order to produce the correct levitation force. Thus, state information was shared in turn, in a cooperative fashion to achieve a shared goal between the parts which

constituted the AMB and the drive of the bearingless pump system.

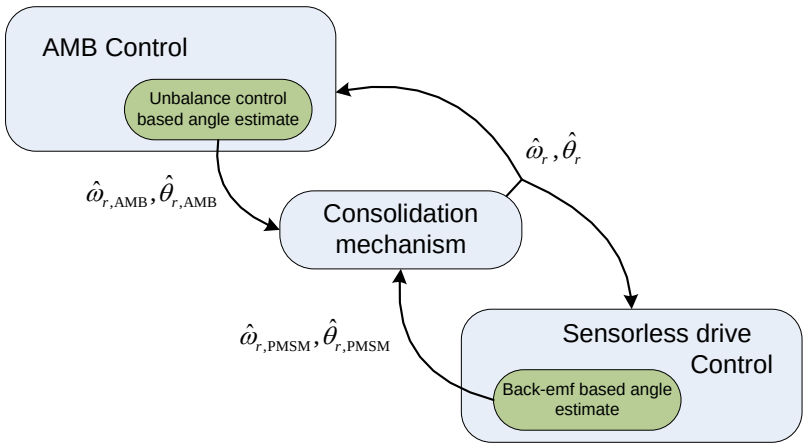

Figure 2.6: Ad-hoc coupling between the AMB and drive control systems.

Other instances, with the noted exception, in which the AMB and sensorless drive control shared state estimation were of an ad hoc nature. Typically, the state estimation of the speed and angle are performed by separate subsystems within the AMB and sensorless drive. The allocation of resources for estimation within each system is thus repeated. The estimated states are shared with the other system by means of a consolidation mechanism, which is typically controlled by means of a finite state machine. Switching over from one estimation source to another result in a transient in the consolidated output state. An instance of cooperative control may be achieved by factoring out the separate state estimation subsystems and replacing it by a single state estimation system, as presented in Fig. 2.7. The mechanism which consolidates the state information of each system should be designed with an awareness of the requirements and attributes of both systems. Also note that it is not the estimated speed and angle itself which are given as inputs to the consolidator, since those estimators have been moved outside of each system. Instead, it is the *antecedents* of the estimated states, indicated by the prime in $\left(\hat{\omega}_r, \hat{\theta}_r\right)'_{\mathrm{AMB}}$ and $\left(\hat{\omega}_r, \hat{\theta}_r\right)'_{\mathrm{PMSM}}$, which are shared with the state estimation consolidator.

The design of the AMB and sensorless vector control is thus performed with the view that the controllers will be integrated into a cooperative controller. The next chapter presents such a design of the AMB control.

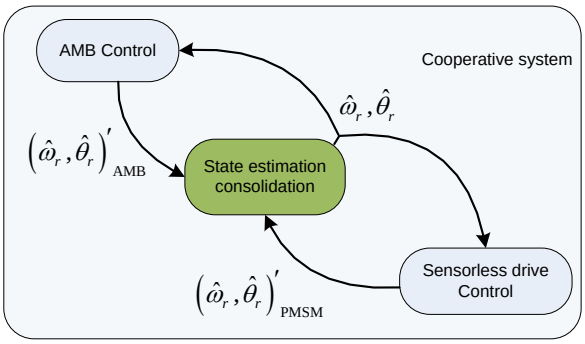

Figure 2.7: Cooperative control by means of system aware state estimation consolidation.

Chapter 3

AMB control

3.1 Introduction

The purpose of this chapter is to present the modelling and control of the AMBs used in the flywheel system studied in this thesis. The flywheel system used in this study was built during the course of three previous Master's degree projects [77, 78, 79]. Due to many non-idealities within the system, its operation did not satisfy the original specification. Thus, one aim of the models presented in this chapter is that the model fidelity should be such that the non-idealities are accounted for so that they may be compensated within the control.

An optimistic viewpoint is taken with regard to the non-idealities in that besides being unwanted, some of them may have exploitable characteristics, i.e. that they may have beneficial features. Irrespective of the presence of a desirable feature of a non-ideality, the non-ideality compensation strategy used, seek to make use of methods where the drive and the AMB system may operate cooperatively in order to address the non-ideality. With this in mind, the model(s) used is thus closely tied to the controller used in this study.

More specifically, the non-ideality which will be exploited for angular estimation of the rotor via the AMB control is the angular dependent force disturbance presented in section 3.6. The AMB control design is based on a force framework using feedback-linearisation in order for the AMB to accurately actuate a reference force, which includes the force disturbance feed-forward term. Any residual force disturbance, caused by inaccurate feed-forward force disturbance compensation is estimated by the force disturbance observer, presented in section 3.4.1.

3.2 AMB control

3.2.1 Synopsis of the test facility

As mentioned, the flywheel system to be used in this study was built during the course of three previous Master's degree projects. One project focused on the design of the three-phase inverter for the flywheel which is driven by a PMSM [79]. The inverter is connected to the PMSM via a three-phase LC low pass filter in order to reduce the electromagnetic noise interference (EMI) of the three-phase inverter. The design of the AMBs and the electrical control cabinet in which the system electronics are integrated is presented by [77]. The electrical control cabinet houses a dSPACE DS1005 controller suited for rapid prototyping control development and is equipped with the applicable expansion I/O cards. The mechanical design of the flywheel rotor and its enclosure is presented by [78]. The flywheel enclosure housing is designed as several modular units such that it is capable of supporting a vacuum for the high-speed rotor in order to reduce windage loss. The reader is referred to those Master's theses for further information regarding e.g. technical drawings, etc.

The components housed by the enclosure such as the flywheel, AMBs, PMSM, and sensors are presented in Fig. 1.1.

3.2.2 AMB modelling

A simplified diagram of a heteropolar AMB with its associated sensors, interface electronics, controller and power amplifiers is depicted in Fig. 3.1. The eddy current probes sense the position of the rotor and feed back the measured position to the controller via a signal conditioning interface board. The controller samples the signal and computes a new current reference for each AMB coil which is actuated by a current controlled power amplifier (PA), such that the rotor position maintains the desired trajectory.

The force produced by the top electromagnetic actuator/pole is given by [1]:

$$F\left(i_{y+},\, y_{+}\right) = K\left(\frac{i_{y+}}{y_{+}}\right)^{2}, \tag{3.1}$$

where i_{y+}, is the current in the actuator that pulls the rotor towards the positive direction of the y-axis, y_{+}, is the resulting air-gap of the top actuator due to the positioning of the rotor and K, equals:

$$K = \frac{1}{4}\mu_0 N^2 A_g \cos\left(\theta\right). \tag{3.2}$$

The parameters of the force gain coefficient, K, are:

- μ_0 is the permeability of free space

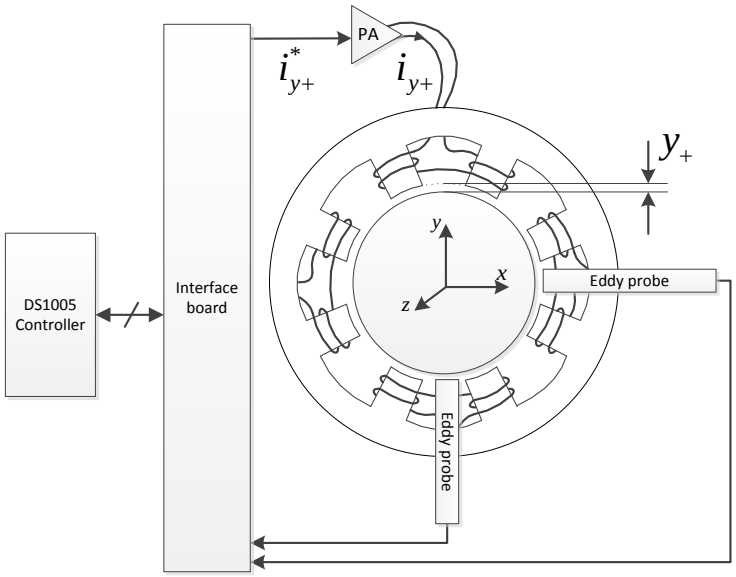

Figure 3.1: Simplified AMB system.

- A_g is the projected pole face area of a single pole
- N is the total number of turns of both pole pairs
- $\cos(\theta)$ is the term which accounts for the pole face surface normal vector being angled at an angle, θ, with respect to the actuator axis.

The force expression can be rewritten as:

$$F(i_{y+},\, y_+) = K_F\,(Li)^2\ , \tag{3.3}$$

where $K_F = \frac{1}{2}K_L\cos(\theta)$, $K_L = \frac{2}{N^2\mu_0 A_g}$ and the inductance is given by:

$$L(y_+) = \frac{N^2\mu_0 A_g}{2y_+} \tag{3.4}$$

$$= \frac{1}{K_L y_+}\,. \tag{3.5}$$

The reason for modelling the force as a function of the inductance is so that the position dependence of the inductance can be computed once and then included in the power amplifier and the force producing models of the AMB. This assumes a linear actuator model, i.e. the saturation region is avoided, such that the total and differential inductances

are equal. The differential inductance is defined as:

$$L_\partial = \left.\frac{\partial\lambda\left(y_+, i_+\right)}{\partial i_+}\right|_{\substack{y_+ = y_0 \\ i_+ = i_0}} , \tag{3.6}$$

and the total inductance as:

$$L_\Delta = \left.\frac{\Delta\lambda\left(y_+, i_+\right)}{\Delta i_+}\right|_{\substack{y_+ = y_0 \\ i_+ = i_0}} . \tag{3.7}$$

The relationship between the two types of inductances are depicted in Fig. 3.2. In order to take the saturating characteristic of the actuator into account for the power amplifier model, it depends on the differential inductance which decreases dramatically as the actuator saturates. The force model of the actuator depends instead on the total flux linkage and thus the "large signal" or total inductance.

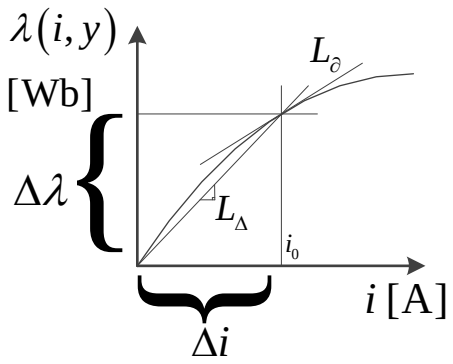

Figure 3.2: Total and differential inductance.

3.2.3 Feedback linearisation

The force reference, F^*_{y+}, produced by the force controller in the previous section needs to be converted to a current reference, i^*_{y+}, in order to be actuated by the power amplifiers which are current controlled. The derivation follows from the force equation relating the inductance and current:

$$F^*_{y+} = K_F\left(Li^*_{y+}\right)^2 \tag{3.8}$$

$$\therefore i^{*2}_{y+} = \frac{F^*_{y+}}{K_F L^2} \tag{3.9}$$

$$= F^*_{y+} K_{\frac{1}{F}} R\left(y_+\right)^2 , \tag{3.10}$$

where $R(y_+)$, is a position-dependent coefficient[1] and, $K_{\frac{1}{F}}$, is the reciprocal of K_F. Thus, the current reference squared can be calculated without performing a divide computation, which saves a significant amount of computation time. Also, instead of calculating the square root on the dSPACE controller (which would have a high computational cost) it is calculated on board by the power amplifier controller with the aid of a look-up table. Hence, the power amplifiers are utilized as a parallel computational aid to lessen the burden on the centralized controller.

Further simplification is possible by combining gains as follows:

$$i_{y+}^{*2} = F_{y+}^{*} K_{iF} y_+^2 \,, \tag{3.11}$$

where $K_{iF} = \frac{K_L^2}{K_F}$, and y_+, is the air-gap.

3.2.4 Force/current bias

In order to yield a linear controller, a force bias must be added to circumvent a finite current slew rate limit near zero force. That is, by looking at the square root function it can be observed that when the force reference is very small and suddenly increases, the corresponding amount that the current needs to increase is large and exceeds the rate that the power amplifier can increase the current. By adding a force bias the controller can stay clear from the slew rate limited region. In order to aid the selection of such a bias force, it is preferable to add the force bias in terms of a current bias. The amount of force bias to add which corresponds to a certain amount of current bias is determined as follows:

$$(F^* + F_0) \quad = \quad K_F \left(L \left(i^* + i_0\right)\right)^2 \tag{3.12}$$

$$\therefore F_0 \quad \overset{F^*, i^*=0}{\approx} \quad K_F \left(L_0 i_0\right)^2 \,, \tag{3.13}$$

where L_0, is the nominal inductance when the rotor is suspended in the centre of the air-gap.

It is important to note that the bias is *not* added in order to linearise the force-current relationship as in current biased control. Thus, the force reference for a pole pair actuating in a differential configuration is generated by:

$$F_+^* \quad = \quad F_0 + F^* \tag{3.14}$$

$$F_-^* \quad = \quad F_0 - F^* \,, \tag{3.15}$$

where F_+^*, and F_-^*, are the forces in the positive and negative directions of the axis of interest.

[1] $R(y_+) = \frac{\mathcal{R}}{N^2}$, where $\mathcal{R}$ is the reluctance.

3.3 Control in centre of gravity coordinates

3.3.1 Rigid rotor model

A rigid rotor model is used for the model of the plant and for centralized control design. Fig. 3.3, depicts the centre of gravity coordinates definition of the rigid rotor supported by AMBs.

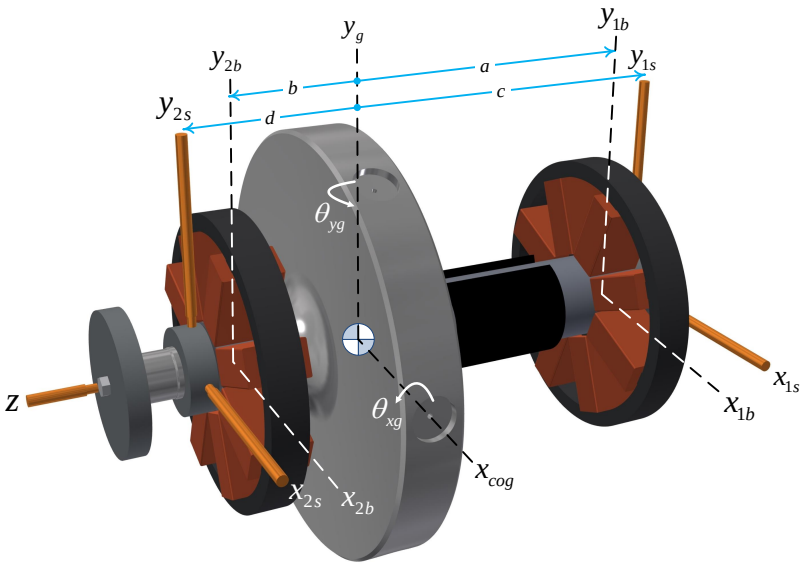

Figure 3.3: Centre of gravity coordinates definition.

The notation used is based on the model presented in [9]. Subscripts with an s denote *sensor* coordinates, b denote bearing coordinates and *cog* the centre of gravity coordinates. The governing equation for the rigid body model is given by:

$$\mathbf{M}\ddot{\mathbf{u}}_g + \Omega\mathbf{G}\dot{\mathbf{u}}_g = \mathbf{f}_{g,\text{AMB}}\,, \tag{3.16}$$

where Ω, is the angular frequency of the rotor. $\mathbf{M}$, is a diagonal inertia matrix:

$$\mathbf{M} = \begin{bmatrix} M & 0 & 0 & 0 \\ 0 & M & 0 & 0 \\ 0 & 0 & J_t & 0 \\ 0 & 0 & 0 & J_t \end{bmatrix}, \tag{3.17}$$

where M, is the mass of the rotor and J_t, is the transverse polar moment of inertia. $\mathbf{G}$, is the gyroscopic matrix:

$$\mathbf{G} = J_p \begin{bmatrix} 0 & 0 & 0 & 0 \\ 0 & 0 & 0 & 0 \\ 0 & 0 & 0 & 1 \\ 0 & 0 & -1 & 0 \end{bmatrix}. \tag{3.18}$$

The governing equation may also be represented as a signal flow diagram as in Fig. 3.4.

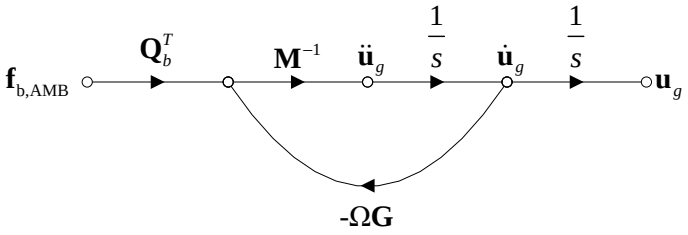

Figure 3.4: Signal flow graph of rigid rotor plant.

The set of vectors for the centre of gravity, sensor and bearing coordinates are defined as:

$$\mathbf{u}_g = \begin{bmatrix} x_{cog} \\ y_{cog} \\ \theta_{xg} \\ \theta_{yg} \end{bmatrix}, \; \mathbf{u}_s = \begin{bmatrix} x_{s1} \\ y_{s1} \\ x_{s2} \\ y_{s2} \end{bmatrix}, \; \mathbf{u}_b = \begin{bmatrix} x_{b1} \\ y_{b1} \\ x_{b2} \\ y_{b2} \end{bmatrix}. \tag{3.19}$$

The transformation from c.o.g. to sensor coordinates is given by:

$$\underbrace{\begin{bmatrix} x_{1s} \\ y_{1s} \\ x_{2s} \\ y_{2s} \end{bmatrix}}_{\mathbf{u}_s} = \underbrace{\begin{bmatrix} 1 & 0 & 0 & -c \\ 0 & 1 & c & 0 \\ 1 & 0 & 0 & d \\ 0 & 1 & -d & 0 \end{bmatrix}}_{\mathbf{Q}_s} \underbrace{\begin{bmatrix} x_g \\ y_g \\ \theta_{xg} \\ \theta_{yg} \end{bmatrix}}_{\mathbf{u}_g}, \tag{3.20}$$

and the transformation from c.o.g. to bearing coordinates is given by:

$$\underbrace{\begin{bmatrix} x_{1b} \\ y_{1b} \\ x_{2b} \\ y_{2b} \end{bmatrix}}_{\mathbf{u}_b} = \underbrace{\begin{bmatrix} 1 & 0 & 0 & -a \\ 0 & 1 & a & 0 \\ 1 & 0 & 0 & b \\ 0 & 1 & -b & 0 \end{bmatrix}}_{\mathbf{Q}_b} \underbrace{\begin{bmatrix} x_g \\ y_g \\ \theta_{xg} \\ \theta_{yg} \end{bmatrix}}_{\mathbf{u}_g}. \tag{3.21}$$

3.3.2 Full-state feedback gain design

For a full-state feedback controller the reference c.o.g. force, to be actuated by the AMB, $\mathbf{f}^*_{g,\text{AMB}}$, is produced by:

$$\mathbf{f}^*_{g,\text{AMB}} = \mathbf{K}\mathbf{x}\,, \tag{3.22}$$

where $\mathbf{K}$, is the feedback gain vector and $\mathbf{x} = [\mathbf{u}_g|\dot{\mathbf{u}}_g]$, is the centre of gravity state vector. In order to generate the reference bearing forces the c.o.g. reference force is transformed

to bearing coordinates with:

$$\mathbf{f}_{b,AMB} = \underbrace{\frac{1}{a+b}\begin{bmatrix} b & 0 & 0 & -1 \\ 0 & b & 1 & 0 \\ a & 0 & 0 & 1 \\ 0 & a & -1 & 0 \end{bmatrix}}_{\mathbf{Q}_b^{T-1}} \mathbf{f}_{g,AMB}\,. \tag{3.23}$$

The feedback gain matrix can be further expanded into terms responsible for stiffness, $\mathbf{K}_p$, and damping, $\mathbf{K}_v$, as in:

$$\mathbf{K} = [\mathbf{K}_p|\mathbf{K}_v]\ . \tag{3.24}$$

The full-state feedback control law is substituted back into the system model, yields:

$$\mathbf{M}\ddot{\mathbf{u}}_g + \Omega\mathbf{G}\dot{\mathbf{u}}_g = \mathbf{K}_p\mathbf{u}_g + \mathbf{K}_v\dot{\mathbf{u}}_g\,, \tag{3.25}$$

Furthermore, if the gyroscopic term is assumed cancelled using a cross-coupling approach, then the model further reduces to:

$$\mathbf{M}\ddot{\mathbf{u}}_g - \mathbf{K}_v\dot{\mathbf{u}}_g - \mathbf{K}_p\mathbf{u}_g = \mathbf{0}\,. \tag{3.26}$$

Taking the Laplace transform, yields:

$$\left(s^2\mathbf{M} - s\mathbf{K}_v - \mathbf{K}_p\right)\mathbf{u}_g\left(s\right) = \mathbf{0}\,. \tag{3.27}$$

Thus, the control design problem reduces to determining the pair ($\mathbf{K}_p$, $\mathbf{K}_v$) which yields a solution for the matrix characteristic equation:

$$s^2\mathbf{M} - s\mathbf{K}_v - \mathbf{K}_p = \mathbf{0}\,. \tag{3.28}$$

The tilt and translation modes[2] may be decoupled if the pair ($\mathbf{K}_p$, $\mathbf{K}_v$) is chosen appropriately. The matrix characteristic equation then reduces to two characteristic equations, one for each mode:

$$\begin{aligned} s^2M - sK_{v,t} - K_{p,t} &= 0 \\ s^2J_t - sK_{v,r} - K_{p,r} &= 0 \end{aligned}\ , \tag{3.29}$$

where $\mathbf{K}_v = \begin{bmatrix} K_{v,t} & K_{v,t} & K_{v,r} & K_{v,r} \end{bmatrix}^T$, and $\mathbf{K}_p = \begin{bmatrix} K_{p,t} & K_{p,t} & K_{p,r} & K_{p,r} \end{bmatrix}^T$, and the second superscript indicates whether the gain is for the *t*ranslation or *r*otational modes. The gains can be chosen determined by equating the characteristic equations to a prototype characteristic equation with coefficients determined by the ITAE criterion [80]. For a second order model the characteristic equation with optimal coefficients for a step

[2] i.e.(x, y) and (α, β) coordinate pair is decoupled.

input is:

$$s^2 + 1.4\omega_n s + \omega_n^2 = 0\,. \tag{3.30}$$

The gain and coefficient relationship are summarized in table 3.1, where the subscript for the natural frequency has been changed to, $_c$, in order to distinguish the natural frequency of the *c*ontroller from that of the *o*bservers which are presented later on.

Table 3.1: Full-state feedback gain design.

Modal equation	Proportional gain	Velocity gain
Translation	$K_{p,t} = \omega_{c,t}^2 M$	$K_{v,t} = 1.4\omega_{c,t} M$
Rotation	$K_{p,r} = \omega_{c,r}^2 J$	$K_{v,r} = 1.4\omega_{c,r} J$

The AMB system parameters are required for the numerical evaluation of the designed controller. The identification of the AMB and rotor parameters are presented in appendix C.

Design gains for high stiffness

The full-state feedback design for decoupled control has thus been reduced to the selection of only two parameters: the natural response frequency, ω_n, for each mode. This parameter, in turn, can be related to the maximum translational and tilt acceleration constrained by the actuator's peak force and torque production.

From [77] the maximal linear force of the AMB was designed to be $\approx 112\,\mathrm{N}$. Assume that the peak force has to be produced over half of the displacement. This results in an equivalent stiffness of:

$$\begin{aligned} K_{eq} &= \frac{\hat{F}}{g_0/2} \\ &= \frac{112\,\mathrm{N}}{500/2\,\mu\mathrm{m}} \\ &= 448 \times 10^3\,\mathrm{N}\cdot\mathrm{m}^{-1}\,. \end{aligned} \tag{3.31}$$

Along with the mass of the rotor, this equivalent stiffness results in an undamped natural frequency of:

$$\begin{aligned} \omega_{c,t} &= \sqrt{\frac{K_{eq}}{M}} \\ &= \sqrt{\frac{448 \times 10^3}{17.6}} \\ &= 159.5\,\mathrm{rad}\cdot\mathrm{s}^{-1}\,, \end{aligned} \tag{3.32}$$

for the translation mode control. Excessive amplitude displacement due to the superposition of translation and tilt modes are prevented by separating the natural frequencies of

the two modes by a certain factor. For the flywheel application in this thesis, the natural frequencies are chosen as: $\omega_{c,r} = 2 \times \omega_{c,t} \approx 319\,\mathrm{rad} \cdot \mathrm{s}^{-1}$. With these two values chosen the resulting gain constants are summarised in table 3.2.

Table 3.2: Full-state feedback gain constants for high stiffness.

Modal equation	Proportional gain	Velocity gain
Translation	$K_{p,t} = 448 \times 10^3$	$K_{v,t} = 3.93 \times 10^3$
Rotation	$K_{p,r} = 11.8 \times 10^3$	$K_{v,r} = 51.8$

Design gains for low stiffness

The design gain based on peak force at half the air-gap displacement results in quite a high stiffness. The flywheel application has relatively low external disturbances and unbalance control may be used to let the rotor rotate about its centre of mass. Thus, high disturbance rejection is not a requirement and a lower stiffness may be used. A lower control stiffness is desirable as this in turn results in a lower observer bandwidth requirement which results in higher noise rejection by the observer. Higher noise rejection results in an audibly quieter flywheel, which is desirable for end-users. In case the unbalance control becomes unstable with an initial prototype control implementation the unbalance control may be safely switched off without large control currents to compensate the unbalance due to the low stiffness. In the case of high stiffness, the control currents could be limited by the power amplifier, resulting in unstable control.

Choosing the peak force in (3.31) as 20 N, results in the control gains listed in table 3.3.

Table 3.3: Full-state feedback gain constants for low stiffness.

Modal equation	Proportional gain	Velocity gain
Translation	$K_{p,t} = 80 \times 10^3$	$K_{v,t} = 1.66 \times 10^3$
Rotation	$K_{p,r} = 2.11 \times 10^3$	$K_{v,r} = 21.9$

The selection of the control integrator gain, K_i, comes as an afterthought. Basically, it is chosen large enough for the rotor to settle fast enough to the centre of the AMB air-gap, but small enough not to significantly influence or compromise the closed-loop dynamics. An integrator gain of 20×10^3 is chosen for the tilt and the translation mode for most of the control experiments to follow.

3.4 AMB observer

The full-state feedback design requires the velocity of the rotor. The velocity can be obtained either by numeric differentiation or with the use of an observer. Numeric differentiation has the disadvantage of increasing the noise in the system which in turn may

excite unmodelled dynamics of the rotor such as the bending mode located at 710 Hz. The increased noise may also saturate the current controller in the case of measured outliers, which in turn may also destabilize the rotor. In order to avoid these problems an observer is employed which has the advantage of significantly reducing the noise of the velocity estimate.

In order to design the observer, it is usually required that the plant model is in state-space form. The state-space plant model is also typically required for the full-state feedback gain design. Instead, the gains were designed by noting that the system characteristic equation could be derived by inspection due to plant simplification. In this case, it is convenient to first transform the model in observer canonical form, since the required observer gains can be calculated via inspection from this form. The rigid rotor model is given by[3]:

$$\mathbf{M}\ddot{\mathbf{u}}_g = \mathbf{f}^*_{g,\mathrm{AMB}}\,, \tag{3.33}$$

where $\mathbf{f}^*_{g,\mathrm{AMB}}$, is the force reference generated by the full-state feedback. The first state variable of the observer is chosen as the estimated position, $\hat{\mathbf{x}}_1 = \hat{\mathbf{u}}_g$, and the second state variable as the estimated velocity $\hat{\mathbf{x}}_2 = \dot{\hat{\mathbf{x}}}_1 = \dot{\hat{\mathbf{u}}}_g$.

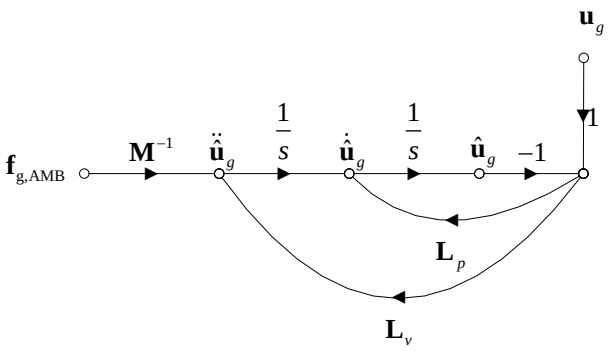

Figure 3.5: Signal flow graph of rigid rotor state observer.

Fig. 3.5 depicts the signal flow graph of the rigid rotor model with the observer gains included in the feedback. $\boldsymbol{L}_p$ is the gain for position and $\boldsymbol{L}_v$ is the gain for velocity. Each gain can be further resolved into the gains for translation and rotation modes, i.e. $\mathbf{L}_p = \begin{bmatrix} L_{p,t} & L_{p,t} & L_{p,r} & L_{p,r} \end{bmatrix}^T$, and $\mathbf{L}_v = \begin{bmatrix} L_{v,t} & L_{v,t} & L_{v,r} & L_{v,r} \end{bmatrix}^T$.
The state equation for the estimated rigid rotor observer, from the signal flow graph, is:

$$\begin{bmatrix} \dot{\hat{\mathbf{x}}}_1 \\ \dot{\hat{\mathbf{x}}}_2 \end{bmatrix} = \begin{bmatrix} 0 & 1 \\ 0 & 0 \end{bmatrix} \begin{bmatrix} \hat{\mathbf{x}}_1 \\ \hat{\mathbf{x}}_2 \end{bmatrix} + \mathbf{M}^{-1}\mathbf{f}^*_{g,\mathrm{AMB}} + \mathbf{L}\left(\mathbf{x}_1 - \hat{\mathbf{x}}_1\right)\,. \tag{3.34}$$

[3] Assuming that the gyroscopic term is cancelled via a feed-forward term.

The required observer gains are determined by considering the observer error dynamics, thus the inputs $\boldsymbol{f}^*_{g,\mathrm{AMB}}$, and $\boldsymbol{x}_1$, can be set equal to zero, resulting in:

$$\begin{bmatrix} \dot{\hat{\mathbf{x}}}_1 \\ \dot{\hat{\mathbf{x}}}_2 \end{bmatrix} = \begin{bmatrix} -\mathbf{L}_p & 1 \\ -\mathbf{L}_v & 0 \end{bmatrix} \begin{bmatrix} \hat{\mathbf{x}}_1 \\ \hat{\mathbf{x}}_2 \end{bmatrix} . \tag{3.35}$$

Two observations[4] can be made:

- The system of equations are seen to be in the observer canonical form, thus the observer gain required to satisfy a desired characteristic equation can be determined from inspection.
- The incredible result that the system of equations is completely free from all model parameters, i.e. the observer poles are freely determined only by the observer gain[5].

Even though it may appear that the observer gains can be selected freely, the selection is still bounded by several factors:

- The measured input to the observer passes through anti-aliasing filters and is also further delayed by the ADC's sample-and-hold. Therefore, the observer bandwidth should at least be less than the measurement bandwidth;
- furthermore, the observer bandwidth is primarily reduced to reject measurement noise.

It is a common requirement that the observer bandwidth should be an order faster than the underlying system dynamics, in order to avoid unwanted phase shift in the observation. The characteristic polynomial for the observer is:

$$\det\left(s\mathrm{I} - \mathrm{A}\right) = s^2 + \mathbf{L}_p s + \mathbf{L}_v \, . \tag{3.36}$$

The prototype characteristic equation is chosen once more using the ITAE criterion [80]:

$$s^2 + 1.4\omega_n s + \omega_n^2 = 0 \, . \tag{3.37}$$

The natural frequency for the observed modes is chosen an order of magnitude greater than the natural frequency for the controlled modes, i.e. $\omega_{o,t} = 10\,\omega_{c,t}$, and $\omega_{o,r} = 10\,\omega_{c,r}$. The design of the observer gains is summarized in table 3.4.

The observer gain constants obtained by the design procedure, corresponding to the high stiffness control, are given in table 3.5.

[4] Pun unintended!

[5] Of course, the observer is not immune to modelling errors, since the observer inputs rely on the bearing-to-c.o.g. coordinate transformation.

Table 3.4: Observer gain design.

Modal equation	Proportional gain	Velocity gain
Translation	$L_{p,t} = 1.4\omega_{o,t}$	$L_{v,t} = \omega_{o,t}^2$
Rotation	$L_{p,r} = 1.4\omega_{o,r}$	$L_{v,r} = \omega_{o,r}^2$

Table 3.5: Observer gain constants for high stiffness control.

Modal equation	Proportional gain	Velocity gain
Translation	$L_{p,t} = 2.23 \times 10^3$	$L_{v,t} = 2.55 \times 10^6$
Rotation	$L_{p,r} = 4.47 \times 10^3$	$L_{v,r} = 10.02 \times 10^6$

Theoretically, the observer gains corresponding to the high stiffness control can also be used for the low stiffness control (i.e. it would still be stable), but this results in unnecessary high bandwidth. The observer gains, corresponding to the low stiffness control, are given in table 3.9.

Table 3.6: Observer gain constants for low stiffness.

Modal equation	Proportional gain	Velocity gain
Translation	$L_{p,t} = 943.9$	$L_{v,t} = 455 \times 10^3$
Rotation	$L_{p,r} = 1.89 \times 10^3$	$L_{v,r} = 1.82 \times 10^6$

3.4.1 Extended observer design

The observer can be extended in order to include the estimation of external (disturbance) load forces. The extended observer state equation is:

$$\begin{bmatrix} \dot{\hat{\mathbf{x}}}_1 \\ \dot{\hat{\mathbf{x}}}_2 \\ \dot{\hat{\mathbf{x}}}_3 \end{bmatrix} = \begin{bmatrix} 0 & 1 & 0 \\ 0 & 0 & 1 \\ 0 & 0 & 0 \end{bmatrix} \begin{bmatrix} \hat{\mathbf{x}}_1 \\ \hat{\mathbf{x}}_2 \\ \hat{\mathbf{x}}_3 \end{bmatrix} + \mathbf{M}^{-1}\mathbf{f}_{g,\mathrm{AMB}}^{*} + \mathbf{L}\left(\mathbf{x}_1 - \hat{\mathbf{x}}_1\right), \tag{3.38}$$

which has the following error dynamics:

$$\begin{bmatrix} \dot{\hat{\mathbf{x}}}_1 \\ \dot{\hat{\mathbf{x}}}_2 \\ \dot{\hat{\mathbf{x}}}_3 \end{bmatrix} = \begin{bmatrix} -\mathbf{L}_p & 1 & 0 \\ -\mathbf{L}_v & 0 & 1 \\ -\mathbf{L}_a & 0 & 0 \end{bmatrix} \begin{bmatrix} \hat{\mathbf{x}}_1 \\ \hat{\mathbf{x}}_2 \\ \hat{\mathbf{x}}_3 \end{bmatrix}. \tag{3.39}$$

Thus, the characteristic polynomial for the extended observer is given by:

$$p\left(s\right) = s^3 + \mathbf{L}_p s^2 + \mathbf{L}_v s + \mathbf{L}_a\,. \tag{3.40}$$

The extended observer frequency is kept the same as for the original observer design. The third order ITAE polynomial is given by [80]:

$$s^3 + 1.75\omega_n s^2 + 2.15\omega_n^2 s + \omega_n^3\,. \tag{3.41}$$

The bearing coordinate force disturbance, from the estimated states, is given by:

$$\hat{\mathbf{F}}_b = \left(\mathbf{Q}_b^{-1}\right)^T \left(\mathbf{M}\dot{\hat{\mathbf{x}}}_2 - \mathbf{f}_{g,AMB}^*\right) , \tag{3.42}$$

where $\mathbf{Q}_b^{-1}$, is a coordinate transformation from c.o.g. to bearing coordinates. Hence, the disturbance force is the difference between the position controller reference force and the actual resultant force as estimated by the observer.

The design of the extended observer gains is summarized in table 3.7.

Table 3.7: Extended observer gain design.

Modal equation	Proportional gain	Velocity gain	Acceleration gain
Translation	$L_{p,t} = 1.75\omega_{o,t}$	$L_{v,t} = 2.15\omega_{o,t}^2$	$L_{a,t} = \omega_{o,t}^3$
Rotation	$L_{p,r} = 1.75\omega_{o,r}$	$L_{v,r} = 2.15\omega_{o,r}^2$	$L_{a,r} = \omega_{o,r}^3$

The extended observer gain constants obtained by the design procedure, corresponding to the high stiffness control gains, are given in table 3.8.

Table 3.8: Extended observer gains for high stiffness control.

Modal equation	Proportional gain	Velocity gain	Acceleration gain
Translation	$L_{p,t} = 2.79 \times 10^3$	$L_{v,t} = 5.47 \times 10^6$	$L_{a,t} = 4.06 \times 10^9$
Rotation	$L_{p,r} = 5.58 \times 10^3$	$L_{v,r} = 21.9 \times 10^6$	$L_{a,r} = 32.5 \times 10^9$

The extended observer gains corresponding to the low stiffness control gains are given in table 3.9.

Table 3.9: Extended observer gains for low stiffness control.

Modal equation	Proportional gain	Velocity gain	Acceleration gain
Translation	$L_{p,t} = 1.18 \times 10^3$	$L_{v,t} = 977 \times 10^3$	$L_{a,t} = 306 \times 10^6$
Rotation	$L_{p,r} = 2.36 \times 10^3$	$L_{v,r} = 3.91 \times 10^6$	$L_{a,r} = 2.45 \times 10^9$

3.5 Unbalanced magnetic pull

Several works have considered the effect of the unbalanced magnetic pull (UMP) due to the permanent magnets of the motor. Within the realm of electrical machines equipped with roller bearings, the disturbance force is of concern as it influences the vibration, audible noise and the bearing lifetime [81]. In [82] the effect of the winding structure, pole-pairs and stator slot number on the UMP is investigated. For a high-speed flywheel application, these machine parameters are constrained for efficiency reasons and the disturbance frequency cannot simply be increased in order to reduce the ripple amplitude. In bearingless drives, the model of the magnetic pull due to the permanent magnets is of importance as it pertains to its main operation, i.e. levitation of the rotor [83].

In this work the drive and AMB magnetic structures are considered decoupled from each other, i.e. they are separate modular units, but the effect of the UMP on the radial AMB controller is considered. A similar setup is considered by [70], in which the force due to the permanent magnet is modelled as a stiffness model. Due to the high number of poles of their motor, the force due to the motor is mainly dependent on the eccentricity and not as much on the angle of the rotor, i.e. only a force ripple results.

The disturbance force due to the permanent magnets of the motor in this work is also approximated with a stiffness model, i.e. Hooke's law. Since the flywheel uses a 2-pole PMSM, the disturbance force is also a function of the angular position of the rotor. Fig. 3.6 depicts the model of the flywheel with a spring located at the centre of the magnet coordinates.

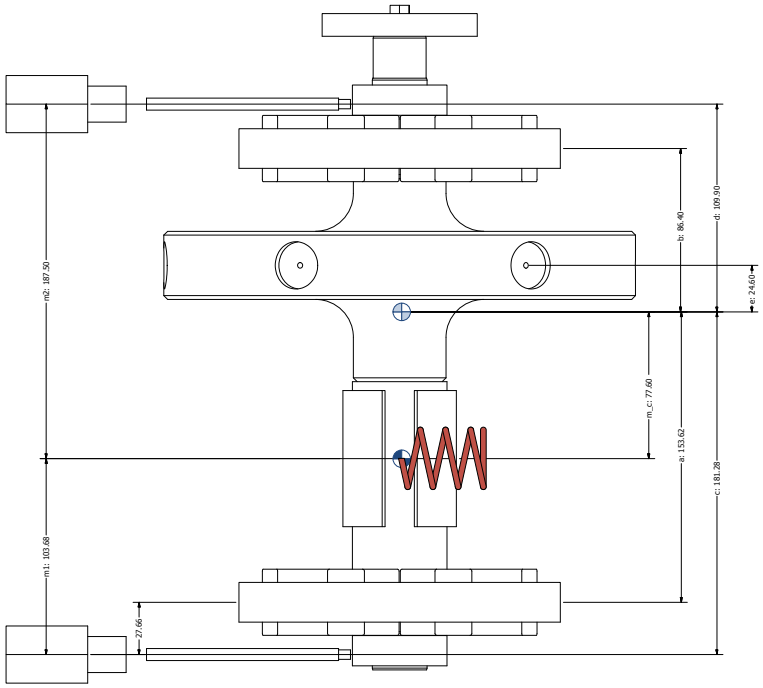

Figure 3.6: Spring force model of unbalanced magnetic pull and coordinates.

The force acting on the centre of gravity due to displacement, (x_{mc}, y_{mc}), of the rotor within the stator air-gap of the PMSM is modelled as:

$$\begin{aligned} F_x^{PM} &= k_x x_{mc} + F_{x0} \\ F_y^{PM} &= k_y y_{mc} + F_{y0} \\ M_x^{PM} &= m_c F_x^{PM} + M_{x0} \\ M_y^{PM} &= m_c F_y^{PM} + M_{y0}\,, \end{aligned} \tag{3.43}$$

where m_c, is the couple length from the magnet centre to the centre of gravity, $k_{x|y}$ is a stiffness associated with the $x|y$-axes, $F_{x|y0}$ is a constant force offset and $M_{x|y0}$ is a constant torque offset. Equation (3.43) can be considered as being the first order terms

of a Taylor expansion of the actual non-linear force relationship. The sensor coordinates are transformed to the magnet centre coordinates by:

$$\underbrace{\begin{bmatrix} x_{mc} \\ y_{mc} \end{bmatrix}}_{\mathbf{u}_{mc}} = \underbrace{\frac{1}{m_1+m_2}\begin{bmatrix} m_2 & 0 & m_1 & 0 \\ 0 & m_2 & 0 & m_1 \end{bmatrix}}_{\mathbf{Q}_{mc}} \underbrace{\begin{bmatrix} x_{1s} \\ y_{1s} \\ x_{2s} \\ y_{2s} \end{bmatrix}}_{\mathbf{u}_s}. \tag{3.44}$$

The parameters of the permanent magnet are determined by the following test procedure:

- The rotor is suspended with a minimal amount of the bias force (current);
- a spiral position reference slowly sweeps the rotor position reference.
- The reference point of the rotor for when the control is active is the magnetic centre (presented in section 3.7).
- The rotor is not rotating during this test.
- During the sweep, the radial AMB control is periodically switched off for a brief period, by setting the reference current to the power amplifiers to zero,
- and then turned back on to allow the rotor to restabilize onto the spiral trajectory.
- During the control-free time, the rotor is free to accelerate into the direction caused by the permanent magnet disturbance force.
- The test is repeated for the rotor aligned from 0° to 340°, in 20° steps.

An example spiral trajectory response using the proposed procedure is as depicted in Fig. 3.7. Note that the top and bottom mean positions differ somewhat, due to differences in the magnetic centre of the top and bottom AMBs. Although not ideal, the deviation from the geometric centre is well within the confines of the air-gap ($\pm 500\,\mu$m) and retainer bearings ($\pm 350\,\mu$m).

The parameters of the UMP model are fitted by comparing the rigid body model response under the influence of the UMP disturbance model with the measured position during the free acceleration. The L_2-norm is used as the cost function. The Response Optimization® tool in Simulink® is used to fit the parameters. The parameters identified by the estimation procedure as a function of the rotor angular position is reported in Figs. 3.8 and 3.9. It can be seen that the stiffness parameter varies with a period of π rad, whilst the offset force and torque varies with a period of 2π rad. Hence, the stiffness and bias force and torque parameters are modelled as:

$$k = a\cos(2\theta) + b\cos(2\theta) + c \tag{3.45}$$

$$F_0|M_0 = a\cos(\theta) + b\cos(\theta) + c\,. \tag{3.46}$$

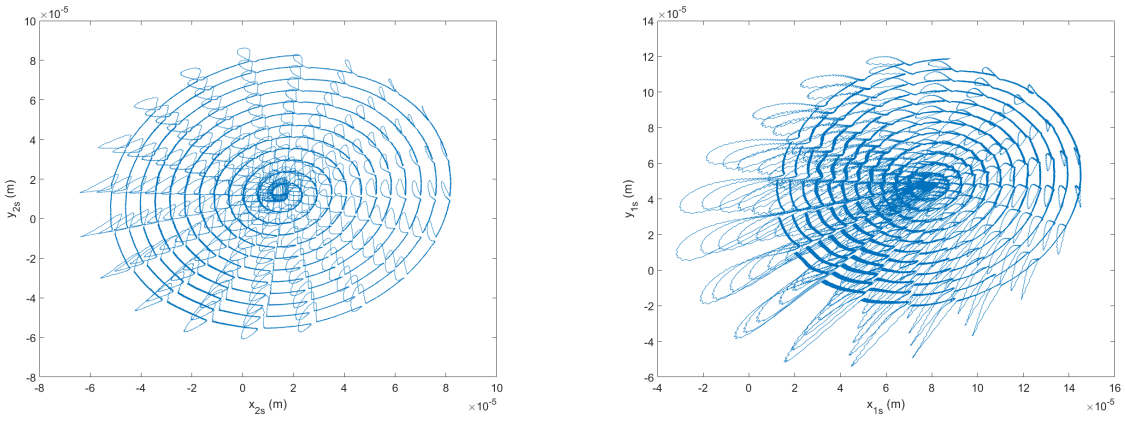

(a) Top AMB rotor response.

(b) Bottom AMB rotor response.

Figure 3.7: Spiral trajectory rotor response with free acceleration during zero control pulse.

The numeric solution for the parameter fit of the permanent magnet disturbance force model is presented in table 3.10.

Table 3.10: Disturbance force trigonometric function fit parameters.

(a) x-axis parameters.

	K_x $[\mathrm{N.m^{-1}}]$	F_{x0} [N]	M_{x0} [N.m]
a	-5576	0.4702	-0.02051
b	987.6	-2.38	0.3056
c	22.75e3	-1.225	-0.01801

(b) y-axis parameters.

	K_y $[\mathrm{N.m^{-1}}]$	F_{y0} [N]	M_{y0} [N.m]
a	5065	-2.253	-0.2993
b	-781.1	-0.4562	-0.01596
c	21.66e3	-0.1297	-0.2903

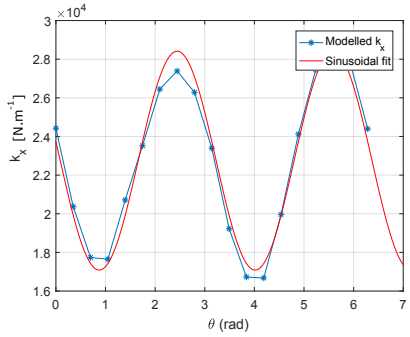

(a) k_x.

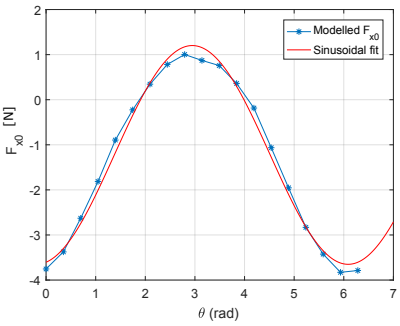

(b) F_{x0}.

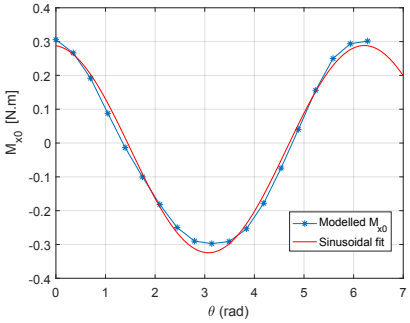

(c) M_{x0}.

Figure 3.8: Fitted unbalanced magnetic pull, x-axis parameters.

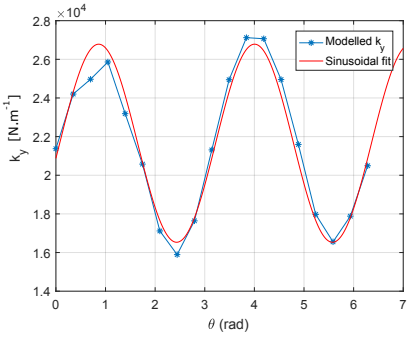

(a) k_y.

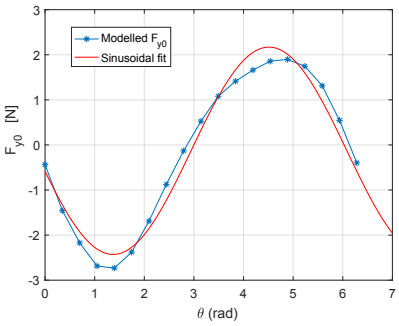

(b) F_{y0}.

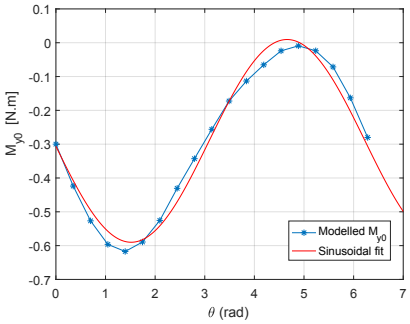

(c) M_{y0}.

Figure 3.9: Fitted unbalanced magnetic pull, y-axis parameters.

The effectiveness of adding the unbalanced magnetic pull compensation to the control is demonstrated by repeating the pulsed spiral test. The difference is that in this case, instead of switching the total reference force to zero as is done to characterize the disturbance force, only the control reference force component is switched to zero. Thus, the unbalanced magnetic pull compensation feed-forward term is still present during the period that the control reference force is pulsed to zero. The rotor response with compensation is demonstrated in Fig. 3.10.

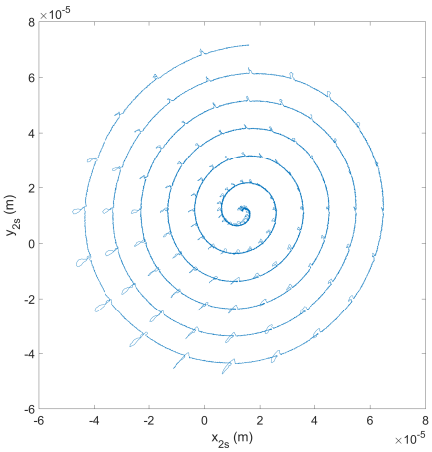

(a) Top AMB rotor response ($i_b = 0.5\,\mathrm{A}$).

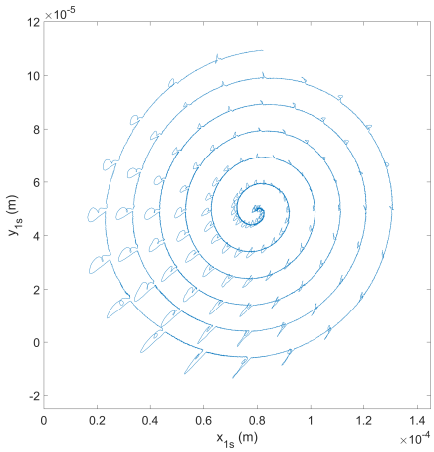

(b) Bottom AMB rotor response. ($i_b = 0.5\,\mathrm{A}$)

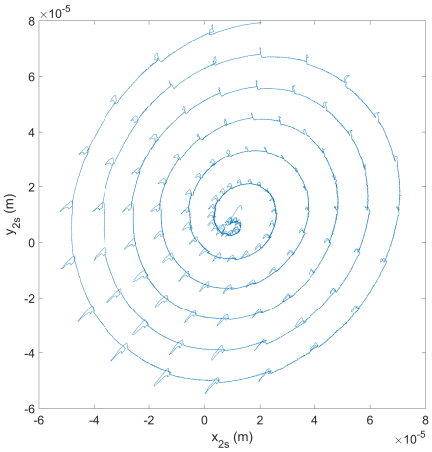

(c) Top AMB rotor response. ($i_b = 1.5\,\mathrm{A}$)

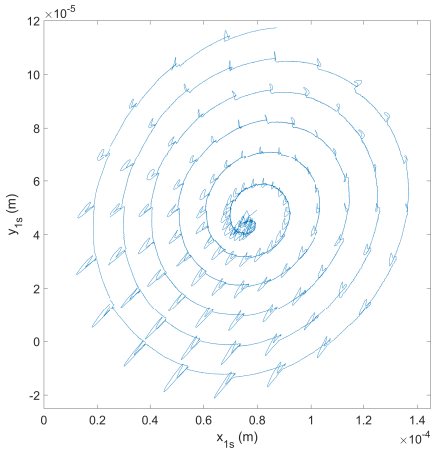

(d) Bottom AMB rotor response. ($i_b = 1.5\,\mathrm{A}$)

Figure 3.10: Spiral trajectory rotor response with feed-forward compensation.

The test is repeated with a reduced bias current of $i_b = 0.5\,\mathrm{A}$, and a normal bias current of $i_b = 1.5\,\mathrm{A}$. It can be seen that in the case of the higher bias current the spiral trajectory response is somewhat ellipsoid, indicating that the unbalanced magnetic pull is not the only source of disturbance, but that inexact reference force actuation by the AMB also need to be compensated. The manner in which the disturbance force was characterised, i.e. by switching off all of the radial AMBs to achieve free acceleration under the influence

of the permanent magnet disturbance force is thus not able to capture the disturbance force due to higher order force function characteristics and cross-coupling due to the AMB. An improved disturbance characterisation and compensation model, which is able to take these other disturbance sources into account, is presented in section 3.6.

3.6 Generalized disturbance force model

3.6.1 Initial model

The rotor control response with the unbalanced magnetic pull compensation is an improvement over the uncompensated case, but there are other sources of disturbance which are unaccounted for by the unbalanced magnetic pull model. In order to exploit the angular dependence of the unbalanced magnetic pull the remaining disturbance forces also need to be accounted for. The aim of the generalized disturbance force model is thus to combine static disturbances due to the permanent magnet and inaccurate force actuation by the AMB. Dynamic disturbance forces such as the unbalance are not accounted for in this model. The remaining force disturbances are caused by higher order non-linearity in the force-current relationship of the AMB, as well as cross-coupling between the AMB's x-and y-axes of each pole.

The force-current relationship of (3.8) is merely an analytical approximation of the true force-current relationship. The non-linear characteristics of the magnetic material, such as saturation, introduce higher order terms into the true force-current function, which can be represented as:

$$F_{y+} = K_F \left(L i_{y+}\right)^2 + \sum_i^n f_i \left(i_{y+},\, y+\right) , \tag{3.47}$$

where the residual term $\sum_i^n f_i \left(i_{y+},\, y+\right)$, captures the higher order terms. The functions, f_i, may be chosen as multinomial functions of the current and the air-gap. The force function accuracy can be arbitrarily increased by adding more higher order terms.

Cross-coupling between the x-and y-axes result due to air-gap irregularities, lamination tolerance, and asymmetric rotor placement within the air-gap. Fig. 3.11, serves as an example where the asymmetry between two poles of the same electromagnet has been exaggerated. The rotor is suspended at the magnetic centre using the procedure presented in section 3.7, thus if cross-coupling results due to lack of rotor centering, some other unaccounted phenomenon is influencing the magnetic centre to deviate. Since the AMB poles are all simultaneously exited during the magnetic centring procedure some magnetic asymmetry (such as magnetic grain orientation of the laminations) may influence the magnetic centre to deviate. Regardless of the exact cause of cross-coupling, the following development accounts for an approximation of the cross-coupling force.

The unequal air-gaps of each pole could also have arisen due to rotor non-circularity. The

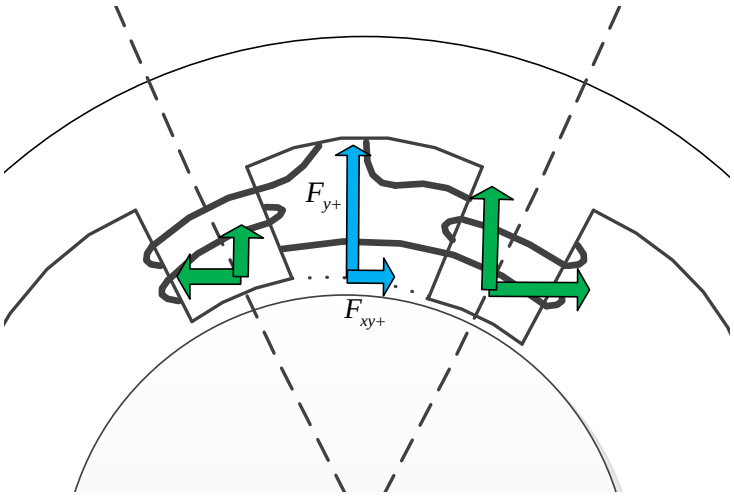

Figure 3.11: Example of AMB pole asymmetry (exaggerated).

result is that the x-axis component of the force does not cancel for each y-axis electromagnet pole. The same is true for the x-axis force producing poles, i.e. it would also generate a non-zero y-axis force. This cross-coupling disturbance force is a function of flux in each electromagnet pole of the heteropolar AMB. Hence, the force function for the positive y-axis should also be a function of the currents in the adjacent x-axis poles:

$$F_{y+} = K_F \left(Li_{y+}\right)^2 + \sum_i^n f_i \left(i_{y+},\, y+\right) + \sum_i^n f_i \left(i_{x+},\, x+\right) + \sum_i^n f_i \left(i_{x-},\, x-\right) . \tag{3.48}$$

The inversion of (3.48), to obtain the required reference current from the reference force, is a highly computationally intensive task (if not impossible in real-time). Fortunately, there are some simplifying assumptions at our disposal in order to obtain an approximation. The first assumption is that the rotor disturbances are such that the control currents do not experience extreme deviations from the operating bias current. The second assumption is that the rotor deviations due to the disturbances are also limited. These assumptions allow for a small signal linearisation of the disturbance forces for the rotor operating about the desired reference point (i.e. the magnetic centre). The higher order terms in the force function and the cross-coupling terms thus become functions of the bias current:

$$F_{y+} = K_F \left(Li_{y+}\right)^2 + \sum_i^n f_i \left(i_b,\, y\right) + \sum_i^n f_i \left(i_b,\, x\right) \tag{3.49}$$

$$= K_F \left(Li_{y+}\right)^2 + F_{by} \left(i_b,\, x,\, y\right) . \tag{3.50}$$

A similar relation in the case of the x-axis force disturbance exists. The disturbance force is assumed in bearing coordinates, hence the b subscript. Equation (3.50), represents only the compensation of the disturbance force due to the AMB bias current. The original aim is to improve the compensation of the unbalanced magnetic pull as presented in section 3.5.

The unbalanced magnetic pull force was considered only as a function of the rotor angular position, θ_r, but in reality it should also be a function of the d-axis current component. The permanent magnet field is aligned to the d-axis. Thus, an increasing i_d causes an increase in the stator field, which causes a repelling force towards the rotor's magnetic field. Hence, the disturbance force may be extended by including the functional dependence on i_d and is thus characterised as:

$$F_{y+} = K_F \left(Li_{y+}\right)^2 + F_{by}\left(i_b,\, x,\, y,\, \theta_r, i_d\right) . \tag{3.51}$$

The disturbance force may be compensated via a feed-forward term which is added to the PD controller generated reference force. Note that only the PD controller reference force feeds into the rigid body observer. Since the disturbance force cancels with the feed-forward term the feed-forward component must not pass into the observer.

The generalized disturbance force is modelled as a linear transformation and offset force in bearing coordinates. The decentralized version of the generalized disturbance force model is given by:

$$\mathbf{F}_b = \underbrace{\mathbf{\Gamma}\left(\mathbf{u}_b - \mathbf{u}_{mc}\left(\theta_r\right)\right)}_{1} + \underbrace{\mathbf{F}_{b0}\left(\theta_r,\, i_d\right)}_{2}, \tag{3.52}$$

where $\mathbf{u}_b = \begin{bmatrix} x_{1b} & y_{1b} & x_{2b} & y_{2b} \end{bmatrix}^{\mathrm{T}}$, is the measured rotor position in bearing coordinates, $\mathbf{u}_{mc}\left(\theta_r\right) = \begin{bmatrix} \mathrm{MC_{x1}} & \mathrm{MC_{y1}} & \mathrm{MC_{x2}} & \mathrm{MC_{y2}} \end{bmatrix}^{\mathrm{T}}$ is the magnetic centre feed-forward term presented in section 3.7.2. $\mathbf{\Gamma}$ is a stiffness matrix, defined as:

$$\mathbf{\Gamma} = \begin{bmatrix} \gamma_{11} & \gamma_{12} & 0 & 0 \\ \gamma_{21} & \gamma_{22} & 0 & 0 \\ 0 & 0 & \gamma_{33} & \gamma_{34} \\ 0 & 0 & \gamma_{43} & \gamma_{44} \end{bmatrix}, \tag{3.53}$$

where each entry is a sum of the first and second harmonic components, including an offset:

$$\gamma_{11} = a\sin\left(2\theta_r\right) + b\cos\left(2\theta_r\right) + c\sin\left(\theta_r\right) + d\cos\left(\theta_r\right) + e\,. \tag{3.54}$$

The off-diagonal zero entries in the stiffness matrix, $\mathbf{\Gamma}$, indicate that there is no coupling between the top and bottom AMBs, only between the axes within an AMB.

The DC offset force, $\mathbf{F}_{b0}(\theta_r) = \begin{bmatrix} \mathrm{F_{bx1}} & \mathrm{F_{by1}} & \mathrm{F_{bx2}} & \mathrm{F_{by2}} \end{bmatrix}^{\mathrm{T}}$, has a similar expansion with the difference that the coefficients are also functions of the drive's d-axis current, i_d:

$$\begin{aligned} F_{b0\_x1}(\theta_r, i_d) &= a\sin(2\theta_r) + b\cos(2\theta_r) + c\sin(\theta_r) + d\cos(\theta_r) + e && (3.55)\\ a(i_d) &= m_a i_d + c_a && (3.56)\\ b(i_d) &= m_b i_d + c_b && (3.57)\\ c(i_d) &= m_c i_d + c_c && (3.58)\\ d(i_d) &= m_d i_d + c_d && (3.59)\\ e(i_d) &= m_e i_d + c_e\,. && (3.60) \end{aligned}$$

The procedure to determine the coefficients of the stiffness matrix (first term in (3.52)) is done by characterising the required control force for a spiral reference rotor trajectory. The spiral sweep is performed at rotor angles which range from $0° - 340°$ in $20°$ steps. It has been found that the stiffness matrix $\mathbf{\Gamma}$ is essentially independent of the PMSM drive current. The spiral sweep which excites the disturbance force as a function of the deviation of the rotor from the magnetic centre is thus performed at a fixed drive current of 2.5 A. Fig. 3.12a, serves as an example of the characterisation procedure which depicts the rotor response to a spiral loop reference. The integrator gain of the PID controller is set quite high (e.g. 200×10^3) so that the reference spiral trajectory is followed closely. The sweep is performed over a long period, i.e. 60 s, which also aids in following the reference trajectory closely. The required controller reference force is depicted in Fig. 3.12. The purpose of the stiffness matrix is thus to transform a circular reference in the position coordinates into an elliptical compensation force. Note that the centroid of the elliptical control force is different at different rotor angles. The stiffness matrix does not account for this. It is instead the purpose of the second term of (3.52) to account for the offset force.

The dependence of the disturbance force offset (second term in (3.52)) on the rotor angle and drive current is in turn independent of the rotor deviation and is thus characterized by slowly rotating the rotor with the d-axis current ranging from $2 - 10$ A in 2 A steps with the rotor held fixed at the magnetic centre. The offset force for different amounts of d-axis drive current is presented in Fig. 3.13.

The difference between the test procedures for the unbalanced magnetic pull and the generalized force disturbance is that for the unbalanced magnetic pull the disturbance force is characterized dynamically (i.e. from acceleration due to the disturbance force) whilst for the generalized force disturbance, the static force produced by the controller is recorded. The unbalanced magnetic pull test procedure thus determines the actual acceleration without any regard to errors in the inverse force model parameters. Residual errors in the inverse force model parameters are indirectly accounted for by the reference force generated by the PID controller. Thus, the generalized disturbance force model accounts for parameter errors, higher order force-current terms and cross-coupling.

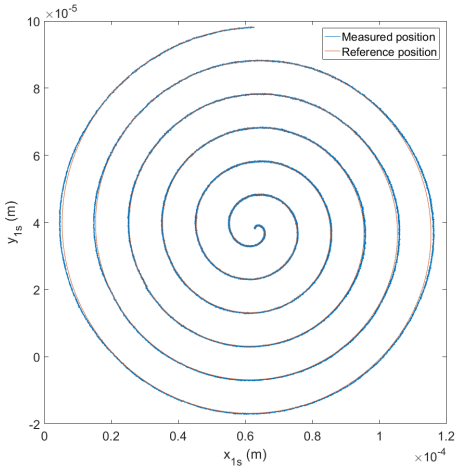

(a) Spiral loop tracking with high integrator gain ($\theta_r = 0°$).

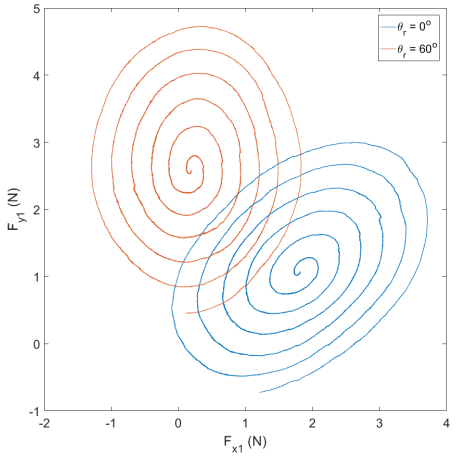

(b) Control force required to track reference spiral trajectory.

Figure 3.12: Stiffness matrix characterization with $i_d = 2.5\,\mathrm{A}$ (bottom AMB only).

The effectiveness of the generalized disturbance force model is evaluated by repeating the sweep for the spiral trajectory, but this time with a low integrator gain (i.e. 20×10^3). The comparison of the rotor response with and without the feed-forward compensation switched on is depicted in Fig. 3.14.

The generalized disturbance force model parameters are listed in table 3.11. In order to improve the computational overhead, those coefficients which had a small impact on the residual error (e.g. less than 15% difference) of the fit were trimmed from the model. It can be seen that with the feed-forward model switched on a small control error results, hence little control effort is required to cancel the disturbance force. It is important to note that the feed-forward model had the correct rotor angle as input. If the rotor angle has an error then more control effort is required to cancel the disturbance force and a larger trajectory deviation results. This property is further exploited in chapter 5, such that the disturbance force is used to search for the true rotor angle which minimizes the

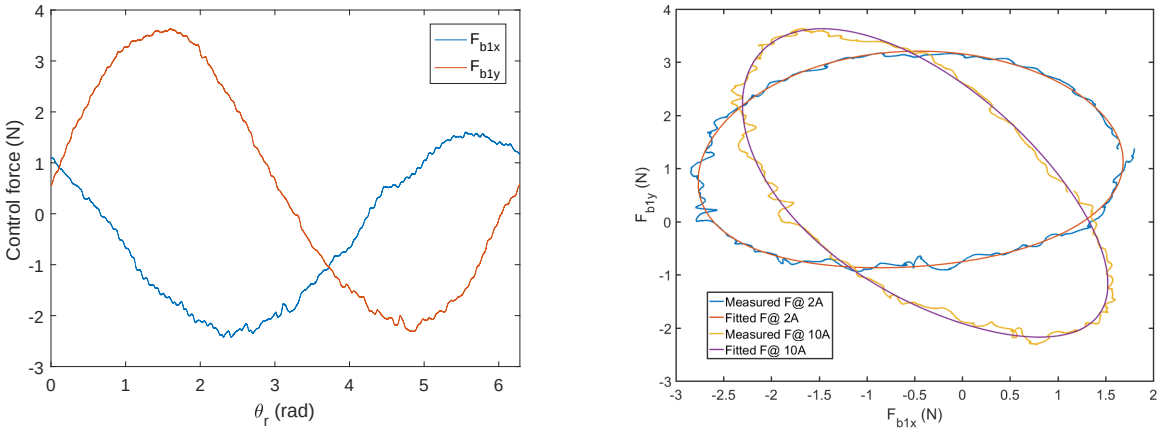

(a) Angular dependence. (b) Drive current dependence.

Figure 3.13: Current dependent disturbance force offset characterisation.

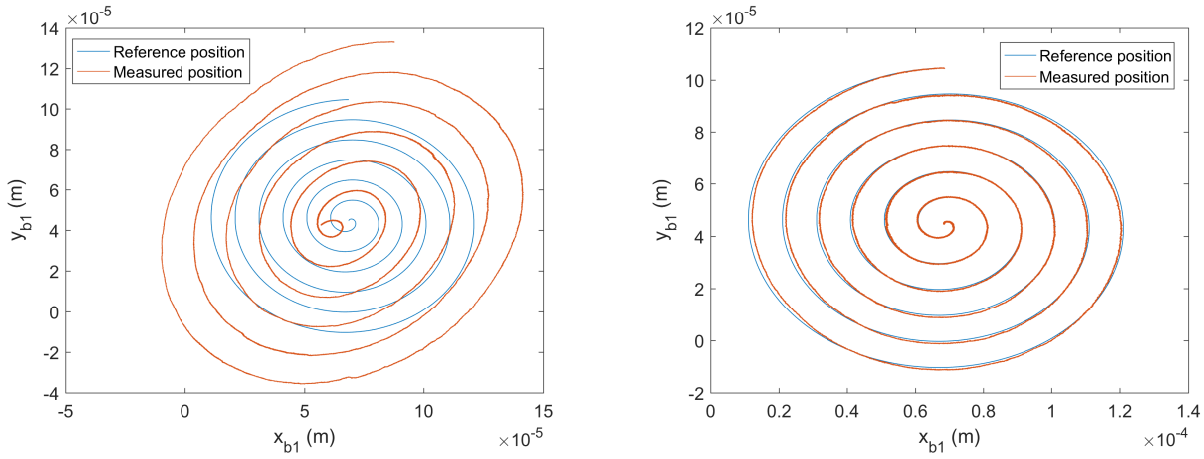

(a) Without compensation. (b) With compensation.

Figure 3.14: Comparison of generalized disturbance force feed-forward compensation.

disturbance force.

Table 3.11: Generalized disturbance force model parameters.

(a) Top AMB.

	γ_{11} [N.m^{-1}]	γ_{12} [N.m^{-1}]	γ_{21} [N.m^{-1}]	γ_{22} [N.m^{-1}]
a	2736	-577.6	-626.1	-2582
b	-709.9	-2682	-2787	353.3
e	-18.56e3	-3880	-1873	-18.1e3

(b) Bottom AMB.

	γ_{11} [N.m^{-1}]	γ_{12} [N.m^{-1}]	γ_{21} [N.m^{-1}]	γ_{22} [N.m^{-1}]
a	4905	-1024	-1234	-4930
b	-1307	-5131	-5299	1041
c	-201.6			
d	407.2			
e	-32.4e3	-3820	-40.83	-32.6e3

(c) Fitted bias force in bearing coordinates.

	F_{b0_x1} [N]	F_{b0_y1} [N]	F_{b0_x2} [N]	F_{b0_y2} [N]
a	0.0098	0.1449	0.0410	0.0613
b	0.0876	-0.1413	0.0773	-0.1075
c	m_c = -0.1049 c_c = -0.1621	m_c = 0.1172 c_c = 1.73	-0.2732	0.5774
d	m_d= -0.08745 c_d = 2.376	m_d= -0.04794 c_d= 0.6374	0.3241	0.0974
e	m_e = 0.02628 c_e = -0.6778	m_e = -0.03714 c_e = 0.9301	0.6296	-0.9771

3.6.2 GDF model for cooperative control

The preliminary model presented in section 3.6.1, introduced an improvement on the unbalanced magnetic pull model presented in section 3.5. However, it still has a few shortcomings. In the drive literature, the q-axis current is generally termed the torque producing current. The q-axis current however also causes a radial disturbance force which was not accounted for in the preliminary model. The second shortcoming is the high computational burden of computing the polynomial fit outputs of the preliminary model. Instead, it is possible to store all terms of the disturbance force model as functions of the rotor angle in look-up tables. The look-up tables also reduce the disturbance force error compared to the residual errors of the polynomial fits. The higher order harmonic perturbations may be accounted for without an increase in computational load by means of using look-up tables. The angular dependent stiffness term is also responsible for only a small fraction of the disturbance force, hence it will be discarded. Thus, the generalised disturbance force model, for use in the cooperative control, is modelled as:

$$\mathbf{F}_b\left(\theta_r,\, i_d,\, i_q\right) \;=\; \mathbf{F}_{b0}\left(\theta_r\right) + \mathbf{K}_{xyd}\left(\theta_r\right) f_d\left(i_d\right) + \mathbf{K}_{xyq}\left(\theta_r\right) f_q\left(i_q\right)\,, \tag{3.61}$$

where $\mathbf{F}_{b0}(\theta_r)$, is an angular dependent offset force term, $\mathbf{K}_{xyd}(\theta_r)$ is a coupling coefficient which couples the d-axis current to the xy-axis force and $\mathbf{K}_{xyq}(\theta_r)$, couples the q-axis current to the xy-axis force. The coupling coefficient terms are a function of the rotational angle, θ_r, as it implicitly includes the inverse Park transformation, but it also takes into account secondary coupling magnitude variation as a function of the rotor angle. The functions $f_d(i_d)$ and $f_q(i_q)$, take into account that the coupling of the current-to-force may not be a direct linear relationship, but that it may be linearly related to a nonlinear function of current. It is expected that the force is related to the square of the current, but other nonlinearities due to e.g. saturation may have an influence.

The offset force dependent term is obtained by slowly rotating the rotor and capturing the required control effort force to counteract the force disturbance. The rotation is performed with a small d-axis current term and the rotor angle is assumed equal to the open-loop reference angle. Unlike the preliminary model, the offset force is no longer a function of the drive current, since this has been accounted for by the current-force coupling terms. The required DC offset force, which is stored in look-up tables as a function of the rotor angle, is presented in Fig 3.15.

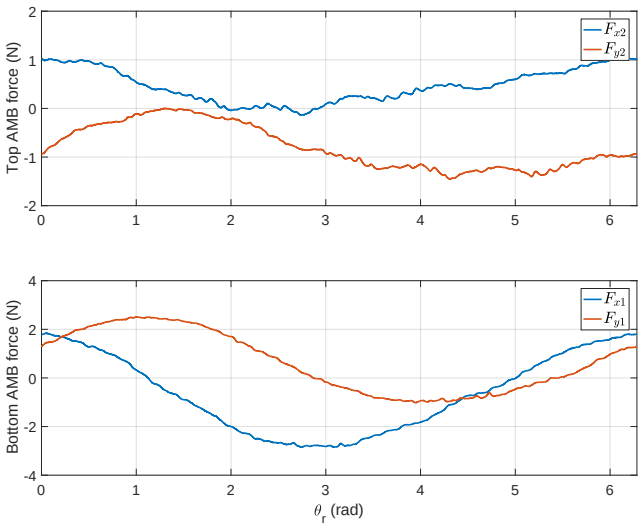

Figure 3.15: Current-free disturbance offset force.

The current-to-force coupling coefficients, $\mathbf{K}_{xyd}(\theta_r)$ and $\mathbf{K}_{xyq}(\theta_r)$, are also determined by slowly rotating the rotor with a small d-axis current. A sinusoidal current, with frequency, $f_e = 10\,\text{Hz}$, is injected into the d-axis to determine the d-axis current to force coupling coefficient. The sweep is repeated using a current injection amplitude of 2 A, 4 A and 8 A, in order to fit the current-to-force coupling functions, $f_d(i_d)$ and $f_q(i_q)$. The sweep is repeated to determine the q-axis current-to-force relationship. The disturbance force (in xy-coordinates), caused by the injected current, is correlated to the injected sinusoidal signal. The correlation magnitude determines the coupling coefficient magnitude. The disturbance force is determined by the extended rigid body dynamics observer presen-

ted in section 3.4.1. As the rotor slowly rotates, the disturbance force appears as a signal modulated according to the rotational angle. The correlation step can thus be considered as a demodulation step. Thus, the demodulation step is performed by multiplying the force disturbance with the injected sinusoid and low pass filtering via integration. The output of the integrator is again modulated with the unit disturbance signal in order to generate an output compensation force, $\mathbf{F}^*_{b,xy}$, which is added to the control reference force, $\mathbf{F}^*_{b,\mathrm{PI}}$. The control reference force is the term that feeds the rigid body observer, thus as the coupling coefficients converge to cancel the disturbance force, the disturbance force is no longer present in the controller reference force and thus also no longer in the observed disturbance. The purpose of the two-step modulator is the same as that used for the unbalance control (presented in section 3.8.1), except that the disturbance force is generated by means of the injected drive current, as opposed to the unbalance force. The coupling-to-force calculator is as depicted in Fig. 3.16. The output of the integrator is the total coefficient required to cancel the disturbance force due to the injected current. The integrator output is saved and post-processed in order to separate the product of the normalized coupling coefficient, $K(\theta_r)$, from the current coupling function, $f(i)$.

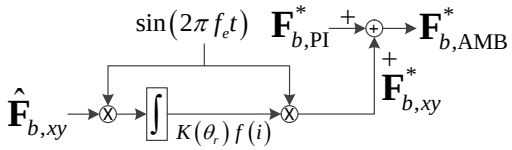

Figure 3.16: Current-to-force coupling coefficient calculator.

The result of the identified current-to-force coupling coefficients is presented in Fig. 3.17. It can be observed that the coupling to the top AMB is much smaller than the coupling to the bottom AMB. This is due to the machine asymmetry with the motor's permanent magnet residing on the bottom of the rotor. The bottom AMB coupling coefficient is dominated by the fundamental, i.e. it varies once per rotation because the PMSM has one pole-pair. The fitted current coupling functions have been identified as:

$$f_d(i_d) = -7.89 \times 10^{-3}\, i_d^2 + 0.884\, i_d + 0.15 \tag{3.62}$$

$$f_q(i_q) = -8.71 \times 10^{-3}\, i_q^2 + 0.868\, i_q + 0.17 \tag{3.63}$$

The negative coefficient of the quadratic term indicates that saturation may have had an influence. Further investigation is required to determine the exact cause.

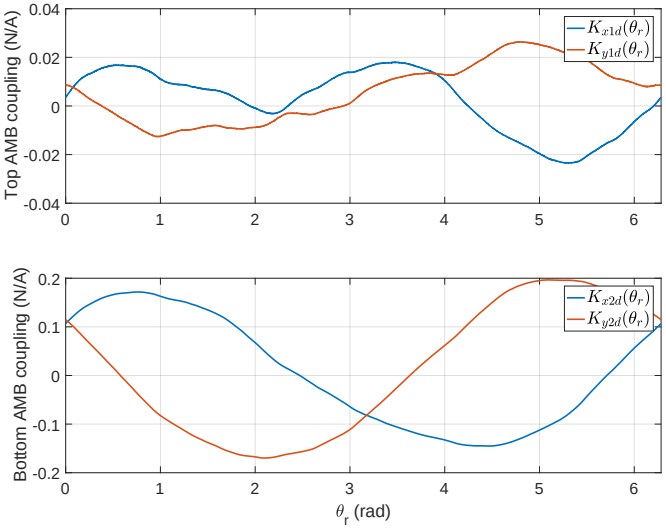

(a) d-axis coupling coefficients.

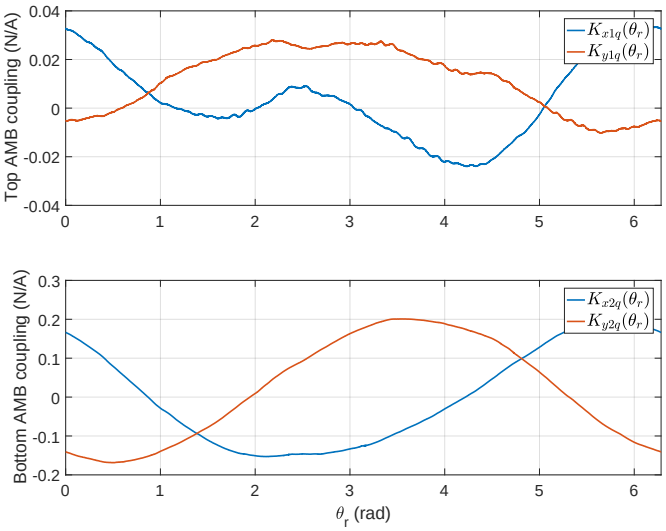

(b) q-axis coupling coefficients.

Figure 3.17: Normalized current-to-force coupling coefficients.

3.7 Magnetic centre identification

A method of determining the effective rotor position within the air-gap of the AMB was originally presented by Marshall [84], known as the multi-point method (MPM). The focus was to provide "*...predictions of the shaft force and rotor position based using only current pairs without air-gap measurements.*" The work was extended by Prins [85] in which the concept of an effective rotor origin is characterized which differs from the rotor geometric centre in order to increase the force estimation accuracy. The effective origin of the rotor within the AMB air-gap is defined by Prins *et al.* [86] as the "*...unique rotor location for which a magnetic circuit based force model of the bearing is satisfied for zero position offset of the rotor along each control axis.*" It is desirable to use the effective rotor origin as the rotor reference point as the control plant is more linearised with the rotor suspended at this point. By knowing the difference between the effective rotor origin and the geometric origin also finds application during commissioning and troubleshooting an AMB [86].

The multi-point method suspends the rotor at different locations within the air-gap with different bias currents in order to generate a set of non-linear simultaneous equations which are solved off-line. Spangler *et al.* [87] extended the work of Marshall and Prins, based on the multi-point method, in order to characterize a full coordinate transformation between the sensed geometric rotor locations and the effective coordinates which satisfy the magnetic circuit model. The result is a reduced force estimation error.

A method of determining the effective origin using an on-line method using bias current injection and observing the rotor deflection caused by the induced disturbance force when the rotor is not at the centre is proposed by Caple *et al.* [88]. The effective rotor origin is also referred to as the magnetic centre to distinguish it from the geometric centre. The magnetic centre and the geometric centre may differ from each other due to runout which in turn is caused by inhomogeneities in the sensor target material [89], mechanical and electrical runout and stresses within the material [90].

Kruger *et al.* [17] proposed a method of identifying an approximation of the magnetic centre in order to increase the convergence rate of the pseudo-magnetic centre identification. Faster estimation of the magnetic centre in turn made it useful for other on-line applications, such as rotor angle estimation during start-up.

3.7.1 True magnetic centre identification

In this section, a method for the on-line determination of the true magnetic centre is presented. Consider the force equation of a differential driving magnetic actuator:

$$F = K\left[\left(\frac{i_0 + i_c}{x_0 - x}\right)^2 - \left(\frac{i_0 - i_c}{x_0 + x}\right)^2\right], \tag{3.64}$$

where i_0, is the bias current, x_0, the nominal air-gap size, x, the rotor deviation and i_c, is the control current. First, assume that the rotor is deflected from the magnetic centre, but that the control current is such that the forces are in equilibrium. From inspection, it then follows that an additional increase in the bias current will result in a net increase of the force towards the side which has the *smaller* air-gap. Thus, to drive the rotor to the true magnetic centre the reference position, $\boldsymbol{u}_b^*$, has to be adjusted in the opposite direction of the disturbance force created by injecting a bias current perturbation. The rotor reference is adjusted until the rotor perturbation due to the current perturbation is nullified.

In order to obtain persistent excitation of the deviation from the magnetic centre a periodic current disturbance, $i_m \sin(\omega t)$, is added to the bias current. The estimated disturbance force is then correlated to the disturbance input signal via the inner product which yields the estimated magnetic centre offset as:

$$\hat{\mathbf{u}}_m = G_{tmc} \int \hat{\mathbf{F}}_b \sin(\omega t)\, dt\,, \tag{3.65}$$

where G_{tmc}, is a gain for setting the rate at which the magnetic centre is identified. The amplitude of the bias current perturbation is in the range of: $0 < i_m < i_0$. As the rotor approaches the true magnetic centre the amplitude of the disturbance force decreases. Thus, the rotor approaches the magnetic centre asymptotically as the input to the integrator converges to zero.

3.7.2 Magnetic centre feed-forward compensation

The magnetic centre as a function of the rotor angle can be identified online from which a look-up table or a sinusoidal fit may be generated off-line. The air-gap disturbance due to the run-out may then be compensated via a feed-forward term which takes as input the estimated rotor angle. This section presents the sinusoidal fit solution because it aids in gaining insight into the predominant terms. For the final control implementation, the magnetic centre is stored as a look-up table with the angular position serving as the table index.

For the bottom AMB a single harmonic term had sufficient accuracy, which had the following form:

$$\mathrm{MC}_{x|y2} = a \sin(\theta_r) + b \cos(\theta_r) + e\,. \tag{3.66}$$

For the top AMB a second harmonic term had to be added to achieve a good fit:

$$\mathrm{MC}_{x|y1} = a \sin(\theta_r) + b \cos(\theta_r) + c \sin(2\theta_r) + d \cos(2\theta_r) + e\,. \tag{3.67}$$

The magnetic centre is measured online by using the true magnetic centre identification procedure presented in section 3.7.1. During the identification, the rotor is slowly rotated

by an open-loop drive current. The rotor angle is assumed to coincide with the open-loop reference angle due to the slow rotation. The measured and fitted magnetic centres are displayed in Fig. 3.18.

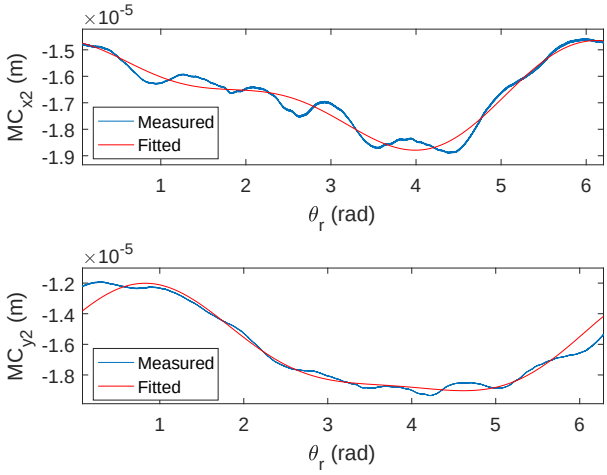

(a) Top AMB.

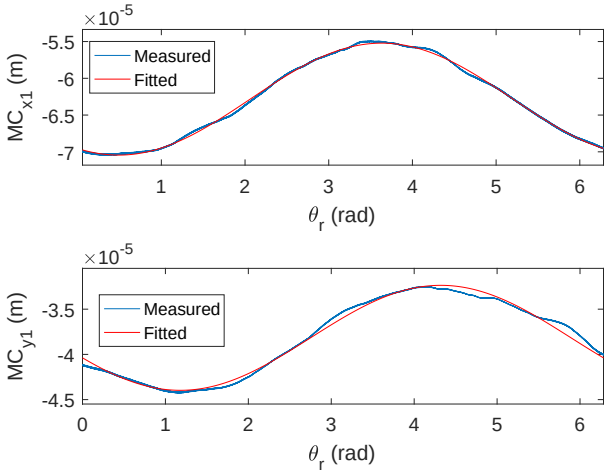

(b) Bottom AMB.

Figure 3.18: Magnetic centre identification results.

Due to run-out present on the sensor ring and the angular dependent sized air-gap in the AMB itself, the measured rotor position does not constitute the true rotor position and hence not the true air-gap. The true air-gap is required by the feedback linearisation where a force reference is transformed into a current reference, as presented in section 3.2.3. In order to correct for the variation in the air-gap due to a non-circular rotor and sensor ring, the magnetic centre deviation needs to be added to the measured rotor signal.

Table 3.12: Trigonometric function fit parameters for the magnetic centres.

	MC_{x1} [m]	MC_{y1} [m]	MC_{x2} [m]	MC_{y2} [m]
a	-3.59e-06	-5.37e-06	-6.05e-07	9.41e-07
b	-6.72e-06	-2.22e-06	4.38e-07	3.73e-08
c			6.40e-07	2.65e-06
d			1.52e-06	2.13e-06
e	-62.8e-06	-38.2e-06	-16.7e-06	-16.3e-06
R^2	0.993	0.985	0.961	0.884

Thus, the true air-gaps for use in the feedback linearisation of (3.11), are computed using:

$$u_{x2+} = \bar{u}_{x2+} - (x_{2s} + \mathrm{MC}_{x2}) \tag{3.68}$$
$$u_{x2-} = \bar{u}_{x2-} + (x_{2s} + \mathrm{MC}_{x2}) \tag{3.69}$$
$$u_{y2+} = \bar{u}_{y2+} - (y_{2s} + \mathrm{MC}_{y2}) \tag{3.70}$$
$$u_{y2-} = \bar{u}_{y2-} + (y_{2s} + \mathrm{MC}_{y2}) \tag{3.71}$$
$$u_{x1+} = \bar{u}_{x1+} - (x_{1s} + \mathrm{MC}_{x1}) \tag{3.72}$$
$$u_{x1-} = \bar{u}_{x1-} + (x_{1s} + \mathrm{MC}_{x1}) \tag{3.73}$$
$$u_{y1+} = \bar{u}_{y1+} - (y_{1s} + \mathrm{MC}_{y1}) \tag{3.74}$$
$$u_{y1-} = \bar{u}_{y1-} + (y_{1s} + \mathrm{MC}_{y1}) \ , \tag{3.75}$$

where the nominal effective air-gaps, $\bar{u}$, are obtained from table C.2, subscripts $x|y$ indicate the axis of interest, subscripts $1|2$ indicate the bottom or top AMBs respectively and subscripts $+|-$ indicate the positive or negative force producing pole of the AMB.

3.8 Unbalance control

3.8.1 Unbalance control principle

The unbalance control used for the flywheel is quite similar to that presented by Herzog *et al.* [8] in that it implements a generalized notch filter using the two-step modulator, with the notable difference that it is not the position disturbance which is the filter input but instead the force disturbance as estimated by the force observer.

The force disturbance at the centre of gravity coordinates from the estimated states is given by:

$$\hat{\boldsymbol{F}}_{cog} = \mathbf{M}\dot{\hat{\mathbf{x}}}_2 - \mathbf{f}^*_{g,AMB} \, . \tag{3.76}$$

Hence, the disturbance force is the difference between the position controller reference force and the actual resultant force as estimated by the observer. The adaptation gain used for the unbalance control is selected as $\epsilon = 10 \times 10^{-6}\mathrm{M}^{-1}$. This reduces the computational burden, since instead of using the disturbance force as the signal to be filtered

the disturbance *acceleration* can be used directly. Using the disturbance acceleration the mass term is thus cancelled, i.e. $\epsilon = 10 \times 10^{-6}$.

The block diagram of the two-step modulator is depicted in Fig. 3.19.

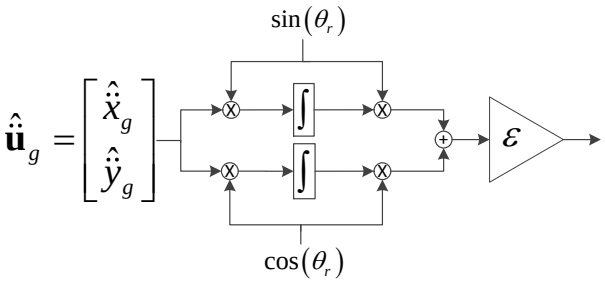

Figure 3.19: Two step modulator notch filter.

The integration of the two-step modulator with the observer, controller and plant is depicted in Fig. 3.20, where $O(s)$ is the force observer, $C(s)$ is the control and $G(s)$ is the plant. The two-step modulator is represented by the TSM block.

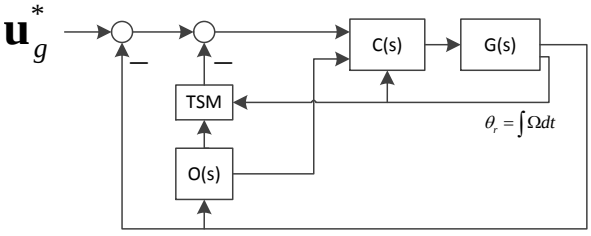

Figure 3.20: Disturbance force notch filter included with control.

3.8.2 Simulation response

The unbalance control is verified via simulation in Simulink® using a detailed model of the AMB force, rigid body model and control in centre of gravity coordinates as designed. Fig. 3.21, depicts the unbalance control response for an eccentricity of 176 μm.kg, i.e. the centre of mass is displaced by 10 μm. At, $t = 1$ s, the rotor is accelerated from 0 to 6000 r/min. At, $t = 10$ s, the unbalance control is switched on. As can be seen, the response of the centre of gravity coordinates decays and the rotor spins about its centre of mass.

A simulation model of the AMB control with unbalance control is included in appendix E.6.

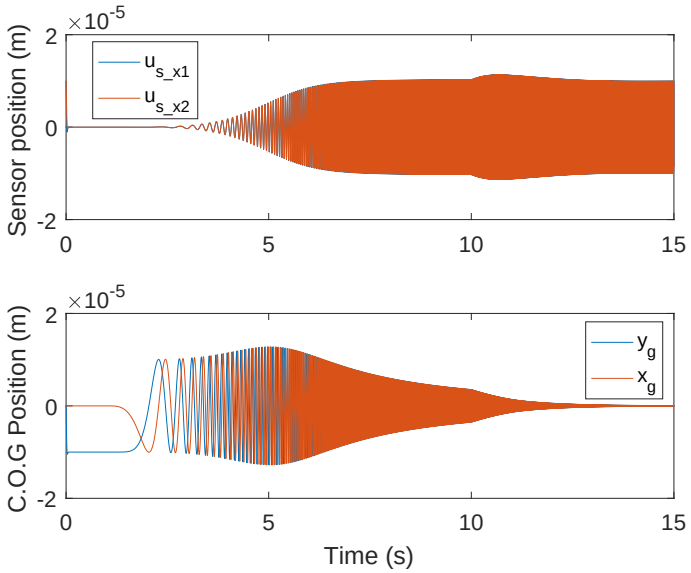

Figure 3.21: Unbalance control response.

3.8.3 Measured unbalance control response

The experimental result of the unbalance control is presented in Fig. 3.22. At, $t = 1\,\mathrm{s}$, the unbalance control algorithm is switched on by switching the adaptation gain from zero to $\epsilon = 2 \times 10^{-6}$, with the rotor spinning at $4500\,\mathrm{r/min}$. The unbalance control was stable with the original gain of $\epsilon = 10 \times 10^{-6}$, but the Fourier coefficients generated at the integrator outputs of the two-step modulation notch filter was influenced by the measurement noise and it was decided to lower the adaptation gain. The top AMB x-axis had severe resonance excitation which was dissimilar from the other AMBs. This is due to a structural mode excitation which is discussed in appendix C.4.2. It can be observed that the current does decrease from $\approx 1.5\,\mathrm{A_{pk-pk}}$ to $\approx 0.5\,\mathrm{A_{pk-pk}}$, in the axis with the highest amount of vibration. The current in the other axes decrease, but only slightly. The measured position response is from a relatively small orbit to an increased orbit of $\approx 25\,\mu\mathrm{m}$ in the top and bottom AMBs, as expected since the rotor should rotate about the centre of mass. Thus, the geometric centre, as measured by the sensors, rotates almost about the centre of mass. The AMB control used the low stiffness gains as designed in section 3.3.2.

It was observed that in order for the unbalance control to function as desired, i.e. cause a reduction in the reference AMB currents, the generalized disturbance force (GDF) feed-forward model as presented in section 3.6, had to be switched off. If it is switched off the unbalance control output generates an output position such that the centripetal force due to the rotor mass unbalance cancels with the unbalanced magnetic pull. This results in a reduced current ripple in the AMB. This may be explained by first noting that the input to the unbalance control is not the synchronous component of the measured *position* as usually done in the literature, instead the synchronous component of the observed

disturbance force is used as the input to the unbalance notch filter. Secondly, the reference force which feeds into the disturbance force observer is that produced by the PID control. When the GDF feedforward is activate, the disturbance force observer does not account for the UMP as a disturbance force. Thus, the resulting orbit generated accounts only for the unbalance disturbance. After the position control has been compensated by the unbalance control, the GDF feedforward still produces a current reference to counteract the UMP, resulting in a larger total control current. When the GDF feedforward is inactive the reference control force also includes the component required to compensate UMP. Hence, the disturbance force which feeds into the unbalance control now also includes the UMP component (as if it is unbalance).

The reference orbit generated by the unbalance control is such that the disturbance force which feeds into the unbalance control (in effect the control effort) is minimized. Thus, when the GDF is switched off, the reference orbit generated by the unbalance control is such that the control effort to compensate for the sum of the unbalance and UMP is minimized. In essence, the rotor orbit is such that the negative stiffness force cancels with the external disturbance force, resulting in minimized control effort and hence smaller current ripple. Thus, in the case that the GDF is switched on, some of the AMB force is used to counteract the UMP. When the GDF is switched off, the resulting orbit is such that the control effort generated to counteract the UMP and mass unbalance, is minimized. Thus, a smaller control effort is expected with the GDF switched off.

The unbalance control subtracts the fundamental component of the sensor runout, but higher order harmonics present in the rotor measurement due to rotor runout pass through to the control, which limits the amount of current ripple reduction. Thus, there is a difference in the simplified model of the unbalance and runout, and that of the actual presented system. The unbalance control is thus developed further in the following sections to improve the current ripple (and vibration).

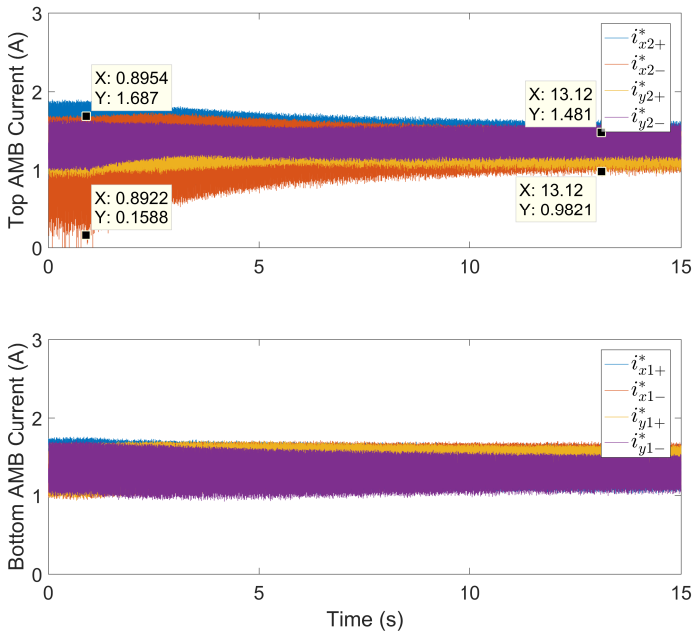

(a) AMB reference currents.

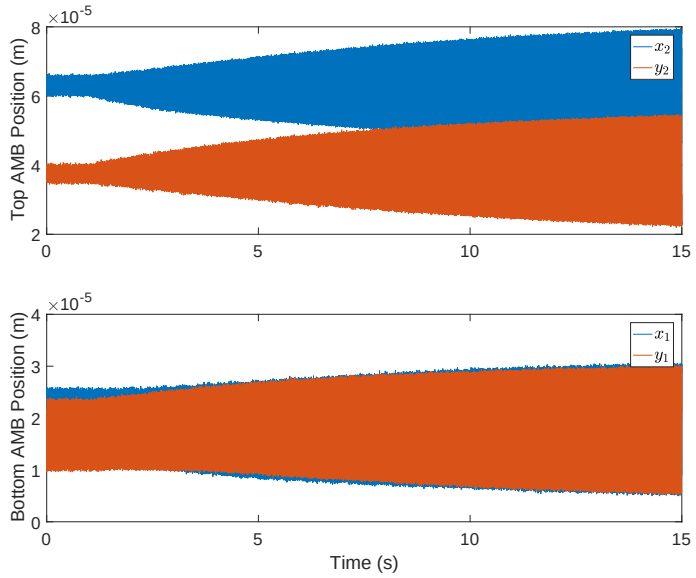

(b) Measured position.

Figure 3.22: Unbalance control switch-on response.

3.8.4 Higher order harmonic compensation

Due to runout of the sensing surface which is sensed by the eddy current position sensors, higher order harmonics of the rotational frequency are present in the measured rotor position. The unbalance control, presented in section 3.8.1, compensates only for the fundamental component of the runout and unbalance. The higher order harmonics pass through and are still reacted upon by the controller. The derivative component of the controller is especially responsible for generating a current ripple due to the higher order harmonics. The residual force disturbance due to the higher order harmonics may still excite rotor bending modes or structural modes. The magnitude or severity of the higher order harmonics is in part determined by the machining surface finish quality.

Fig. 3.23, illustrates that the higher order harmonics present in the runout may be approximated by adding Fourier series terms using the two-step modulation notch filter and replacing the rotor angle, θ_r, with the n-th harmonic multiple of the angle. The adaptation gain is selected such that $\epsilon_1 > \epsilon_2 > \ldots \epsilon_n$.

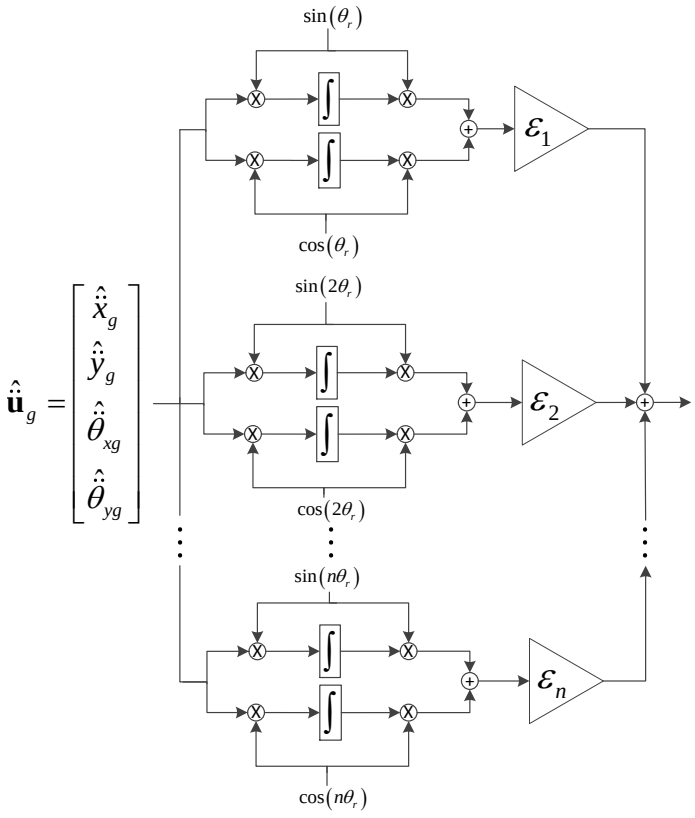

Figure 3.23: Higher order harmonic two step modulator notch filter.

The measured unbalance control response, with a 2^{nd} harmonic term added, is depicted in Fig. 3.24, again with the rotor spinning at 4500 r/min. The 2^{nd} harmonic adaptation gain was selected as: $\epsilon_2 = 0.1 \times 10^{-6}$. At, $t = 1$ s, the unbalance control for the fundamental

component is switched on and the current ripple decreases to a steady state value. At, $t = 18\,\mathrm{s}$, the 2nd harmonic unbalance control term is switched on and the current ripple decreases further from $\approx 0.65\,\mathrm{A_{pk-pk}}$, to $\approx 0.35\,\mathrm{A_{pk-pk}}$. The bottom AMB current ripple is essentially unchanged. The envelope of the rotor position response is similar to the fundamental unbalance control response presented in Fig. 3.22 and is not presented again.

In order to reduce the current ripple even further, more and more harmonic component terms need to be added, with diminishing returns in current ripple reduction compared to the computational cost.

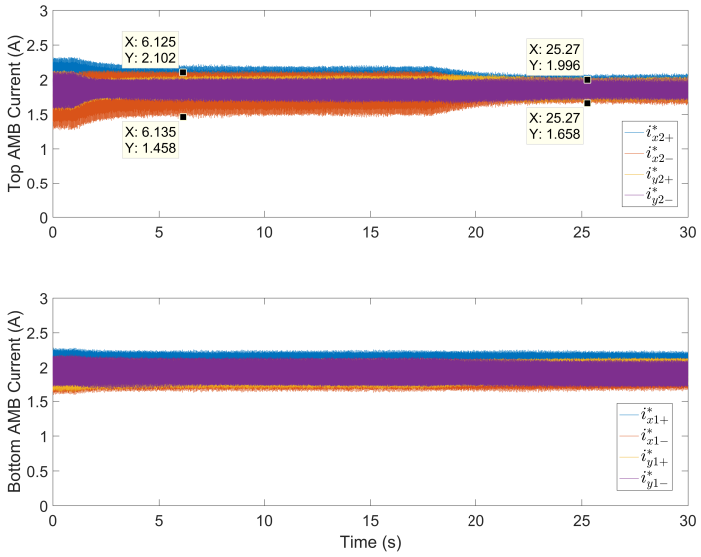

Figure 3.24: Unbalance control response with 2nd harmonic term included.

3.8.5 Runout compensation and unbalance control via look-up tables

Increasing the number of harmonic unbalance control terms, as in the previous section, is computationally expensive and unwarranted since a better alternative is possible. Instead, the runout and unbalance combination may be identified as a function of the rotor angular position and stored in a look-up table. Since the estimated rotor angle is available from the sensorless drive, the runout may be compensated via the LUT acting as an open-loop feed-forward term.

The influence coefficient method of runout identification is presented by Kim and Lee [91] for geometric centre control. Usually, when considering runout identification in the literature, geometric centre control is implied [92, 93, 94, 95]. Geometric centre control requires the separation of the unbalance and the sensor runout components, since the unbalance *force* increases as the speed increases, but the sensor runout manifests as sensor *displacement*. Thus, separate components are required for feed-forward compensation in the case of geometric centre control.

Centre of mass unbalance control does not require the separation of the two components, since if the rotor rotates about the inertial axis, no speed dependent unbalance force is generated since it is supposed to be zero. In the flywheel application of this thesis, centre of mass unbalance control is preferred, since it results in less rotor-AMB vibration, reduced AMB current and less noise.

An iterative method for identifying the *combined* sensor runout and mass unbalance is presented next. Given a low stiffness control gain and an unbalance controller for the fundamental and second harmonic components, the rotor will tend to rotate about the centre of mass if the rotor speed has surpassed the first and second rigid body modes, albeit with some error, due to phase lag and unaccounted higher order harmonic components in the sensor runout. By measuring the AMB sensor position and rotor angular position, the sensor runout[6] may be stored as a look-up table with the rotor angle as the LUT index. On the next iteration, the sensor runout is subtracted from the measured rotor position. Since there is now less disturbance at the control output, because the runout is at least partially compensated by the runout LUT, the unbalance control is able to achieve a control response with a smaller current ripple. Hence, the rotor is rotating closer to the centre of mass due to less disturbance. The sensor position is again measured from which an updated sensor runout LUT is generated. This simple iterative technique is possible because the unbalance and runout components do not need to be separated in the case of centre of mass control. The look-up table has to be generated with the unbalanced magnetic pull feed-forward model compensation switched on. If it is not switched on the unbalance control output will generate an output position such that the centripetal force due to the rotor mass unbalance cancels with the unbalanced magnetic pull. This results in a reduced current ripple, but only for that particular speed, because the rotor is not spinning about its principal axis of inertia. It may be possible to measure runout LUTs at different speeds, with the unbalanced magnetic pull switched off, and compute a speed weighted linear combination of the sensor runout for the sensor runout at a particular speed.

The result of the identified sensor runout using the iterative identification technique is shown in Fig. 3.25. The measurements were performed with the rotor spinning about its centre of mass at 4500 r/min for the first two iterations and at 6000 r/min for the last two. The higher rotor speed aided in faster runout identification convergence. For successive iterations, the amplitude of the runout changes decreased, especially at higher speeds. This indicates that the rotor is still not spinning perfectly about its centre of mass at the lower speed. At a higher speed, this condition is closer to being satisfied. One possible explanation for the deflection from the centre of mass is that the UMP may be speed dependent (possibly due to eddy currents) and that the GDF model which compensates the static UMP, does not match the UMP at a higher speed.

[6] The runout, relative to the centre of mass, is approximated as the sensor position with the mean component removed.

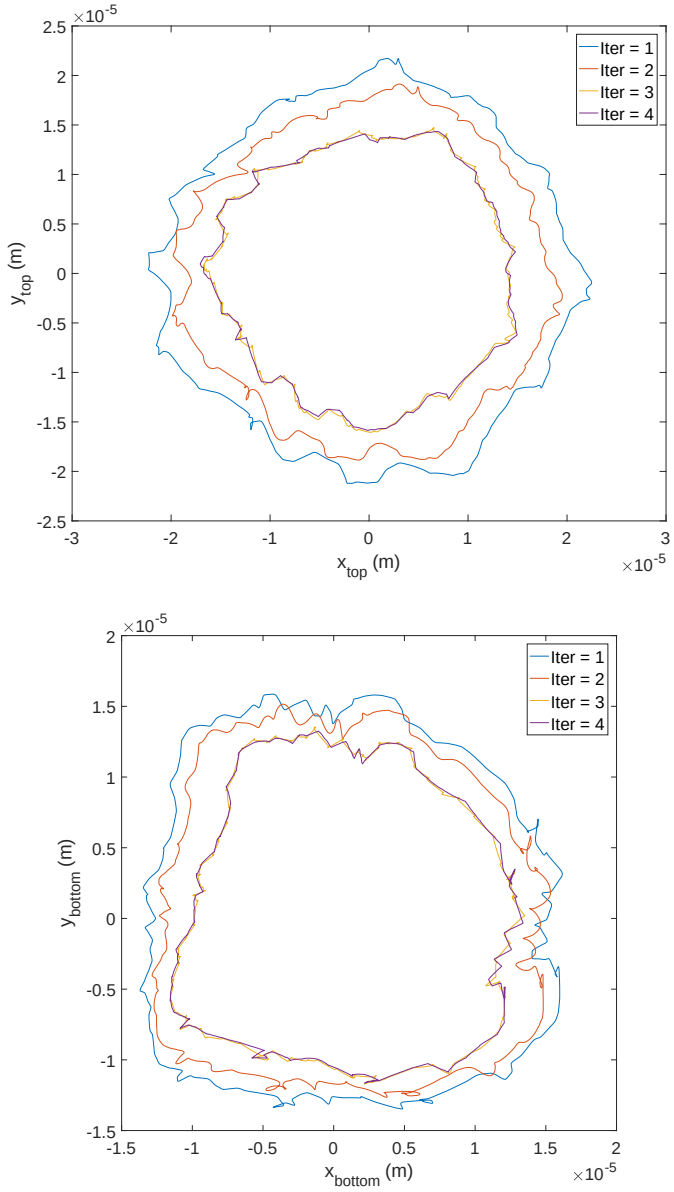

Figure 3.25: Iterative runout identification.

The displacement vector from the geometric centre to the centre of mass is implicitly included in the look-up tables. Hence, the unbalance controllers for the fundamental and second harmonic, which are computationally expensive, may be removed. The flywheel system may now be started with the LUT feed-forward compensation switched on. It may also be switched on at a higher speed, without concern of possible instability, since the look-up table based runout compensation is now open-loop.

The AMB current response to enabling the sensor runout LUT at, $t = 1\,\mathrm{s}$, is displayed in Fig. 3.26. The rotor is spinning at $6000\,\mathrm{r/min}$. As can be observed the LUT based runout compensation and unbalance control, yields superior results in terms of current ripple magnitude, compared to the simple harmonic unbalance controllers presented in

the previous section. The current ripple, ignoring the lower frequency transient, is $\approx 0.12\,\mathrm{A_{pk-pk}}$. The reason why such a low current ripple was achieved is because the LUT used to compensate the sensor runout in the result Fig. 3.26, was generated with the unbalanced magnetic pull feedforward compensation switched off. At a higher speed, a higher current ripple will result, since the rotor is not spinning about its principal axis of inertia.

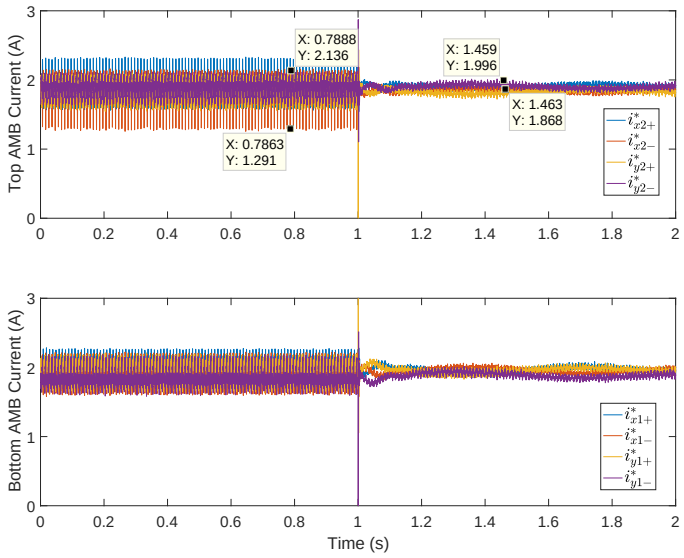

Figure 3.26: Unbalance control response with look-up tables.

Fig. 3.27, presents the unbalance control result where the sensor runout LUT has been generated with the unbalanced magnetic pull switched on. The AMB current ripple is not quite as low as for the case where the LUT has been generated by switching the unbalanced magnetic pull feed-forward compensation off. The difference is that the current for the LUT associated with Fig. 3.27 should remain relatively constant even at higher speed since the rotor is spinning about the principal axis of inertia.

If the flywheel is spun up with the runout compensation already switched on, the resulting displacement orbit is dependent upon the disturbance force which results due to the error in the estimated rotor angle used as the LUT input. As the speed increases the angle estimation of the sensorless drive improves and the sensor runout error decreases, which in turn results in lower AMB current and vibration. The estimated angle also undergoes a transient error during sensorless drive transients, such as speed set-point changes, or a switch from motoring to generating mode, which in turn results in a disturbance in the LUT based unbalance control. The two-step modulation notch filter using the sensorless drive's estimated angle would also be influenced by a sensorless drive transient. The dependence of the unbalance control on the sensorless drive's angle estimation error thus needs to be investigated further, in order to quantify these interactions, which will be presented in chapter 5 dealing with the cooperative control.

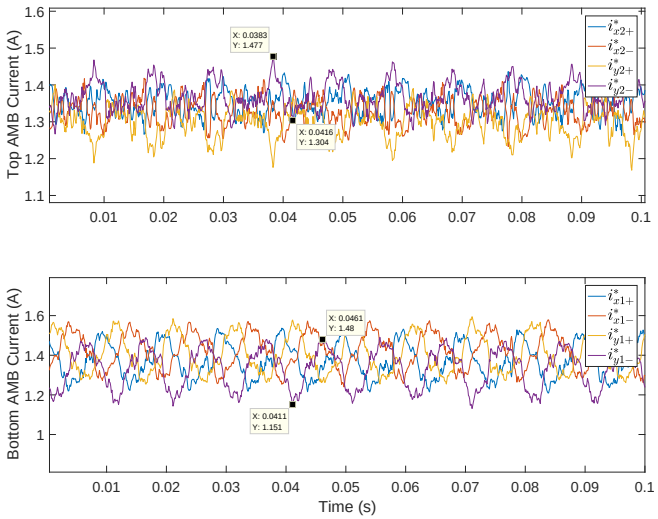

Figure 3.27: AMB currents with principal axis based sensor runout LUT.

Another non-ideality which needs to be compensation is the delay due to the phase shift caused by the power amplifiers. In the notch filter implementation, the phase shift due to the power amplifiers *should* be implicitly compensated. Any phase shift due to the power amplifiers causes an increase in the synchronous component of the current ripple which is corrected for by the notch filter. Nevertheless, Peng *et al.* [96] have shown that the synchronous vibration component improves when the delay due to the power amplifier is explicitly compensated. In the case of the open-loop LUT based unbalance control any additional phase shift, such as that due to the power amplifiers, has to be compensated using a model-based approach. Hence, it is recommended to compensate for the power amplifier delay in order to achieve higher operating speeds of the flywheel when using the LUT based unbalance control.

3.9 Conclusion

This chapter presented the AMB control design in the centre of gravity coordinates using a force-based framework by means of feedback linearisation. Models of increasing fidelity of the force disturbance caused by the unbalanced magnetic pull were derived. Procedures for parameter fitting of these models were also described which included the parameter results of each procedure. The final force disturbance model, appropriate for the cooperative control, was presented in section 2.5.

The AMB design ended with a presentation of the unbalance control design. The online unbalance control was also progressively improved by accounting for higher order harmonics in the sensor runout. For efficient control implementation, the sensor runout was accounted for by means of look-up tables.

The force disturbance model and the unbalance sensor runout look-up tables are dependent upon the rotor angular position. At standstill and low speed, the rotor angle is estimated by means of the estimated force disturbance which results due to incomplete cancellation of the unbalanced magnetic pull and the angular dependent force disturbance feed-forward model. The estimation of the rotor angle using the force disturbance is presented in chapter 5. At higher operational speed the source of the estimated speed is gradually transferred to the sensorless vector controller. The sensorless vector control design is presented in the next chapter.

Chapter 4

Sensorless vector control

4.1 Introduction

The aim of this chapter is to present the design and implementation of the sensorless vector control of the flywheel system used for this thesis. The main contribution to sensorless control is the bumpless start-up method, presented in section 4.3. The preceding sections are presented in order for the work to be self-contained, namely the modelling of the motor combined with the three-phase filter, the current and speed control design and the observer design. The observer design is extended in section 4.4 in order to account for the frequency dependent resistance and the current dependent inductance of the machine as determined during the PMSM parameter identification presented in appendix B.

4.2 Sensorless vector control design

4.2.1 PMSM model

Many introductory sources present the modelling and control of electrical machines, such as [97, 98] (and will therefore not be repeated here). The derivation of the mathematical model of a three-phase permanent magnet machine is also presented in [13]. The state space model of a three-phase PMSM in the rotor reference frame is given by (adapted from [99]):

$$\begin{aligned}
\frac{d}{dt}i_{sd} &= -\frac{1}{\tau_s}i_{sd} + \omega_r \sigma i_{sq} + \frac{v_{sd}}{L_d} \\
\frac{d}{dt}i_{sq} &= -\frac{\omega_r}{\sigma}\left(\frac{\lambda_p}{L_d} + i_{sd}\right) - \frac{1}{\sigma\tau_s}i_{sq} + \frac{v_{sq}}{L_q} \\
\frac{d}{dt}\omega_m &= \frac{1}{J_p}\left(T_e - B\omega_m - T_l\right) \\
T_e &= \frac{3}{2}z_p\left(\lambda_p i_q + L_d\left(1-\sigma\right)i_{sq}i_{sd}\right) ,
\end{aligned} \tag{4.1}$$

where $\frac{d}{dt}$, is the time differential operator, z_p is the number of pole pairs, $\sigma = \frac{L_q}{L_d}$ is the saliency factor, $\tau_s = \frac{L_d}{r_s}$ is the d-axis stator electrical time constant, λ_p is the peak flux linkage due to the permanent magnet, L_d and L_q, are the direct and quadrature axis inductances, respectively, B, is the viscous friction coefficient and, J_p is the polar moment of inertia. The transformed terminal voltage, $\mathbf{v}_{sdq}$, and load torque, T_l, are the inputs to the model. The state variables of the model are the transformed stator current, $\mathbf{i}_{sdq}$, and the rotor angular frequency ω_m[1]. The PMSM used in this study has a surface mounted permanent magnet, for which the saliency factor is assumed unity. The mechanical angular frequency of the PMSM is coupled to that of the AMB model. In certain simulations, it is sufficient to couple an existing PMSM speed response simulation to the AMB, whilst in others, where the PMSM control is dependent on the AMB unbalance control response, both models have to be coupled in the same simulation.

The parameters of the machine and more importantly, the identification thereof, is presented in section B.

4.2.2 Three-phase LC filter model

The drive used for the flywheel system has a three-phase LC filter in order to reduce the noise coupled from the drive to the AMB's eddy current position sensors [100]. The design of the filter used in this system is presented by de Klerk [79]. The influence of the filter on the sensorless control is presented by Salomäki [18]. Fig. 4.1 depicts a simplified control, inverter, filter and PMSM. Ideally, the controller uses the inverter current, $\mathbf{i}_A$, in order to compensate the dead-time. This requires however an extra set of current sensors and typically the stator current reference, $\mathbf{i}_s^*$, is used instead[2].

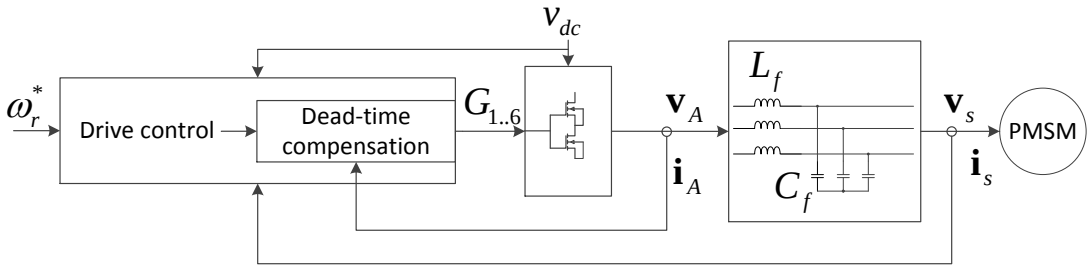

Figure 4.1: PMSM drive equipped with three-phase LC filter.

[1] Note that, $\omega_r = z_p\omega_m$, is the angular frequency in electrical coordinates.

[2] Note that the reference frame of the three-phase variables is purposefully kept ambiguous in Figure 4.1.

The state space model of the three-phase filter is given by [18]:

$$\begin{aligned}
\frac{d}{dt}i_{Ad} &= -\frac{1}{\tau_A}i_{Ad} + \omega_r i_{Aq} + \frac{v_{Ad} - v_{sd}}{L_f} \\
\frac{d}{dt}i_{Aq} &= -\frac{1}{\tau_A}i_{Aq} - \omega_r i_{Ad} + \frac{v_{Aq} - v_{sq}}{L_f} \\
\frac{d}{dt}v_{sd} &= \frac{i_{Ad} - i_{sd}}{C_f} + \omega_r v_{Aq} \\
\frac{d}{dt}v_{sq} &= \frac{i_{Aq} - i_{sq}}{C_f} - \omega_r v_{Ad}\,,
\end{aligned} \tag{4.2}$$

where ω_r, is the PMSM electrical angular speed, $\tau_A = \frac{L_f}{r_{lf}}$ is the time constant of the filter inductance, and r_{lf}, L_f, C_f is the filter resistance, inductance and capacitance, respectively. Thus, the filter inputs are the inverter output voltage, $\mathbf{v}_A = \begin{bmatrix} v_{Ad} & v_{Aq} \end{bmatrix}^T$, and the PMSM stator current, $\mathbf{i}_s = \begin{bmatrix} i_{sd} & i_{sq} \end{bmatrix}^T$. The inverter output current, $\mathbf{i}_A = \begin{bmatrix} i_{Ad} & i_{Aq} \end{bmatrix}^T$, represents an internal state to the filter and the stator terminal voltage, $\mathbf{v}_s = \begin{bmatrix} v_{sd} & v_{sq} \end{bmatrix}^T$, is an output which in turn serves as an input to the PMSM model of (4.1).

Salomäki's approach to estimating the speed and position was to use a full-order observer in order to account for the states of the filter and the machine. In the event that the filter's cutoff frequency is sufficiently high above the machine's highest operating frequency the delay introduced by the filter may be neglected [101]. A reduced order model of the filter is thus considered and the filter is taken into account simply by adding the inductance of the filter to that of the stator inductance.

4.2.3 Cascaded control design strategy

The sensorless vector-control design strategy presented by Kshirsagar *et al.* [4] is based on classical frequency domain techniques. In the design of the sensorless controller, several controllers are cascaded. Each inner loop needs to be "faster" than the preceding outer loop by successively increasing the control bandwidth. The outermost loop is the speed control, after which the current control follows. The state variables for the current control loop assumes that the angle used for transforming the measured currents to the rotating reference frame is accurately observed. The estimated angle is derived from the estimated electrical states by a phase-lock loop, thus the electrical domain observer has the "fastest" dynamics of all the loops. Since the outer-most loop is the speed control loop, all other loop control bandwidths are set relative to the speed loop which acts as a normalizing factor. The sensorless vector control bandwidths are selected according to the design procedure developed by Kshirsagar *et al.* [4] and are summarized in table 4.1. Note that the observers follow the controllers which break the numerically increasing bandwidth

pattern. The observers are not cascaded to the controllers in the strictest sense but are somewhat parallel to the controllers.

Table 4.1: Bandwidth selection for sensorless vector controller [4].

Control loop	Symbol	Value relative to ω_s
Speed controller	ω_s	1
Current controller	ω_c	50
Angular speed observer	ω_t	20
Electrical state observer	ω_o	200

4.2.4 Current control

The current control design for a drive equipped *with* an angular position sensor is presented in [13]. Assuming that the angular position is accurately measured the design of the current control PI gains boils down to choosing the current control bandwidth. In the case of a sensor*less* vector control, the current control bandwidth is bounded in its relation to the electrical state observer. Nevertheless, the design procedure is essentially the same.

The key to the current control design is with the aid of feed-forward linearisation terms. In the case of the AMB control presented in section 3.3, the non-linear gyroscopic term was cancelled with a feed-forward term. After the cancellation of the non-linear term, the residual system dynamics was linear and a full-state feedback control design could be performed. In the case of the PMSM, the speed-dependent cross-coupling terms may also be cancelled via a speed-dependent feed-forward term. Due to the resulting linear system, the classical frequency domain design can be employed. Much of the sensorless vector control design presented here is based on the design presented in that article and readers are encouraged to consult the reference. As stated previously the design is repeated here so that the thesis is self-contained to a certain degree.

As opposed to the design of the current control in the sensored case, one first assumes that an accurate estimated rotor angle, $\hat{\theta}_r$, is available for the Park transform to be used. The estimation of the angle is presented later in section 4.2.6. After cancellation of the speed dependent terms of (4.1) the residual dynamic behaviour is that of a simple RL-load:

$$\begin{aligned} \frac{d}{dt} i_{sd}^{\hat{r}} &= \frac{1}{L}\left(r i_{sd}^{\hat{r}} + v_d^*\right) \\ \frac{d}{dt} i_{sq}^{\hat{r}} &= \frac{1}{L}\left(r i_{sq}^{\hat{r}} + v_q^*\right) , \end{aligned} \tag{4.3}$$

where v_d^* and v_q^*, are reference voltages generated by the PI current control loop. The superscript, $\hat{r}$, indicates that the variables are in the estimated reference frame. The inductance, L, is the sum of the stator and three-phase filter inductance. The same holds for the resistance: $r = r_s + r_{lf}$. A saliency factor of unity is assumed since a surface mount

PMSM is used in this work. The feed-forward decoupling term is produced by:

$$\mathbf{v}_{dq}^{DN} = -\hat{\omega}_r \begin{bmatrix} 0 & L \\ -L & 0 \end{bmatrix} \begin{bmatrix} \hat{i_{sd}^r} \\ \hat{i_{sq}^r} \end{bmatrix}, \tag{4.4}$$

where $\hat{\omega}_r$, is the estimated angular speed. In the design presented by Kshirsagar *et al.* the decoupling term is set to zero during the open-loop start-up. For the modified start-up procedure, presented in 4.3, the estimated angle slides from an initial open-loop signal to a closed-loop signal and the decoupling term is thus added even from start-up.

Besides the machine dynamic cross-coupling which is cancelled by the feed-forward term, the delays due to the anti-aliasing filter and sampling delays also produce cross-coupling. This cross-coupling is decoupled with the aid of a speed-dependent rotation matrix, as originally presented by Sepe and Lang [102]. An implementation of the rotation matrix decoupling for a high-speed PMSM is presented in [50] as part of the non-ideality compensation of a $\frac{V}{f}$-controlled drive, but is also applicable to vector controlled drives. In fact, the derivation of the speed dependent rotation matrix makes use of the small angle approximation for trigonometric quantities. In the case of a vector controlled drive, where the angle is available either via measurement or estimation, the angle may be corrected with a speed-dependent phase delay term explicitly, which does not make the small angle approximation by correcting the cross-coupling with a rotation matrix. Thus, the delay is compensated in the angle used for the Park transform and yields a more accurate delay compensation. The compensation of the delay is presented in section B.2.2.

As presented in [13], the open-loop gain for the PI control combined with the linear plant of (4.3), is:

$$\begin{aligned} G_c(s)\, G_P(s) &= \left(K_{p\_c} + \frac{K_{i\_c}}{s}\right) \frac{1}{sL + r} \\ &= \frac{\omega_c}{s} \left(s\frac{K_{p\_c}}{\omega_c} + \frac{K_{i\_c}}{\omega_c}\right) \frac{1}{sL + r}, \end{aligned} \tag{4.5}$$

where ω_c, is the cross-over frequency. K_{p_c} and K_{i_c}, are the proportional and integral gains of the PI current controller. The PI gains are thus chosen in order to cancel with the plant [13]:

$$\begin{aligned} K_{p\_c} &= \omega_c L \\ K_{i\_c} &= \omega_c r\,. \end{aligned} \tag{4.6}$$

Thus, in order to complete the current control design, one needs to select the cross-over frequency, ω_c, as per table 4.1.

4.2.5 Speed control

A PI speed controller is used for speed control. The viscous friction is considered negligible, thus the mechanical dynamics result in a pure integrator. Consequently, the PI controller

gains cannot be chosen directly in order to cancel with the plant, as was done for the current control design. Hence, a zero in the transfer function remains. The closed-loop dynamics of the speed controller is given by [4]:

$$G_{s\_cl}(s) = K_T z_p \frac{sK_{p\_s} + K_{i\_s}}{J_p s^2 + \left(sK_{p\_s} + K_{i\_s}\right) K_T z_p}, \tag{4.7}$$

where $K_T = \frac{3}{2} z_p \lambda_p$, is the torque constant, and K_{p_s}, K_{i_s}, are the position and integral gains, respectively. The zero of the closed-loop transfer function is cancelled by adding a pre-filter [4]:

$$G_{pf}(s) = \frac{K_{i\_s}}{sK_{p\_s} + K_{i\_s}}. \tag{4.8}$$

The closed-loop dynamics incorporating the pre-filter thus results in a second-order system and the PI gains are set by equating terms to the generalized second-order polynomial. This results in the following speed control PI gain expressions:

$$\begin{aligned} K_{p\_s} &= 2\zeta\omega_s \frac{J_p}{K_T z_p} \\ K_{i\_s} &= \omega_s^2 \frac{J_p}{K_T z_p}, \end{aligned} \tag{4.9}$$

where ω_s, is the speed control bandwidth which is chosen as per table 4.1.

4.2.6 Observer

4.2.6.1 Estimated reference frame state equations

In order to estimate the states of the system described in (4.1), one first has to note that the state variables of the system described in (4.1) are in a known reference frame. For the sensorless vector control, the states are estimated in a reference frame which itself is estimated. Theoretically, a stable electrical state observer can be designed to observe the states in *any* reference frame, but only the true rotor reference frame is of practical value. By casting the voltage equation in the estimated reference frame and noting the properties of the estimated states when the estimated reference frame and the actual rotor reference frame have an angular difference a corrective law for the estimated angle may be deduced in order to drive the estimated reference frame to align with the true rotor reference frame.

The voltage equation of the stator, in the rotor reference frame, is given by:

$$\begin{bmatrix} v_{Ad} \\ v_{Aq} \end{bmatrix} = \begin{bmatrix} r & -\omega_r L \\ \omega_r L & r \end{bmatrix} \begin{bmatrix} i_{ds} \\ i_{qs} \end{bmatrix} + L\frac{d}{dt} \begin{bmatrix} i_{ds} \\ i_{qs} \end{bmatrix} + \omega_r \begin{bmatrix} 0 \\ \lambda_p \end{bmatrix}, \tag{4.10}$$

where, $r = r_{lf} + r_s$ and $L = L_f + L_s$, are the combined stator and three-phase filter

resistance and inductance, λ_p is the pole flux and v_{Ad}, v_{Aq}, are the direct and quadrature inverter output voltage in the rotor reference frame. The total back-emf adds only to the q-axis voltage in the machine equation when the actual rotor angle aligns with the d-axis.

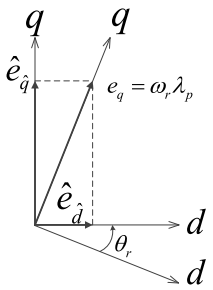

Figure 4.2: Back-emf in true and estimated coordinates [4].

Fig. 4.2, depicts how the true back-emf projects onto the estimated reference frame for the case that an angular error exists between the estimated and the true rotor angle. The angular error is defined as:

$$\tilde{\theta}_r = \theta_r - \hat{\theta}_r \,, \tag{4.11}$$

With an angular error present, the back-emf projected to the estimated reference frame is given by:

$$\begin{aligned} e_{\hat{d}} &= \omega_r \lambda_p \sin\left(\tilde{\theta}_r\right) \\ e_{\hat{q}} &= \omega_r \lambda_p \cos\left(\tilde{\theta}_r\right) \,. \end{aligned} \tag{4.12}$$

Thus, the stator voltage equation in the estimated rotor reference frame is given by [4]:

$$\begin{bmatrix} v_{A\hat{d}} \\ v_{A\hat{q}} \end{bmatrix} = \begin{bmatrix} r & -\omega_r L \\ \omega_r L & r \end{bmatrix} \begin{bmatrix} i_{\hat{d}s} \\ i_{\hat{q}s} \end{bmatrix} + L\frac{d}{dt} \begin{bmatrix} i_{\hat{d}s} \\ i_{\hat{q}s} \end{bmatrix} + \begin{bmatrix} -e_{\hat{d}} \\ e_{\hat{q}} \end{bmatrix} \,. \tag{4.13}$$

If the $\hat{d}$-axis component is positive (negative) the estimated reference frame has to recede (advance) in order to align with the true rotor reference frame. Therefore, the estimated $\hat{d}$-axis back-emf in the estimated reference frame, $\hat{e}_{\hat{d}}$, can be used as an input to a phase-locked loop (PLL), as proposed by [4], to decelerate or accelerate the estimated reference frame angular velocity. If the input to the PLL is zero the estimated reference frame coincides with the true reference frame. This condition is met if the angular velocity of the estimated reference frame is that of the rotor, i.e. $\hat{\omega}_r = \omega_r$.

Since the back-emf in the estimated reference frame, $\mathbf{e}_{\hat{d}q}$, is an unmeasured quantity it is promoted to an internal state variable which has to be estimated, i.e. $\hat{\mathbf{e}}_{\hat{d}q}$.

4.2.6.2 Electrical state estimator

The observer used to estimate the electrical states is a classical[3] Luenberger observer. The estimator has the generalized form [4]:

$$\dot{\hat{\mathbf{x}}} = \mathbf{A}\hat{\mathbf{x}} + \mathbf{B}u + \mathbf{L}\left(\mathbf{y} - \mathbf{C}\hat{\mathbf{x}}\right) , \tag{4.14}$$

where the matrices are given by:

$$\mathbf{A} = \begin{bmatrix} -\frac{r}{L} & \hat{\omega}_r & \frac{1}{L} & 0 \\ -\hat{\omega}_r & -\frac{r}{L} & 0 & -\frac{1}{L} \\ 0 & 0 & 0 & 0 \\ 0 & 0 & 0 & 0 \end{bmatrix} , \tag{4.15}$$

$$\mathbf{B} = \begin{bmatrix} \frac{1}{L} & 0 \\ 0 & \frac{1}{L} \\ 0 & 0 \\ 0 & 0 \end{bmatrix} , \tag{4.16}$$

$$\mathbf{C} = \begin{bmatrix} 1 & 0 & 0 & 0 \\ 0 & 1 & 0 & 0 \end{bmatrix} , \tag{4.17}$$

$$\mathbf{L} = \begin{bmatrix} l_{11} & l_{21} & l_{31} & l_{41} \\ l_{21} & l_{22} & l_{32} & l_{42} \end{bmatrix}^{\mathrm{T}} . \tag{4.18}$$

The state, input and output[4] vectors are respectively given by:

$$\hat{\mathbf{x}} = \begin{bmatrix} \hat{i}_{\hat{d}s} & \hat{i}_{\hat{q}s} & \hat{e}_{\hat{d}s} & \hat{e}_{\hat{q}s} \end{bmatrix}^{\mathrm{T}} , \tag{4.19}$$

$$\mathbf{u} = \begin{bmatrix} v_{\hat{d}s} & v_{\hat{q}s} \end{bmatrix}^{\mathrm{T}} , \tag{4.20}$$

$$\mathbf{y} = \begin{bmatrix} \hat{i}_{\hat{d}s} & \hat{i}_{\hat{q}s} \end{bmatrix}^{\mathrm{T}} . \tag{4.21}$$

The design of the observer consists out of the selection of the observer gains, l_{**}, of the feedback gain matrix, $\mathbf{L}$. Note that the observer is non-linear since the estimated speed, $\hat{\omega}_r$, in the $\mathbf{A}$ matrix is one of the system state variables. Usually, the electrical and mechanical time constants vary significantly, such that it may be assumed that the rotor

[3] Actually, the observer is adaptive due to speed dependence.

[4] In order to design the observer gains, the error dynamics under consideration is that of the current, hence the output is defined as the estimated current. In reality, the estimated back-emf is the "true" output since this is the observer output used for the speed and angle estimation.

speed is constant within one processing cycle of the electrical domain observer. Under this assumption the electrical state observer is linear. The characteristic equation of the observer is given by [4]:

$$C_o(s) \equiv \det(s\mathbf{I} - \mathbf{A} + \mathbf{LC}) \tag{4.22}$$

$$= s^4 + a_1 s^3 + a_2 s^2 + a_3 s + a_4 . \tag{4.23}$$

If the dq-axes are decoupled via feed-forward terms in the estimator (as is done in the control) and the gains are chosen appropriately then the eigenvalues are that of a repeated second-order system:

$$C_o(s) = \left(s^2 + 2\zeta\omega_0 s + \omega_o^2\right)^2 . \tag{4.24}$$

The observer gain selection as presented by [4] is followed. The back-emf in the estimator is decoupled by setting the terms l_{32} and l_{41} equal to zero. The electrical time constant of the machine is overridden by appropriate selection of l_{11} and l_{22}. The dependence on the estimated rotor speed, $\hat{\omega}_r$, is cancelled by l_{12} and l_{21}. The effect of cancelling the dependence on the estimated speed results in the estimator poles being constant over the machine operating speed range. The final estimator gain matrix thus results in:

$$\mathbf{L} = \begin{bmatrix} -\frac{r}{L} + 2\zeta\omega_o & \hat{\omega}_r \\ -\hat{\omega}_r & -\frac{r}{L} + 2\zeta\omega_o \\ \omega_o^2 L & 0 \\ 0 & \omega_o^2 L \end{bmatrix} . \tag{4.25}$$

The design of the electrical state observer is thus reduced to the selection of the observer bandwidth, ω_o, and damping, ζ. The selection of the bandwidth is related to the other cascaded control loops as discussed in section 4.2.6.1 and summarized in table 4.1. The damping is normally selected in the range of $\zeta = [0.7, 1]$.

From the comparison of the gain matrix design presented by [4] to the pole placement design presented by [14], one can observe that the observer gain matrix design by [4] is much simpler due to the design being performed in the estimated rotating reference frame. Cancellation of the observer pole dependence on the estimated speed has the advantage of simplifying observer stability verification. By making the system poles speed independent, then if the system is stable at one speed it should be stable for all other speeds.

4.2.6.3 Phase-locked loop (tracking controller)

The PLL is also called a tracking controller by Kshirsagar *et al.* since the estimated reference frame "tracks" the true rotor reference frame. The tracking controller is depicted

in block diagram form in Fig. 4.3. The norm:

$$|x_{dq}| = \sqrt{\hat{e}_{\hat{d}}^2 + \hat{e}_{\hat{q}}^2}, \tag{4.26}$$

is used to normalize the d-axis estimation error that feeds into the tracking controller, thereby keeping the tracking controller dynamics independent of the rotor speed. The cancellation of the speed dependence may be verified by substituting (4.12) into (4.26):

$$\begin{aligned} |x_{dq}| &= \sqrt{\left(\omega_r \lambda_p \sin\left(\tilde{\theta}_r\right)\right)^2 + \left(\omega_r \lambda_p \cos\left(\tilde{\theta}_r\right)\right)^2} \\ &= |\omega_r \lambda_p| \end{aligned} \tag{4.27}$$

The error in the estimated back-emf thus feeds into a proportional and integral controller, which generates an estimated speed, $\hat{\omega}_r$, which is integrated to yield the estimated rotor angle, $\hat{\theta}_r$. This angle is then used for the Park transform of the drive voltage and current to the estimated rotor reference frame which serves as input to the electrical domain observer, represented by the term $G_{obs}(s)$. In actuality, it is problematic to use the measured drive voltage, since appropriate sampling and filtering has to be employed to remove or reduce the PWM carrier from the measured voltage. Instead, the rotor reference frame voltage may be used as the input to the observer. This, however, necessitates that inverter non-ideality compensation is employed such that the assumption that the reference voltage is sufficiently equal to the actuated drive voltage is valid. The inverter non-ideality compensation is presented in appendix A.

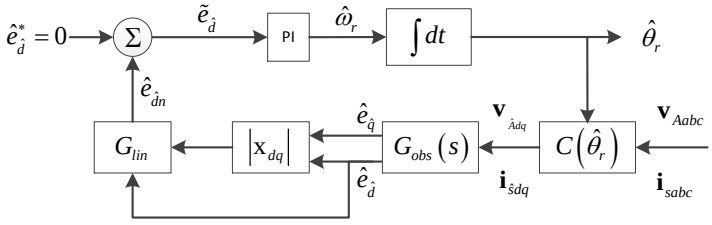

Figure 4.3: Back-emf based tracking controller.

4.2.6.4 Improved back-emf error input for tracking controller

The tracking controller presented by Kshirsagar *et al.* makes use of only the (normalized) estimated d-axis voltage, $\hat{e}_{\hat{d}}$, as input to the tracking controller. Equation (4.12) makes use of the small angle approximation to relate the angular error, $\tilde{\theta}_r$, linearly to the estimated d-axis voltage, $\hat{e}_{\hat{d}}$. It may appear that information in the estimated q-axis voltage, $\hat{e}_{\hat{q}}$, has nothing to contribute to the estimation of the angular speed since it is related by cosine to the angular error, $\tilde{\theta}_r$. In the event that the estimation angle is small, i.e. after the

tracking controller has "locked" on, this is indeed the case. During start-up of the drive, the angular estimation error may be significant however and the estimated q-axis voltage, $\hat{e}_{\hat{q}}$, may aid the tracking controller. During large transients, as the angular error increases, the gain of the sine term reduces, but that of the cosine term increases. Thus, by adding the cosine related q-axis voltage, $\hat{e}_{\hat{q}}$, to the tracking controller, the tracking controller gain is overall, more constant.

The d-axis voltage, $\hat{e}_{\hat{d}}$, was introduced to the tracking controller by noting that a d-axis voltage reference is required which corresponds to an angular estimation error of zero, hence: $\hat{e}^*_{\hat{d}} = 0$. Similarly, the q-axis voltage, $\hat{e}_{\hat{q}}$, may be introduced to the tracking controller by noting that the normalized q-axis voltage reference corresponding to zero estimation error is:

$$\begin{aligned} \hat{e}^*_{\hat{q}} &= \left. \frac{\omega_r \lambda_p \cos\left(\tilde{\theta}_r\right)}{|x_{dq}|} \right|_{\tilde{\theta}_r = 0} \\ &= 1\,. \end{aligned} \tag{4.28}$$

Thus, the tracking controller with improved back-emf error input is as depicted in Fig. 4.4. The total back-emf error feeding into the PI controller is now the sum of the normalized d- and q-axes error components. The addition of the q-axis voltage error term to the tracking controller requires a small amount of extra computation.

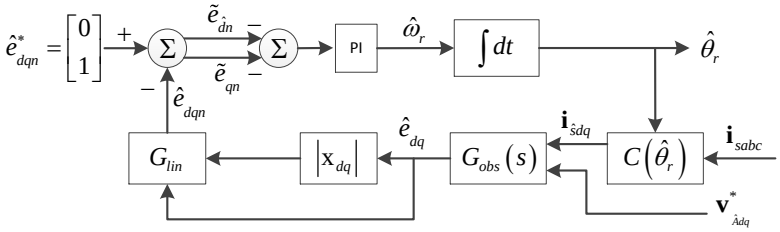

Figure 4.4: Tracking controller with improved error input terms.

4.3 Bumpless start-up method

4.3.1 Background

The sensorless vector controller described thus far is mainly from the design proposed by Kshirsagar *et al.* [4], which has been extended to incorporate the three-phase line filter. The proposed start-up method differs significantly from that presented by Kshirsagar and is novel. The start-up method has the advantage that it is simpler and has no transient

compared to Kshirsagar's method. The start-up method is a contribution in its own right with respect to drives, but the purpose of the new start-up method is that it has the capability of blending angular position sensor estimates from other sources as presented in the next chapter.

The general term applied to techniques aiming to reduce the incurred transient upon switching from one controller to another is known as bumpless transfer [103].

Two main ideas from the literature are combined to yield a start-up method which in its combined form has not yet been proposed. The first idea is to implement a current control-loop right from the start instead of using an open-loop V/f control. Current control at start-up has been suggested by several researchers. The $I - f$ starting method proposed by Fatu *et al.* [57] and the start-up strategy proposed by Wang *et al.* [104] both propose to use current regulation during start-up. The idea to use a single reference frame for estimation and control is presented by Taghirad *et al.* [105], but their control used a voltage control loop. Elsewhere in the literature computation of the reference voltage in the open-loop reference frame coordinates is presented in the $\gamma\delta$-coordinates. If an open-loop voltage controlled strategy is used beyond a certain speed a stabilization loop has to be added [106]. If the open-loop start-up can transition to a closed-loop controller before the intermediate destabilizing speed is reached the stabilization loop may be discarded.

The current- and voltage control start-up methods each have their own merits. The current control inherently compensates for the inverter non-ideality, i.e. the voltage reference generated by the current control loop compensates for voltage disturbances due to dead-time effects and unknown stator winding resistance. The current-controlled start-up is also less dependent on known motor parameters, as pointed out by Fatu *et al.* [57]. The disadvantage of the current control is that the stator voltage induced due to rotor speed perturbations are not allowed to cause a corresponding current. Such a current, which is allowed by a voltage controlled start-up, helps to dampen the rotor speed perturbations at start-up. Increased rotor speed perturbation at start-up increases the possibility of the rotor losing synchronization with the open-loop generated stator-field with the rotor thus failing to start-up. The voltage controlled start-up is a bit of a misnomer since the voltage is not typically controlled by a feedback loop. Instead, the inverter output voltage produced is the result of an open-loop generated voltage reference based on the model of the machine. Due to the model dependency, the voltage controlled start-up is more sensitive to machine parameters. The inverter non-ideality is overcome by the addition of a so-called "boost" voltage, which has to be tuned during the drive commissioning.

A compromise or hybrid control is possible with a reduced current control gain at start-up which allows the inverter non-ideality to be overcome, whilst simultaneously providing at least some damping to the rotor speed perturbations [13].

In a sensorless drive which uses an open-loop start-up, regardless of whether it is current- or voltage controlled, at some point the drive has to transition from open-loop to closed-

loop control. Typically, estimation of the electrical state variables for speed and angle estimation is processed in addition to the open-loop start-up. This results in increased computational load. During the switchover from open- to closed-loop the estimator states and drive current control experiences an unwanted transient.

Various means have been proposed to dampen the transient response upon transitioning from open- to closed-loop at start-up. One method is to re-initialise the speed and current controller integrator outputs to what the outputs would have been in the new reference frame upon switching over to the new reference frame. Such a method is proposed and demonstrated by Kruger *et al.* [16]. Although a satisfactory transient is obtained it requires extra computation to perform the reinitialization. Also, the transition algorithm is not symmetrical for run-up and run-down.

The initialization problem of reference or off-line controller is also experienced by other bumpless transfer methods. Turner and Walker [103] presented a method of bumpless transfer based on ideas from linear quadratic theory. Their method assumes that all controller realizations are completely controllable and all states observable. In the case of the PMSM control, the back-emf is analytically unobservable at standstill and practically unobservable at low speed.

Arafa *et al.* [58] present an observer-based sensorless control of the PMSM with a focus on the drive's start-up. They used a current controlled open-loop start-up with a pre-alignment step (which they referred to as homing). They investigated the open-loop start-up with two different common types of load profiles, i.e. a fan ($T_L \propto \omega^2$) and roller ($T_L \propto \omega$) load profile. In addition, they considered the possibility of not using a fixed homing step[5] and thus the start-up at various error offset angles. With the two different load types, the open-loop start-up was successful for the different initial angle errors, except for the fan type load with an initial offset angle greater than $\frac{4\pi}{3}$.

Two possible solutions to the failed start-up are proposed by Arafa *et al.* The first is to reduce the start-up ramp slope and the second is to use a homing current for a short period of time (the rotor is not allowed to settle) before the open-loop ramp starts. In the experimental result, they presented for the angular tracking of the open-loop, the real and estimated angles all converge prior to switchover to closed-loop control. This indicates that although they considered different types of loads in simulation the experimental result is for no-load during start-up. Also, the ramp rate is relatively low given the inertia of their experimental start-up, otherwise the open-loop angle would lead the measured rotor angle. Upon transitioning from open- to closed-loop control the authors also applied a speed reference step input. This made it impossible to distinguish whether the current transient originated from the transitioning algorithm or due to the speed reference step.

The start-up strategy proposed by Fatu *et al.* [57] performed a transition to a back-emf based sensorless control by blending the estimated rotor angle, $\hat{\theta}_r$, and the open-loop

[5] That is an alignment step in which the rotor is allowed to reach a steady state and thus a know rotor angle before the open-loop ramp begins.

reference angle, θ_r^*, using a first-order lag compensator after reaching a certain critical threshold speed. The time constant of the lag compensator implies a dynamic response for the angle and has thus to be chosen according to the open-loop speed ramp slope. If the speed ramp slope is changed during commissioning, for example, decreased ten fold, then it would appear that the blending angle transient reaches steady state much sooner relative to the final speed and exposes the algorithm to speed estimate disturbances.

In order to overcome this time-dependent blending, Ştirban *et al.* [107] proposed that the angle blending should strictly be a function of a speed dependent weighting ratio and do away with the lag compensator blending strategy. The angle is estimated by a PLL based observer and blending occurs *after* the output of the PLL.

Wang *et al.* [104] also recognized the transitioning problem at start-up and critiqued the proposed start-up transition methods of [57, 107], and point out the difficulty in selection of the parameters required for the transition algorithm. Wang *et al.* present their own start-up and transition algorithm which takes a novel approach and addresses the design of the start-up and transitioning algorithms. They also present a large signal stability analysis which was lacking in the previous start-up and transitioning algorithm presentations. This has to be distinguished from the small signal stability analysis performed to ensure the stability of the V/f controlled drive and verify the efficacy of the stabilization loop.

The method proposed by Wang *et al.* can be divided into four regions. First an alignment step, which is common amongst the start-up procedure. Secondly, a constant current reference i_q^* in the synchronous reference frame is used to ramp up the speed to a threshold speed. Thirdly, upon reaching the threshold speed, the speed is kept constant whilst the current reference i_q^* is gradually reduced, whilst the estimator for the field oriented control is active in the background. As the current is reduced the difference between the open-loop angle and estimated rotor angle decays. Upon reaching an angle difference threshold the control may switchover to the sensorless vector controller, which constitutes the fourth region. There are mainly three parameters which have to be selected for the start-up:

- The peak open-loop reference current i_q^* which is dependent on the load profile which is assumed known. Only the average load during start-up has to be known.
- The start-up ramp rate, K_ω, which is a function of the open-loop reference current i_q^*,
- and lastly, the current reduction rate, K_i, during the constant speed region.

The design of the proposed method by Wang *et al.* [104] is much clearer, but with the drawback that the start-up method is dependent on the constant speed region to reduce the open-loop reference current until it equals the estimated q-axis current. This prolongs the time required for start-up. In addition, there is no *usable* rotor angle and speed estimation information available until the transition to field oriented control has

completed. In practice, the angle and speed estimation during start-up improve linearly as the speed increases and a good start-up strategy has to be able to make use of the information available.

4.3.2 Proposed start-up method

4.3.2.1 Modified tracking controller

The proposed method modifies the previous methods of [57] and [107] to blend the open-loop reference and estimated *speeds* as opposed to the angle. This is achieved by moving the blending *before* the PLL (tracking controller presented in section 4.2.6.3) instead of at the PLL output. The blending weight is calculated as:

$$W_{obs} = \text{sat}\left[M_t\left(\frac{\omega_r^*}{\omega_{r\_th}} - 1\right)\right]_0^1 , \tag{4.29}$$

where W_{obs}, is the observer enable weight, which is saturation limited to the range [0, 1], ω_r^* is the reference speed, ω_{r_th} is a threshold speed, M_t is a transition slope. From standstill up to the threshold speed the start-up is pure open-loop. The weight for enabling the observer is visualized in Fig. 4.5. At the threshold speed, ω_{r_th}, blending of the reference and estimated angular speeds start until reaching a reference speed equal to $\omega_r^* = \omega_{r\_th}/M_t$ where the input to the tracking controller is purely from the back-emf error term. It is important to note that upon reaching the closed-loop reference speed no distinct switching action is performed. The blending step *is* the transition from open-loop to closed-loop control. The proposed method thus has a smaller number of distinct regions during start-up compared to the previous methods.

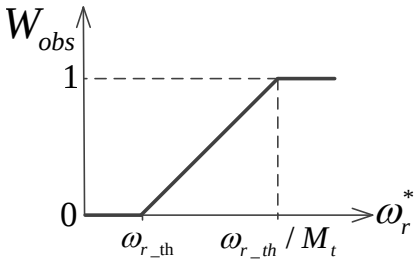

Figure 4.5: Observer enable weighting function.

A simple application of the observer weight to the PI controller input of the PLL is by:

$$e_{PLL} = \tilde{e}_{\hat{d}} W_{obs} + \omega_r^* \left(1 - W_{obs}\right) , \tag{4.30}$$

where $\tilde{e}_{\hat{d}}$, is the back-emf estimation error of the tracking controller as presented in Fig. 4.3.

From simulation, it has been found that application of the simple weighting method is not sufficiently "smooth". If a large back-emf estimation error-disturbance is present at the input, even at a relatively low speed, the resulting estimated speed, ω_r^*, may deviate without a bound from the reference speed. The deviation of the estimated speed from the reference speed may be bounded by adding a disturbance rejection loop at the input to the reference speed:

$$e_{PLL} = \tilde{e}_{\hat{d}} W_{obs} + \left(\omega_r^* - \hat{\omega}_{r\_k-1}\right)(1 - W_{obs}) \ . \tag{4.31}$$

Due to the direct feed-through of the proportional gain in the tracking controller an algebraic loop results if the estimated speed, $\hat{\omega}_r$, is fed back directly. In order to break the algebraic loop the previous control cycle's speed estimate, $\hat{\omega}_{r\_k-1}$, is fed back instead.

The modified tracking controller, with the reference speed dependent weights, is displayed in Fig. 4.6. As can be seen, the feedback loop of the estimated speed has as input the reference speed. Thus, with respect to this loop, the weighted back-emf input term appears as a disturbance. This loop thus serves as a secondary measure to transfer the reference speed to the back-emf more smoothly than a merely fixed weighting scheme.

When the reference speed exceeds the threshold speed the angle used in the coordinate transformations is the open-loop reference angle blended with the estimated reference angle. The blended angle is still denoted by, $\hat{\theta}_r$, as it is the output of the tracking controller.

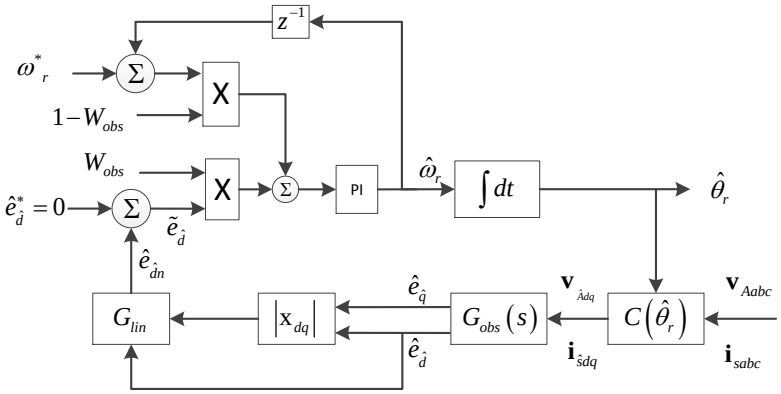

Figure 4.6: Modified tracking controller.

4.3.2.2 Speed controller start-up

The rotor is aligned with an open-loop reference current in the d^*-axis, with reference angle, $\theta_r^* = 0$. The magnitude of the reference current, i_d^*, is set according to the load torque required for start-up. In the flywheel application, the load torque is that of the load inertia. Hence, the reference magnitude current is determined by the ramp rate. As

the reference angle starts to rotate the true rotor angle falls behind the reference angle, such that d^*-axis is decomposed into direct and quadrature axes components in the true rotor reference frame. Thus, a torque producing current results which cause the rotor to accelerate even though the torque producing current reference is zero. Fig. 4.7, illustrates the decomposition of the current in the applicable reference frames during the alignment and acceleration steps. The true rotor angle lags the reference angle according to the amount of required torque. If the rotor angle lags the reference angle by more than $\frac{\pi}{2}$ the stator current is insufficient to provide enough torque. Beyond $\frac{\pi}{2}$ the torque decreases and the rotor loses synchronism.

A different convention is used to denote the current reference in the start-up procedure proposed by Wang *et al.* [104]. They set the reference current as i_q^*. Usually, different conventions are equivalent as long as the convention is consistently applied. This is not so in this case. The proposed convention here, that the reference current should be, i_d^*, has further benefits as will be explained.

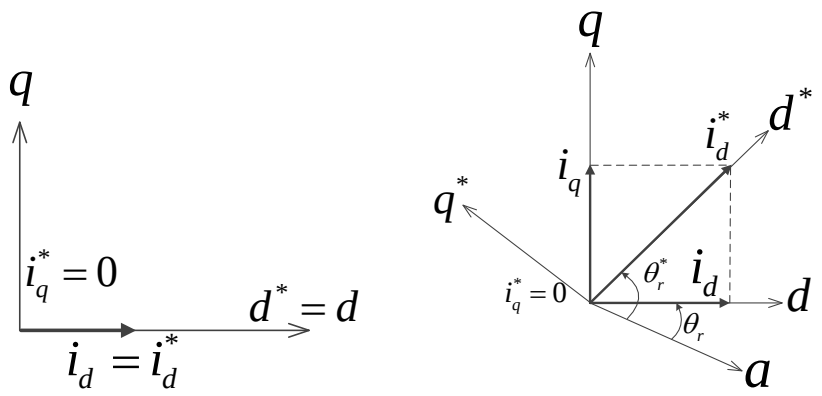

(a) Alignment step ($\omega_r^* = 0$). (b) Open-loop acceleration ($\omega_r^* < \omega_{r\_th}$).

Figure 4.7: Decomposition of reference rotor currents in real and reference coordinates during start-up.

During the transitioning from open- to closed-loop, the speed controller in the proposed start-up is already active. As the tracking controller speed is transferred from the reference speed to the estimated speed, the speed error is transferred from zero to the actual amount of error. Hence, the speed controller becomes gradually switched on, implicitly due to the modified tracking controller, and a reference torque producing current is automatically generated to accelerate the rotor to track the reference speed. In the convention proposed by Wang *et al.* the controller is limited to keeping i_q^* constant during the ramp-up phase. This is also the reason why their method requires a distinct transfer step in order to reduce the reference current, i_q^*, until it equals the estimated torque producing current, $\hat{i}_q$, after the ramp-up has completed, but before the field oriented control can be switched on. Thus, the speed controller cannot take over the task of providing i_q^* during the ramp-up phase, due to the convention that Wang *et al.* used.

The excess open-loop reference current which had to be reduced by the method of Wang *et al.* is also reduced in the proposed method. As the speed controller takes over the task of generating a q-axis reference current in the estimated reference frame, $i^*_{\hat{q}}$, the total stator current may exceed the inverter current limit if the d^*-axis reference current is not reduced. The d-axis current reference is generated by:

$$i^*_d = \begin{cases} i_{d\_init}\,, & W_{obs} \leq cc_{th} \\ \left(i_{d\_init} - \left|i^*_q\right| W_{cc}\right)(1 - W_{cc}) + i_{d\_bias} W_{cc}\,, & W_{obs} > cc_{th} \end{cases} \tag{4.32}$$

where

$$W_{cc} = \frac{1}{1 - cc_{th}} \left(W_{obs} - cc_{th}\right)\,, \tag{4.33}$$

and cc_{th}, is a user selected current control threshold percentage between the initial transition, $\omega^*_{r\_th}$, and the transition completion speed, $\frac{\omega^*_r}{M_t}$, in the range of [0, 1][6]. The current control threshold is used to generate a sliding weight for the d-axis current reference function in (4.32). The current control weight, W_{cc}, is automatically limited to the range [0, 1] due to the limiting on W_{obs} and is displayed in Fig. 4.8. With $cc_{th} = 0.5$, i^*_d will start to decrease midway in the transfer of open- to closed-loop control. The d-axis current is limited by two mechanisms. The first is by means of the current control weight term, $(1 - W_{cc})$. The second means is by the negative correlation with the q-axis reference current. Thus, as the speed controller progressively takes over the task of generating torque producing current the d-axis reference current is reduced.

The reason why the speed controller is able or allowed to progressively take over the task of producing torque producing current is that the tracking controller angle output is converging towards the true rotor angle. Hence, the current control in the estimated reference frame is partially able to produce real torque producing current, with decreasing error as the observer and tracking controller is gradually switched to full back-emf mode.

The d-axis reference current is decreased to a minimum bias current level, i_{d_bias}. A current value of 1 A (0.04 pu)[7], is used for the flywheel application. This is in order to allow a minimum three-phase current amplitude, with well defined current zero crossings, in case of low loads. Well defined current zero crossings are required for the chatter-free operation of the inverter non-ideality compensation.

[6] Typically 0.5 is used.

[7] pu - per unit. The normalization factors used is the rated value specified in the electrical machine design [77] or drive design [79]. Throughout the following text, the per unit value is presented in parentheses with the actual value somewhere in the paragraph. Thus, the normalization value used, if desired, may be calculated.

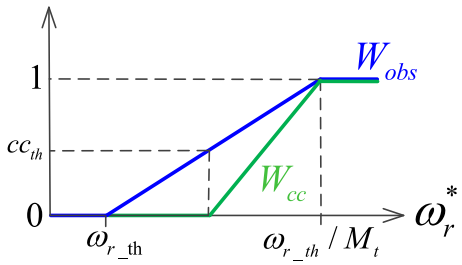

Figure 4.8: Current control weight function.

4.3.2.3 Start-up parameter selection

In total, there are four primary parameters and one secondary parameter to be tuned for the start-up. These are:

$i^*_{d\_init}$ The maximum d-axis start-up current. This is set according to the initial load and ramp-up rate.

ω_{r_th} The threshold frequency where the back-emf feedback *starts* to blend with the reference frequency term to yield the blended rotor angle.

M_t The transition slope. This is determined by the transition completion speed, $\omega_{r\_fin} = \frac{\omega_r^*}{M_t}$.

cc_{th} The current control threshold percentage. This determines the d-axis current switch off, which starts at: $W_{obs} = cc_{th}$, and is completed at: $W_{obs} = 1$.

i_{d_bias} This sets the minimum d-axis control current reference, to ensure a residual current for the inverter non-ideality compensation to function correctly. It does not influence the start-up performance as such but ensures that the sensorless control functions correctly *after* the transition is completed.

The start-up parameters were mainly "tuned by hand" using simulations of the drive to yield the desired response. In the start-up procedure proposed for the sensorless control by Kshirsagar *et al.* [4] the speed at which the observer is turned on is determined by the condition that the motor's back-emf must exceed the distortion due to the inverter:

$$\omega_{r\_init} \geq \frac{1}{\lambda_p} \frac{T_{DT}}{T_{sw}} V_{dc}\,, \tag{4.34}$$

where λ_p, is the peak magnet flux linkage, T_{sw} is the switching period, T_{DT} is the dead-time, and V_{dc} is the DC bus voltage. For the PMSM and drive in this work the observer turn-on frequency using their method would be 10 Hz (≈ 0.03 pu). The speed at which Kshirsagar *et al.* switches to field oriented control is 0.03 pu after enabling the observer estimation. In this work the observer is partially switched on much earlier, i.e. at 3 Hz (≈ 0.01 pu), but with little weight in the control. At 10 Hz, the observer is only 58 % on,

but is fully operative and in sensorless control mode at a higher speed of approximately 15 Hz (0.05 pu).

4.3.2.4 Simulated start-up

The response of the simulated start-up is shown in Fig. 4.9. All of the subplots share two x-axes. The top x-axis presents the reference speed, whilst the bottom x-axis presents the time. The first second is an alignment step (for simulation the rotor starts at the correct angle). The start-up initial frequency threshold, ω_{r_th} is set to 3 Hz (0.01 pu). Start-up completes at 15 Hz (0.05 pu). From 15 Hz to the final frequency of 20 Hz, the drive is in full sensorless mode, with a minimum i_d due to maximum torque per ampere control. The initial start-up current is set to 20 A and the start-up ramp rate is set accordingly to 10 rad.s^{-1}[8]. From the figure, it should be noted that the current transient during start-up is "smooth" or "bumpless". No high-frequency current transient is observable during the switchover.

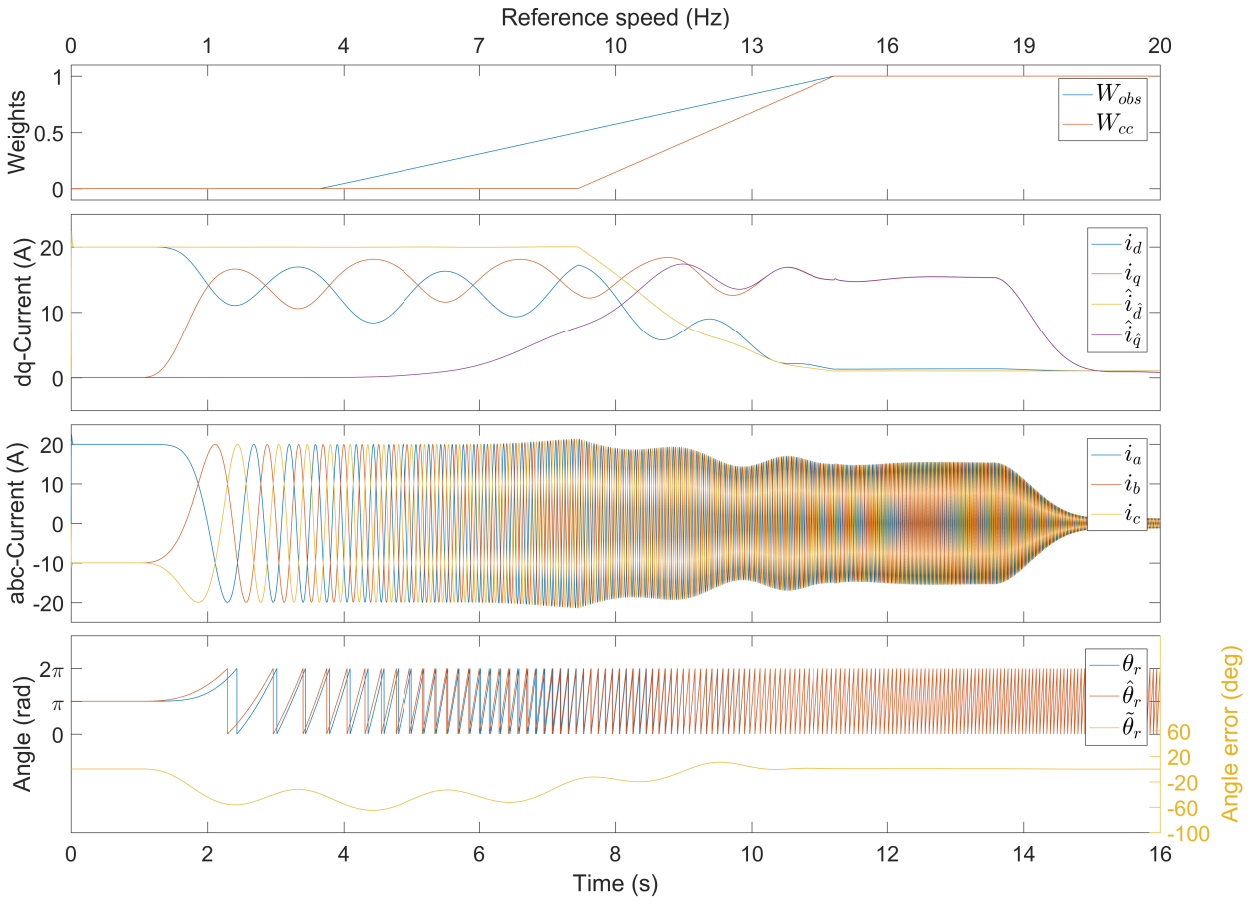

Figure 4.9: Simulated bumpless start-up method response.

[8]The speed reference generator presented by Kruger is used for the ramp [13].

The start-up response, shown in Fig. 4.9, used the standard tracking controller error input term, as proposed by Kshirsagar *et al.* [4]. Fig. 4.10, compares the angular estimation error using the standard and improved back-emf error input terms of the tracking controller, as developed in section 4.2.6.4. The same start-up conditions are used as for the previous test. During the first four seconds of the pure open-loop phase, the tracking controller output is unchanged. During the transition from open-to closed-loop, the tracking controller which included the q-axis back-emf error term yielded a smaller estimation angle error. The estimation angle settles at the same time towards zero because the small signal angular error dynamics is determined by the d-axis term. The q-axis term is useful for limiting the error during the large signal error dynamics. The addition of the q-axis back-emf error term to the tracking controller may thus be beneficially employed in the bumpless start-up method.

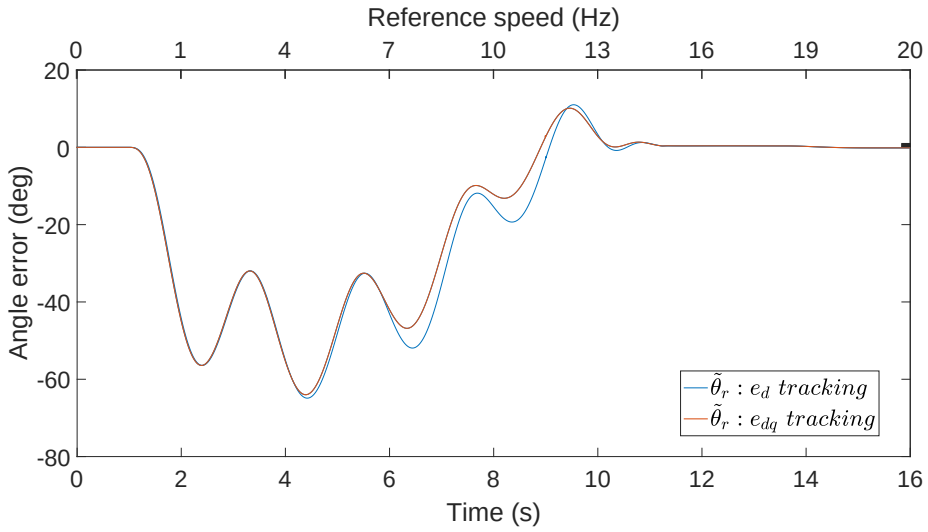

Figure 4.10: Tracking controller back-emf error input comparison.

A simulation model of sensorless vector control using the bumpless start-up technique is provided in appendix E.7.

4.3.2.5 Measured start-up response

The measured start-up and run-down response are shown in Figs. 4.11a and 4.11b, respectively. Since the rotational angle of the flywheel cannot be measured the estimated angle is uninformative and is not plotted. Instead of the angle, the estimated back-emf is displayed. After about 12.5 Hz, at 10 s the d-axis back-emf tends to zero, indicating that the observer has settled. The current show no high-frequency transients during the bumpless start-up. The start-up is in good agreement with the simulation. For the run-down, the DC bus voltage increases due to the braking action of the drive which returns energy to the DC bus capacitors. After reaching about 180 V, the DC bus brake is activated.

The large ripple on the DC bus brake is due to a hysteresis controller used for the DC bus braking circuit[9]. As can be observed, despite the disturbance on the DC bus, no disturbance is observable on the back-emf estimates or in the controlled current. This is due to accurate sensing and compensation of the inverter's gain dependence on the DC bus voltage in the current control loop.

The proposed start-up algorithm could successfully be used for run-up and run-down of the rotor without asymmetric boundary conditions, unlike the previous methods found in the literature discussed in section 4.3.1.

[9]Despite an hysteresis voltage controller, the switching action is clocked synchronously with the system clock used for the PWMs in order to reduce EMI.

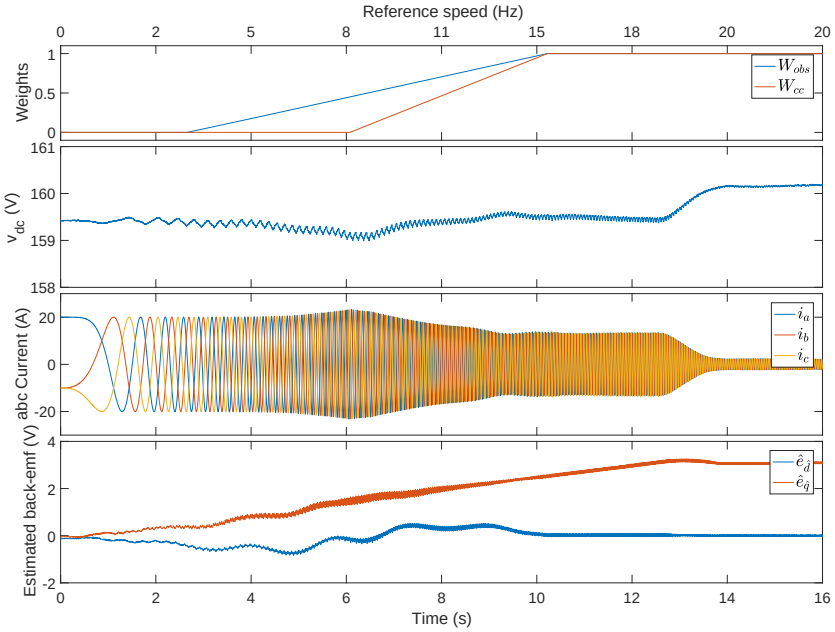

(a) Run-up.

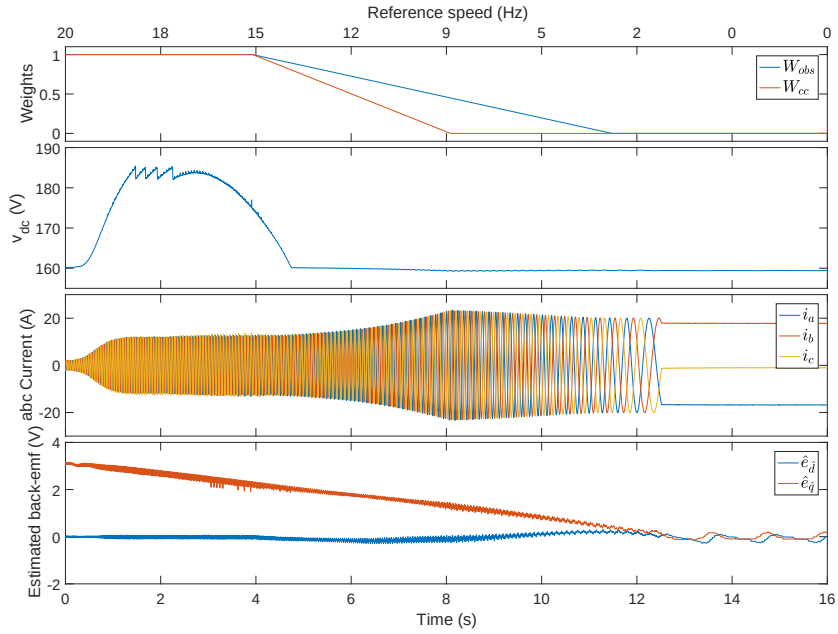

(b) Run-down.

Figure 4.11: Measured start-up and run-down response using the bumpless start-up method.

4.4 Observer with time-varying parameters

4.4.1 Observer equations for salient machine

The observer with time-varying parameters uses the polynomial fit of inductance and resistance presented in section B.2.4. The current dependence of the inductance causes a dynamic saliency to result. The observer developed by Kshirsagar *et al.* and used in section 4.2.6.2 assumed a non-salient machine. Hence, the equations must be adjusted to take the saliency into account. The resulting **A** matrix is thus:

$$\mathbf{A} = \begin{bmatrix} -\frac{r}{L_d} & \frac{L_q}{L_d}\hat{\omega}_r & \frac{1}{L_d} & 0 \\ -\frac{L_d}{L_q}\hat{\omega}_r & -\frac{r}{L_q} & 0 & -\frac{1}{L_q} \\ 0 & 0 & 0 & 0 \\ 0 & 0 & 0 & 0 \end{bmatrix}, \tag{4.35}$$

and the observer gain is:

$$\mathbf{L} = \begin{bmatrix} -\frac{r}{L_d} + 2\zeta\omega_o & \frac{L_q}{L_d}\hat{\omega}_r \\ -\frac{L_d}{L_q}\hat{\omega}_r & -\frac{r}{L_q} + 2\zeta\omega_o \\ \omega_o^2 L_d & 0 \\ 0 & \omega_o^2 L_q \end{bmatrix}. \tag{4.36}$$

The resistance is computed using the polynomial fit, given by:

$$r(f) = 8.99 \times 10^{-7} f^2 + 4.06 \times 10^{-4} f + 0.165\,, \tag{4.37}$$

and the inductances are calculated using:

$$L_d\left(i_d\right) = -2.48 \times 10^{-6}\left|i_d\right|^2 + 53.3 \times 10^{-6}\left|i_d\right| + 465 \times 10^{-6} \tag{4.38}$$

$$L_q\left(i_q\right) = -2.48 \times 10^{-6}\left|i_q\right|^2 + 53.3 \times 10^{-6}\left|i_q\right| + 465 \times 10^{-6}\,. \tag{4.39}$$

The time-varying resistance and inductance are also used in the feed-forward terms of the current control.

In the non-parameter varying observer, the only time-varying parameter was the rotational speed. The time-varying inductance implies that division is now required. The division is computationally expensive. Since the rate of change of the current is limited the division is instead computed using the Newton-Raphson approximation. The Newton-Raphson approximation of computing the reciprocal of the DC bus voltage is presented in-depth in appendix A.4 and is not repeated here for the inductance.

4.4.2 Time-varying parameter observer results

Ideally, the parameter varying observer is compared to the non-parameter varying observer by comparing the estimated and measured angular position of both observers. Unfortunately, the rotor angle is not measured in the flywheel system. Another means of determining the efficacy of the time-varying parameter salient observer is by means of current step responses. The aim of accounting for the time-varying parameters in the control is so that it should cancel out with the varying parameters of the actual machine so that it is perceived externally as if the control and machine are both non-parameter varying.

The measured d-axis current step response comparison for constant and varying parameters is shown in Fig. 4.12. As can be observed the step response is more self-similar for the varying parameter observer. This indicates that the drive's eigenvalues are more constant over operating conditions. This is a desirable feature, especially if another system, such as the AMB is made dependent upon the drive's estimated angle.

The self-similarity in response is also apparent in the estimated d-axis back-emf, as shown in Fig. 4.13.

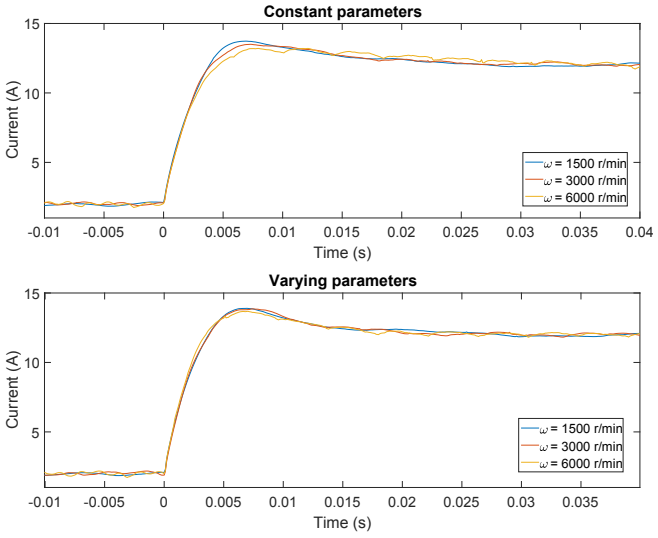

Figure 4.12: d-axis current step response comparison.

The estimated q-axis back-emf response to the d-axis current step response is shown in Fig. 4.14. The coupling of the d-axis current to the estimated q-axis back-emf causes a large offset in the case of the constant parameter observer. This coupling is less apparent in the case of the parameter varying observer. Since the tracking controller rotates the estimated reference frame so that $e_d^* = 0$, the offset in the q-axis voltage may also be an offset in the d-axis, which is suppressed by tracking controller. Thus, the q-axis back-emf offset may indicate an error in the estimated angle. The angular estimation error will be investigated further in the next chapter by observing the disturbance force compensation which takes the estimated angle as an input.

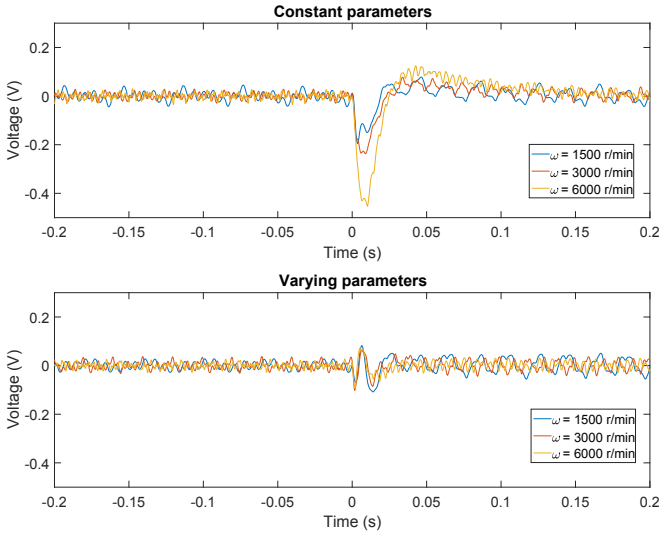

Figure 4.13: Estimated d-axis back emf comparison.

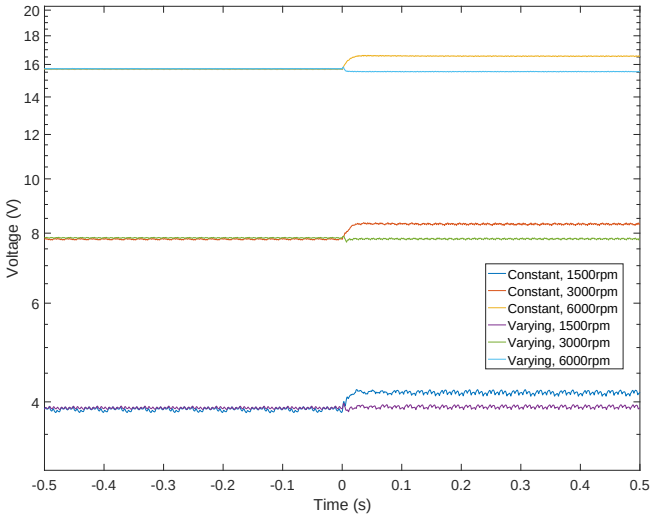

Figure 4.14: Estimated q-axis back emf comparison.

4.5 Conclusion

This chapter presented the design of the sensorless vector control. The electrical domain observer was modified to account for the machine's parameter dependencies on the rotational speed and current. The structure which allowed for the bumpless start-up of the drive was by means of modifying the tracking controller (PLL) which estimates the rotational speed and angle. The bumpless start-up method reduced the computational load because the open-loop reference angle and estimated angle are no longer separate structures. The unified structure is capable of gradually changing its characteristic as the control transitions from open- to closed-loop control.

The modified tracking controller is further modified in the next chapter which presents the cooperative control of the AMB and sensorless drive. The tracking controller is modified by replacing the open-loop start-up with the disturbance force based angle estimation, presented in the previous chapter. The start-up of the drive using the estimated angle from the AMB and switching over to the sensorless vector control using the bumpless start-up strategy is a form of cooperative control between the AMB and the sensorless drive.

Chapter 5

Cooperative control integration

5.1 Introduction

The disturbance force experienced by the AMB due to the permanent magnet of the PMSM is a function of the angular position of the rotor. With a feed-forward term, the disturbance force may be cancelled if an accurate angular position of the rotor is used as input to the feed-forward term. If an estimated angle, with a residual error, is used as input to the disturbance model a residual disturbance force results because the feed-forward term has incomplete cancellation with the actual disturbance force due to the error in the angle input. The residual disturbance force may be estimated by an observer and used as a corrective input to the angle estimation. The proposed control loop structure used for angle estimation using the residual disturbance force is a phase-locked loop (PLL)[1].

The key to the cooperative control is that the *same* phase-locked loop used for the back-emf based angular estimation is also used for the angular estimation based on the residual disturbance force. Originally, the PLL formed only part of the sensorless vector control. Since the disturbance force observed in the AMB control may also be used to estimate the speed and angle using a PLL, the PLL may be factored out of each system and serves as a point of interface or coupling between both systems, as illustrated in Fig. 5.1. The inputs to the PLL are active during different operating phases, determined by the reference angular speed. By interfacing both systems to the same PLL, a smooth transition from one operating phase to another is possible vs. a hard transition from one angle estimation to another using two separate estimation schemes. The sharing of a common PLL structure also reduces the computational footprint. Referring back to chapter 2, in which the cooperative control was introduced in general terms in section 2.5, it can be seen that Fig. 5.1 is an instantiation of the general idea for a cooperative control presented in Fig. 2.7. The antecedents of the state consolidation inputs, $\left(\hat{\omega}_r,\, \hat{\theta}_r\right)'_{\text{AMB}}$ and $\left(\hat{\omega}_r,\, \hat{\theta}_r\right)'_{\text{PMSM}}$, are realized as the estimated force disturbance, $\mathbf{F}_{b,d}$, and the estimated

[1] The PLL is elsewhere referred to as a tracking controller in the literature [4].

back-emf, $\hat{e}_d$.

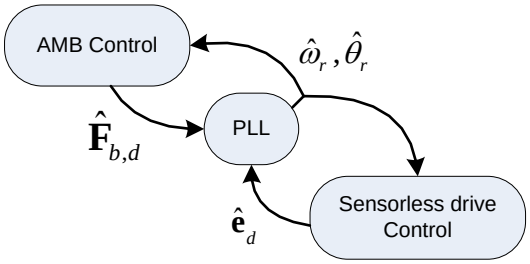

Figure 5.1: PLL as interface between AMB and sensorless drive.

The AMB disturbance force compensation for the permanent magnet may be used as an angular position sensor, which can estimate the angle at standstill and the low-speed region. Hence, the drive control may start-up in sensored vector control and transition to sensorless mode. A sensored start-up is preferable to open-loop start-up because it allows for a faster and more reliable drive start-up without a pre-alignment step. Additionally, the rigid mode frequencies of the AMB are passed with less excitation due to the unbalanced magnetic pull, because the error of the angle used for the feed-forward disturbance force compensation is smaller in comparison to the open-loop start-up.

5.2 Angular estimation fusion

5.2.1 Open-loop force error model

In order to determine how the rotor angle can be estimated using a phase-locked loop from the disturbance force, an understanding of the force error model has to be gained. The force disturbance model used to investigate the error dynamics is the generalized disturbance force (GDF) model presented in section 3.6. Fig. 5.2, depicts the force error model. For the following development, to gain understanding, the force disturbance model with the true rotor angle, θ_r, as input is assumed to represent the real force disturbance experienced by the AMB due to the PM. The force disturbance model using the estimated angle, $\hat{\theta}_r$, as input represents the feed-forward term that will be used in the control to cancel the force disturbance due to the unbalanced magnetic pull. The force error is later substituted by the estimated disturbance force obtained by the rigid rotor dynamics observer presented in section 3.4.1.

The force error in stationary bearing coordinates, resulting due to a difference between the real rotor angle and the estimated rotor angle, is given by:

$$\tilde{\mathbf{F}}_{b,xy} = \mathbf{F}_{b,xy}\left(\theta_r\right) - \mathbf{F}_{b,xy}\left(\hat{\theta}_r\right) . \tag{5.1}$$

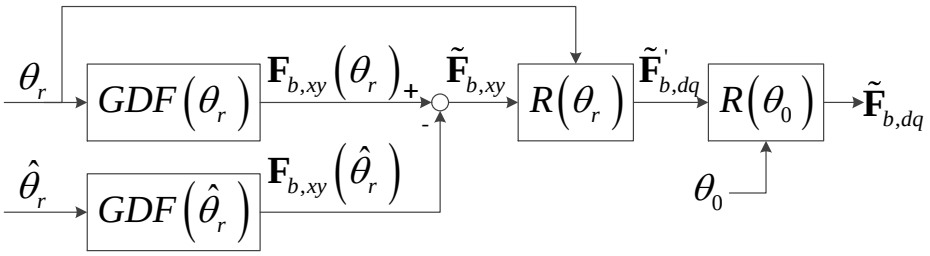

Figure 5.2: Force error model.

The force error model is evaluated numerically by sweeping $\hat{\theta}_r$ relative to θ_r. The actual rotor angle, θ_r, is rotated at a fixed angular frequency, ω_r. The estimated rotor angle is equal to the actual rotor angle plus a modulating phase shift:

$$\hat{\theta}_r = \theta_r + \phi\,. \tag{5.2}$$

The angle error is defined as:

$$\tilde{\theta}_r = \theta_r - \hat{\theta}_r \tag{5.3}$$

$$= -\phi\,. \tag{5.4}$$

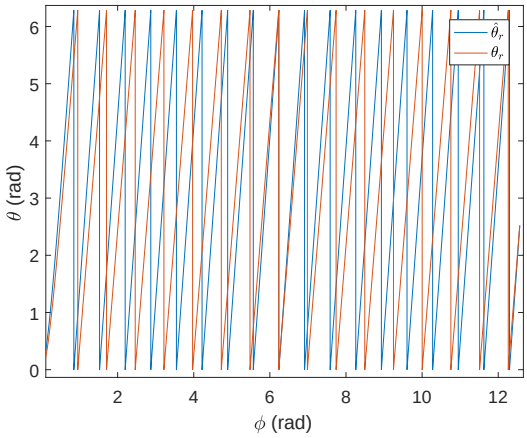

(a) Angle for force sweep.

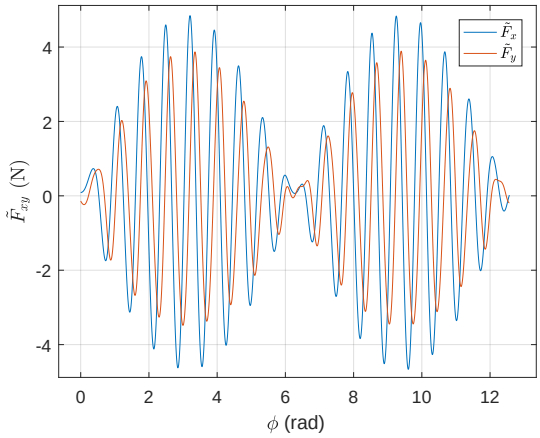

(b) Force error in stationary coordinates.

Figure 5.3: Open-loop force error characterization.

Fig. 5.3a, depicts the swept input angles for the force error model for two periods of the modulation angle, ϕ. The drive current input to the force model is set to zero for the sweep. During the sweep, the rotor is held at the magnetic centre and not allowed to move about due to the disturbance force. Fig. 5.3b, depicts the resultant force error in stationary bearing coordinates[2] which appears as an amplitude modulated wave, which

[2]Only the bearing force for the bottom AMB is depicted since this is the side which experiences the

suggests transforming the force error in stationary coordinates to a rotating reference frame, rotating at an angular frequency ω_r. Transforming the force disturbance to a rotating reference frame eliminates the fundamental component of variation of force due to the rotation. Thus, the only variation of force is that due to the swept modulation angle, ϕ. Transforming the force error in stationary coordinates to a rotating reference frame using:

$$\tilde{\mathbf{F}}'_{b,dq} = \underbrace{\begin{bmatrix} \cos(\theta_r) & \sin(\theta_r) \\ -\sin(\theta_r) & \cos(\theta_r) \end{bmatrix}}_{\mathbf{R}(\theta_r)} \tilde{\mathbf{F}}_{b,xy}\,, \tag{5.5}$$

results in the force error depicted in Fig. 5.4. From the force error in rotating coordinates, it can be concluded that the force error is modulated sinusoidally as a function of the phase shift angle between the actual rotor angle and the angle used for the feed-forward term. Higher order harmonics are present due to asymmetry in the force magnitude in the stationary xy-axis, 2^{nd} harmonic dependency of the force model and non-orthogonal basis vectors of the unbalanced magnetic pull[3].

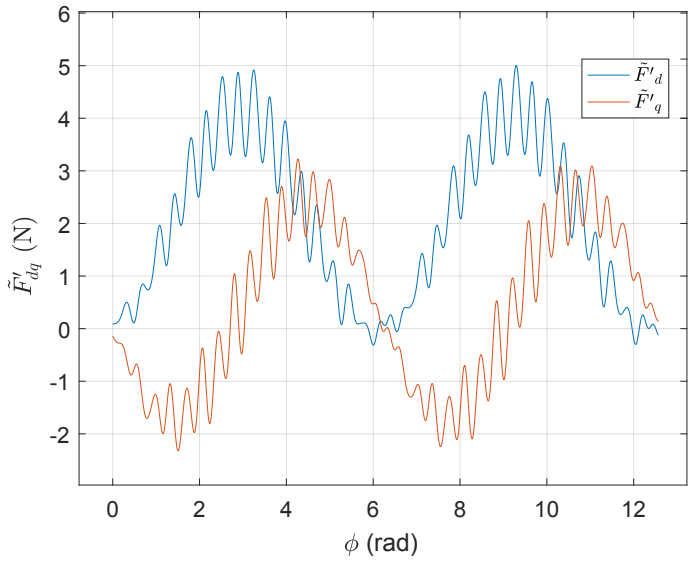

Figure 5.4: Force error in rotating coordinates.

5.2.2 Angle estimation with PLL

The force error in rotating coordinates is analogous to the estimated back-emf in dq-coordinates (see section 4.2.6). For the force to serve as an input to the phase-locked loop angle estimation, in a similar manner as the back-emf based angle estimation, the d-axis component has to vary linearly through zero (small angle approximation). This is not yet true for the force error in rotating coordinates depicted in Fig. 5.4. In order to satisfy the

greatest disturbance by the permanent magnet due to the rotor asymmetry.

[3] i.e. the force disturbance is an ellipsoid.

required condition the force in rotating coordinates requires a further fixed angle rotation, rotated by an offset angle, θ_0:

$$\tilde{\mathbf{F}}_{b,dq} = \mathbf{R}(\theta_0)\tilde{\mathbf{F}}'_{b,dq}\,. \tag{5.6}$$

Fig. 5.5, reveals that the desired force characteristic is achieved after rotating the force error in rotating coordinates by an additional offset angle of $\theta_0 = 75°$. The fixed angle rotation accounts for the angle offset between the d-axis of the permanent magnet for back-emf estimation and the angle for the peak force disturbance. This offset angle is not universal, i.e. it will vary from system to system and has to be calibrated for each system.

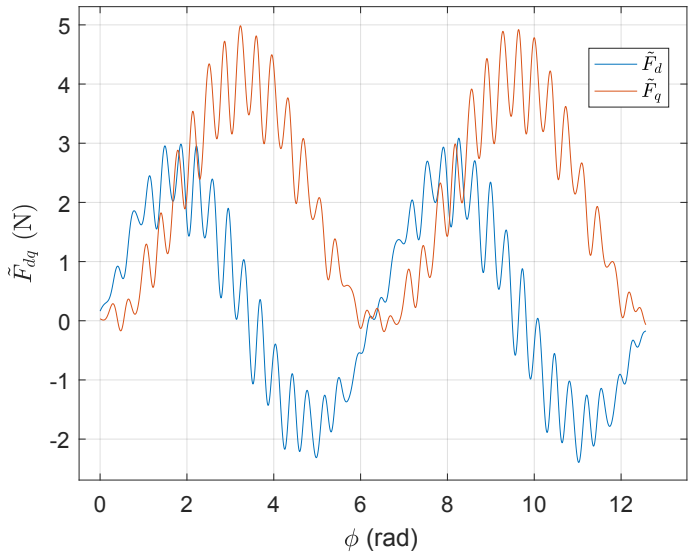

Figure 5.5: Force error in rotating coordinates, including fixed rotation, $\mathbf{R}(\theta_0)$.

The phase-locked loop for estimation of the angle by means of the force disturbance compensation loop is depicted in Fig. 5.6. The input to the loop is the rotor sensor position, angular speed and drive current. The rotor position and speed are inputs to the rigid rotor observer which estimates the disturbance force in bearing coordinates. The drive current is required by the generalized disturbance force (GDF) compensation term. The disturbance force is transformed to rotating coordinates via the rotation matrix, $\mathbf{R}\left(\hat{\theta}_r\right)$, and a further rotation by a fixed offset angle, θ_0. The total rotation transformation could have been performed in a single step via:

$$\mathbf{R}\left(\hat{\theta}_r + \theta_0\right) = \mathbf{R}\left(\hat{\theta}_r\right) + \mathbf{R}\left(\theta_0\right)\,, \tag{5.7}$$

which is avoided however in order to reduce computational complexity, because the trigonometric entries in the rotation matrix, $\mathbf{R}\left(\hat{\theta}_r\right)$, are obtained from the same LUT generated trigonometric entries used by the Park transformation in the drive control. The trigonometric entries of the Park transformation would thus be invalid for use in the drive

if the fixed offset angle was added prior to the table look-up. The fixed offset angle rotation matrix entries are generated at compile time and therefore do not require trigonometric function evaluation at run-time. The required offset angle is obtained from the numeric evaluation of the open-loop force error model in section 5.2.1. The reliance on the rotation matrix entries used in the drive control for the feed-forward force disturbance compensation in the AMB control, is another example of cooperative control in that variables required for the control of one system may be usefully re-employed in another system, to achieve the shared goal of reducing the computational load.

The PI controller takes the d-axis force disturbance component as input and (de)accelerates the estimated reference frame speed, $\hat{\omega}_r$, in order for the d-axis force disturbance component to be equal to zero. The estimated rotor angle is obtained directly via numerical integration. The estimated angle is used by the force rotation matrix, $\mathbf{R}\left(\hat{\theta}_r\right)$, as well as the Park transformation, $\mathbf{C}\left(\hat{\theta}_r\right)$, which is required for the drive current input to the GDF feed-forward term. In fact, the trigonometric terms for the Park transformation are computed only once in the drive control and are shared with the force disturbance model.

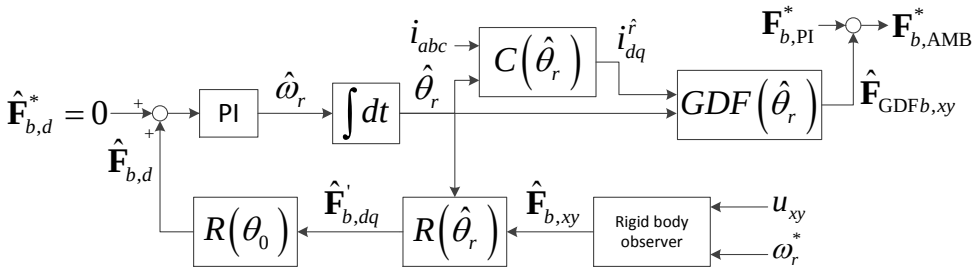

Figure 5.6: Disturbance force based tracking controller.

5.2.2.1 Simulation of force disturbance based rotor angle estimation

The angle estimation based on the disturbance force is tested by means of simulation, prior to implementation on the physical hardware. The simulation model is represented in Fig. 5.7, which consists of the AMB controller, the rigid rotor plant model, and the unbalanced magnetic pull model. The drive simulation model is not directly incorporated. The rotor angle is varied using an open-loop model, by integrating a rotor speed which is the substitute speed of the drive. The disturbance force on the rotor is modelled using the generalized disturbance force model. The sum of the AMB force, $\mathbf{F}_{b,\mathrm{AMB}}$, and the unbalanced magnetic pull force, $\mathbf{F}_{\mathrm{GDF}b,\mathrm{xy}}$, is the net force, $\mathbf{F}_b$, which is acted upon the rotor. The rigid rotor plant output is the measured position in sensor coordinates, $\mathbf{u}_s$, which in turn is the input to the AMB controller. Internal to the AMB controller the tracking controller (PLL) estimates the rotor angle, $\hat{\theta}_r$, using the estimated force disturbance, $\hat{\mathbf{F}}_{b,xy}$, as input.

The force disturbance caused by the drive current is taken into account, by assuming a fixed

dq-current in the unbalanced magnetic pull model. The reference dq-current is transformed into stationary three-phase coordinates using the open loop angle, θ_r. The three-phase current is then transformed to the estimated reference frame using the estimated angle output of the tracking controller, $\hat{\theta}_r$, similar to what would have occurred if a drive was present in the simulation. The additional disturbance force due to an error in the dq-current caused by an estimation error in the angle is thus accounted for.

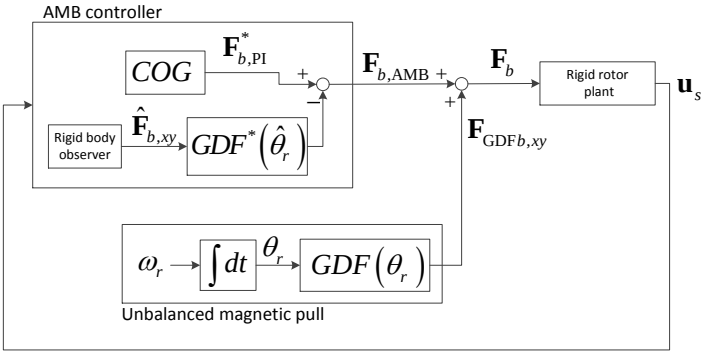

Figure 5.7: Force based angle estimation simulation model.

Fig. 5.8, displays the response of the force disturbance based angle estimation. The same tracking controller gain as designed for the sensorless drive is used. The AMB control gains used here correspond to the low stiffness gain design. The force disturbance is reduced by an additional attenuation of 0.1, before feeding into the tracking controller. The rotor is spun-up at, $t = 1\,\mathrm{s}$, from standstill to $600\,\mathrm{r/min}$. The PLL output, $\hat{\omega}_r$, is able to track the open-loop reference speed, ω_r^*. At, $t = 8\,\mathrm{s}$, a disturbance angle step input of $\frac{\pi}{6}\,\mathrm{rad}$ is added to the estimated reference angle. This mismatch between the force feed-forward model and the unbalanced magnetic pull model results in an estimated force disturbance of approximately $2\,\mathrm{N_{pk}}$. The force disturbance based PLL tracking is able to correct for the error in the angle estimate in about $0.5\,\mathrm{s}$. Quite a large disturbance in the speed estimate is apparent, $100\,\mathrm{r/min_{pk}}$. Band-limited white noise is added to the simulated drive current and rotor position with amplitudes of $0.1\,\mathrm{A_{pk}}$ and $5\,\mu\mathrm{m_{pk}}$, respectively. The output speed estimate has a ripple of approximately $30\,\mathrm{r/min_{pk}}$ due to the added noise. It is thus advisable to use the reference speed wherever possible in the cooperative control start-up[4].

A simulation model of the rotor angle estimation from the UMP force disturbance in the AMB system is provided in appendix E.8.

5.2.3 Integration of force and back-emf based estimation

Section 5.2.2, presented the estimation of the rotor angle using the same PLL structure as was used for the sensorless drive angle estimation. The difference resides in the PLL input

[4]Such as in the calculation of speed dependent decoupling terms.

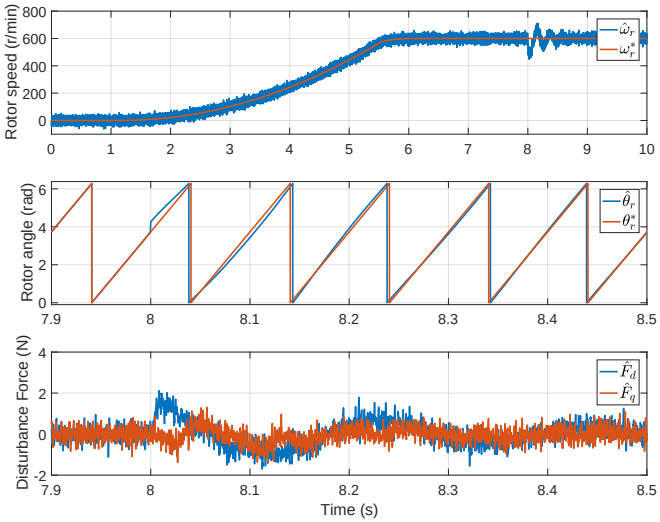

Figure 5.8: Simulation response of PLL using disturbance force input.

terms. The input of one is based on the estimated back-emf, whilst the other is based on the estimated disturbance force.

A modification of the PLL for sensorless drive angle estimation was presented in section 4.3.2.1, in order to allow the bumpless start-up method to smoothly switch from the open-loop reference angle, θ_r^*, to the back-emf estimated angle, $\hat{\theta}_r$. In this section the open-loop control input to the tracking controller is replaced by the estimated disturbance force. The PLL thus switches smoothly from one angle estimation source to another, depending on the rotor reference speed. Such a fused tracking controller is displayed in Fig. 5.9. The estimated force disturbance and back-emf both feed into the *same* tracking controller, with their inputs weighted according to the reference speed. The weighting is performed using the weights, w_e and w_F. In this thesis, the same design for the weights as for the open-loop control is used[5]. The back-emf weight, w_e, is thus equal to the observer enable weight, W_{obs}, as presented in section 4.3.2.1. The weight for the estimated force disturbance input, w_F, is thus equal to $1 - W_{obs}$.

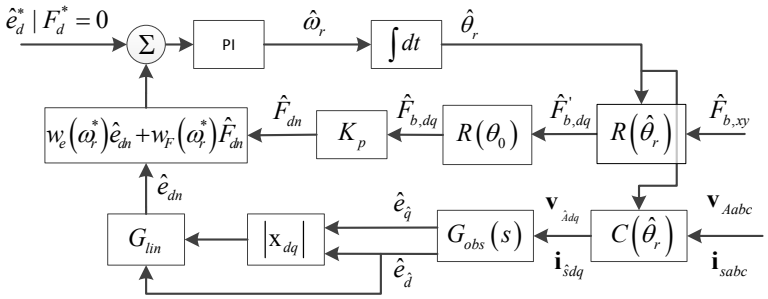

Figure 5.9: Tracking controller fusion.

[5] A different weight design could have been used considering the unique attributes of the tracking controller inputs.

The idea to use the PLL as the appropriate structure to transition from one estimated source to another was discovered independently during the course of this thesis. After implementation, it was found that other researchers, Yang and Hsu [53], have proposed the same idea to use the PLL to transition from a saliency-based estimation to a back-emf based estimation of the drive. Another difference in the application of the idea here is that two *different* systems, the AMB and the drive, are used to integrate into the PLL.

5.2.4 Cooperative start-up

5.2.4.1 Drive response

The result of the fusion between the back-emf and disturbance force into the PLL tracking is evaluated with respect to the drive in this section.

Fig. 5.10, presents the response to the initial turn-on of the PLL estimation for various initial angle misalignments. Prior to turning the PLL tracking controller on[6], the rotor is aligned to a known initial angle, θ_{init}. The initial angle estimation settles in approximately 1 s to within 10 % of the true initial angle. In the case of zero initial angle error, the estimator does not experience any additional transient behaviour due to the turn-on process of the estimator. It is thus possible to store the last known rotor angle as estimated by the force disturbance based angle estimation before system turn-off and initialize the estimated angle to the last known angle again upon system turn-on. The initial angle estimation is much quicker compared to the time required to wait for the rotor to settle during an alignment step when using an open-loop start-up.

The cooperative control start-up is presented in Fig. 5.11. The cooperative PLL estimation has been switched on prior to start-up. At $t = 0\,\mathrm{s}$, the speed reference is ramped from standstill to 1200 r/min. Initially, a significant estimated speed ripple is observed which leads to a reference q-axis current ripple.

In order to get the start-up to work as desired, the speed control-loop proportional gain, K_{p_s}, had to be gain scheduled using the observer enable weight:

$$K^*_{p\_s} = K_{p\_s}\,(0.1 + W_{obs})\ . \tag{5.8}$$

A high-frequency disturbance loop in the force disturbance compensation is present which tends to amplify the disturbance. A disturbance in the current reference produced by fluctuations in the speed controller causes force disturbances due to inexact force disturbance compensation. The force disturbance has a high-frequency loop along the proportional gain path of the tracking controller and the speed controller, as indicated by the red lines in Fig. 5.12. The gain scheduling of the speed controller proportional gain reduces the

[6]Note that before the PLL integrators are released from reset, it is critical that the AMB must be suspended, otherwise the control reference from the AMB is interpreted as a disturbance which corrupts the PLL state estimation integrators to Inf values.

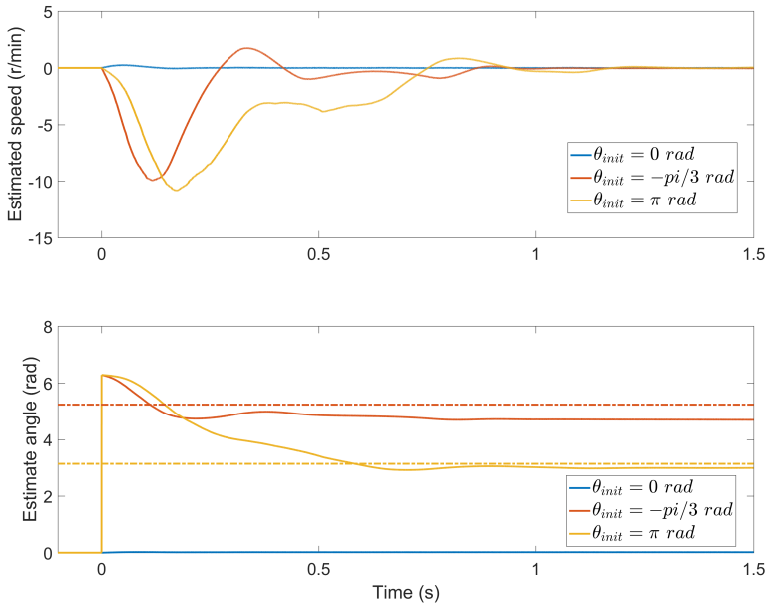

Figure 5.10: Initial angular estimation response.

amplification of the force disturbance via this loop. In the selection of which proportional gain should be reduced to break the high-frequency disturbance loop, the speed controller proportional gain was chosen instead of the tracking controller gain. This maintains the constraint that the tracking controller bandwidth has to be larger than the speed controller bandwidth.

As the rotor is spun up, using the cooperative control, the back-emf observer is gradually enabled by means of the bumpless start-up as presented in section 4.3. At 50 % of the final reference speed the back-emf and force disturbance inputs to the tracking controller are weighted equally. The same inverter current limit is used for the cooperative start-up, as for the open-loop bumpless start-up, but the cooperative start-up can make better utilization of the available current limit so that the effective torque producing current is much higher. This allowed a faster cooperative control start-up in 9 s vs the 13 s of the open-loop start-up (*excluding* the time required for rotor pre-alignment for the open-loop start-up). It can also be foreseen that the cooperative start-up will be able to better handle different torque load profiles, but this could not be validated on the flywheel test system. Also, note that the estimated back-emf during the cooperative start-up did not present the same low-frequency transient compared to the open-loop start-up presented in Fig. 4.11a, which also indicates an improved electrical domain observer convergence at lower speed because the current fed into the observer has been transformed to a rotating reference frame with a smaller error in the estimated angle.

By modifying the bumpless start-up method to replace the open-loop start-up region with the force disturbance based angle estimation, the bumpless characteristic has been

maintained, i.e. there is no high-frequency transient present during the handover of the disturbance force based angle estimation to the back-emf based angle estimation.

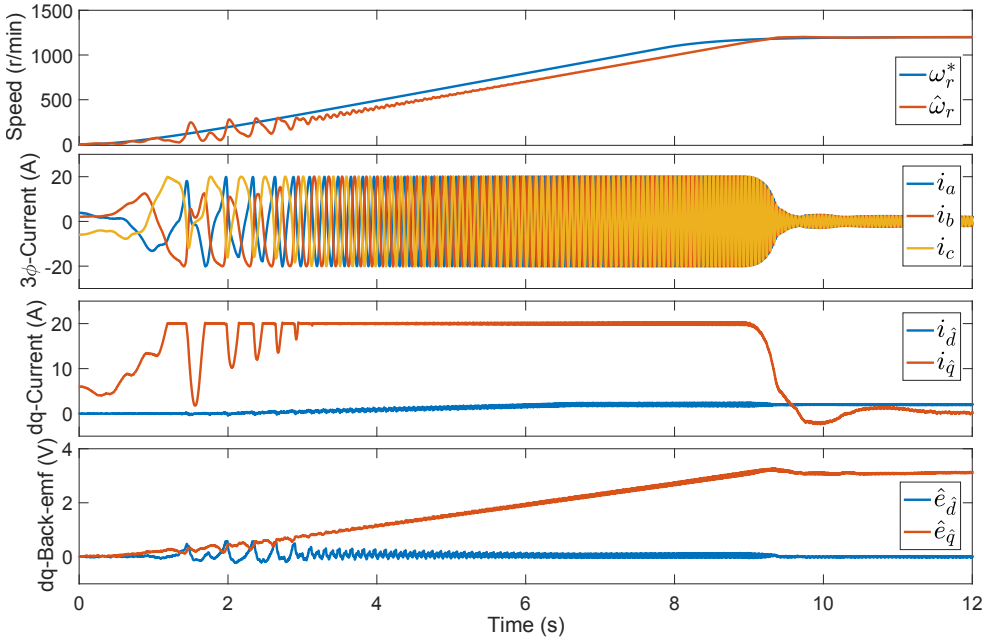

Figure 5.11: Cooperative control start-up response.

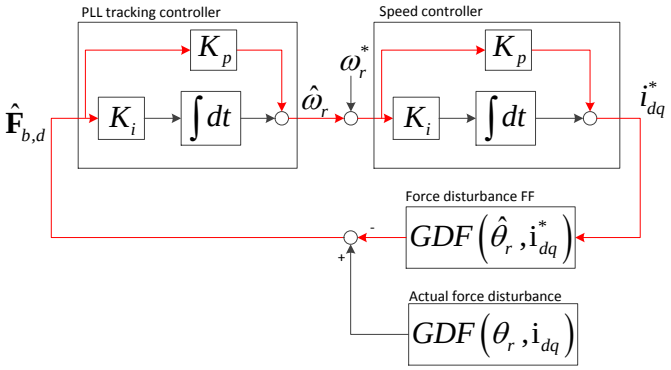

Figure 5.12: High-frequency disturbance propagation loop.

The run-down test result is presented in Fig. 5.13. Once again, a faster ramp rate was possible using cooperative control. The large current perturbation near zero speed is due to the decreased speed controller proportional gain, hence a large oscillatory speed ripple is caused by the dominating integrator gain of the speed controller. This is however unavoidable due to the necessity to decrease the speed controller proportional gain to break the high-frequency force perturbation loop mentioned earlier.

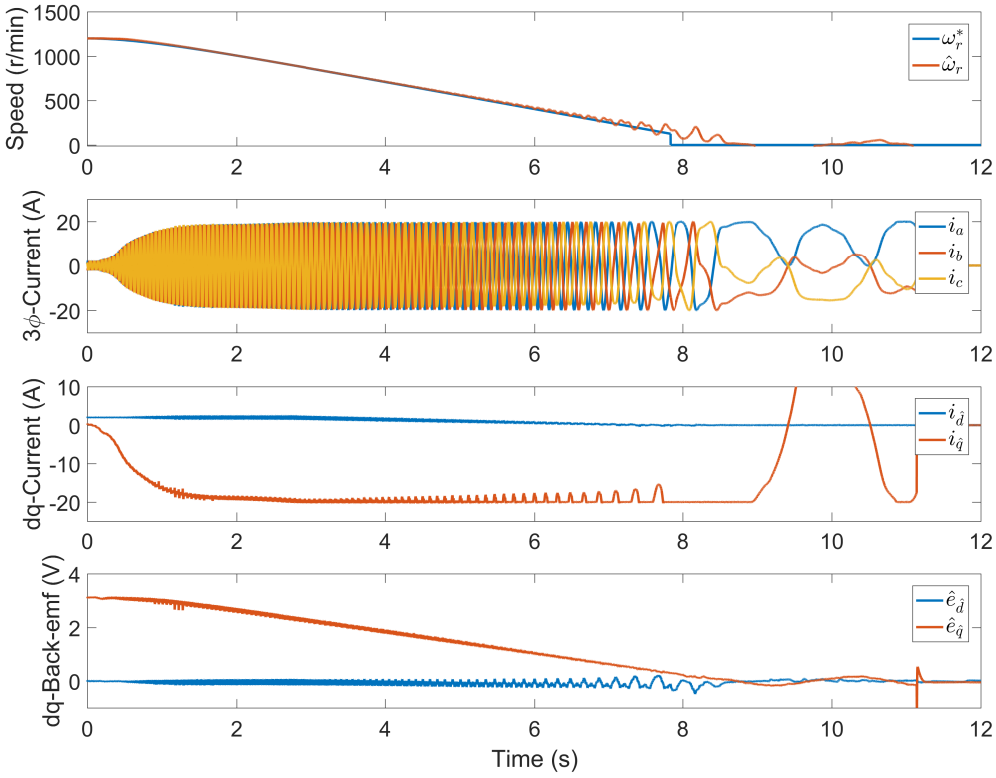

Figure 5.13: Cooperative control run-down response.

5.2.4.2 AMB response

The cooperative response with respect to the AMB performance is presented in this section. In order to compare the cooperative control to the uncooperative control case, the ramp-up rate of the drive in the cooperative control case has been reduced to match that of the uncooperative control. The drive is ramped-up from standstill to 1200 r/min.

Fig. 5.14, presents the AMB control response comparison between the cooperative and the uncooperative control case. The uncooperative control case consists of an open-loop start-up which transitions to the back-emf sensorless control using the bumpless transfer. The rotor geometric centre has been specified as the position control reference[7]. In the case of the cooperative control start-up, a much smaller position deflection can be observed, especially for the bottom AMB. This is because the angle input to the force disturbance compensation has a smaller error during start-up, hence there is less residual disturbance force present during start-up of the cooperative control. After the drive has switched to back-emf based sensorless control the two responses are basically the same.

In Fig. 5.15, the cooperative and uncooperative control is again compared, but with the

[7]The geometric reference has been specified to rotate about the magnetic centre. The mean position offset has been subtracted for clarity of the plots.

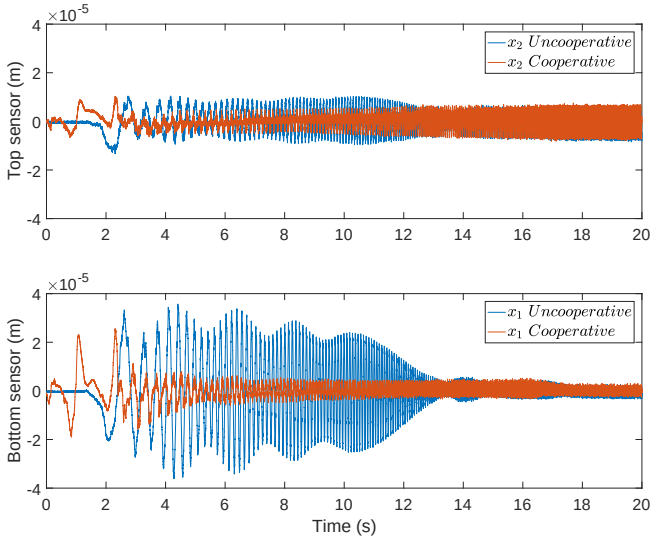

Figure 5.14: AMB position control response comparison with geometric centre reference.

position reference now being the centre of gravity. This is accomplished by subtracting the sensor runout from the measured position using the runout compensation and unbalance control using look-up tables, as presented in section 3.8.5. Again, the cooperative control response yields less disturbance and the sensor position variation remains essentially flat. The uncooperative control case excites the rigid body modes as those frequencies are passed. The low stiffness control gains are used during the test, hence the rigid body mode frequencies are relatively low.

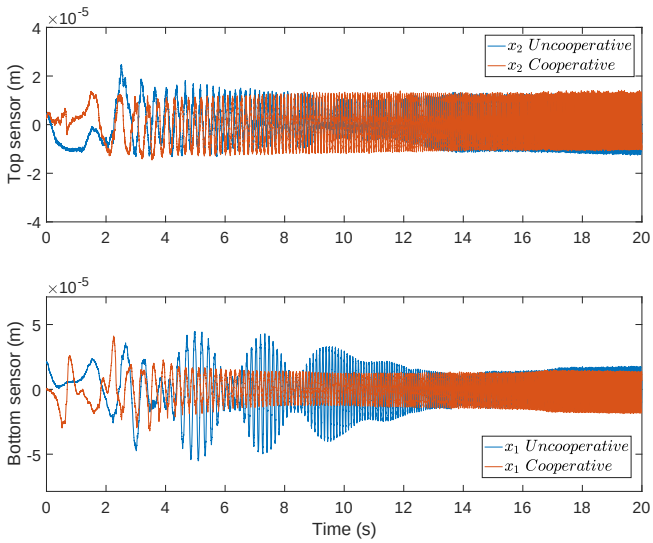

Figure 5.15: AMB position control response comparison with centre of mass reference.

5.3 Unbalance control dependency analysis

Since the flywheel system did not include an angular position sensor some indirect methods are required to evaluate the effectiveness of the electrical domain observer with time-varying parameters presented in section 4.4. In the initial presentation of the time-varying parameter observer[8] the observer was evaluated by means of current step responses.

The unbalance control of the AMB serves as another means to indirectly evaluate the electrical domain observer of the sensorless drive. The unbalance is compensated by means of look-up tables which contain the information of the sensor runout and unbalance which have a fixed relation as regard to the angular position of the rotor. Hence, any error in the angular position of the sensorless drive will reflect in the ability of the AMB unbalance control to reject the unbalance and maintain a minimum control effort.

Fig. 5.16, presents the AMB control current for one axis which results using the constant and the adaptive observer of the sensorless drive. For the experiment the rotor is spinning at 6000 r/min. At, $t = 0$ s, a current of 10 A is injected to the d-axis drive current reference. For clarity, a constant current of 0.4 A is added to the displayed current for the adaptive observer case. In the constant observer case, a larger AMB current ripple results, compared to the current ripple for the adaptive observer. The estimated angle used for the sensor runout look-up table has a larger disturbance in the case of the constant observer.

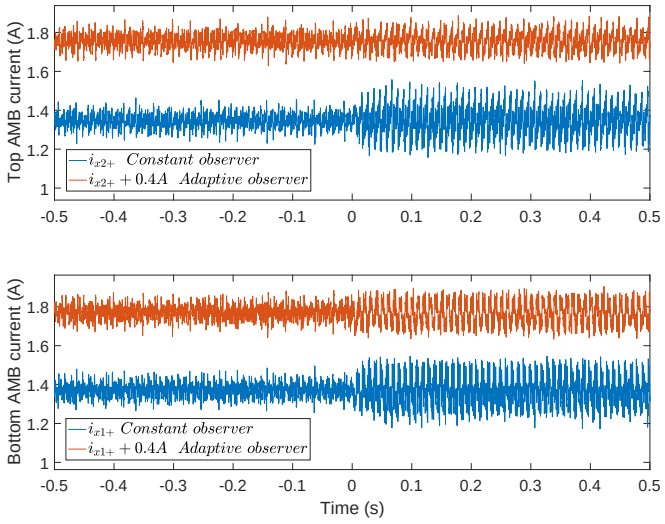

Figure 5.16: Unbalance control response comparison with different electrical domain observers.

The AMB's unbalance control response could thus be used to validate the improved performance of the angle estimation of the adaptive observer. The use of the AMB control to infer useful information on the performance or parameter tuning of the sensorless vector

[8] Also referred to as the adaptive observer.

controlled drive is here also considered under the category of cooperative control. In the future, current control ripple of an AMB dependent on the sensorless drive's estimated angle could be used as a cost function for an on-line parameter tuning optimization loop of the drive.

5.4 Angular estimation redundancy

In section 5.2, the cooperative control start-up with the AMB acting as an angular position sensor for the sensorless drive was presented. After start-up, the angular position and speed of the sensorless drive are in turn shared with the AMB. In case of a failure in the motor drive, the angular position information used in the unbalance control is no longer available. This problem was pointed out by Hutterer *et al.* [43] and proposed a solution to this problem by estimation of the angular position and speed from the unbalance control as a redundant mechanism. The aim of their solution is to yield the AMB control independent of the drive in case of a failure. The algorithmic structure which they proposed that estimates the angular position from the unbalance is separate from the original angular position estimation of the drive. Hence, some type of switchover from the drive state estimates to the AMB state estimates is required. This may result in a transient during the switchover and a bumpless transfer mechanism comes as an afterthought. The unbalance observer that Hutterer *et al.* proposed have to operate in the background even whilst the AMB control relies on the drive control.

The switchover from the sensorless drive to the AMB unbalance observer is a form of interdependence, even perhaps cooperation, but not in the fullest degree. In order to count as cooperative control, the sensorless drive and AMB unbalance estimation have to use a shared algorithmic structure. This would make it possible for the state estimation of the AMB unbalance control to be shared in return with the drive. In case a redundant drive is used, then upon failure of one drive the angular estimation via the AMB unbalance control can be used to correct for the angular and speed estimation. Upon switching over to a redundant drive the sensorless control state estimation experiences a transient, due to estimator initialization, because of the shared state information of the AMB with the sensorless drive.

5.4.1 Phase detector

A correction mechanism which feeds into the tracking controller (PLL), based on the unbalance and sensor runout, should be developed in order to be used as a redundant angular estimation source. Such a mechanism is a phase detector. The phase detector is based on the orthogonality property of two sinusoidal signals which are $\frac{\pi}{2}$ rad out of phase. Since the two signals are orthogonal, e.g. $\sin(\omega t)$ and $\cos(\omega t)$, the internal product of

the two signals:

$$P = \int \sin(\omega t)\cos(\omega t)\, dt\,, \tag{5.9}$$

is equal to zero. The x- and y-signal pairs of the runout have the property of orthogonality. The internal dot product of the measured AMB[9] y-coordinate position signal projected unto the x-coordinate of the estimated reference frame thus has to be zero if the angular position error is zero. If there is a difference in the angle of the true and estimated reference frames, a non-zero projection results. Such a projection is depicted in Fig. 5.17, where the estimated reference frame is leading the true reference frame.

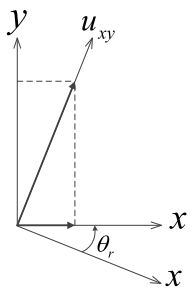

Figure 5.17: Runout depicted in misaligned true and estimated reference frames.

The projection of the sensor runout signal unto the orthogonal pair of that signal can thus be used to derive phase error between the true and estimated reference frames. The phase difference can thus be computed using:

$$\boldsymbol{PD} = \left(\boldsymbol{u}_{xy} - \boldsymbol{u}_{xy}\left(\hat{\theta}_r\right)\right) \circ \boldsymbol{u}_{xy}\left(\frac{\pi}{2} + \hat{\theta}_r\right)\,, \tag{5.10}$$

where $\circ$ denotes the dot product, $\boldsymbol{u}_{xy}$ is the measured rotor position, $\boldsymbol{u}_{xy}\left(\hat{\theta}_r\right)$ is the sensor runout LUT accessed as a function of the estimated angle. Since the x- and y-pairs are orthogonal to each other, an estimate of the phase advanced sensor runout may be computed as:

$$\boldsymbol{u}_{xy}\left(\frac{\pi}{2} + \hat{\theta}_r\right) \approx \begin{bmatrix} u_{y1}\left(\hat{\theta}_r\right) \\ -u_{x1}\left(\hat{\theta}_r\right) \\ u_{y2}\left(\hat{\theta}_r\right) \\ -u_{x2}\left(\hat{\theta}_r\right) \end{bmatrix}\,, \tag{5.11}$$

which saves on computation time since the LUT does not have to be accessed again with the phase shifted angle, $\frac{\pi}{2} + \hat{\theta}_r$. The phase difference can thus be zero in two cases, either the sensor runout cancels with that present in the measured signal, or the two signals are orthogonal to each other. The phase difference vector needs to be further reduced in dimension. Since each dimensional component provides phase information, they all may be summed. Each dimension of the $\boldsymbol{PD}$ computation presents an integration step.

[9] For either the top or bottom AMB.

Integration and summation are linear operators, hence they may be interchanged and only one integrator is required. The purpose of the integrator is to obtain the average phase difference and suppress higher intermodulation harmonics. In order to yield a faster transient estimate of the mean component, but still suppress the higher harmonics, the integrator is replaced with a low pass filter. In order to prevent the low-frequency rotor response from interacting with the mixing process, the sensor runout error signal is also high-pass filtered, prior to the mixing step. Thus, the scalar PD is calculated according to:

$$PD = LPF\left(\Sigma_1^4\left[HPF\left(\boldsymbol{u}_{xy} - \boldsymbol{u}_{xy}\left(\hat{\theta}_r\right)\right).\boldsymbol{u}_{xy}\left(\frac{\pi}{2} + \hat{\theta}_r\right)\right]\right) . \tag{5.12}$$

Thus, the runout LUT is subtracted from the measured position signal, which is projected unto the $\frac{\pi}{2}$ phase shifted runout signal, after which the dimensions are summed and integrated. The PD signal may be fed into the tracking controller, by a proportional gain, which consolidates the estimated states of the drive and the AMB. The low-pass filter cut-off frequency is chosen as 10 Hz and the high-pass filter cut-off frequency is chosen as 2 Hz.

The proposed phase detector is, in essence, an open-loop method. Therefore, it is sensitive to AMB controller gain variation and compensation of inexact external forces. Any uncompensated external force, which results in a difference in the rotor orbit from the sensor runout orbit, results in a non-zero phase detector offset. Such an offset is a function of the angular speed and needs to be compensated:

$$PD_{PLL} = K_p\left(PD + PD_o\left(\omega_r\right)\right) , \tag{5.13}$$

where PD_{PLL}, is the compensated phase detector output fed to the tracking controller, $PD_o\left(\omega_r\right)$, is the speed dependent phase detector offset and K_p is the phase detector gain. Since the signals of the AMB are in the μm range, the phase detector gain is quite high. For this system a gain of 3×10^9 has been selected via simulation. An example of an external force disturbance, accounted by the phase detector offset, would be inexact unbalanced magnetic pull feed-forward compensation.

5.4.2 Redundant angle estimation result

In case the drive fails, the estimated back-emf is switched to zero and thus no-longer drives the tracking controller in order to align the estimated reference frame with that of the rotor. Using the phase detector of the unbalance/sensor runout signals the tracking controller angle can be kept synchronized to the angle of the rotor. Fig. 5.18, presents the result of the redundant angle estimation by means of the runout phase detector.

At $t = 5\,\text{s}$, the drive is switched off which simulates a drive failure. As can be seen, the speed of the motor is able to track the rotor speed, which now decays due to windage friction loss. At $t = 57\,\text{s}$, the drive is switched back on, without the speed controller

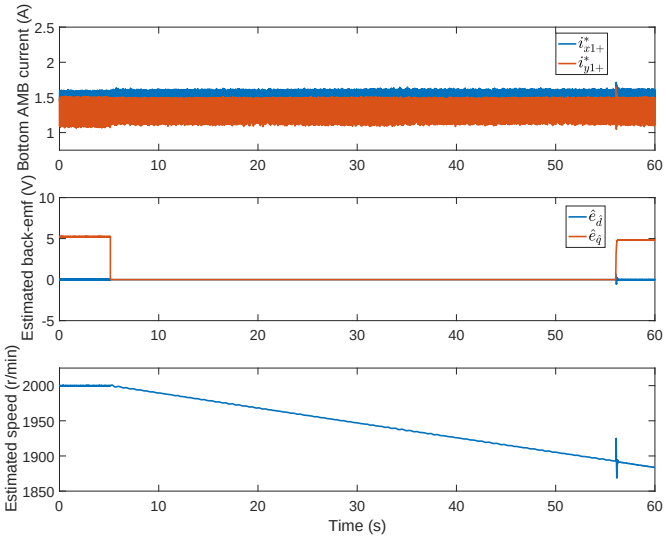

Figure 5.18: Drive response with AMB redundant angle estimation response.

enabled, otherwise a current transient would obscure the presented result. It can be seen that the drive's estimated speed is continuous to the region where it was tracked by the runout phase detector. During the time that the drive is off, the estimated angle of the tracking controller is still used by the sensor runout look-up table. Since there is no visible increase in the AMB current ripple it can be concluded that the estimated angle of the rotor is still correct.

A noticeable transient in the estimated speed is visible when switching the drive back on. This is related to the current control step response. The resulting transient in the drive estimator is however smaller compared to the case had the angle estimate not been tracked. The initialization of the drive upon coming back on-line, has to be further improved, since the transient in the estimated speed may cause instability in the AMB gyroscopic compensation. The phase detector gain design also has to be improved to verify stability at higher speeds.

5.5 Conclusion

This chapter presented the cooperative control between the AMB and the sensorless drive. The force disturbance due to the unbalanced magnetic pull was used to estimate the angle of the rotor using a PLL. The angular estimation of the force disturbance was merged with the angular estimation of the back-emf using the *same* PLL. The angular estimation using the force disturbance estimation was able to estimate the rotor position at standstill and low speed and was subsequently used to replace the open-loop start-up component in the bumpless start-up method presented in the previous chapter. The AMB and sensorless drive thus cooperated to yield faster start-up than the open-loop start-up by allowing a

higher ramp-up rate and doing away with the need for a pre-alignment step.

In order to complete the cooperative control, the redundant estimation of the angular position was integrated into the tracking controller by means of a sensor runout phase detector so that the unbalance control is still possible in case of a drive failure. It was also possible to switch the drive back on which simulated a redundant drive replacing a failed drive.

The AMB control response using the cooperative control was analysed and showed an improvement over the open-loop control, due to an increase in accuracy of the angular dependent force disturbance compensation.

In the absence of a true angular position sensor, the angular dependent sensor runout / unbalance control could be used to gain insight into the performance of the sensorless drive's angular estimation when comparing a parameter varying observer to a constant parameter observer.

Chapter 6

Conclusions

6.1 Summary

The work presented in this thesis aimed to show that an active magnetic bearing and its drive can perform cooperatively to satisfy a control objective. Traditionally, these two systems operate as two separate modular units with the exception of the bearingless drives when the two units are combined into a single electromagnetic structure. The cooperative control proposed in this work is aimed towards the case that the drive and AMB are traditional separate modular units, in order to show that even for that case the two systems may benefit by sharing the control state information.

In chapter 3, the AMB control is designed which includes identification of the force disturbance model. The force disturbance's angular dependence, due to the permanent magnet, serves as the basis for angular estimation of the rotor at standstill and low speeds which is presented in chapter 5. The angular estimation by the AMB allowed for the drive to start-up in sensored vector control mode. Designing the AMB control in a force framework with feedback linearisation allowed for accurate actuation, without which the rotor angle estimation based on the force disturbance would not have been possible. The force-based controller required accurate AMB parameters and the estimation thereof is presented in appendix C. Exploitation of the relatively small force disturbance due to the PMSM required that the eddy current sensors have good S/N. This was achieved by synchronous sampling of the ADCs which required synchronising the PWMs of both the drive's inverter and the AMB power amplifiers. In addition to synchronisation, the power amplifiers were designed with a modified topology which allowed for soft switching, which aided in the reduction of EMI and thus cleaner eddy current position sensor signals. The design of the power amplifiers is presented in appendix D.

The sensorless vector control presented in chapter 4 is based on the back-emf based sensorless vector control presented by Kshirsagar *et al.* [4]. The drive used in this study has a three-phase line filter which had to be taken into account for the sensorless control. Also,

it was found in the parameter estimation presented in appendix B that the PMSM combined with the filter had non-linear parameters. In stand-alone operation, the start-up of the sensorless vector control algorithm was modified in order to allow a smooth, bumpless start-up procedure, which also reduced the computational complexity. For the open-loop start-up procedure to work well, compensation of the inverter non-linearities was essential. A novel improvement in the characterisation of the inverter non-linearity is presented in appendix A.

The bumpless start-up method revealed that the phase-locked loop is an appropriate structure for the two modular systems to integrate with each other. The overlap in functionality of the phase-locked loop for angle estimation by force and back-emf allowed for a *single* phase-locked loop to be employed which allows for a reduction in computational overhead which facilitates towards the goal of processing the drive and AMB control on a single processor. The redundant angle estimation, by means of sensor runout phase detection, was also integrated into the same PLL.

6.2 Unique contributions

The unique contributions in this work are as follows:

- Development of an empirical model and parameter identification procedure for the characterization of the permanent magnet's force disturbance.

- An algorithmic advancement in the open-loop start-up of the sensorless vector control which allows for a bumpless transition from open-loop to closed-loop operation. The bumpless start-up procedure also reduces the computational complexity of the sensorless vector control.

- Utilization of the permanent magnet's force disturbance to estimate the rotor angular position at standstill and to allow for sensored vector control start-up. The bumpless start-up method is modified to allow for the vector control to start-up with the AMB functioning as the angular position sensor and smoothly transitioning to the drive's estimated angular position.

- The development of novel inverter non-linearity identification procedure and post-processing algorithm which is able to recover the zero voltage component algebraically and thus decouple the non-linearity so that look-up tables may be generated to compensate the non-linearity as it originates in each individual phase as a function of the phase current.

6.3 Recommendations for future work

Some of the results in the thesis had some loose ends, which may be improved upon by future work. For example, it has been shown in Fig. 5.16 that the sensor runout / unbalance control using look-up tables is sensitive to variation in the estimated angle. The focus of the result presented in Fig. 5.16 was on the improvement of the parameter varying observer over the constant parameter observer. This sensitivity indicates that the AMB control current ripple may be used to construct a cost function which feeds into the tracking controller, by means of an on-line optimization algorithm, in order to correct for sensorless drive angle estimation error due to parameter variation or non-linear response. The angle offset correction may be performed by overriding the reference d-axis back-emf voltage, e_d^*, with the AMB control current ripple cost function.

Other future work includes the following:

- The reinitialization of the sensorless drive may be improved, such that the drive control does not experience a significant disturbance when the drive turns back on. Such a reinitialization would be beneficial in a scenario which could occur where redundant drives interface with the same flywheel. The fusion of the tracking controller presented in this thesis is already an improvement since the estimated angle is already converged when the drive turns back on, but it may be improved further.

- The phase detector gain design for the redundant angle estimation has to be improved and tested at higher speeds.

- The parameters, or "knobs", of the proposed bumpless start-up method require a more rigorous analytical foundation. It has been shown that the number of start-up parameters using the bumpless start-up method is potentially less than other start-up methods, due to less distinct start-up phases.

- The force disturbance based angle estimation has to be extended to horizontally levitated systems. It is foreseen that the disturbance due to gravity may require extra compensation terms.

- The cooperative control may be extended to other types of electrical machines (besides the PMSM), such as an induction machine. Although an induction machine does not have a d-axis which is fixed to the rotor the induced drive currents will still produce a disturbance force which may be beneficially compensated.

- The signal-to-noise of the estimated angle from the disturbance force may be improved by performing measures which increase the disturbance force when the angle estimate has an error. In this work, the rotor was spun up relatively in the centre of the air-gap of the AMB stator. The eccentricity in the electrical machine air-gap may

be increased by starting the rotor further away from the AMB air-gap centre. This could potentially increase the disturbance force and hence the angular estimation accuracy.

- The force disturbance based angular estimation made use of eddy current position sensors. Further research should be performed to test if the force disturbance observer is accurate enough if the rotor position sensors are replaced by a self-sensing scheme.

6.4 Closing

The cooperative control presented in this thesis showed that the AMB and drive control can have a mutually symbiotic relationship. The main benefit for the sensorless drive is that it can start in sensored vector control due to the angle estimation by the AMB. This furthered the aim of self-sensing to reduce the sensor count in an AMB-drive system. Various mechanisms for estimation of the angle by the AMB were presented based on non-idealities within the AMB system. The AMB control, in turn, benefited from the sensorless speed estimation of the drive which was used as an input to the gyroscopic compensation of the AMB which permits the use of a linearised AMB control law. The AMB control also benefited by using the estimated angle of the drive in the unbalance control. The symbiotic interchange of state information between the two systems to yield a synergistic system behaviour was by no means exhaustive. A unifying foundation to combine previously disparate non-idealities with the aim of exploiting those non-idealities for improved functionality was presented. Future discovery of non-idealities within the AMB-drive system may be added under the umbrella term: “cooperative control”.

Bibliography

[1] G. Schweitzer, E. H. Maslen, H. Bleuler, M. Cole, P. Keogh, R. Larsonneur, R. Nordman, Y. Okada, and A. Traxler, *Magnetic bearings: theory, design, and application to rotating machinery.* 2009.

[2] V. Tamisier, F. Carrère, and S. Font, "Synchronous unbalance cancellation across critical speed using a closed-loop method," in *8th International Symposium on Magnetic Bearings*, pp. 399–404, 2002.

[3] J. Kejian, Z. Changsheng, and T. Ming, "A uniform control method for imbalance compensation and automation balancing in active magnetic bearing-rotor systems," *Journal of Dynamic Systems, Measurement, and Control*, vol. 134, no. 2, p. 021006, 2012.

[4] P. Kshirsagar, R. P. Burgos, J. Jang, A. Lidozzi, F. Wang, D. Boroyevich, and S. K. Sul, "Implementation and sensorless vector-control design and tuning strategy for SMPM machines in fan-type applications," *IEEE Transactions on Industry Applications*, vol. 48, no. 6, pp. 2402–2413, 2012.

[5] J. De Miras and A. Charara, "Unbalance cancellation with rotating reference control for a horizontal shaft," *Proceedings of the Sixth International Symposium on Magnetic Bearings*, 1998.

[6] J. De Miras and A. Charara, "A vector oriented control for a magnetically levitated shaft," *IEEE Transactions on Magnetics*, vol. 34, no. 4, pp. 2039–2041, 1998.

[7] J. De Miras and A. Charara, "Vector desired trajectories for high rotor speed magnetic bearing stabilization," in *14th IFAC World Congress*, 1999.

[8] R. Herzog, P. Bühler, C. Gähler, and R. Larsonneur, "Unbalance compensation using generalized notch filters in the multivariable feedback of magnetic bearings," *IEEE Transactions on Control Systems Technology*, vol. 4, no. 5, pp. 580–586, 1996.

[9] T. Dimond, P. Allaire, S. Mushi, Z. Lin, and S. Y. Yoon, "Modal tilt/translate control and stability of a rigid rotor with gyroscopics on active magnetic bearings," *International Journal of Rotating Machinery*, vol. 2012, 2012.

[10] S. Zheng and R. Feng, "A Notch Filter for Magnetically Suspended Rotors Based on Rotating Coordinate Transformation," in *14th International Symposium on Magnetic Bearings*, no. 37, pp. 83–86, 2014.

[11] K. Lum, "Adaptive autocentering control for an active magnetic bearing supporting a rotor with unknown mass imbalance," *IEEE Transactions on Control Systems Technology*, vol. 4, no. 5, 1996.

[12] V. Tamisier, "Optimal control of the gyroscopic effects," *2006 IEEE International Symposium on Industrial Electronics*, pp. 2556–2561, jul 2006.

[13] G. L. Kruger, "Implementation and evaluation of V/f and vector control in high-speed PMSM drives," Master's thesis, North-West University, Potchefstroom, 2011, http://hdl.handle.net/10394/7609.

[14] T. D. Batzel, *Electric propulsion using the permanent magnet synchronous motor without rotor position transducers*. PhD thesis, The Pennsylvania State University, 2000.

[15] W.-L. Lee, W. Schumacher, and W.-R. Canders, "Unbalance compensation on AMB system without a rotational sensor," in *8th International Symposium on Magnetic Bearings*, vol. 46, pp. 211–216, 2002.

[16] G. Kruger, G. Van Schoor, and P. Van Vuuren, "Control of magnetically suspended rotor combined with motor drive system," in *Proceedings of the 19th IFAC World Congress*, 2014, https://doi.org/10.3182/20140824-6-ZA-1003.02761.

[17] G. L. Kruger, G. van Schoor, and P. A. Vuuren, "Pseudo-magnetic centre identification of an active magnetic bearing for sensorless drive control start-up," in *IFAC-PapersOnLine*, vol. 50, pp. 4837–4842, 2017, https://doi.org/10.1016/j.ifacol.2017.08.971.

[18] J. Salomäki, *Sensorless Control of AC Drives equipped with an Inverter Output Filter*. PhD thesis, Helsinki University of Technology, 2007.

[19] F. Worlitz, "Active magnetic bearings - A product of mechatronics," in *10th International Workshop on Electronics, Control, Measurement and Signals*, June 2011.

[20] M. Swann, N. Davies, R. Gao, Z. Guo, R. Jayawant, R. Leung, and R. Shultz, "The design of high reliability magnetic bearing systems for helium cooled reactor machinery," in *7th International Topical Meeting on High Temperature Reactor Technology: The modular HTR is advancing towards reality*, 2014.

[21] C. W. Lee, "Compensation of tool axis misalignment in active magnetic bearing spindle system," *KSME International Journal*, vol. 11, no. 2, pp. 155–163, 1997.

[22] R. Larsonneur, "Modeling and analysis of dynamic mechanical systems with a special focus on rotordynamics and active magnetic bearing (AMB) system," tech. rep., Mecos, Switzerland, 2006.

[23] M. Aenis, E. Knopf, and R. Nordmann, "Active magnetic bearings for the identification and fault diagnosis in turbomachinery," *Mechatronics*, vol. 12, pp. 1011–1021, 2002.

[24] J. Sawicki, M. Friswell, and G. Baaklini, "Rotor crack detection using induced combination resonances," in *4th European Workshop on Structural Health Monitoring*, pp. 142–149, 2008.

[25] A. Lees, J. Sinha, and M. Friswell, "Model-based identification of rotating machines," *Mechanical Systems and Signal Processing*, vol. 23, pp. 1884–1893, aug 2009.

[26] R. Gouws and G. van Schoor, "Multiple frequency fault detection, correction and identification of vibration forces on the rotor of a rotational active magnetic bearing system," *SAIEE Africa Research Journal*, vol. 99, no. December, pp. 114–123, 2009.

[27] R. S. Blom, *Model-based process monitoring and control of micro-milling using active magnetic bearings.* PhD thesis, TU Delft, 2011.

[28] A. Chiba, T. Fukao, O. Ichikawa, M. Oshima, M. Takemoto, and D. G. Dorrell, *Magnetic bearings and bearingless drives.* Elsevier, 2005.

[29] H. Bleuler, C. Gahler, R. Herzog, R. Larsonneur, T. Mizuno, and R. Siegwart, "Application of digital signal processors for industrial magnetic bearings," *IEEE Transactions on Control Systems Technology*, vol. 2, no. 4, pp. 280–289, 1994.

[30] B. Polajžer, ed., *Magnetic bearings, theory and applications.* Sciyo, 2010.

[31] M. Mekhiche, S. Nichols, J. Oleksy, J. Young, J. Kiley, and D. Havenhill, "50 KRPM, 1,100 degF, Magnetic Bearings for Jet Turbine Engines," in *7th International Symposium on Magnetic Bearings*, 2000.

[32] BSI, "ISO 14839 Mechanical vibration - Vibration of rotating machinery equipped with active magnetic bearings - Part 1: Vocabulary," 2002.

[33] W. Khoo, S. Garvey, and K. Kalita, "The specific load capacity of radial-flux radial magnetic bearings," *IEEE Transactions on Magnetics*, vol. 43, pp. 3293–3300, jul 2007.

[34] P. Allaire, J. Imlach, and J. McDonald, "Design, construction and test of magnetic bearings in an industrial canned motor pump," in *6th International pump users symposium*, pp. 65–73, 1989.

[35] H. Bleuler, *Decentralized control of magnetic rotor bearing systems.* PhD thesis, Swiss Federal Institute of Technology, 1984.

[36] P. Mouille and J. Lottin, "Digital control of magnetic bearings: inversion of actuator model," in *3rd International Symposium on Magnetic Bearings*, 1992.

[37] R. Jastrzebski, R. Pöllänen, and O. Pyrhönen, "Linearization of force characteristics of active magnetic bearings for the FPGA-based LQ-controller," in *IEEE International Conference on Industrial Technology*, pp. 2420–2426, 2006.

[38] E. Krämer, *Dynamics of rotors and foundations.* Sprin, 1993.

[39] R. Beatty, "Notch filter control of magnetic bearings to improve rotor synchronous response," Master's thesis, M.I.T., 1988.

[40] H. Habermann and M. Brunet, "The active magnetic bearing enables optimum damping of flexible rotor," in *ASME 1984 International Gas Turbine Conference and Exhibit*, pp. 1–9, 1984.

[41] B. Shafai, P. Larocca, and E. Cusson, "Adaptive Forced Balancing for Magnetic Bearing Systems This paper presents an autobalancing algorithm with," in *3rd International Symposium on Magnetic Bearings*, pp. 601–611, 1994.

[42] E. Vahedforough, B. Shafai, and S. Beale, "Estimation and rejection of unknown sinusoidal disturbances using a generalized adaptive forced balancing method," in *Proceedings of the American Control Conference*, pp. 3529–3534, 2007.

[43] M. Hutterer, G. Kalteis, and M. Schrödl, "Redundant unbalance compensation of an active magnetic bearing system," *Mechanical Systems and Signal Processing*, vol. 94, pp. 267–278, 2017.

[44] M. Hutterer, *Regelung von magnetgelagerten Rotoren für den Einsatz in Turbomolekularpumpen Danksagung.* PhD thesis, TU Wien.

[45] A. M. Mohamed and F. P. Emad, "Nonlinear oscillations in magnetic bearing systems," *IEEE Transactions on Automatic Control*, vol. 38, no. 8, pp. 1242–1245, 1989.

[46] M. Ahrens and L. Kucera, "Cross feedback control of a magnetic bearing system: Controller design considering gyroscopic effects," in *3rd International Symposium on Magnetic Suspension Technology*, pp. 177–191, 1995.

[47] M. Hutterer, M. Hofer, T. Nenning, and M. Schrödl, "LQG control of an active magnetic bearing with a special method to consider the gyroscopic effect," in *14th International Symposium on Magnetic Bearings*, pp. 54–59, 2014.

[48] M. Hutterer, M. Hofer, and M. Schrödl, "Decoupled control of an active magnetic bearing system for a high gyroscopic rotor," *2015 IEEE International Conference on Mechatronics (ICM)*, no. 1, pp. 210–215, 2015.

[49] M. Hutterer, M. Hofer, and M. Schrödl, "Selfsensing unbalance rejection and reduction of the gyroscopic effect for an active magnetic bearing system," *2015 10th Asian Control Conference (ASCC)*, 2015.

[50] G. Kruger, A. Grobler, and S. Holm, "Improved non-ideality compensation for the V/f controlled permanent magnet synchronous motor," in *Proceedings of the IEEE International Conference on Industrial Technology*, 2013, https://doi.org/10.1109/ICIT.2013.6505694.

[51] F. Poulain, L. Praly, and R. Ortega, "An observer for permanent magnet synchronous motors with currents and voltages as only measurements," in *Decision and Control, 2008. CDC 2008. 47th IEEE Conference on*, pp. 5390–5395, IEEE, 2008.

[52] G. Xie, K. Lu, S. K. Dwivedi, and J. R. Rosholm, "Improved INFORM method by minimizing the inverter nonlinear voltage error effects," *Proceedings - 2015 IEEE Workshop on Electrical Machines Design, Control and Diagnosis, WEMDCD 2015*, pp. 188–194, 2015.

[53] S. C. Yang and Y. L. Hsu, "Full speed region sensorless drive of permanent-magnet machine combining saliency-based and back-emf-based drive," *IEEE Transactions on Industrial Electronics*, vol. 64, no. 2, pp. 1092–1101, 2017.

[54] X. Wu, H. Wang, S. Huang, K. Huang, and L. Wang, "Sensorless speed control with initial rotor position estimation for surface mounted permanent magnet synchronous motor drive in electric vehicles," *Energies*, vol. 8, no. 10, pp. 11030–11046, 2015.

[55] M. L. Corradini and A. Cristofaro, "A sensorless speed-tacking controller for permanent magnet synchronous motors with uncertain parameters," in *Proceedings of the 19th IFAC World Congress*, vol. 19, pp. 7749–7754, IFAC, 2014.

[56] M. Jansson, L. Harnefors, O. Wallmark, and M. Leksell, "Synchronization at startup and stable rotation reversal of sensorless nonsalient PMSM drives," *IEEE Transactions on Industrial Electronics*, vol. 53, no. 2, pp. 379–387, 2006.

[57] M. Fatu, R. Teodorescu, I. Boldea, G.-D. Andreescu, and F. Blaabjerg, "I-F starting method with smooth transition to emf based motion-sensorless vector control of PM synchronous motor / generator," *2008 IEEE Power Electronics Specialists Conference*, pp. 1481–1487, jun 2008.

[58] O. M. Arafa, G. A. A. Aziz, M. I. A. El-sebah, and A. Aly, "Observer-based sensorless speed control of PMSM : A focus on drive's startup," *Journal of Electrical Systems and Information Technology*, vol. 3, no. 2, pp. 181–209, 2016.

[59] V. Šmídl, R. Nedvěd, T. Košan, and Z. Peroutka, "FPGA implementation of Rao-Blackwellized particle filter and its application to sensorless drive control," in *Proceedings of the 19th IFAC World Congress*, vol. 19, pp. 8669–8674, IFAC, 2014.

[60] G. Van Schoor, A. C. Niemann, and C. P. Du Rand, "Evaluation of demodulation algorithms for robust self-sensing active magnetic bearings," *Sensors and Actuators, A: Physical*, vol. 189, pp. 441–450, 2013.

[61] F. Blaabjerg and J. K. Pedersen, "An ideal PWM-VSI inverter using only one current sensor in the DC-link," in *Fifth International Conference on Power Electronics and Variable-Speed Drives*, pp. 458–464, 1994.

[62] Y. S. Lai, Y. K. Lin, and C. W. Chen, "New hybrid pulsewidth modulation technique to reduce current distortion and extend current reconstruction range for a three-phase inverter using only DC-link sensor," *IEEE Transactions on Power Electronics*, vol. 28, no. 3, pp. 1331–1337, 2013.

[63] F. Blaabjerg, J. K. Pedersen, and P. Thøgersen, "Improved modulation techniques for PWM-VSI drives," *IEEE Transactions on Industrial Electronics*, vol. 44, pp. 87–95, 1997.

[64] D. C. Meeker, *Optimal solutions to the inverse problem in quadratic magnetic actuators*. PhD thesis, University of Virginia, 1996.

[65] A.-H. G. Abulrub, M. N. Sahinkaya, P. S. Keogh, and C. R. Burrows, "Experiments on ROLAC to Recover Rotor Position Following Contact," in *10th International Symposium on Magnetic Bearings*, 2006.

[66] B. Corne, J. Knockaert, and J. Desmet, "Misalignment and unbalance fault severity estimation using stator current measurements," in *IEEE 11th International Symposium on Diagnostics for Electrical Machines, Power Electronics and Drives (SDEMPED)*, pp. 247–253, 2017.

[67] B. Ebrahimi and J. Faiz, "Diagnosis and performance analysis of three-phase permanent magnet synchronous motors with static, dynamic and mixed eccentricity," *IET Electric Power Applications*, vol. 4, no. 1, pp. 53–66, 2010.

[68] B. Ebrahimi, J. Faiz, and B. Araabi, "Pattern identification for eccentricity fault diagnosis in permanent magnet synchronous motors using stator current monitoring," *IET Electric Power Applications*, vol. 4, no. 6, pp. 418–430, 2010.

[69] B. M. Ebrahimi and J. Faiz, "Magnetic field and vibration monitoring in permanent magnet synchronous motors under eccentricity fault," *IEEE Transactions on Magnetics*, vol. 6, no. 1, pp. 35–45, 2012.

[70] B. Han, S. Zheng, X. Liu, B. Han, S. Zheng, and X. Liu, "Unbalanced magnetic pull effect on stiffness models of active magnetic bearing due to rotor eccentricity in brushless DC motor using finite element method," *Mathematical Problems in Engineering*, vol. 2013, pp. 1–10, 2013.

[71] A. Manninen, V. Mukherjee, J. Pippuri, and K. Tammi, "A self-bearing 8/6 switched reluctance motor presentation," in *15th International Symposium on Magnetic Bearings*, pp. 387–394, 2016.

[72] V. Mukherjee, A. Manninen, J. Pippuri, and A. Belahcen, "Analysis of electromagnetic force ripple on the rotor of a bearingless synchronous reluctance motor," in *15th International Symposium on Magnetic Bearings*, pp. 589–593, 2016.

[73] C. Zhao and Z. Huangqiu, "Design and Analysis of Flux-Switching Permanent Magnet Motor," *IEEE Transactions on Industrial Electronics*, vol. 64, no. 8, pp. 6127–6136, 2014.

[74] W.-J. Lee, S. S. Oh, and D. Cheong, "Rotor unbalance compensation without angular position sensor for active magnetic bearing," in *8th International conference on Power Electronics*, pp. 2446–2449, 2011.

[75] B. Shafai, S. Beale, P. Larocca, and E. Cusson, "Magnetic bearing control systems and adaptive forced balancing," *IEEE Control Systems*, vol. 14, pp. 4–13, apr 1994.

[76] K. Raggl, B. Warberger, T. Nussbaumer, S. Burger, and J. W. Kolar, "Robust angle-sensorless control of a PMSM bearingless pump," vol. 56, no. 6, pp. 2076–2085, 2009.

[77] S. Myburgh, "The development of a fully suspended AMB system for a high-speed flywheel application," Master's thesis, The School of Electrical, Electronic and Computer Engineering, North-West University, Potchefstroom, 2007, http://hdl.handle.net/10394/2314.

[78] J. J. Janse van Rensburg, "Development of a flywheel energy storage system - uninterrupted power supply (FLY-UPS)," Master's thesis, North-West University, Potchefstroom, 2007, http://hdl.handle.net/10394/2322.

[79] A. de Klerk, "Drive implementation of a permanent magnet synchronous motor," Master's thesis, The School of Electrical, Electronic and Computer Engineering, North-West University, Potchefstroom, 2007, http://hdl.handle.net/10394/2634.

[80] R. C. Dorf and R. H. Bishop, *Modern control systems*. Pearson Prentice Hall, 12 ed., 2011.

[81] W. Zhu, S. Pekarek, B. Fahimi, and B. Deken, "Investigation of force generation in a permanent magnet synchronous machine," *IEEE Transaction on Energy Conversion*, vol. 22, no. 3, pp. 557–565, 2007.

[82] C. Bi, N. L. H. Aung, H. N. Phyu, Q. Jiang, and S. Lin, "Unbalanced magnetic pull induced by drive current in PM-BLDC motor operation," in *Proceeding of International Conference on Electrical Machines and Systems, ICEMS 2007*, no. 1, pp. 780–785, 2007.

[83] M. Ooshima, T. Kurokawa, M. Sakagami, A. Chiba, M. Rahman, and T. Fukao, "An identification method of suspension force and magnetic unbalance pull force parameters in buried-type IPM bearingless motors," *IEEE Power Engineering Society General Meeting, 2004.*, pp. 1–4, 2004.

[84] J. T. Marshall, "A multi-point measurement technique for the enhancement of force measurement with active magnetic bearings," master's thesis, Virginia Polytechnic Institute and State University, 2001.

[85] R. J. Prins, *System identification and calibration techniques for force measurement in active magnetic bearings system identification and calibration techniques for force measurement in active magnetic bearings.* Docter's thesis, Virginia Polytechnic Institute and State University, 2005.

[86] R. J. Prins, M. E. F. Kasarda, and S. C. B. Prins, "A System Identification Technique Using Bias Current Perturbation for Determining the Effective Rotor Origin of Active Magnetic Bearings," *Journal of vibration and acoustics*, pp. 317–322, 2007.

[87] D. Spangler, R. Prins, and M. Kasarda, "A System Identification Technique Using Bias Current Perturbation for the Determination of the Magnetic Axes of an Active Magnetic Bearing," *Actuators*, vol. 6, no. 4, p. 13, 2017.

[88] M. Caple, E. Maslen, J. Nagel, and J. Wild, "Control of an AMB to Zero Static Force," in *15h International Symposium on Magnetic Bearings*, no. 1, pp. 558–564, 2016.

[89] M. Kimman, H. Langen, R. M. Schmidt, A. Borislavljevic, and H. Polinder, "Design and Realization of a Miniature Milling Spindle with Active Magnetic Bearings," in *11th International Symposium on Magnetic Bearings*, 2008.

[90] C. Kim and C. Lee, "In-situ runout identification in active magnetic bearing system by extended influence coefficient method," in *5th International Symposium on Magnetic Bearings*, 1996.

[91] C. S. Kim and C. W. Lee, "In situ runout identification in active magnetic bearing system by extended influence coefficient method," *IEEE/ASME Transactions on Mechatronics*, vol. 2, no. 1, pp. 51–57, 1997.

[92] T.-J. Park, Y. Kanemitsu, S. Kijimoto, K. Matsuda, and Y. Koba, "Identification Of Unbalance And High Order Sensor Runout On Rigid Rotor Supported By Magnetic Bearings," in *8th International Symposium on Magnetic Bearings*, 2002.

[93] Y. Kanemitsu, S. Kijimoto, K. Matsuda, and T. J. Park, "Identification of mass unbalance and sensor runout on a rotor equipped with magnetic bearings," in *7th International Symposium on Magnetic Bearings*, 2000.

[94] J. Setiawan, R. Mukherjee, and E. Maslen, "Variable Magnetic Stiffness Approach for Simultaneous Sensor Runout and Mass Unbalance Compensation in Active Magnetic Bearings," in *7th International Symposium on Magnetic Bearings*, 2000.

[95] E. Schmidt, T. Platter, and H. Springer, "Force and Stiffness Calculations in Magnetic Bearings - Comparison between Finite Element Method and Network Theory," in *5th International Symposium on Magnetic Bearings*, 1996.

[96] C. Peng, X. Zhou, T. Wei, and Y. Ren, "High precision synchronous vibration suppression for a msfw subject to phase lag influence," *Mechanical Systems and Signal Processing*, vol. 120, pp. 408–421, 2019.

[97] P. C. Krause, O. Wasynczuk, and S. D. Sudhoff, *Analysis of electric machinery and drive systems*. Wiley-IEEE Press, 2 ed., 2002.

[98] J. Chiasson, *Modeling and high-performance control of electric machines*. Wiley-IEEE Press, 2005.

[99] P. D. C. Perera, F. Blaabjerg, J. K. Pedersen, and P. Thogersen, "A sensorless, stable V/f control method for permanent-magnet synchronous motor drives," *IEEE Transactions on Industry Applications*, vol. 39, no. 3, pp. 783–791, 2003.

[100] W. Santiago, "Inverter Output Filter Effect on PWM Motor Drives of a Flywheel Energy Storage System," in *2nd International Energy Conversion Engineering Conference*, no. September, p. 5628, 2004.

[101] T. D. Batzel and K. Y. Lee, "Electric Propulsion With the Sensorless Permanent Magnet Synchronous Motor: Model and Approach," *IEEE Transaction on Energy Conversion*, vol. 20, no. 3, pp. 818–825, 2005.

[102] R. B. Sepe and J. H. Lang, "Implementation of discrete-time field-oriented current control," *IEEE Transactions on Industry Applications*, vol. 30, no. 3, pp. 723–728, 1994.

[103] M. C. Turner and D. J. Walker, "Linear quadratic bumpless transfer," *Automatica*, vol. 36, no. 8, pp. 1089–1101, 2000.

[104] Z. Wang, K. Lu, and F. Blaabjerg, "A simple startup strategy based on current regulation for back-emf-based sensorless control of PMSM," *IEEE Transactions on Power Electronics*, vol. 27, no. 8, pp. 3817–3825, 2012.

[105] H. Taghirad, N. Abedi, and E. Noohi, "A new sensorless vector control method for permanent magnet synchronous motor without velocity estimator," in *7th International Workshop on Advanced Motion Control*, pp. 242–246, 2002.

[106] J.-I. Itoh, N. Nomura, and H. Ohsawa, "A Comparison between V/f control and position-sensorless vector control for the permanent magnet synchronous motor," in *Proceedings of the Power Conversion Conference (PCC Osaka 2002)*, vol. 3, pp. 1310–1315, 2002.

[107] A. Stirban, I. Boldea, G.-D. Andreescu, D. Iles, and F. Blaabjerg, "Motion sensorless control of bldc pm motor with offline fem info assisted state observer," in *2010 12th International Conference on Optimization of Electrical and Electronic Equipment (OPTIM)*, pp. 321–328, IEEE, 2010.

[108] A. Gaeta, P. Zanchetta, F. Tinazzi, and M. Zigliotto, "Advanced self-commissioning and feed-forward compensation of inverter non-linearities," *Proceedings of the IEEE International Conference on Industrial Technology*, vol. 2015-June, no. June, pp. 610–616, 2015.

[109] G. Pellegrino, P. Guglielmi, E. Armando, and R. I. Bojoi, "Self-commissioning algorithm for inverter nonlinearity compensation in sensorless induction motor drives," *IEEE Transactions on Industry Applications*, vol. 46, no. 4, pp. 1416–1424, 2010.

[110] A. R. Weber and G. Steiner, "An accurate identification and compensation method for nonlinear inverter characteristics for AC motor drives," in *2012 IEEE International Instrumentation and Measurement Technology Conference Proceedings*, pp. 821–826, IEEE, may 2012.

[111] B. Weber, T. Brandt, and A. Mertens, "Compensation of switching dead-time effects in voltage-fed PWM inverters using FPGA-based current oversampling," in *Conference Proceedings - IEEE Applied Power Electronics Conference and Exposition - APEC*, pp. 3172–3179, 2016.

[112] S. Bolognani, S. Calligaro, and R. Petrella, "Design issues and estimation errors analysis of back-emf-based position and speed observer for SPM synchronous motors," *IEEE Journal of Emerging and Selected Topics in Power Electronics*, vol. 2, no. 2, pp. 159–170, 2014.

[113] G. Wang, Y. Wang, J. Qi, R. Ni, W. Chen, and D. Xu, "Offline inductance identification of PMSM with adaptive inverter nonlinearity compensation," *9th International Conference on Power Electronics - ECCE Asia: "Green World with Power Electronics", ICPE 2015-ECCE Asia*, pp. 2438–2444, 2015.

[114] A. Imura, T. Takahashi, M. Fujitsuna, T. Zanma, and S. Doki, "Dead-time compensation in model predictive instantaneous-current control," *IECON Proceedings (Industrial Electronics Conference)*, pp. 5037–5042, 2012.

[115] X. Ding, M. Du, J. Cheng, F. Chen, S. Ren, and H. Guo, "Impact of Silicon Carbide Devices on the Dynamic Performance of Permanent Magnet Synchronous Motor Drive Systems for Electric Vehicles," *Energies*, vol. 10, no. 364, pp. 1–19, 2017.

[116] K. F. Hoffmann and J. P. Karst, "High frequency power switch - improved performance by MOSFETs and IGBTs connected in parallel," in *Power Electronics and Applications, 2005 European Conference on*, pp. 1–11, 2005.

[117] R. A. Minamisawa, U. Vemulapati, A. Mihaila, C. Papadopoulos, and M. Rahimo, "Current sharing behavior in Si IGBT and SiC MOSFET cross-switch hybrid," *IEEE Electron Device Letters*, vol. 37, no. 9, pp. 1178–1180, 2016.

[118] X. Ding, F. Chen, M. Du, H. Guo, and S. Ren, "Effects of silicon carbide MOSFETs on the efficiency and power quality of a microgrid-connected inverter," *Applied Energy*, vol. 201, pp. 270–283, 2017.

[119] M. Novak, J. Novak, and O. Sivkov, "An SiC inverter for high speed permanent magnet synchronous machines," *41st Annual Conference of the IEEE Industrial Electronics Society, IECON*, pp. 2397–2402, 2015.

[120] M. C. Kang, S. H. Lee, and Y. D. Yoon, "Compensation for inverter nonlinearity considering voltage drops and switching delays of each leg's switches," in *IEEE Energy Conversion Congress and Exposition, ECCE*, 2016.

[121] J.-W. Choi and S.-K. Sul, "Inverter output voltage synthesis using novel dead time compensation," *IEEE Transactions on Power Electronics*, vol. 11, no. 2, pp. 221–227, 1996.

[122] D. Leggate and R. J. Kerkman, "Pulse based dead time compensator for PWM voltage inverters," *IEEE Transactions on Industrial Electronics*, vol. 44, no. 2, pp. 191–197, 1997.

[123] Ben-Brahim, "The analysis and compensation of dead-time effects in three phase PWM inverters," in *IEEE Industrial Electronic Society Annual Conference*, pp. 792–797, 1998.

[124] R. B. Sepe and J. H. Lang, "Inverter Nonlinearities And Discrete-Time Vector Current Control," *IEEE Transactions on Industry Applications*, vol. 30, pp. 62–70, 1994.

[125] D. M. Park and K. H. Kim, "Parameter-independent online compensation scheme for dead time and inverter nonlinearity in ipmsm drive through waveform analysis," *IEEE Transactions on Industrial Electronics*, vol. 61, no. 2, pp. 701–707, 2014.

[126] L. Buchta, "Online adaptive compensation scheme for dead-time and inverter nonlinearity in PMSM drive," in *IFAC-PapersOnLine*, vol. 49, pp. 43–48, 2016.

[127] A. R. Muñoz and T. A. Lipo, "On-line dead-time compensation technique for open-loop PWM-VSI drives," *IEEE Transactions on Power Electronics*, vol. 14, no. 4, pp. 683–689, 1999.

[128] H.-S. Kim, K.-H. Kim, and M.-J. Youn, "On-line dead-time compensation method based on time delay control," *IEEE Transactions on control systems technology*, vol. 11, no. 2, pp. 279–285, 2003.

[129] N. Urasaki, T. Senjyu, K. Uezato, and T. Funabashi, "An adaptive dead-time compensation strategy for voltage source inverter fed motor drives," *Power Electronics, IEEE Transactions on*, vol. 20, no. 5, pp. 1150–1160, 2005.

[130] L. Ben-Brahim, "On the compensation of dead time and zero-current crossing for a PWM-inverter-controlled AC servo drive," *IEEE Transactions on Industrial Electronics*, vol. 51, no. 5, pp. 1113–1117, 2004.

[131] S. H. Hwang and J. M. Kim, "Dead time compensation method for voltage-fed PWM inverter," *IEEE Transactions on Energy Conversion*, vol. 25, no. 1, pp. 1–10, 2010.

[132] S. Bolognani, L. Peretti, and M. Zigliotto, "Repetitive-control-based self-commissioning procedure for inverter nonidealities compensation," *IEEE Transactions on Industry Applications*, vol. 44, no. 5, pp. 1587–1596, 2008.

[133] R. J. Kerkman, D. Leggate, D. W. Schlegel, and C. Winterhalter, "Effects of parasitics on the control of voltage source inverters," *IEEE Transactions on power electronics*, vol. 18, no. 1, pp. 140–150, 2003.

[134] N. Urasaki, T. Senjyu, T. Kinjo, T. Funabashi, and H. Sekine, "Dead-time compensation strategy for permanent magnet synchronous motor drive taking zero- current clamp and parasitic capacitance effects into account," pp. 845–853.

[135] N. Bedetti, S. Calligaro, and R. Petrella, "Self-commissioning of inverter dead-time compensation by multiple linear regression based on a physical modell," *IEEE Transactions on Industry Applications*, vol. 51, no. 5, pp. 3954–3964, 2015.

[136] J. M. Schellekens, R. A. M. Bierbooms, and J. L. Duarte, "Dead-time compensation for PWM amplifiers using simple feed-forward techniques," in *19th International Conference on Electrical Machines, ICEM 2010*, 2010.

[137] G. Pellegrino, R. I. Bojoi, P. Guglielmi, and F. Cupertino, "Accurate inverter error compensation and related self-commissioning scheme in sensorless induction motor drives," *IEEE Transactions on Industry Applications*, vol. 46, no. 5, pp. 1970–1978, 2010.

[138] I. R. Bojoi, E. Armando, G. Pellegrino, and S. G. Rosu, "Self-commissioning of inverter nonlinear effects in AC drives," in *2012 IEEE International Energy Conference and Exhibition, ENERGYCON 2012*, pp. 213–218, 2012.

[139] W. H. Press, S. A. Teukolsky, W. T. Vetterling, and B. P. Flannery, *Numerical Recipes in C*. Cambridge University Press, 1992.

[140] Y. Wang and R. D. Lorenz, "Using Volt-sec. sensing to extend the low speed range and the disturbance rejection capability of back-EMF-based self-sensing," in *18th European Conference on Power Electronics and Applications (EPE'16 ECCE Europe)*, pp. 1–10, IEEE, sep 2016.

[141] M. Pande, G. Joos, and H. Jin, "Output voltage integral control technique for compensating nonideal DC buses in voltage source inverters," *IEEE Transactions on Power Electronics*, vol. 12, no. 2, pp. 302–310, 1997.

[142] R. J. Kerkman, D. Leggate, B. J. Seibel, and T. M. Rowan, "Operation of PWM voltage source-inverters in the overmodulation region," *IEEE Transactions on Industrial Electronics*, vol. 43, no. 1, pp. 132–141, 1996.

[143] D. Fowler and J. Smith, "An accurate, high speed implementation of division by reciprocal approximation," *Proceedings of the 9th Symposium on Computer Arithmetic*, pp. 60–67, 1989.

[144] R. J. Kerkman, J. D. Thunes, T. M. Rowan, and D. Schlegel, "A frequency-based determination of transient inductance and rotor resistance for field commissioning purposes," *IEEE Transactions on Industry Applications*, vol. 32, no. 3, pp. 577 – 584, 1996.

[145] C. Zhong and Y. Lin, "Model reference adaptive control (MRAC)-based parameter identification applied to surface-mounted permanent magnet synchronous motor," *International Journal of Electronics*, vol. 104, pp. 1854–1873, nov 2017.

[146] S. Ichikawa, M. Tomita, S. Doki, and S. Okuma, "Sensorless control of permanent-magnet synchronous motors using online parameter identification based on system identification theory," *IEEE Transactions on Industrial Electronics*, vol. 53, no. 2, pp. 363–372, 2006.

[147] A. Balamurali, A. Mollaeian, S. M. Sangdehi, and N. Kar, "Parameter identification of permanent magnet synchronous machine based on metaheuristic optimization," in *IEEE International Electric Machines and Drives Conference (IEMDC)*, pp. 1729–1734, 2015.

[148] M. J. Duran, J. L. Duran, F. Perez, and J. Fernandez, "Induction-motor sensorless vector control with online parameter estimation and overcurrent protection," *IEEE Transactions on Industrial Electronics*, vol. 53, no. 1, pp. 154–161, 2006.

[149] S. L. Kellner, M. Seilmeier, and B. Piepenbreier, "Impact of iron losses on parameter identification of permanent magnet synchronous machines," *Proceedings of the 1st International Electric Drives Production Conference (EDPC)*, pp. 11–16, 2011.

[150] M. Novak, A. Flah, J. Novák, and S. Lassaad, "Online high-speed PMSM parameters estimation and stability analysis," *Acta Polytechnica Hungarica*, vol. 11, no. 9, pp. 75–94, 2014.

[151] A. Wijenayake and P. Schmidt, "Modeling and analysis of permanent magnet synchronous motor by taking saturation and core loss into account," *Proceedings of Second International Conference on Power Electronics and Drive Systems*, vol. 2, pp. 530–534, 1997.

[152] D. Reigosa, P. García, D. Raca, F. Briz, and R. D. Lorenz, "Measurement and Adaptive Decoupling of Cross- Saturation Effects and Secondary Saliencies in Sensorless-Controlled IPM Synchronous Machines," *IEEE Transactions on Industry Applications*, vol. 44, no. 6, pp. 1758–1767, 2008.

[153] F. Gao and L. Han, "Implementing the Nelder-Mead simplex algorithm with adaptive parameters," *Computational Optimization and Applications*, vol. 51, no. 1, pp. 259–277, 2012.

[154] P. Mercorelli, "A decoupling dynamic estimator for online parameters indentification of permanent magnet three-phase synchronous motors," in *16th IFAC Symposium on System Identification*, vol. 16, pp. 757–762, IFAC, 2012.

[155] S. Seung-Ho, C. Jong-Woo, and S. Seung-Ki, "Current measurements in digitally controlled AC drives," *Industry Applications Magazine, IEEE*, vol. 6, no. 4, pp. 51–62, 2000.

[156] B.-H. Bae and S.-K. Sul, "A compensation method for time delay of full-digital synchronous frame current regulator of PWM AC drives," *IEEE Transaction on Industry Applications*, vol. 39, no. 3, pp. 802–810, 2003.

[157] R. Volkert, O. Radler, E. Weißenborn, T. Ströhla, and V. Zöppig, "Position Controller with Hysteresis Compensation for Magnetic Bearings," in *10th International Symposium on Magnetic Bearings*, 2006.

[158] A. Masala, G. Vannini, M. Lacour, F.-M. Tassel, and M. Camatti, "Lateral rotordynamic analysis and testing of a vertical high speed 12.5MW motorcompressor levitated by active magnetic bearings," in *12th International Symposium on Magnetic Bearings*, 2010.

[159] S. Carabelli, C. Delprete, F. Maddaleno, M. Mittino, M. Muzzarelli, and M. Ugazio, "High efficiency linear power amplifier for active magnetic bearings," in *5th International Symposium on Magnetic Bearings*, 1996.

[160] J. Zhang, J. Schulze, and N. Barletta, "Synchronous three-level PWM power amplifier for active magnetic bearings," in *5th International Symposium on Magnetic Bearings*, 1996.

[161] J. Ferreira, E. Maslen, and R. Fittro, "Transpermeance amplifier applied to magnetic bearings," *Actuators*, 2017.

[162] C. M. Zingerli and J. W. Kolar, "Novel Observer Based Force Control for Active Magnetic Bearings," in *International Power Electronics Conference - ECCE ASIA*, 2010.

[163] D. Zhou and C. Zhu, "A novel hysteresis current control strategy for switching power amplifiers in active magnetic bearings," in *11th International Symposium on Magnetic Bearings*, 2008.

[164] L. Zhang, R. Born, X. Zhao, J.-s. Lai, and H. Ma, "A parabolic current control based digital current control strategy for high switching frequency voltage source inverters," in *2016 IEEE Applied Power Electronics Conference and Exposition (APEC)*, 2016.

[165] N. Mo, X. Fu, Y. Zhou, and S. Yu, "Study on EMI of power amplifiers in active magnetic bearing systems," in *12th International Symposium on Magnetic Bearings*, 2010.

[166] P. Kumar, D. D. Wright, and R. Jayawant, "Sending PWM down extended magnet cables," in *13th International Symposium on Magnetic Bearings*, 2012.

[167] T. G. Habetler, R. Naik, and T. A. Nondahl, "Design and implementation of an inverter output LC filter used for dv/dt reduction," *IEEE Transactions on Power Electronics*, vol. 17, no. 3, pp. 327–331, 2002.

[168] J. Y. Hung, S. M. Ieee, R. M. Nelms, S. M. Ieee, F. Xia, and M. Story, "Three-mode variable structure control for a pulse-density modulated current feedback amplifier," *IEEE International Symposium on Industrial Electronics*, pp. 736–740, 1995.

[169] F. Xia, N. Albritton, J. Hung, and R. Nelms, "A hybrid nonlinear control scheme for active magnetic bearings," in *3rd International Symposium on Magnetic Suspension Technology*, vol. 5, pp. 317–326, 1996.

[170] J. Wang and L. Xu, "Application of power amplifier for active magnetic bearing using soft switching technology," *Transactions of China Electrotechnical Society*, 2009.

[171] M. Krogemann, *The parallel resonant DC link inverter: a soft-switching inverter topology with PWM capability.* PhD thesis, University of Nottingham, 1997.

[172] P. Köllensperger, R. U. Lenke, S. Schröder, and R. W. De Doncker, "Design of a flexible control platform for soft-switching multilevel inverters," *IEEE Transactions on Power Electronics*, vol. 22, no. 5, pp. 1778–1785, 2007.

[173] J. M. Schellekens, J. L. Duarte, H. Huisman, and M. A. M. Hendrix, "Elimination of zero-crossing distortion for high-precision amplifiers," *Proceedings of the Industrial Electronics Conference, IECON*, pp. 3370–3375, 2011.

[174] G. R. Stanley and K. M. Bradshaw, "Precision DC-to-AC power conversion by optimization of the output current waveform - The half bridge revisited," *IEEE Transactions on Power Electronics*, vol. 14, no. 2, pp. 372–380, 1999.

[175] Y. Zhou, N. Mo, G. Yang, Z. Shi, and L. Zhao, "The electro magnetic compatibility analysis and experiment of the electronic system in AMB," in *15th International Symposium on Magnetic Bearings*, 2016.

[176] J. Jansen van Rensburg, "An integrated controller for an active magnetic bearing system," Master's thesis, North-West University, Potchefstroom, 2007, http://hdl.handle.net/10394/2306.

[177] R. R. Le Roux, "An embedded controller for an active magnetic bearing and drive electronic system," Master's thesis, North-West University, 2009, http://hdl.handle.net/10394/3992.

Appendix A

Inverter non-idiality compensation

A.1 Introduction

Compensation of the inverter non-idealities is essential for the sensorless vector (and scalar) control to function appropriately, especially during start-up [108, 50, 109, 110, 111, 112]. Accurate compensation of the inverter non-idealities also aid other applications, such as motor parameter identification [111, 113, 108] and model based predictive current control [114]. Since this thesis is concerned with accurate angle estimation of the drive for use in the AMB vibration control the inverter non-ideality compensation used is presented for repeatability of the angle estimation results. Besides meeting this requirement the inverter non-ideality compensation is presented since a novel method for characterizing the inverter non-ideality from which look-up tables (LUT) are generated for feed-forward compensation has been developed.

A.2 Inverter upgrade

The development of the inverter used in this study was presented by de Klerk [79]. The inverter design at that time opted to use IGBTs. Recent advances in power electronics in the form of Silicon carbide (SiC) MOSFETs have improved on the capabilities of the IGBT based inverter. Ding *et al.* [115] have investigated the impact of using the SiC-based inverter in a PMSM drive. They found that the SiC-based inverter can reduce both switching and conduction loss. Due to the decreased switching times a lower dead-time can be used which in turn reduces the inverter voltage distortion.

Thus, as a first improvement on the inverter non-ideality the inverter is upgraded by swapping the IGBTs[1] out with SiC MOSFETs[2]. The ultrafast freewheeling diode[3] used for

[1] IRG4PC50W by International Rectifier®.
[2] C3M0065090D by Cree®.
[3] HFA25PB60 by International Rectifier®.

the IGBT which featured soft recovery has been replaced by the SiC Schottky diode[4] which features zero reverse recovery and low device capacitance. The IGBTs had a continuous current rating of 27 A @ 100 °C whilst the SiC MOSFETs have a rating of 23 A @ 100 °C. Despite the lower current rating the improvement in conduction and switching loss means that the device will operate at a lower temperature and does not have to be de-rated as much. In order to understand why the drop-in replacement for this inverter is possible the losses need to be compared. The continuous conduction losses for the IGBT and SiC MOSFET given a constant device current are:

$$P_{c\_IGBT} = v_{ce(on)} i_c \tag{A.1}$$

$$P_{c\_SiC} = R_{ds(on)} i_d^2 , \tag{A.2}$$

where $v_{ce(on)}$, is the IGBT on-state voltage drop, i_c the collector current, $R_{ds(on)}$ the SiC MOSFET on-state resistance and i_d is the drain current. For the current range where the SiC MOSFET device voltage drop, $v_{ds} = R_{ds(on)} i_d$, is lower than the IGBT's voltage drop, the SiC MOSFET will have lower conduction loss than the IGBT. The on-state voltage drop for the IGBTs used in the old inverter was 1.8 V @ 100 °C $\wedge$ 27 A. The on-state resistance of the selected SiC MOSFET is 80 mΩ @ 100 °C $\wedge$ 20 A. Thus, the SiC MOSFET will have lower conduction loss for a continuous current up to 22.5 A. The inverter load current operates sinusoidally and not with a constant continuous current, thus in reality the SiC MOSFET losses will be much lower than the break even case of 22.5 A used to show that the losses will be lower.

The decrease in conduction loss does not generalize to higher current drives in which the constant voltage drop of the IGBT is advantageous. In order to obtain "best of both worlds" researchers have considered hybrid switches which is obtained by paralleling combinations of both types of transistors, e.g. [116, 117]. At lower currents most of the current is conducted by the SiC MOSFET and as the current increases the conduction loss is clamped by the IGBT. By turning the IGBT off before the SiC MOSFET the increased turn-off loss due to the IGBT tail current can also be avoided.

The SiC MOSFET has lower input and output capacitance, therefore the driver used for the IGBT is also capable of driving the SiC MOSFET. Since the capacitance is lower, switching times are shorter and the SiC-based drive has lower switching loss [118]. The upgrade to the SiC MOSFET is not as straight forward as it first seems. The increased switching speed leads to increased ringing and resulting EMI. The self-turn on phenomenon where the switch opposite to the one being turned off in the same half-bridge may turn itself on due to the Miller capacitance is of a concern. Due to this it is generally recommended to switch the SiC MOSFET off with a negative gate voltage. The gate threshold voltage of the SiC MOSFET is lower but its turn-on after the threshold voltage is much more gradual than that of IGBTs or Si MOSFETs, hence the self turn-on is not that severe as for the

[4] IDW12G65C5 by Infineon®.

aforementioned transistor types. Another method of reducing the chance of self turn-on is to use an asymmetrical gate driver impedance, i.e. decrease the turn-on slew rate by increasing gate driver impedance and to decrease the impedance that keeps the switch in the off state. These observations and proposed solution has also been recommended by Novak *et al.* [119]. The modified gate driver circuit used is shown in Fig. A.1. The original gate driver for the IGBT had only a 10 Ω gate resistor. The circuit component values were obtained after extensive SPICE simulations which included parasitic inductance. The gate capacitance, C_g, and gate resistance, R_g, is placed as close to the switch as possible to reduce ringing caused by the $TO-247$ package lead inductance. The added gate capacitance and resistance is placed on the component and not on the PCB, this is done by replacing the gate lead with the gate resistance oriented towards the source lead. The gate capacitance is soldered onto the source lead in the direction of the gate lead, thereby minimizing the parasitic loop inductance L_g. The gate driver component values were chosen such that the ringing was minimized without increasing the total loss to more than what the original IGBT switching losses were. Compared to the IGBT the resulting turn-on loss is greater but the turn-off loss is smaller.

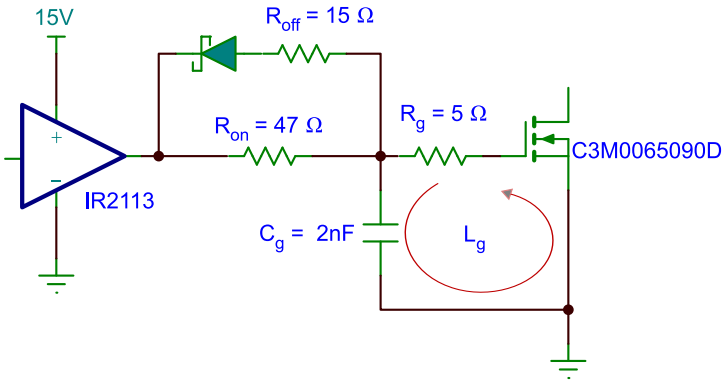

Figure A.1: Gate driver modification for SiC MOSFET.

With the inverter upgraded to use SiC MOSFETs along with the modified gate driver, the dead-time used could be reduced from 1 μs to 250 ns. This is the minimum dead-time allowed by the DS5101 digital waveform output board used to generate the PWM signals. Considering unequal turn-off and turn-on delay and driver delay skew the resulting effective dead-time is on the order of 150 ns. The overall reduction in distortion is actually greater than the factor of four improvement in dead-time since the on-state voltage drop across the device adds in a similar manner due to that off the dead-time voltage distortion. This can be verified by noting the average output voltage for phase x as derived by Kang

et al. [120] is:

$$V_x(i_x) = V_x^* - i_x\frac{R_T + R_D}{2} - V_{off}sign(i_x) \quad (A.3)$$

$$V_{off} = \frac{V_{T0} + V_{D0}}{2} + \frac{T_{DT} + T_{on} - T_{off}}{T_{sw}}V_{dc}\,, \quad (A.4)$$

where $R_{T/D}$, and $V_{T/D}$, are the linearised resistance and offset voltage of the transistor and anti-parallel diode transfer characteristic, T_{sw} is the switching period, T_{DT} is the dead-time, $T_{on/off}$ is the turn-on and turn-off delays and V_{dc} is the DC bus voltage. For a SiC MOSFET V_{T0} is zero. Also, due to synchronous rectification by the MOSFET the effective diode voltage drop, V_{D0}, is also nearly reduced to zero. The offset voltage can be decomposed into two contributing terms according to (A.4), one for the device offset voltage and another for the dead-time. For the dead-time used after the upgrade the contribution of the dead-time to the offset voltage is approximately 0.9 V, which is in the same order of magnitude as the IGBTs threshold voltage, $\approx 1\,\text{V}\,@\,100\,^\circ\text{C} \wedge 1\,\text{A}$.

After accounting for the device voltage drops and switching delays the total offset voltage reduction is closer to a factor of seven. Thus, exchanging the IGBTs for SiC MOSFETs has a considerable improvement as regards to reducing the combined inverter distortion caused by the dead-time effect and device voltage drops.

The next section (A.3) presents the compensation of the dead-time (and other non-linearities) with the aid of look-up tables. This raises the question: "Why reduce the non-linearity with the hardware approach?" This is answered by noting that the non-linearity compensation with the LUTs would still have a residual error. If it is assumed that the correction of the original voltage distortion, v_D, with a LUT has multiplicative uncertainty, γ, then the residual voltage distortion is given by:

$$\tilde{v}_D = \gamma v_D\,. \quad (A.5)$$

It is reasonable to assume that the multiplicative uncertainty would be the same regardless whether the inverter is upgraded. Hence, the residual voltage distortion would be reduced if the original voltage distortion has been reduced a priori with a hardware upgrade.

A.3 Dead-time compensation

A.3.1 Background

The most obvious and direct way of compensating for the inverter non-ideality is to measure the output voltage and correct for the voltage error with a voltage control loop as noted by Blaabjerg *et al.* [63]. Due to the increased cost of the voltage sensors and complications which arise due to averaging of the PWM voltage by signal conditioning circuits a feed-forward compensation of the voltage distortion is preferred. Dead-time compensation

methods presented in literature can be divided into off-line [121, 50, 122, 120, 123, 124] and on-line methods [125, 126, 127, 128, 129, 130].

On-line methods often operate on an internal model principle which tracks the harmonics (sixth) caused by the distortion created by the dead-time effect. From the tracked harmonics a voltage is generated to reject the harmonic, e.g.. [131]. On-line methods have the advantage that the control loop which generates the compensation voltage can adapt to changes in the disturbance voltage due to effects such as temperature variation, current slope at the zero crossing, DC bus voltage variation, switching device deterioration and other unforeseen disturbances. On-line methods have the disadvantage of adding computational burden on the control processor, possible instability in the adaptation algorithm if plant characteristics fall outside of the assumed range and ineffective compensation during load variation and the consequent transients. For these reasons, the off-line methods are the first choice for compensation.

The amount of correction achieved by the non-adaptive methods is usually acceptable despite the possible variation in operating conditions. Also, the off-line compensation is usually effective during machine transients. The off-line methods have lower computational burden during control, but comes at the cost of an a priori commissioning procedure. The method presented by Bolognani *et al.* [132] has the peculiarity that they generate a LUT for feed-forward compensation by storing a period of the waveform generated by a repetitive controller which is an on-line method, but the final compensation in the form that the LUT used is an off-line method.

Of course, a combination of an off-line method as a first-order correction and an on-line method for the residual error will yield good accuracy during transients and reduce the harmonics at steady-state operation.

Many of the presented off-line methods, especially earlier methods, consider the model of the dead-time effect to be merely a voltage offset which depends on the current polarity [63], such as in (A.3), [120]. A further improvement on dead-time modelling considers the effect of the parasitic capacitance of the switching device and cables connecting the electrical machine [133, 134]. The parasitic capacitance causes the voltage distortion to no longer exhibit a step change but instead to have a finite slope at small current amplitudes. Over the years the fidelity of the models for dead-time and other inverter non-idealities has progressively increased. A detailed model with physically representative parameters is presented by Bedetti *et al.* [135]. The identification of the model parameters via a self-commissioning procedure is also presented. The paper concludes with a table comparing various compensation strategies, including amongst others LUTs, piecewise-linear approximation, voltage measurement, harmonic based and their own proposed compensation.

A.3.2 Compensation using look-up tables

Schellekens *et al.* [136] investigate and compare the performance of various dead-time compensation strategies where the feed-forward models have varying levels of fidelity. As the fidelity increases the feed-forward model complexity (and hence computational burden) increases with the notable exception of compensation via LUTs. From the results presented by Schellekens *et al.*, LUTs arguably obtained the best compensation.

From the literature, it is apparent that the trend for accurate compensation of the inverter non-idealities first progressed by increasing model complexity, which has become too burdensome and yields diminishing returns for further investment in model complexity. Compensation methods have moved on towards quantitative black-box models in the form of higher order regression models which are implemented as LUTs. Due to computational complexity, the higher order model is evaluated off-line and stored as a LUT. Depending on the amount of memory a high-resolution LUT can be stored or a lower resolution LUT can be stored with some of the resolution regained with on-line interpolation. Hence, the usual trade-off between memory and computation time.

Compensation via LUTs has the added benefit of taking second-order non-linearities into account [132]. One example of such a second-order non-linearity is the turn-on/off delay dependence on the commutated current which causes the effective dead-time to vary with current magnitude. Usually, the turn-on/off delay is assumed independent of current, such as in (A.4). For large dead-time values, the assumption is justified. For newer generation drives the dead-time decreases and the variable turn-on/off delay may be taken into account in order to improve the drive's performance.

Various methods of characterizing the inverter non-ideality and generating the LUT entries have been proposed in the literature. The most representative methods are presented in [132, 136, 137, 110, 138, 52, 108, 111, 109]. A selection of the aforementioned methods will be discussed with the aim of exposing the assumptions made by previous authors during the experimental characterisation of the inverter non-ideality. The method proposed in section A.3.3 aims to overcome these assumptions *without* adding extra hardware in the inverter non-ideality characterisation.

One of the methods of characterizing the dead-time is to step the current in the α-axis and keep the β-axis current zero whilst the machine is stationary [110]. The non-linear distortion of the inverter can be separated into two terms, one component of the distortion has units in Volt and the other component is unitless. The component which has units in Volt originates from sources such as anti-parallel diode voltage drop while the switch is off and IGBT voltage drop while the switch is on. The distortion due to this component does not vary as a function of the DC bus voltage. The unitless component originates due to the dead-time and the voltage distortion which results at the output of the inverter which varies as a function of the DC bus voltage. In order to take this into account, the voltage distortion is often measured at different DC bus voltages. The effective load resistance

voltage drop, which consists of the combination of the machine and switch resistive voltage drops, manifests as a DC bus independent voltage drop. This is separated from the DC bus dependent voltage drop by measuring the effective resistance at two high current values where it is assumed that the variation in the non-linear distortion terms are zero. Bojoi *et al.* [138] also *assumed* that the non-linear component is symmetrical for positive and negative load current. By exciting the load with current steps only in the α-axis the machine load impedance is assumed symmetrical. The non-linear voltage distortion is also *assumed* equal in each phase.

Each phase's non-linearity can be separated from each other by introducing extra hardware into the measurement setup. An extra RL-load impedance is connected between the phase output and ground by Xie *et al.* [52]. This can be repeated for each phase. Xie *et al.* [52] also suggest that excitation in the α-axis only may result in characterisation of the inverter non-linearity which "...might not be accurate enough". Xie *et al.* assumed that the voltage distortion for the top and bottom switch is equal, otherwise, an extra set of measurements are required with the RL-load impedance connected to the positive rail of the DC bus.

Gaeta *et al.* [108] also introduced a method for accurate inverter non-linearity characterisation by adding a circuit with two relays connected to the three-phase inverter. The purpose of the relays is to bypass the voltage drop of one of the switches in a leg (top or bottom, hence two switches). This allows characterisation of the inverter non-linearity without assuming that the voltage drop of the top and bottom transistors are equal or that the non-linearly of each phase is equal. The previous two methods does away with most of the assumptions made by previously mentioned authors, but does so at the expense of extra hardware.

A.3.3 Proposed dead-time characterisation

A.3.3.1 Corrective reference voltage from current control loop

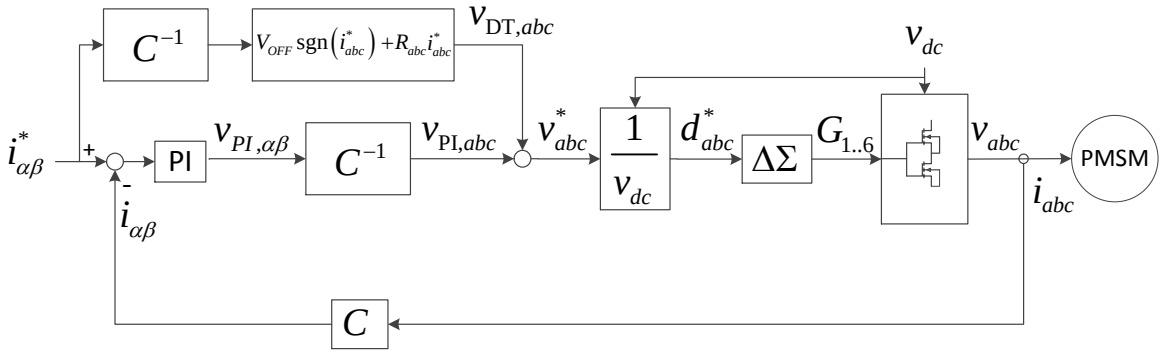

Figure A.2: Inverter non-linearity characterization.

The characterisation of the inverter non-linearity is explained with the aid of Fig. A.2. A current reference in the $\alpha\beta$-plane is generated and applied to the input of the current control loop. The PMSM rotor is assumed stationary and locked. An isolated wye connection is assumed such that the zero sequence component (γ component) is null. The terms, C and C^{-1}, denote the Clarke transform and its inverse. As opposed to the methods in literature the current reference is not stepped in the α-axis, but instead a rotating current reference is applied with the amplitude ramped. The rotation frequency is higher compared to the slope of the ramp. The current reference, $i^*_{\alpha\beta}$, can, therefore, be represented with a spiral, as depicted in the left of Fig. A.3. The same spiral reference for phases a and b in the stationary reference are on the right side of Fig. A.3. Thus, the whole $\alpha\beta$-plane, which is representative of all current combinations that the load can be subjected to within the rated current range, is excited. The rate of change of the current reference is so small such that the inductive voltage drop of the stator can be considered negligible.

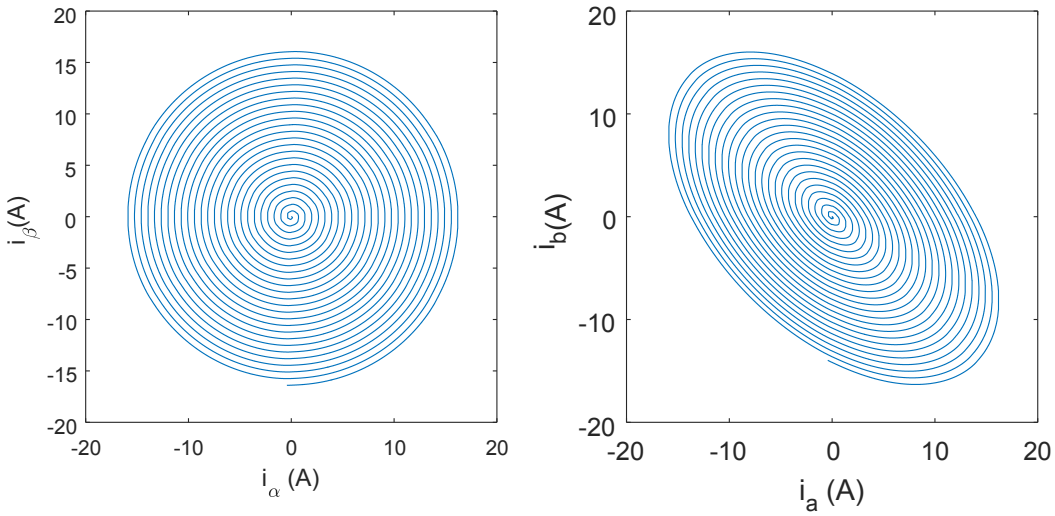

Figure A.3: Spiralling current reference.

The proportional and integrator (PI) terms in the current control loop correct for the non-linear inverter voltage drop and compensates for the load's resistive impedance. In order to have a very small current error, a large PI current control gain is required. The combination of a large current control gain and inverter non-linearity causes a limit cycle to be excited when the current passes through zero. This limit cycle appears in the form of chatter in the voltage reference as the current passes through zero. In order for the reference voltage to have a smoother transition in time through zero, the current reference slope is reduced as it approaches the zero crossings. Thus, to prevent the unwanted chattering the current reference depicted in Fig. A.3 can be expressed in the three-phase reference frame and in the time domain as depicted in Fig. A.4. Another means of reducing the chatter caused by the large gain and inverter non-linearity is to add the traditional means of dead-time compensation with the feed-forward term, $v_{DT,abc}$, to the PI generated

reference voltage, $v_{PI,abc}$. The sum of the PI control voltage and the feed-forward voltage yields the resultant three-phase reference voltage, v^*_{abc}.

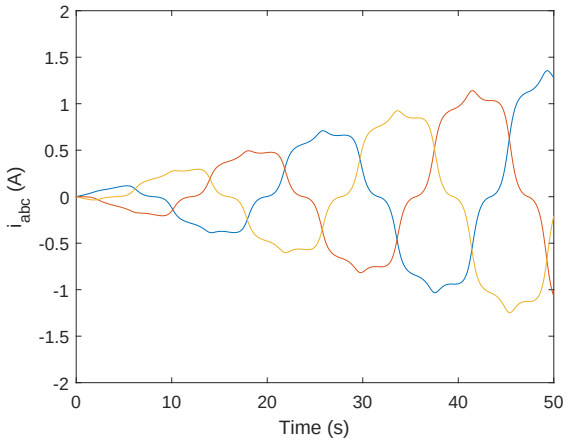

Figure A.4: three-phase current reference in the time domain.

By capturing the resultant reference voltage, v^*_{abc}, and transforming it back to a two-phase coordinate system, $v^*_{\alpha\beta}$, as a function of the applied current reference a feed-forward functional relationship for the steady-state voltage required to overcome the inverter non-linearity and DC voltage drop can be generated, i.e. $v^*_{\alpha\beta}\left(i^*_{\alpha\beta}\right)$. This functional relationship can be stored as two 2D LUTs. The problem with this approach is that the LUTs require a large amount of memory to be stored, i.e. it suffers from the "curse of dimensionality".

One method to overcome the memory requirement to store the 2D LUTs is to approximate the look-up tables. This can be achieved by considering the 2D LUT as a matrix. This matrix can be decomposed by using the singular value decomposition (SVD) [139]. Using SVD, a matrix can be decomposed into:

$$\mathbf{M} = \mathbf{U}\boldsymbol{\Sigma}\mathbf{V}^* \,, \tag{A.6}$$

where the matrices, $\mathbf{U}$ and $\mathbf{V}^*$, are unitary matrices and, $\boldsymbol{\Sigma}$, is a diagonal matrix containing the singular values. After the decomposition has been performed only those columns and rows which correspond to a relatively large singular value is kept, e.g. the first three columns of $\mathbf{U}\boldsymbol{\Sigma}$ and $\mathbf{V}$. An entry to the original matrix is thus approximated with:

$$M_{ij} \approx U_{i1}\Sigma_{11}V_{1j} + U_{i2}\Sigma_{22}V_{2j} + U_{i3}\Sigma_{33}V_{3j} \,. \tag{A.7}$$

The problem with this approach is firstly the requirement of on-line computation required to obtain the inputs for the LUT in the desired reference frame which is not necessarily available depending on the chosen reference frame for the sensorless vector control implementation and the computation of regenerating the desired output. Secondly, the inherent loss of accuracy due to the SVD approximation.

Ideally, the inverter non-linearity should be represented by three look-up tables with a phase current reference as input and a phase reference voltage as output. Thus, one look-up table per phase. This is justifiable since the non-linearity for each phase is dependent on that phase's current and is independent of the current in the other phases. The reader might be perplexed at this point since this seems entirely obvious. What then is the difficulty? The problem with this approach is that upon transforming the reference voltage, $v^*_{\alpha\beta\gamma}$, to the three-phase reference voltage, v^*_{abc}, the zero component in the $\alpha\beta\gamma$-plane is assumed null. This causes the component of the reference voltage which corrects for the distortion to become coupled in the *abc*-stationary reference frame. Thus, there is no longer a 1:1 correspondence between a phase's current and that phase's reference voltage.

Bolognani *et al.* [132] addressed this coupling due to the lost information of the zero component, referred by them as the homopolar component, by assuming that the distortion couples equally between the different phases. They then proceed to approximate the uncoupled phase voltage by multiplying the coupled phase voltage with a factor of $\frac{2}{3}$. The look-up table entries corresponding to high current value inputs are limited to be equal to the traditional dead-time compensation. In order for this multiplication factor to be valid, the load impedance has to be symmetrical and the non-linearity for each phase also has to be equal. Due to asymmetry in the load and differing non-linearity for each phase, a residual error will remain in the LUT using their technique. Other authors have solved this coupling by isolating the distortion in each phase by using extra hardware during the characterisation, e.g. [52, 108].

A.3.3.2 Algebraic recovery of the zero sequence component

The zero sequence component can be recovered mathematically by realizing that the measurement combination of, $i^*_{\alpha\beta}$ and $v^*_{\alpha\beta}$, after transforming it into the three-phase reference frame, can be formulated as an overdetermined system of equations.

Suppose that the look-up table is discretised into n entries, i.e. the input phase current sequence is arranged as:

$$i_{x1..n} = \{i_{x1},\, i_{x2},\, ...i_{xn}\}\ , \tag{A.8}$$

where i_{x1}, corresponds to the minimum input current and i_{xn}, the maximum input current. The look-up table voltage output sequence is arranged as:

$$v_{x1..n} = \{v_{x1}\,(i_{x1})\,,\, v_{x2}\,(i_{x2})\,,\, ...v_{xn}\,(i_{xn})\}\ . \tag{A.9}$$

In order to handle the effects of quantization, it will be assumed that the look-up table has a number of entries equal to a power of two. The inputs can thus be represented with a range of B-bits, such that the total number of entries are:

$$n = 2^B\,. \tag{A.10}$$

With an indexing system for the look-up table entries established, indexing to distinguish the same measurement sample in different reference frames amongst numerous samples still needs to be established. The samples will be denoted with a #ℕ in the superscript of an $\alpha\beta$-reference frame sample, but in the subscript with the associated phase, i.e. current sample number #1 in the $\alpha\beta$-reference frame after transforming to the three-phase reference frame is denoted with:

$$Q_B\left(Ci_{\alpha\beta}^{\#1}\right) = \begin{bmatrix} i_{a\#1} \\ i_{\#1b} \\ i_{\#1c} \end{bmatrix}. \tag{A.11}$$

The purpose of the #ℕ is to denote the numerical location of the sample within that phase's look-up table. Thus, $a\#1$ denotes the index of the first sample in the look-up table associated with phase a, it has a numerical value within the range $[1..n]$. Since the look-up table inputs are quantized and the $\alpha\beta$-reference frame sample is not, an extra quantization operator, Q_B, with B-bits is required to round off the three-phase reference current value to the nearest valid look-up table input address.

The power variant Clarke transform given by [14]:

$$\begin{bmatrix} v_\alpha \\ v_\beta \\ v_\gamma \end{bmatrix} = \underbrace{\frac{2}{3}\begin{bmatrix} 1 & -\frac{1}{2} & -\frac{1}{2} \\ 0 & \frac{\sqrt{3}}{2} & -\frac{\sqrt{3}}{2} \\ \frac{1}{\sqrt{2}} & \frac{1}{\sqrt{2}} & \frac{1}{\sqrt{2}} \end{bmatrix}}_{\mathbf{C}} \begin{bmatrix} v_a \\ v_b \\ v_c \end{bmatrix}, \tag{A.12}$$

is used in the formulation of the system of equations to recover the zero component. For a single reference voltage, $v_{\alpha\beta}^*\left(i_{\alpha\beta}^*\right)$, the inverse of $\mathbf{C}$ would have resulted in a coupled three-phase voltage if v_γ is assumed zero. In fact, the quantity of interest is actually the decoupled three-phase voltage, v_{abc}, and not necessarily the zero component. Once the uncoupled voltage is estimated the zero component can indeed be calculated. Thus, it is mathematically equivalent to recovering the zero component, which was the root cause of the coupling to occur and which caused an erroneous non-linearity characterisation.

For the first pair of current reference and voltage values the following equation can be formulated:

$$\begin{aligned} v_\alpha\left(i_{\alpha\beta}^{\#1}\right) &= C_{11}v_a\left(i_{a\#1}\right) + C_{12}v_b\left(i_{b\#1}\right) + C_{13}v_c\left(i_{c\#1}\right) \\ v_\beta\left(i_{\alpha\beta}^{\#1}\right) &= C_{21}v_a\left(i_{a\#1}\right) + C_{22}v_b\left(i_{b\#1}\right) + C_{23}v_c\left(i_{c\#1}\right) \\ v_\gamma\left(i_{\alpha\beta}^{\#1}\right) &= C_{31}v_a\left(i_{a\#1}\right) + C_{32}v_b\left(i_{b\#1}\right) + C_{33}v_c\left(i_{c\#1}\right). \end{aligned} \tag{A.13}$$

Equation (A.13) is not invertible, because v_γ is still unknown. Therefore, there are more unknowns than equations for measurement pair #1. For a different measurement sample, e.g. sample $q\,\#\,sample\,count$, one of the entries on the right hand side may correspond

to some of the entries corresponding to the equation for the first sample. For example, $i_{a\#1} = i_{a\#q}$. This can be justified with the aid of Fig. A.5. The red horizontal line crosses the red phase current at the same current value for each cycle. For each red line crossing the vertical green line indicates what the other phase current values are which correspond to that measurement set. Thus, for each sample occurrence in the figure, one phase current (the red phase) has the same value, but the other phases have different values. Hence, the solution procedure for the unknown, v_γ, is to add the equations which correspond to the other samples to the system of equations. The number of unknowns for the look-up tables is $3n$, one for each phase voltage. Thus, at least $3n$ equations are needed in order to solve for all the unknowns. Due to measurement noise, more equations result in reducing the noise in the solution of the look-up tables. There are a total number of $N > 3n$ equations.

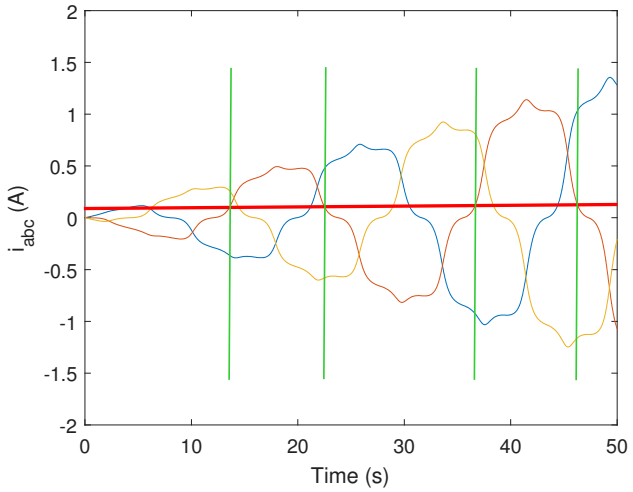

Figure A.5: Repeated sample occurrences of three-phase current reference.

In order to prepare for expressing the system of equations for all the samples, the equation for a single sample, (A.13), is reformulated in block matrix notation:

$$\begin{bmatrix} v_\alpha\left(i_{\alpha\beta}^{\#1}\right) \\ v_\beta\left(i_{\alpha\beta}^{\#1}\right) \\ v_\gamma\left(i_{\alpha\beta}^{\#1}\right) \end{bmatrix} = \underbrace{\left[\begin{array}{c|c|c} \overbrace{\begin{matrix}\cdots C_{1,a\#1}^{11} \cdots \\ \cdots C_{2,a\#1}^{21} \cdots \\ \cdots C_{3,a\#1}^{31} \cdots\end{matrix}}^{1..n} & \overbrace{\begin{matrix}\cdots C_{1,b\#1}^{12} \cdots \\ \cdots C_{2,b\#1}^{22} \cdots \\ \cdots C_{3,b\#1}^{32} \cdots\end{matrix}}^{1..n} & \overbrace{\begin{matrix}\cdots C_{1,b\#1}^{13} \cdots \\ \cdots C_{2,b\#1}^{23} \cdots \\ \cdots C_{3,b\#1}^{33} \cdots\end{matrix}}^{1..n} \end{array}\right]}_{\mathbf{M}} \left[\begin{array}{c} v_a\left(i_{a1}\right) \\ \vdots \\ v_a\left(i_{an}\right) \\ \hline v_b\left(i_{b1}\right) \\ \vdots \\ v_b\left(i_{bn}\right) \\ \hline v_c\left(i_{c1}\right) \\ \vdots \\ v_c\left(i_{cn}\right) \end{array}\right], \tag{A.14}$$

where the change in super-and subscripts in the term, $C_{1,a\#1}^{11}$, denotes that the value of the Clarke transform matrix, C_{11}, is located in the first row at the $a\#1$-th column. Note how the index has been transferred from the transformation *operand*, $v_a\left(i_{a\#1}\right)$, to the *operator*, $C_{1,a\#1}^{11}$.

For the set of all samples, the system of equations can be formulated in block matrix notation as:

$$\begin{bmatrix} v_\alpha\left(i_{\alpha\beta}^{\#1}\right) \\ v_\alpha\left(i_{\alpha\beta}^{\#2}\right) \\ \vdots \\ v_\alpha\left(i_{\alpha\beta}^{\#N}\right) \end{bmatrix} = \underbrace{\left[\begin{array}{c|c|c} \begin{matrix}\cdots C_{1,a\#1}^{11} \cdots \\ \cdots C_{2,a\#N}^{11} \cdots \\ \vdots \\ \cdots C_{N,a\#N}^{11} \cdots\end{matrix} & \begin{matrix}\cdots C_{1,b\#1}^{12} \cdots \\ \cdots C_{2,b\#2}^{12} \cdots \\ \vdots \\ \cdots C_{N,b\#N}^{12} \cdots\end{matrix} & \begin{matrix}\cdots C_{1,b\#1}^{13} \cdots \\ \cdots C_{2,b\#2}^{13} \cdots \\ \vdots \\ \cdots C_{N,b\#N}^{13} \cdots\end{matrix} \end{array}\right]}_{\mathbf{M}_\alpha} \left[\begin{array}{c} v_a\left(i_{a1}\right) \\ \vdots \\ v_a\left(i_{an}\right) \\ \hline v_b\left(i_{b1}\right) \\ \vdots \\ v_b\left(i_{bn}\right) \\ \hline v_c\left(i_{c1}\right) \\ \vdots \\ v_c\left(i_{cn}\right) \end{array}\right]. \tag{A.15}$$

Even though the terms, $C_{1,a\#1}^{11}$ and $C_{2,a\#N}^{11}$, are written in the same column, they are not necessarily in the same column. They are only somewhere in the same column matrix. Null entries are denoted with, "$\cdots$ ". For each row, there are only three non-zero entries. The resulting system of equations is thus highly sparse. A similar set of equations as (A.15) exist for phase β. There is no such set of equations for γ. Augmenting matrices

$\mathbf{M}_\alpha$ and $\mathbf{M}_\beta$ constitute the full system of equations, i.e.

$$\mathbf{M} = \left[\frac{\mathbf{M}_\alpha}{\mathbf{M}_\beta}\right] . \tag{A.16}$$

The solution of the complete system of equations is:

$$\boldsymbol{v}_{\alpha\beta\_1..N} = \mathbf{M}\boldsymbol{v}_{abc\_1..n} , \tag{A.17}$$

which yield the desired entries of the uncoupled voltage look-up tables for each phase, $\boldsymbol{v}_{abc\_1..n}$. The matrix, $\mathbf{M}$, is rather large, but fortunately also sparse. Hence, a sparse solver is used. Also note, that the inverse of $\mathbf{M}$ is not desired which would have taken quite a lot of resources to compute. Instead, only $\boldsymbol{v}_{abc\_1..n}$[5] is of interest.

A.3.3.3 Algorithmic generation of system matrix from measurements

From (A.15), it is clear that the entries of the matrix, $\mathbf{M}$, need to be populated algorithmically from the set of measurements. Algorithm A.1, presents such an algorithm in pseudocode. Line 6 declares the quantized array of current value addresses for the look-up table. Lines 10 and 11 declares a nested for-loop with counters for phase-a and phase-b. The counters for phase-a and phase-b, #**a**[6] and #**b**, sweeps a grid of indices which represents all combinations of current values within that grid. Therefore, the complete input domain is composed of the Cartesian product of two look-up tables. Referring back to Fig. A.3, it is clear that only the current values in the slanted elliptical domain of the ab-plane are valid current values which have been excited by the spiralling current excitation in the $\alpha\beta$-plane. Hence, the next step is to check if the phase-a and phase-b current combination produced with the nested for-loop does indeed fall within the radius of the $\alpha\beta$ current range. This is performed by generating the phase-c current from the algebraic relation assuming a wye connection (Line 15):

$$i_c = -\left(i_a + i_b\right) . \tag{A.18}$$

With i_{abc} now known, $i_{\alpha\beta}$ can be computed with the Clarke transform (Line 19), after which, its norm can be determined to check if it lies within the swept radius (Line 21). If $i_{\alpha\beta}$ does indeed lie within the radius, then an interpolative surface fit of the measured voltage reference, **Valpha** and **Vbeta**, is evaluated and assigned to the **V_AB** vector (Lines 23 & 29). The row location is determined by **equation_number** which is incremented each time a new equation is added. The column positions for the entries into the system matrix, $\mathbf{M}$, is thus now determined with the aid of the for-loop counters, #**a** and #**b**. The index for phase-c, #**c**, is derived from the other two phases by finding the index

[5] The method used to calculate $\boldsymbol{v}_{abc\_1..n}$ in this work is with the 'lsqr' function in Matlab.
[6] Bold characters in this section refers to identifiers within the listed algorithm.

in i_x where i_c resides.

The interpolative surface fit of the measured voltage,$v^*_{\alpha\beta}$, is required to approximate the voltage reference value generated by the control loop at the location of the grid points generated with the nested for-loop, since these points do not coincide exactly with the current reference values, $i^*_{\alpha\beta}$, used to excite the plant. Other methods such as directly interpolating the measured response voltage using the transformation of grid points to the original reference points, without an in-between step of a surface fit, could also have been used.

The rank of $\mathbf{M}$ in (A.17) is $3n$. With the algorithm's grid generation method, an upper bound of $2n^2$ equations are generated. Not all of the equations are valid though, because not all of the points in the *abc*-coordinate grid, generated by the nested for-loop, maps to within the disc generated by the excitation radius in $\alpha\beta$-coordinates. Supposing that the limiting radius of $i_{\alpha\beta}$ is 15 A, then the length of the semi-minor axis of the elliptical region shown in Fig. A.6, can be determined by noting that the semi-minor axis corresponds to the vector $i_{abc} = \begin{bmatrix} 7.5 & 7.5 & 15 \end{bmatrix}^T$ A which has a length of ≈ 15 in $\alpha\beta$-coordinates. Similarly, the vector $i_{abc} = \begin{bmatrix} 12.95 & -12.95 & 0 \end{bmatrix}^T$ A, also transforms to a vector with length ≈ 15. Thus, the ratio of the area of the ellipse to the area of the square grid is representative of the effective number of equations. This ratio is independent of the actual limiting current radius. The ratio, with the aid of our numerical example, is thus:

$$\begin{aligned} \frac{Area\,of\,ellipse}{Area\,of\,square} &\approx \frac{\pi ab}{s^2} \\ &= \frac{\pi \times \left(\sqrt{2} \times 7.5\right)\left(\sqrt{2} \times 12.95\right)}{s^2} \\ &= \frac{2\pi\, 7.5 \times 12.95}{30^2} \\ &= 0.6781\,. \end{aligned} \tag{A.19}$$

Hence, the effective number of equations is $0.6781 \times 2n^2 = 1.36n^2 > 3n$ which is strictly greater than $3n$ for $n > 2$. Thus, the system of equations generated by the algorithm is always overdetermined.

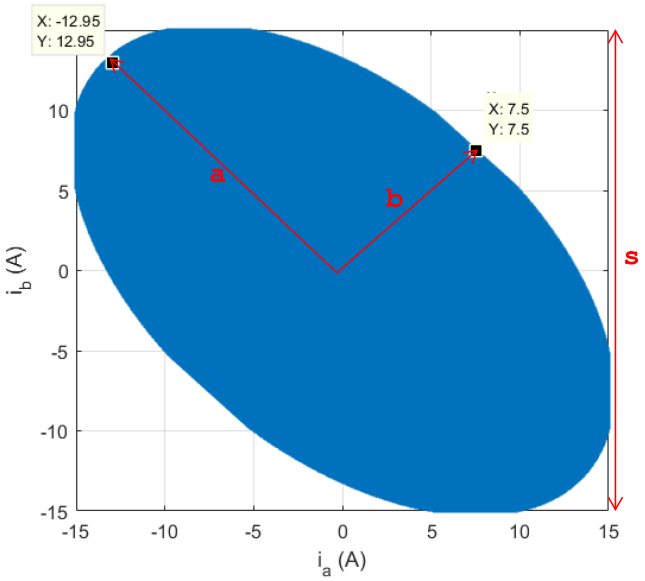

Figure A.6: Elliptical region in *abc*-plane which maps to the valid disc in the $\alpha\beta$-plane.

Algorithm A.1 Generation of system of equations from inverter sweep measurements.

```
1  const n   %LUT size
2  const i_n %Most negative current value for LUT
3  const i_p %Most positive current value for LUT
4  const i_ab_radius %Sweep radius in alpha-beta plane
5
6  ix = i_n:(i_p-i_n)/n:i_p; %Range for LUT current values
7
8  equation_number = 0;
9
10 for #a = 1:n
11         for #b = 1:n
12
13         ia = ix(#a);
14         ib = ix(#b);
15         ic = -(ia + ib);
16
17         #c = Find location of ic in ix;
18
19         i_alpha_beta = C*[ia ib ic]';
20
21                 if |i_alpha_beta| <= i_ab_radius
22                         equation_number++;
23                         V_AB(number_equations) = Valpha(i_alpha_beta);
24                         M(equation_number, 0*n + #a) = C11;
25                         M(equation_number, 1*n + #b) = C12;
26                         M(equation_number, 2*n + #c) = C13;
27
28                         number_of_equations++;
29                         V_AB(number_equations) = Vbeta(i_alpha_beta);
30                         M(equation_number, 0*n + #a) = C21;
31                         M(equation_number, 1*n + #b) = C22;
32                         M(equation_number, 2*n + #c) = C23;
33                 end
34         end
35 end
```

A.3.3.4 Extension to separate voltage dependent and independent parts

The entries of the look-up table identified from the solution of (A.17), i.e. $\boldsymbol{v}_{abc\_1..N}$, has Volt as units. Since the inverter non-linearity has a component which varies with the DC bus voltage and a component which is independent of the DC bus voltage the separation of the non-linearity in these two components would aid in DC bus disturbance rejection. This can be achieved by identifying the LUT entries in terms of a unitless duty cycle and a three-phase resistance. The duty cycle component corrects for the distortion which varies due to the DC bus voltage and the resistance component approximates the voltage load which is independent of the DC bus voltage.

In order to achieve this aim (A.17) is modified to determine the LUT entries in duty cycle units and extended to estimate the three-phase load resistance, as shown in:

$$\boldsymbol{v}_{\alpha\beta\_1..N} = \underbrace{\left[\begin{array}{c|ccc} v_{dc}^{\#q}\mathbf{M}_{\alpha} & C_{11}\boldsymbol{i}_a & C_{12}\boldsymbol{i}_b & C_{13}\boldsymbol{i}_c \\ \hline v_{dc}^{\#q}\mathbf{M}_{\beta} & C_{21}\boldsymbol{i}_a & C_{22}\boldsymbol{i}_b & C_{23}\boldsymbol{i}_c \end{array}\right]}_{\mathbf{M}^{v_{dc}\#r}} \left[\begin{array}{c} \boldsymbol{d}_{abc\_1..n} \\ \hline R_a \\ R_b \\ R_c \end{array}\right] \tag{A.20}$$

where $\#q$ denotes the voltage of the q-th sample. Assuming the same LUT resolution, (A.20) compared to (A.17) has the same number of rows, but has three columns more. In order to obtain an accurate separation of the DC bus dependent and independent components, the measurement has to be repeated for several DC bus voltages and the set of equations is adjoined to obtain the full system of equations. The superscript in, $v_{dc}\#r$, denotes the r-th measurement set corresponding to a certain DC bus voltage.

A.3.4 Verification on simulated non-linearity

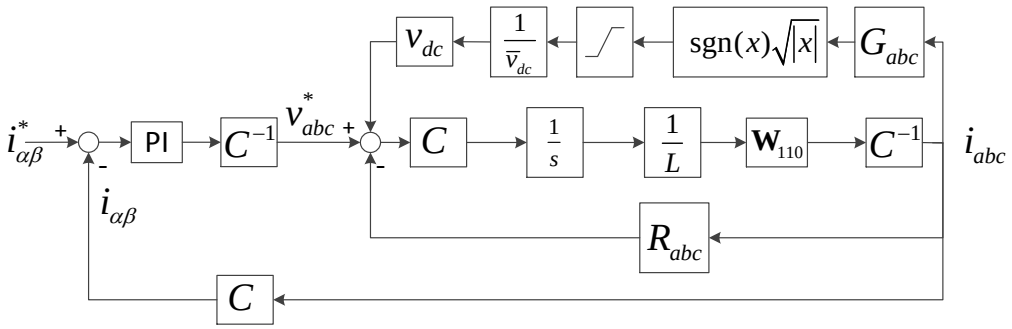

Figure A.7: Current control loop of simulated asymmetrical load with dissimilar non-linearity.

In order to verify the claim that an asymmetrical load and dissimilar non-linearities for each phase can be identified the proposed method is first tested on a known load via simulation. The simulation is conducted in the Matlab Simulink® environment. The

diagram representing the simulation is shown in Fig. A.7. An RL-load is simulated with the current solved in $\alpha\beta\gamma$-coordinates. The isolated neutral point constraint is imposed by forcing the zero component equal to zero by multiplying the $\alpha\beta\gamma$-coordinate current with the matrix $\mathbf{W}_{110}$, i.e.:

$$\boldsymbol{i}_{\alpha\beta} = \underbrace{\begin{bmatrix} 1 & 0 & 0 \\ 0 & 1 & 0 \end{bmatrix}}_{\mathbf{W}_{110}} \boldsymbol{i}_{\alpha\beta\gamma} \,. \tag{A.21}$$

The dissimilar gain, G_{abc}, and a signed square root followed by a saturation represents a non-linearity approximating a curve similar to the dead-time effect. A fictitious non-linearity is used as opposed to a switch-level simulation representation of the dead-time effect because the simulation time would take prohibitively long otherwise. The spiralling current reference as discussed in section A.3 is applied to the current control loop. The example numerical values used in the simulation is: $G_{abc} = \begin{bmatrix} 1.7 & 2 & 2.3 \end{bmatrix}^T$ and $R_{abc} = \begin{bmatrix} 1 & 1.25 & 0.75 \end{bmatrix}^T$. The DC bus voltage dependence of the non-linearity is taken into account by first normalizing the distortion with the nominal DC bus voltage, $\bar{v}_{dc}$, and then calculating the voltage distortion by multiplying with the DC bus voltage, v_{dc}, for that particular measurement. The extended look-up table identification presented in section A.3.3.4 is used.

If so desired, the extended identification can be reduced to the simple identification by setting $v_{dc} = \bar{v}_{dc} = 1$ in the simulation and in (A.20). In this case, the resistance is still identified but does not have a physical interpretation. It still has a mathematical interpretation, i.e. it corresponds to the linear component of the non-linear voltage which correlates with the current. The total non-linear voltage is then determined by:

$$v_{x1..n} = d_{x1..n} + R_x i_{x1..n} \,, \tag{A.22}$$

where d_x, has the unit of Volt for the special case that $v_{dc} = 1$, and x, is the phase of interest and i_x, is the quantized array of LUT input currents.

The result of the three-phase non-linearity's reduced identification is shown in Fig. A.8. The corresponding estimated resistances are: $\hat{\mathbf{R}}_{abc} = [1.097, 1.350, 0.848]\ \Omega$. Since $v_{dc} = 1\,\mathrm{V}$ for the simplified case, there is no way of separating the voltage component due to the non-linearity and that due to the resistance. This results in the overestimation of the resistance and the resulting LUT entries are not monotonically increasing.

The extended identification result is shown in Fig. A.9. The estimated resistance for various combinations of DC bus voltages used is reported in table A.1. A nominal voltage, $\bar{v}_{dc}$, of 80 V was used. For two DC bus voltage measurement sets a close approximation to the true resistance is obtained. The result does not converge any further for more than two DC bus voltage measurement sets. Since these results are for a noiseless simulation

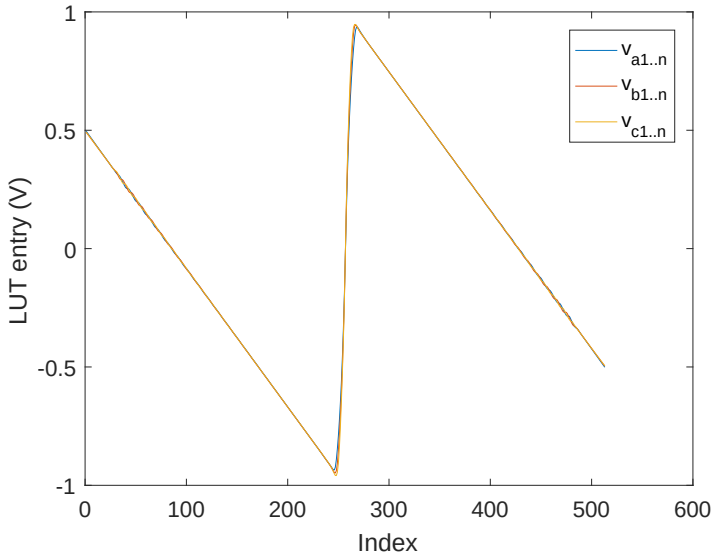

Figure A.8: Look-up tables of identified non-linearity for a single DC bus voltage measurement.

one must be careful not to generalize. For real-world data, more measurement sets will produce more accurate parameter estimates. The steady state error in the regression of the estimated resistance is expected since the non-linear voltage disturbance has a linear component which correlates with the linear voltage of the resistive voltage drop.

The error of the look-up table is shown in Fig. A.10. In order to reduce the error due to the higher slope near the zero crossing a higher resolution LUT has to be used. It has been found that the accuracy of the estimated resistance is also a function of the LUT resolution. For a 1025 entry LUT, the estimated resistance is: $\hat{\mathbf{R}}_{abc} = [0.999, 1.2503, 0.7503]\ \Omega$, after one iteration. The estimation of the non-linearity also has an iterative characteristic upon the error. This is due to the residual current error in the current control loop during the excitation. By replacing the first order dead-time correction in Fig. A.2, by the identified look-up table the current error in the current control loop is smaller due to better feed-forward correction upon a second iteration of characterizing the inverter non-ideality. Indeed, the estimated resistance upon a second iteration with a 1025 entry LUT is: $\hat{\mathbf{R}}_{abc} = [1, 1.25, 0.75]\ \Omega$ (i.e. exact).

From the obtained results it can be concluded that the algebraic zero component recovery is indeed capable of decoupling the voltage distortion amongst the three-phase voltages, because the asymmetric three-phase resistance could be identified and the per-phase error asymptotically approaches zero as the LUT resolution increases and the characterization is repeated with the updated LUT as the feed-forward term in the current control loop (disregarding numerical aberrations).

The application of algorithm A.1 is better understood at the hand of the actual implementation added in appendix E.1 which was used to post-process the simulated measurements

for the verification presented in this section.

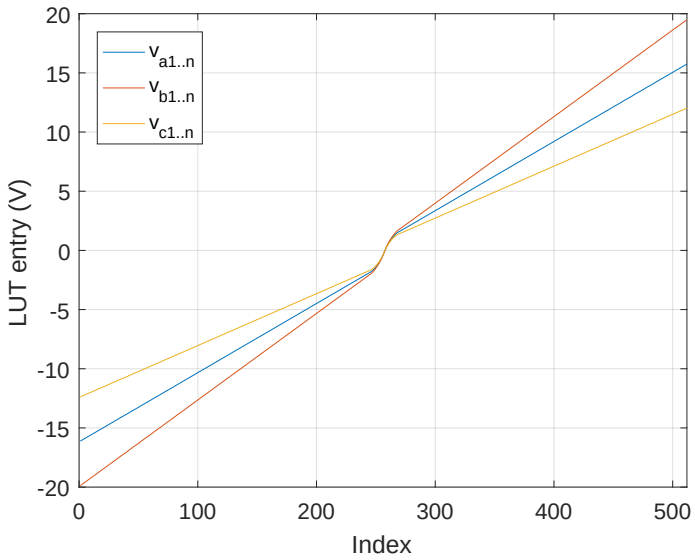

Figure A.9: Identified look-up tables of non-linearity for three DC bus voltage measurements.

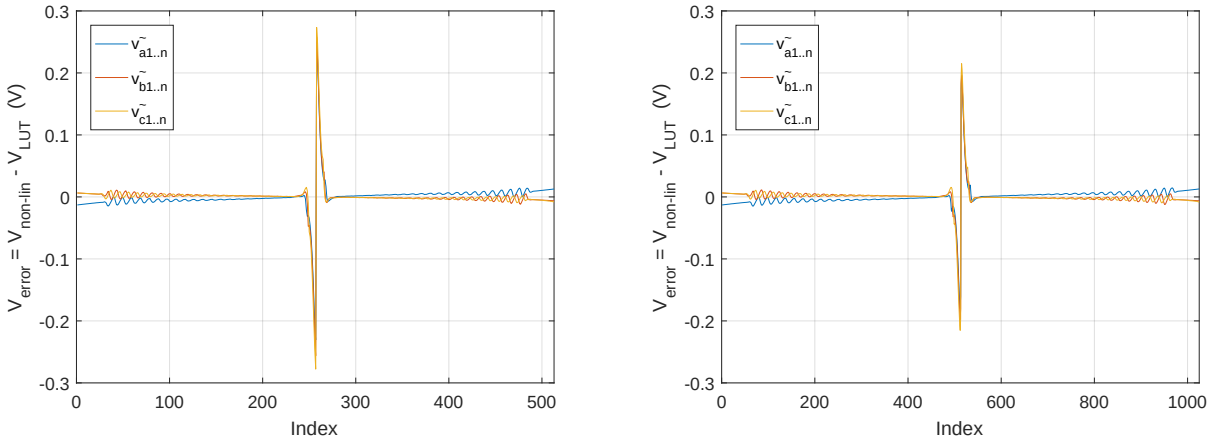

(a) Error for a 513 entry LUT.

(b) Error for a 1025 entry LUT.

Figure A.10: Look-up table error.

Table A.1: Estimated resistance as a function of DC bus voltage.

$\#v_{dc}$	v_{dc} [V]	$\hat{\mathbf{R}}_{abc}$ [Ω]
1	1	[1.097 1.350 0.848]
1	80	[0.941 1.156 0.727]
2	75, 85	[0.997 1.248 0.748]
3	75, 80, 85	[0.997 1.248 0.748]

A.3.5 Validation on PMSM drive

This section presents the measurements and the non-linearity characterization of the PMSM drive used in this work. The drive is controlled with the modular dSPACE® system using the DS1005 controller. The experiment is coordinated from within the ControlDesk® environment in which signals are logged and afterward processed in Matlab®.

Before the measurements are conducted the hall-effect current sensor offsets are carefully calibrated, by first allowing the sensors thermal drift to settle. The current sensors have a small hysteresis window, thus the current sensor offset is not simply subtracted, instead the maximum and minimum current are first applied to the drive and switched off, after which the current offset is noted each time. The correct offset is thus determined when the resulting hysteresis window has zero bias.

The drive's current is swept with a spiral current reference as previously discussed. The resulting reference voltage $v^*_{\alpha\beta}$ is captured and interpolated with a surface fit, as shown in Fig. A.11. Another viewpoint of the algebraic zero recovery algorithm is that the displayed 2D-functions are decomposed into three 1D-functions to yield the desired look-up tables.

The chosen look-up table resolution is 12-bits, i.e. $2^{12} = 4096$ entries. The extended decomposition is performed with the measurement sweeps performed at DC bus voltages of 155 V, 160 V and 165 V. The result of the full measurement decomposition is shown in Fig. A.12. The estimated resistances are: $\hat{\mathbf{R}}_{abc} = [0.167, 0.157, 0.166]$ Ω. Some notable features from the identified non-linearity should be highlighted. Firstly, the non-linearity is not symmetrical about the zero current index (2048). Secondly, a higher order non-linearity for a small negative current is visible. Thirdly, the LUT is not monotonically increasing for larger positive current values. The latter may be caused by different resistances for positive and negative current for each phase, i.e. corresponding to the on resistance for each separate SiC MOSFET. The physical explanation of the origin of these irregularities is beyond the scope of this thesis, except to note that the author has not come across these higher order non-linearities in previous literature regarding non-ideality compensation.

The original measured surface can be reconstructed from the look-up tables and the difference calculated to yield the residual error of the fit, which is displayed in Fig. A.13. By characterising the inverter non-linearity over the complete domain of interest (and not

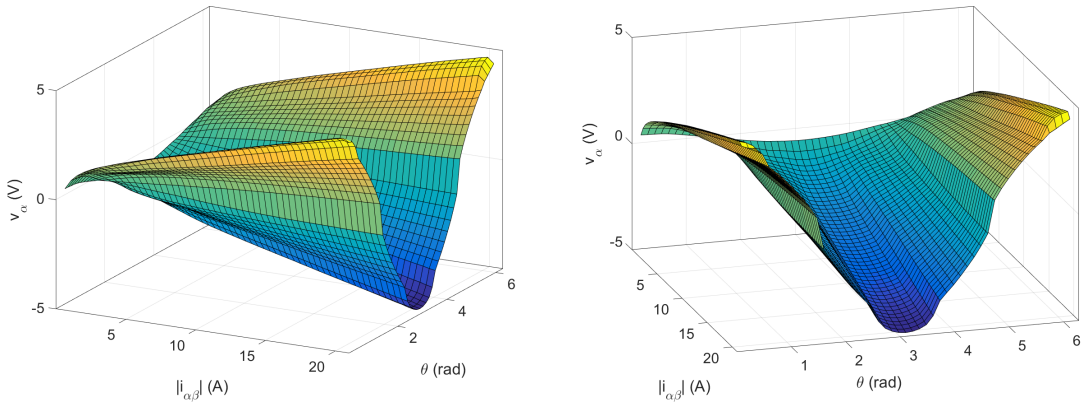

(a) $v^*_\alpha\,(i_{\alpha\beta})$

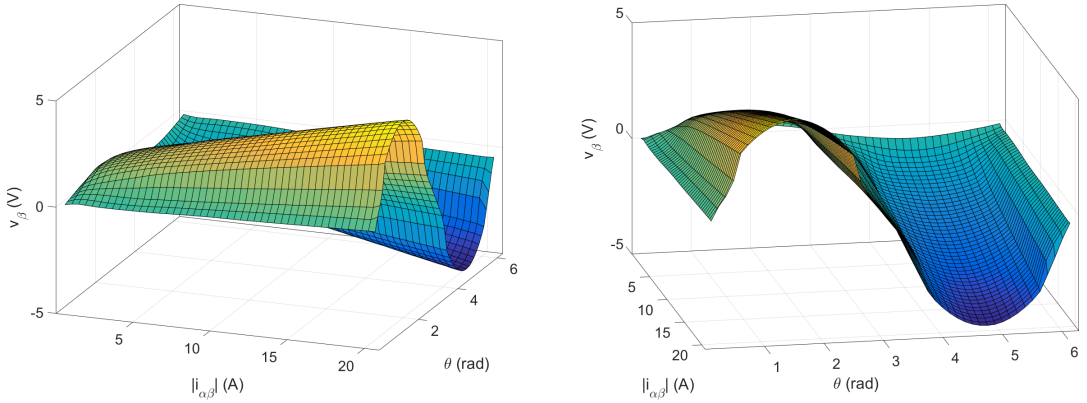

(b) $v^*_\beta\,(i_{\alpha\beta})$

Figure A.11: Surface fit of $v^*_{\alpha\beta}$ on polar coordinate domain.

just the α-axis) the deviation of the residual from the zero plane is minimized in a least squares sense. Some of the structure of the original surfaces are apparent in the residual. This suggests that there is still room for improvement in order to achieve an exact compensation of the inverter non-linearity, viz. when the residual error appears as noise.

The effectiveness of using the look-up tables is investigated by comparing the residual control effort of the PI current controller whilst employing the LUTs in the feed-forward compensation. The current is swept as shown in Fig. A.14a and the resulting residual control voltage required to keep the current error zero is shown in Fig. A.14b. The LUT based feed-forward compensation has much lower residual control effort compared to the "traditional" dead-time compensation shown in Fig. A.15. The "traditional" dead-time compensation in this example is defined as a piecewise linear feed-forward compensation, equal for each phase.

Another classical means of evaluating the compensation is by visual confirmation of the drive's ability to track a sinusoidal current reference. A measured sinusoidal current with a reference frequency of 5 Hz and amplitude of 1 A is shown in Fig. A.16. No current

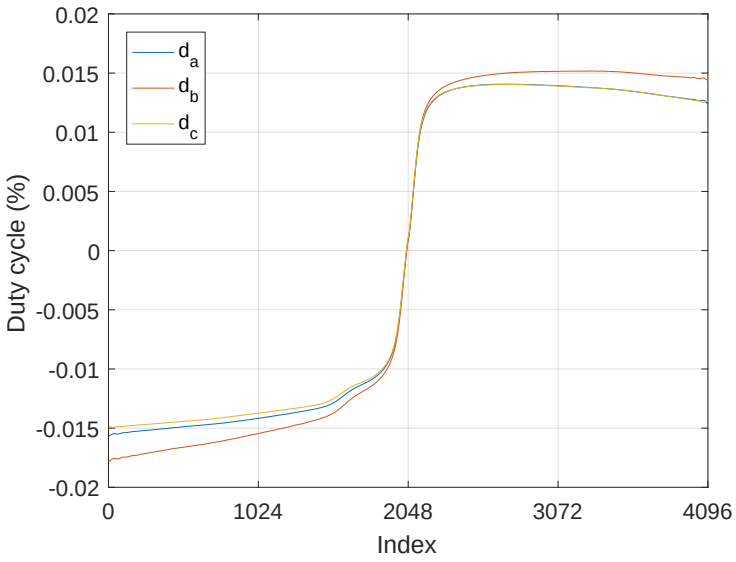

Figure A.12: Estimated three-phase inverter non-linearity.

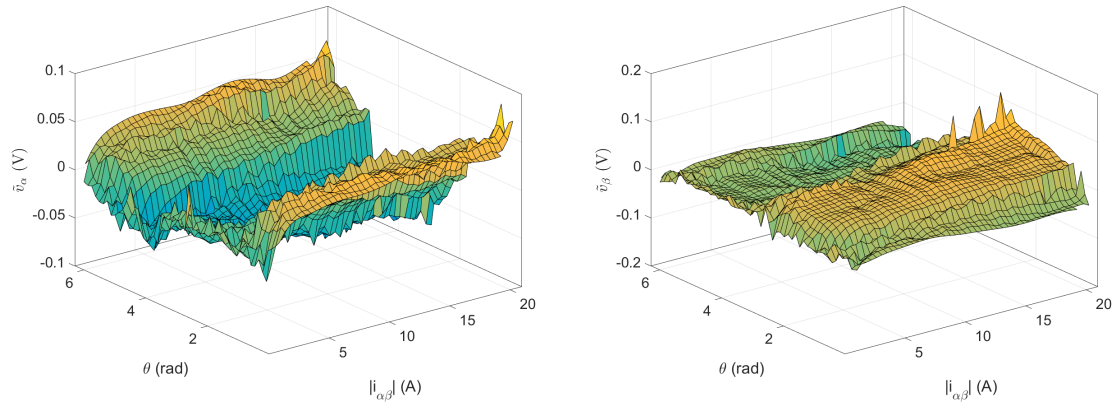

Figure A.13: Residual error for 2D fit reconstructed from 3×1D LUTs.

clamping phenomenon is visible and the total harmonic distortion (THD) of 0.37 % is exceptionally low for a three-phase drive. Typically, authors in the literature marginalize the current clamping phenomenon by showing the current tracking performance for the *rated* current. In this case, no current clamping is visible, even for a small current amplitude.

A comparison of the THD for load currents varying as a function of the fundamental frequency and magnitude is presented in Fig. A.17

One possible cause for the residual error (i.e. the inability of the LUT to exactly cancel the voltage drop required for zero current error) is that due to the "thermal noise" in the measurement procedure. Fig. A.18, shows the residual voltage error, before and after applying a current reference, $\left\| i^*_{\alpha\beta} \right\| \approx 20\,\mathrm{A}$, for approximately 20 s. The same current sweep as in Fig. A.14a, is applied. As shown, the voltage generated by the control loop to compensate the residual error is quite different even for such a small time period of

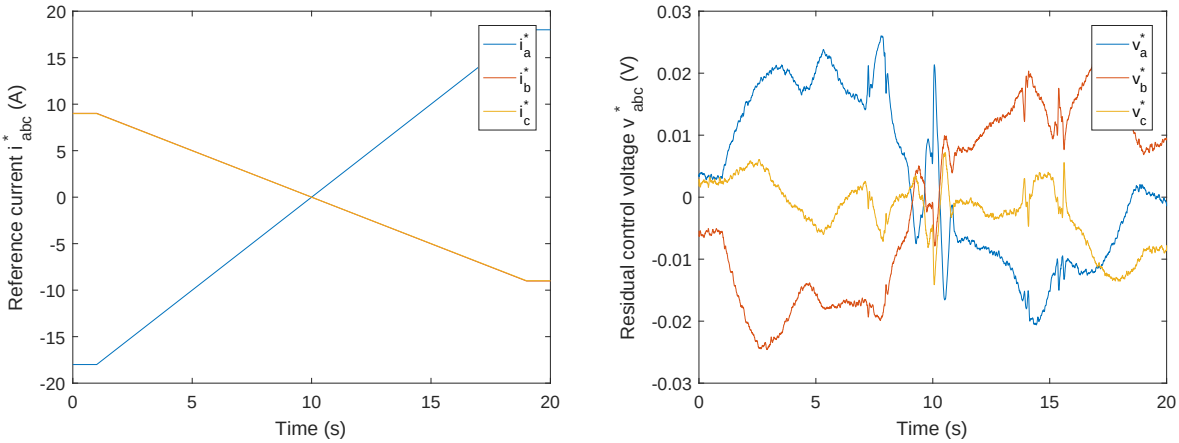

(a) Current reference.

(b) Residual control reference voltage with LUT compensation.

Figure A.14: Look-up table effectiveness as feed-forward non-linearity compensation.

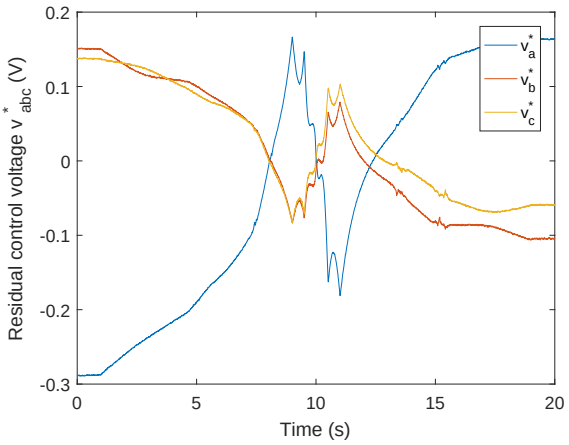

Figure A.15: Residual control effort for "traditional" dead-time compensation.

self-heating. This suggests a future development to adjust the LUT output (or add a dimension) according to the measured or estimated temperature of the load.

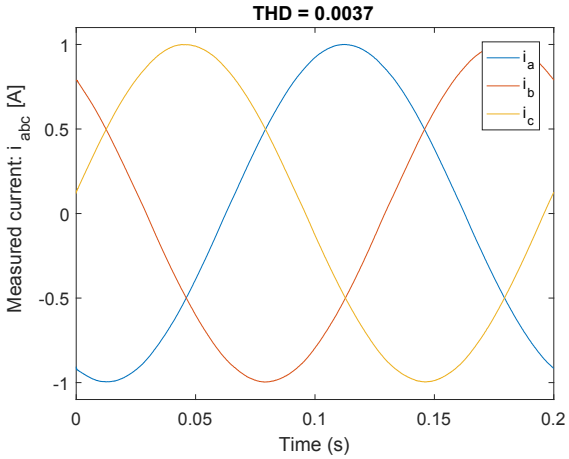

Figure A.16: Sinusoidal current tracking.

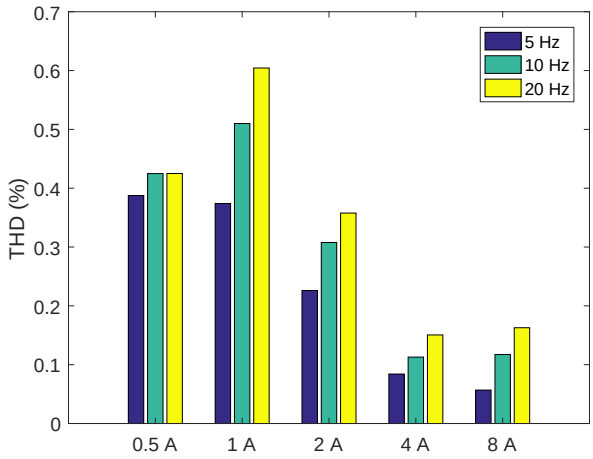

Figure A.17: THD comparison.

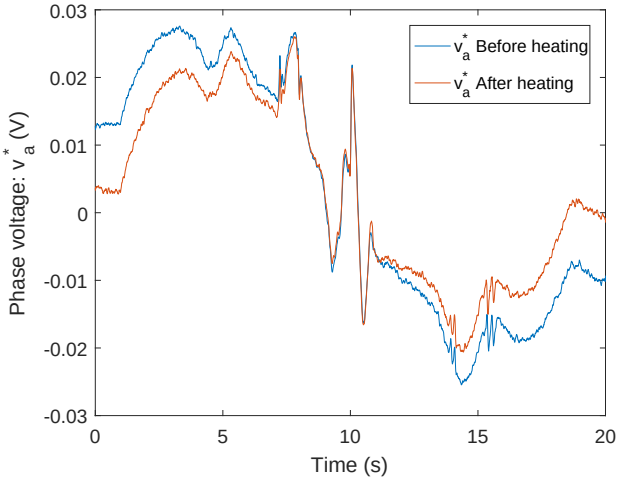

Figure A.18: Effect of self-heating on residual error.

A.3.6 Modified three-phase filter

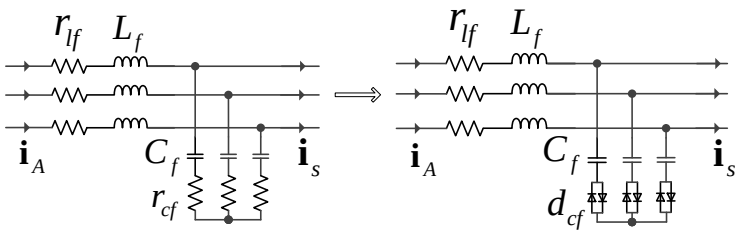

Figure A.19: Modified three-phase LC filter.

The three-phase filter presented in section 4.2.2, can be slightly modified as depicted in Fig. A.19. The series resistance, r_{lf}, is the parasitic resistance of the filter inductor, L_f. The resistance, r_{cf}, in series with the filter capacitor, C_f, is an intentionally added series resistor which helps to dampen the high Q of the LC filter at the resonant frequency and helps to prevent instability of the inverter. It has been found that the winding resistance (which includes core loss) of the filter inductor is sufficient for damping of the large signal response of the resonant frequency for stabilizing the inverter control. Therefore, the series capacitor resistor may be removed.

In order to accurately compensate for the dead-time, the dead-time compensation should ideally be calculated according to the inverter output current, $\mathbf{i}_A$. This entails measurement of the inverter output current for the dead-time compensation as well as the machine stator current for the back-emf angle estimator. The increased number of current sensors considerably increases the cost and complexity of the system. Instead of using the measured *inverter* output current, the *stator* current may be used instead, if the phase delay of the filter is sufficiently small, i.e. the cutoff frequency of the filter is sufficiently high. Additionally, instead of using the *measured* stator current it is better to use the *reference* stator current as it is less affected by measurement noise which disturbs the dead-time compensation. The addition of the antiparallel diode pair, d_{cf}, provides better small signal damping than the resistor, r_{cf}. This can be seen by noting that the diode loss is greater than the resistor loss for small currents that satisfy:

$$\begin{aligned} P_r &< P_d \\ i_{C_f}^2 r_{cf} &< i_{C_f} v_d \\ i_{C_f} &< \frac{v_d}{r_{cf}}\,, \end{aligned} \tag{A.23}$$

where v_d, is the diode voltage drop. For a resistance of $1\,\Omega$, as used in the design by de Klerk [79], the current for which the diode provides higher damping is in the order of 700 mA. Higher damping of small current perturbations results in a smaller phase shift between the inverter and stator current, hence in better dead-time compensation when

the stator current is used in the dead-time compensation.

Thus, to recapitulate, the filter inductor parasitic resistance provides large signal damping for inverter stabilization (especially if it is *not* wound with Litz wire) and the antiparallel diode pair provides better small signal damping which improves the dead-time compensation.

The damping characteristics is validated via simulation. Fig. A.20, compares the drive currents using the two different filter configurations. The filter legs are symmetrical in each case of the filter configurations. Different phases are compared using the two different filters, so that the influence of one current zero crossing on another phase may be apparent. The inverter current control uses the same dead-time compensation for both simulations. The difference in current distortion and ripple is thus determined by the difference in filter configurations. From the figures it can be seen that the current has a ripple in the configuration with no diodes in the filter. The ripple is excited afresh by each zero current crossing. In the case of the filter with diodes, the ripple decays before the next zero current crossing is reached. Due to the decaying current ripple, the dead-time compensation performs better, since the current zero crossing of the current reference and the actual current is in closer agreement.

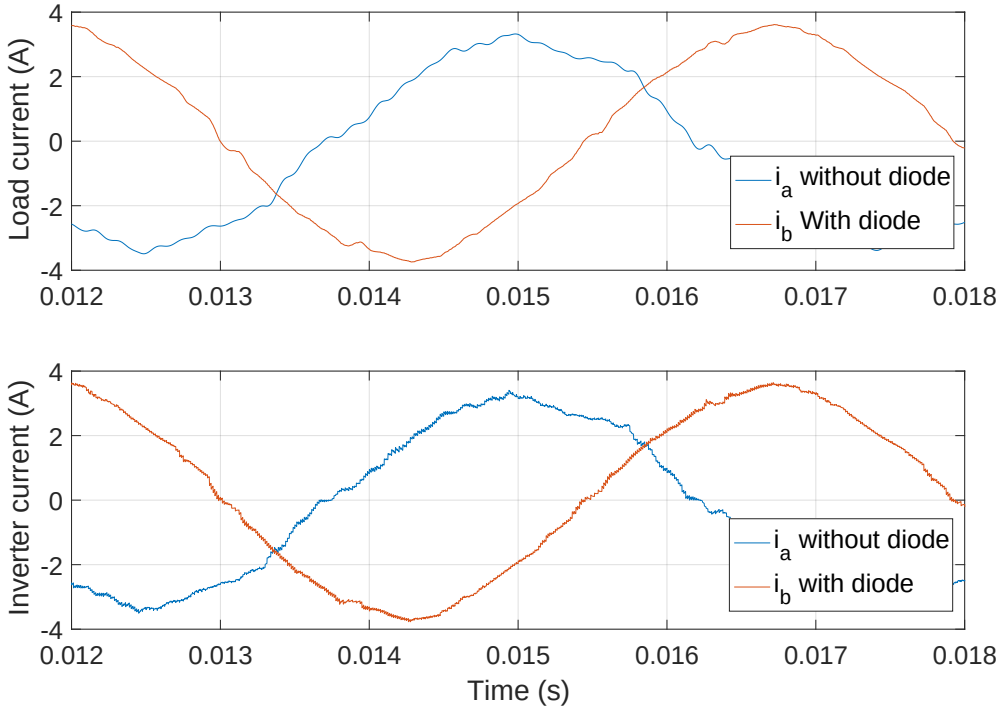

Figure A.20: Comparison of dead-time compensation for original and modified filter.

A.4 DC bus disturbance rejection

For accurate angle estimation in sensorless vector control, a varying DC bus voltage and its ripple need to be accounted [140]. The varying steady state value of the DC bus voltage, obtained by passive rectification of the AC input, arises due to various sources of fluctuation on the AC grid. A ripple on the DC bus voltage is also caused due to the passive rectification. The ripple component can be reduced via passive filters, but this adds extra volume, weight, and cost to the drive [141].

The current control loop of the vector control rejects the disturbance on the output current [13, 50]. The current control loop is able to reject the DC bus disturbance by varying the reference voltage applied to the pulse width modulator. In the sensorless vector control it is this reference voltage which is taken as the input to the back-emf based speed and angle estimator, thus the varying DC bus voltage directly affects the observer estimates. Therefore, another means of DC bus disturbance rejection is required which does not rely on the current controller's ability to reject the disturbance. This is usually accomplished via cancellation of the inverter's gain dependence on the DC bus voltage when converting the reference voltage to a duty cycle value. In analogue modulation circuits, this was done by making the amplitude of the triangle carrier dependent on the DC bus voltage. In digital control, the required duty cycle is calculated directly from the reference voltage

$$d^*_{abc} = \frac{v^*_{abc}}{G_i\left(v_{dc}\right)}, \tag{A.24}$$

where the inverter gain in the linear region is given by [142]:

$$G_i\left(v_{dc}\right) = \frac{v_{dc}}{2}. \tag{A.25}$$

Since the embedded controller used in this thesis (DS1005) has to control both the AMB and PMSM drive systems, the high computational cost of the division in (A.24), is unwanted. One means of approximating the division is to linearise the reciprocal function using its Taylor series expansion:

$$f\left(v_{dc}\right) = \frac{1}{v_{dc}} \tag{A.26}$$

$$= \frac{1}{\bar{v}_{dc}} - \frac{v_{dc} - \bar{v}_{dc}}{\bar{v}^2_{dc}} + \dots, \tag{A.27}$$

where the expansion has been evaluated about the nominal voltage, $\bar{v}_{dc}$. The reciprocal of the nominal voltage is calculated at compile time. The linearisation is obtained by truncating the expansion after the first two terms and is only accurate for a certain variation of the nominal DC bus voltage.

Another means of approximating the reciprocal is by recursive calculation using the Newton-Raphson iterative method [143]. The function whose roots are sought is defined

as:

$$f(x) = \frac{1}{x} - v_{dc}\,. \tag{A.28}$$

Applying the Newton-Raphson method leads to the iterative formula:

$$\begin{aligned} x_{i+1} &= x_i - \frac{f(x_i)}{f\prime(x_i)} \\ &= x_i + \left(x_i - v_{dc}x_i^2\right) \\ &= x_i\left(2 - v_{dc}x_i\right)\,. \end{aligned} \tag{A.29}$$

Since the variation in the instantaneous DC bus voltage is bounded, the iterative calculation for the current control cycle can be initialized from the previous control cycle's calculation. For one iteration, the number of computation cycles[7] is 3 compared to 31 for the full reciprocal[8].

A third means of computing the reciprocal is with a look-up table. Since the time required to convert the floating point value to an integer for use as an address input to the LUT is already long, compared to the iterative method, the LUT based method will not be investigated any further.

A.4.1 Evaluation of iterative DC bus voltage reciprocal calculation

The accuracy of the iterative calculation for the reciprocal is evaluated via simulation. A chirp voltage, v_r, is added to a nominal DC bus voltage and the reciprocal is calculated. The reciprocal estimate is computed using n-iterations per control cycle. The percentage error is used for evaluation and is calculated as:

$$e_{1/v} = \frac{\frac{1}{v_{dc}} - x_i}{\frac{1}{v_{dc}}} \times 100\,, \tag{A.30}$$

where $\frac{1}{v_{dc}}$, is the exact inverse and x_i, is the reciprocal estimate computed using (A.29).

The nominal DC bus voltage is chosen as 160 V and the voltage ripple magnitude is chosen as 10 % of $\bar{v}_{dc}$, i.e.16 V. The chirp signal is swept from $0.1 - 1$ kHz. The relatively large percentage voltage ripple (compared to the real ripple magnitude on the drive's DC bus) and frequency range serves as a means to "stress test" the limits of the iterative calculation's accuracy.

Fig. A.21, presents the percentage error of the estimated reciprocal for the described test with $n = 1$, 2. The percentage error at the maximum frequency is less than 1 % for $n = 1$ and less than 0.01 % for $n = 2$. The accuracy with $n = 1$ is deemed sufficient for use on the drive. The iterative calculation is able to attain such high accuracy because it does not

[7] IBM PowerPC750 processor.

[8] The cost of the instruction level floating point divide is actually in effect even worse than 31 cycles because it blocks the processor's pipeline unit.

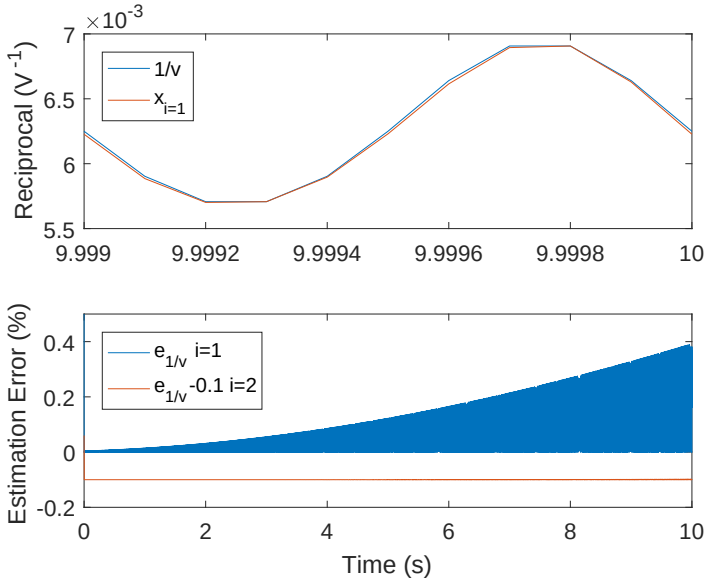

Figure A.21: Percentage error of reciprocal estimation via Newton-Raphson.

have to restart the approximation each control cycle but uses the estimate of the previous control cycle to update the new estimate.

A.5 PWM quantization noise suppression

Another type of non-ideality which may be compensated is the quantization of the PWM period. If left uncompensated, the PWM quantization noise would result in a disturbance which the current control loop would need to reject. The voltage reference in the current control loop would contain the information of the disturbance and end up deteriorating the speed and position estimated by the sensorless vector control. The origin, analysis and compensation of the PWM quantization noise via a Delta-Sigma Modulator (DSM) is presented more in-depth in [13, 50] and is only briefly repeated here, as it generally lacks attention in the broader literature.

It should be noted that the PWM generator in newer microcontrollers have increased the timer resolution, such that the PWM quantization noise becomes negligible and the DSM can be disregarded since the computational overhead of the DSM is unwarranted. The switching frequency in most drives is such that the PWM quantization noise can be disregarded.

It should be noted that due to the nature of the PWM quantization that it cannot be compensated by the LUTs used in the feed-forward compensation of the dead-time effect. In fact, the DSM was used during the inverter non-ideality characterization, represented by the $\Delta\Sigma$-block in Fig. A.2. Without the DSM, a current reference sweep as in Fig. A.14a, results in a residual control voltage reference as shown in Fig. A.22. Compared

to Fig. A.14b, a significant ripple can be observed and the peak-peak variation is more than doubled ($\approx 120\,\mathrm{mV}$ vs. $\approx 60\,\mathrm{mV}$). Yet, the total residual control voltage can still be considered relatively small. Hence, the DSM may be left out during the sensorless control for the drive used in this work.

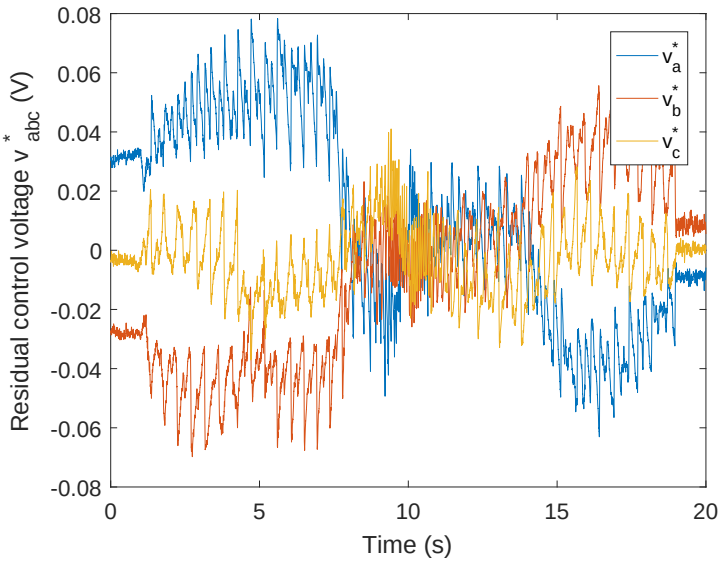

Figure A.22: Control voltage distortion due to PWM quantization.

Appendix B

PMSM parameter identification

B.1 Introduction

A large number of parameter identification methods for electrical machines are presented in the literature. Parameter identification methods for field commissioning can be broadly classified into statistical and deterministic procedures [144]. Statistical methods use estimation theory to minimize a chosen cost function with system measurements as inputs. The cost function is minimized when the estimated parameters correspond to the desired values which best "explains" the measured inputs. Deterministic methods rely on specific tests to measure each parameter. Often, statistical methods estimate many parameters simultaneously. Deterministic methods follow an elimination process such that each test is set up in such a manner that one parameter is measured per test so that unknown parameters do not affect that test's measurement result and parameters which do affect the result are available from a previous test and may be substituted to solve for the unknown for which that particular test was constructed.

Statistical methods can be further sub-classified into online and off-line methods. Popular versions of online statistical methods are the model reference adaptive system (MRAS) technique [145] and the recursive least-squares method (RLS) [146]. Balamurali *et al.* [147] present an off-line parameter identification technique for a Line-Start PMSM using improved particle swarm optimization on an extended model.

Despite the large array of parameter identification methods, little attention has been given to frequency dependence of the parameters for use in sensorless vector control with a few exceptions. Duran *et al.* [148] take the skin effect into account when estimating the parameters of the induction machine online. Kerkman *et al.* [144] considered two different deterministic methods to identify the machine inductance and showed that the result using the existing pulse-based method is affected by the skin effect. Their newly proposed method was not affected by skin effect. Kellner *et al.* [149] studied the impact of the iron losses on the identified parameters of the PMSM. They introduced iron loss parameters

into the PMSM model which are frequency dependent. Without these parameters, the identified inductance would have been influenced by the excitation frequency. Novak *et al.* [150] have implemented an on-line (MRAS) technique for estimation of a high-speed PMSM's parameters, in which they have reported on the speed dependence of the identified parameters. They considered the effect of time delay in the system as with regards to control stability but did not indicate the influence of the delay on the estimated parameters.

The other main non-ideality of concern is saturation dependent inductance [151, 152]. Taking saturation into account improves the estimation accuracy of salient machines using high-frequency injection methods.

B.2 Proposed parameter identification technique

B.2.1 Principle of control effort minimization

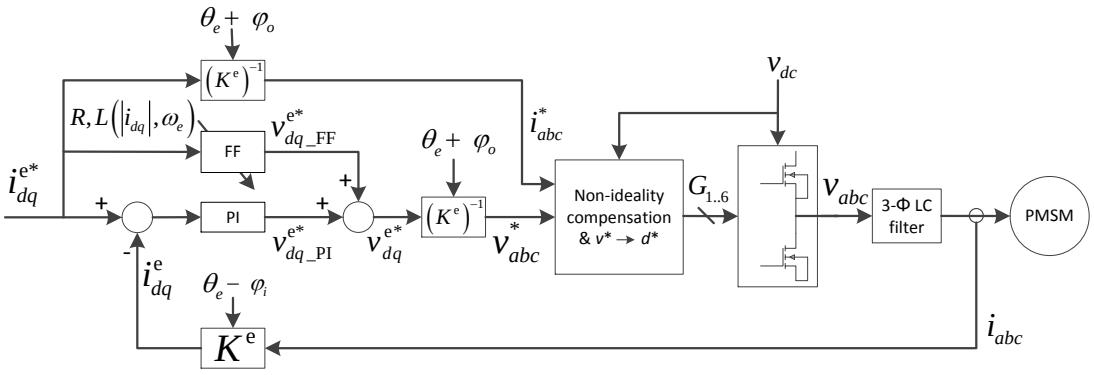

Figure B.1: Synchronous current control for control effort minimization.

The parameter identification of the PMSM stator parameters used in this study is based on a novel off-line statistical measurement procedure which considers the machine parameters to be frequency dependent. The method is explained with the aid of Fig. B.1 in which current control in the synchronous reference frame is depicted. The rotor is assumed locked during the identification procedure. Given a constant current reference in the synchronous reference frame, i^{e*}_{dq}, two sources of control effort are responsible for actuation, namely the proportional and integral (PI) controller and the feed-forward (FF) compensation term. The feed-forward term represents the current-to-voltage relationship of the stator, i.e. the stator impedance. Since a surface mounted PMSM is considered the saliency is assumed one, thus $L_d = L_q = L$. The feed-forward term also includes the decoupling term. The

feed-forward term is given in (B.1).

$$\begin{aligned} v_d &= r_s i_d - \omega_e L i_q \\ v_q &= r_s i_q + \omega_e L i_d \,. \end{aligned} \tag{B.1}$$

The total reference voltage is the sum of the PI controller and the feed-forward term:

$$v_{dq}^{e*} = v_{dq\_PI}^{e} + v_{dq\_FF}^{e*} \quad . \tag{B.2}$$

The feed-forward term is updated with resistance and inductance values which are determined by an on-line optimization algorithm. In this study, a modified version of the Nelder-Mead simplex search is used in which some of the optimization parameters are adapted according to the search dimension [153]. The simplex search algorithm has been implemented to process in the background process of the DS1005 controller. The background process consists of the remaining time after all the control code has been executed in the real-time processor before the next control period starts. The cost function used in the optimization is the control effort by the PI controller, which is computed as:

$$F(v) \quad = \quad \sqrt{v_{d\_PI}^2 + v_{q\_PI}^2} \,, \tag{B.3}$$

The control effort used by the simplex search is low-pass filtered with a cut-off frequency of 0.5 Hz. After each update of the resistance and inductance terms the control effort is allowed to settle before it is sampled for the next iteration of the simplex search. When the feed-forward term has settled to the "true" resistance and inductance, ideally all of the reference voltage, v_{dq}^{e*}, is generated by the feed-forward term, $v_{dq\_FF}^{e*}$. The resistance and inductance are evaluated over the operating frequency range of interest, i.e. $0 - 400$ Hz.

For accurate parameter identification it is important that the actual three-phase voltage reference follow the reference three-phase voltage reference, hence the inclusion of the "Non-ideality compensation" block in Fig. B.1. Under- or overcompensation of the dead-time effect results in a too large or too small identified stator resistance, respectively.

The parameter identification presented here is very similar to that proposed by Mercorelli [154], but with some key differences. Instead of minimizing the control effort, his cost function for optimization minimizes the variance between the measured current and the estimated current predicted by an ARMAX model. An algebraic relation exists between the estimated ARMAX coefficients and the inductance and resistance parameters of interest. Only the estimated inductance is used in the decoupling term. He goes forth to prove that the cost function for the optimization is minimized when the difference between the feed-forward decoupling term and the actual machine coupling is minimized in a stochastic sense.

Since the proposed identification procedure is with the motor locked, only the stator impedance parameters are identified. The back-emf constant can be identified separately.

One example is to use a deterministic test by spinning the rotor to a known reference speed and turning the current control off. The measured terminal voltage with zero stator current thus corresponds to the induced voltage by the PM. Another example is to note that the sensorless control method used in this thesis estimates the back-emf directly without using the PM flux linkage parameter. Hence, the back-emf constant follows from:

$$\lambda_p = \frac{\hat{e}_q}{\hat{\omega}_r} \,. \tag{B.4}$$

B.2.2 Delay compensation

The angle used for the rotating reference is generated by integrating the reference synchronous frequency, ω_e:

$$\theta_e = \int \omega_e dt \,. \tag{B.5}$$

In transforming the synchronous reference voltage, v_{dq}^{e*}, to stationary coordinates the synchronous reference angle is compensated with an output delay compensation angle:

$$\theta_o \;\; = \;\; \theta_e + \phi_o \,, \tag{B.6}$$

where the output delay compensation angle is computed by the product of the time delay and the reference frequency:

$$\phi_o \;\; = \;\; T_o \omega_e \,. \tag{B.7}$$

Compensation of the delay in the inverter has been discussed extensively in the literature e.g. [155, 156] in order to reduce cross-coupling and improve stability. Delay in the output voltage reference results in a rotation which is ambiguous to cross-coupling. Hence, no or improper compensation of the inverter delay results in frequency dependent stator impedance parameters as identified by the simplex search.

For the parameter identification at standstill, it is only the total loop delay, T_Σ, which affects the parameter identification. At this stage, the input and output delays cannot be distinguished yet, so the input delay, ϕ_i, is assumed zero whilst the total is attributed to T_o.

After the stator impedance parameters have been identified (and other commissioning steps have been completed) it is possible to *distinguish* between the input and output delay with additional tests. With the speed control loop of the sensorless vector controlled drive set to spin at a reference frequency, ω_r^*, the reference current in the estimated reference frame required to keep the speed constant is $i_q^{\hat{r}*}$. Due to the input delay there is an error between the actual torque producing current and that in the estimated reference frame, i.e. $i_q \neq i_q^{\hat{r}*}$. The input delay, which minimizes reference current generated by the speed control loop, is then searched for. With the reference current minimized the true delay

has been identified. The constraint that the total delay has to be kept constant has to be enforced during the search. Thus, the input and output delays have to be scheduled simultaneously, using:

$$\phi_i = T_i\omega_e \tag{B.8}$$

$$\phi_o = T_\Sigma\omega_e - \phi_i\,. \tag{B.9}$$

In the drive control the transformation of stationary reference frame to rotor reference frame variables, the input delay is compensated using:

$$\hat{\theta}_{r\_in} = \hat{\theta}_r + T_i\hat{\omega}_r\,, \tag{B.10}$$

whilst the output delay is compensated in the angle used for the transformation of rotor reference frame variables to stationary reference frame variables:

$$\hat{\theta}_{r\_o} = \hat{\theta}_r + T_o\hat{\omega}_r\,. \tag{B.11}$$

The input and output transformation angles are used as inputs for a look-up table procedure which returns the trigonometric quantities required for the Park transformation matrix. In addition, the double angle trigonometric quantities are also returned by the look-up table procedure as required for the generalized force disturbance model (GDF) presented in section 3.6. Thus, the AMB control benefits by making use of the drive's software routines (with a small extension) which already generates the trigonometric quantities. By sharing computed quantities required in the control of both is another form of cooperative control by the AMB and drive.

B.2.3 Output delay characterisation

The estimated parameters $\hat{R}$, $\hat{L}$, $\hat{T}_o$, cannot be uniquely identified by the simplex search, because the optimization converges to a local minimum which is determined by the initial parameter values. Thus, the problem arises as to what output delay is the *true* delay. This can be determined by relating the output power according to the estimated resistance and the measured input power, i.e. a linear correlation should exist in the case of the true output delay.

The predicted output power according to the estimated resistance is calculated according to:

$$\hat{P}_o = \left|i_{dq}^{e*}\right|^2 \hat{R}\left(\omega_e\right)\,, \tag{B.12}$$

where $\left|i_{dq}^{e*}\right|$, is the modulus of the reference current in the synchronous reference frame. The average input power is calculated as the product of the measured average DC bus

input voltage and line current:

$$P_i = I_{dc} V_{dc} \,. \tag{B.13}$$

Figs. B.2a and B.2b, show the resistance and inductance as identified by the proposed parameter identification scheme for various output delays used in the delay compensation. For determining the correct output delay a coarse frequency domain is used. With the underestimated output delay of $0.5 \times \mathrm{T_s}$ the resistance first increases and then decreases according to the frequency, which does not have a physical explanation. With the output delay greater than $1 \times \mathrm{T_s}$ the resistance is monotonically increasing, which is physically plausible.

The estimated output power vs. measured input power is shown in Fig. B.3 from which it can be deduced that the true delay is $1.25 \times \mathrm{T_s}$, since it has the closest linear relationship.

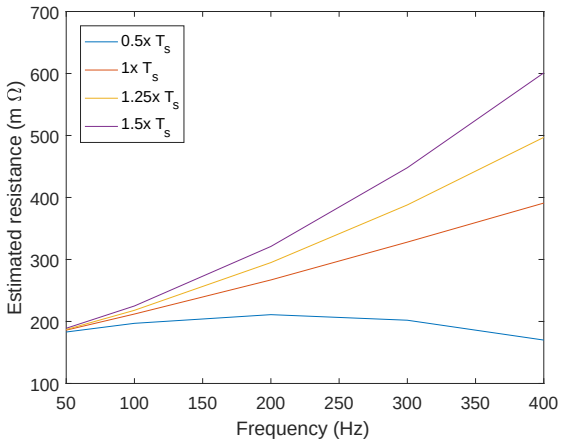

(a) Estimated resistance.

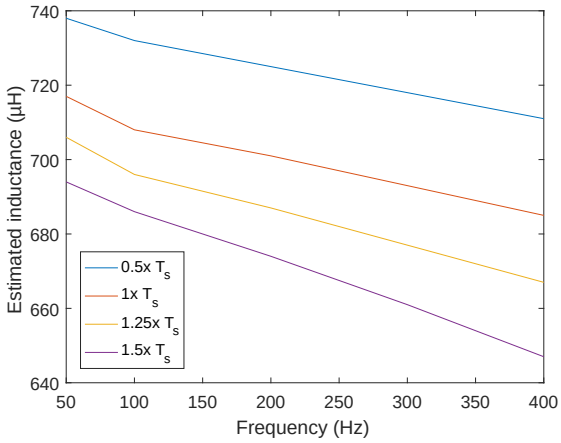

(b) Estimated inductance.

Figure B.2: Estimated parameter as a function of excitation frequency and output delay.

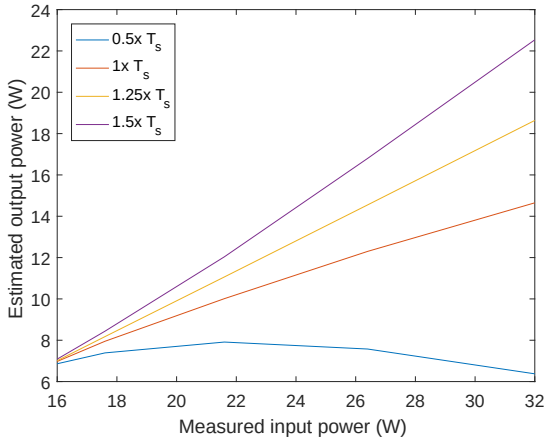

Figure B.3: Estimated output power vs. measured input power.

B.2.4 Identified stator parameter results

With the correct output delay compensation determined in the previous section, the stator parameter identification is repeated over a finer frequency and current domain. Figs. B.4a and B.4b, show the identified resistance and inductance for the output delay of $1.25 \times \mathrm{T_s}$ for a frequency range of $0 - 400\,\mathrm{Hz}$ and a current range of $0.5 - 16\,\mathrm{A}$. From the figures, it can be deduced that the resistance is primarily a function of the frequency and the inductance is primarily a function of the current.

In order to use the measured resistance and inductance in the sensorless control a polynomial fit of each measurement is conducted. The resistance's current dependence is averaged out and fitted as a function of frequency only. In a similar manner, the inductance's dependence on the frequency is averaged out and fitted as a function of the current only.

The result for the fit of the resistance and inductance is as shown in Fig. B.5, along with the equations of the fitted polynomials.

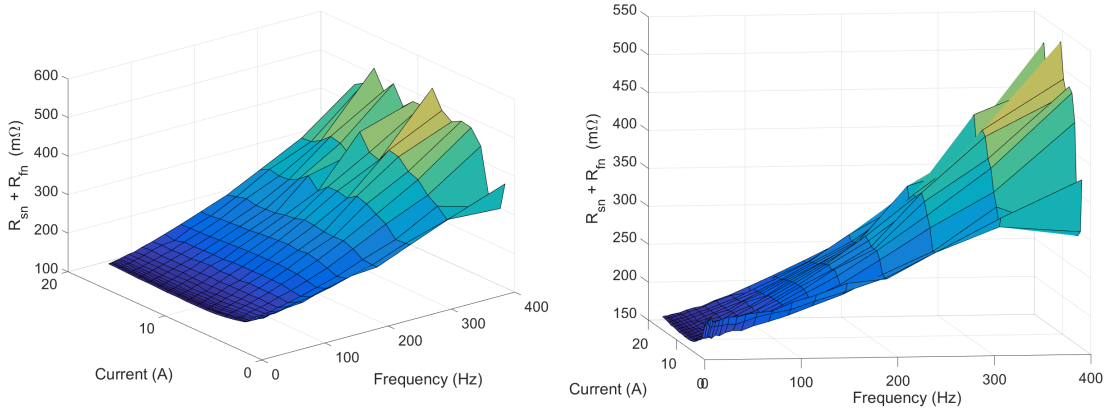

(a) Estimated resistance.

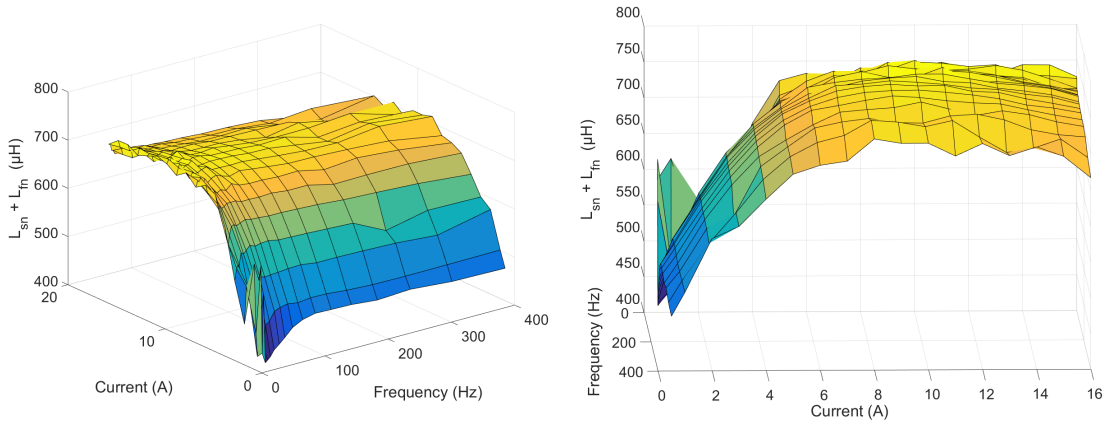

(b) Estimated inductance.

Figure B.4: Frequency and current dependence of estimated stator parameters.

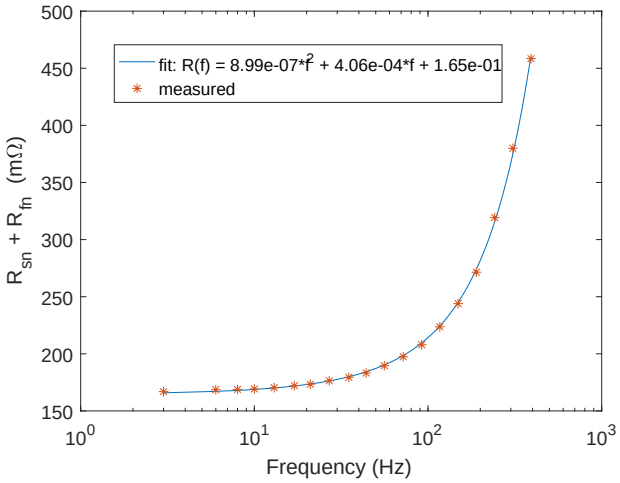

(a) Fit of resistance as a function of frequency.

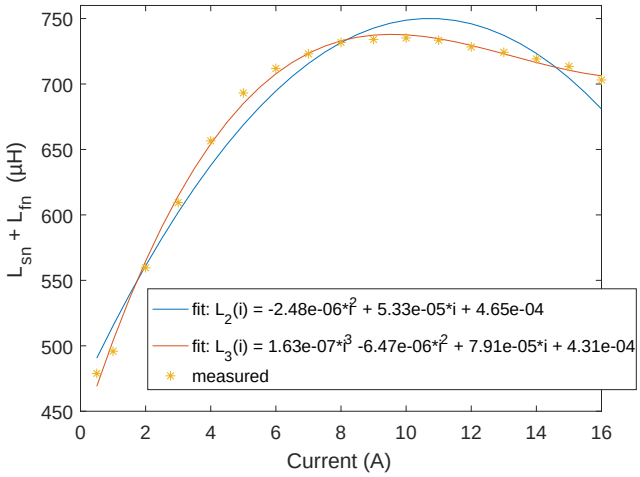

(b) Fit of inductance as a function of current.

Figure B.5: Fit result of identified PMSM stator parameters.

B.2.5 Other PMSM parameters

The nominal PMSM parameters are presented in table B.1. The rotor inertia is from the rotor design presented in [78].

Table B.1: PMSM parameters.

Parameter description	Symbol	Value
#Pole pairs	z_p	1
Nominal stator inductance	L_d	500×10^{-6} H
Stator resistance	r_s	$0.172\,\Omega$
Permanent magnet flux linkage	λ_p	46.4×10^{-3} Wb.t
Rotor polar moment of inertia	J_p	$0.107\,\text{kg.m}^2$
Viscous friction loss coefficient[1]	B	$87 \times 10^{-6}\,\text{N.m.s.rad}^{-1}$

[1] Without vacuum in the enclosure.

Appendix C

AMB parameter identification

C.1 Axial AMB calibration

C.1.1 Sensor gain calibration

The eddy current sensor gain has to be calibrated for the specific material unto which the eddy probe senses. For the axial degree of freedom, the eddy current sensor gain is fitted by comparing the measured position to that predicted according to the analytical solution for free-fall. Thus, the rotor is suspended with some preliminary control and then dropped. Due to the non-negligible magnetization of the axial AMB and induced eddy currents in the thrust disc the initial force, after setting the axial AMB current to zero, is not zero and is unknown. Fortunately, the rotor bounces on the axial retainer bearing and on the second drop the magnetization and eddy currents have decayed and the residual force is close to that of gravity alone. The analytical solution for free fall is:

$$z\left(t\right) = z_{t0} - \frac{1}{2} g \left(t - t_0\right)^2 \,, \tag{C.1}$$

where t_0, is the time of peak amplitude and where the initial velocity is equal to zero.

Fig. C.1, shows the comparison of the measured and predicted drop response. It turns out that the axial sensor gain required to match the measured response is close to unity, i.e. 0.96. The calibrated axial sensor gain is thus $7.55\,\mathrm{mV}/\mu\mathrm{m}$. This is because the material of the bolt which holds the thrust disc in place, unto which the eddy current sensor senses, has characteristics similar to that of 4140 steel, which is the material for which the SKF CMSS65 series 5mm sensor was calibrated for [77].

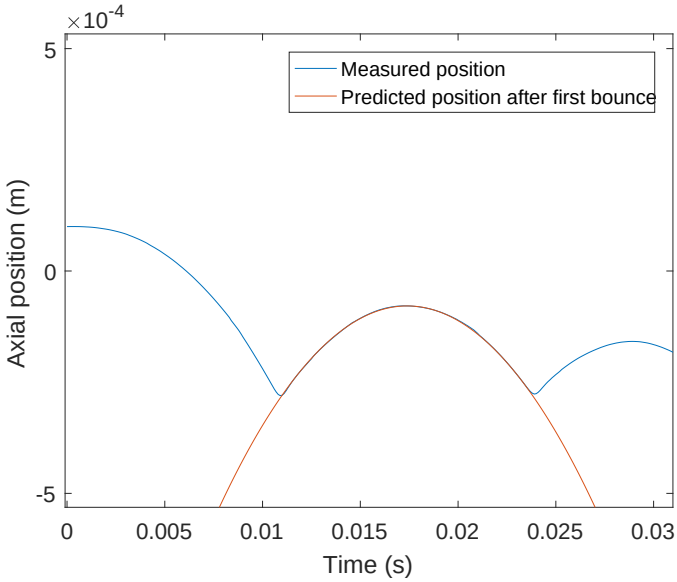

Figure C.1: Axial rotor drop for sensor calibration.

C.1.2 AMB force function identification

The AMB force function parameters are used in the inverse function to derive a current reference for the amplifiers from a force reference. Since the disturbance force is known, i.e. gravity, the force function parameters of the axial AMB can be fitted by using the sum of squared difference of the analytically predicted axial force and the known force. Sufficient equations are generated by sweeping the rotor from bottom to top. The equation describing the axial force is given by:

$$F_z = K_{Ft} \left(L_{zt} \left(z \right) i_t \right)^2 - K_{Fb} \left(L_b \left(z \right) i_b \right)^2 \,, \tag{C.2}$$

where the subscripts, t, and, b, denote the top and bottom AMBs, respectively. The force gain coefficients are given by:

$$K_{Ft/b} = \frac{1}{2} K_{Lt/b} \,. \tag{C.3}$$

The inductances are given by:

$$L \left(z \right)_{t/b} \quad = \quad \frac{1}{K_{Lt/b} \left(g - \left(z + z_{ot/b} \right) \right)} \,, \tag{C.4}$$

where g, is the nominal air-gap. z_{ot} and z_{ob} are air-gap offsets to be fitted in order to adjust the effective air-gap of the top and bottom AMBs respectively. The inductance coefficients are given by:

$$K_{Lt/b} = \frac{2}{N_{t/b}^2 \mu_0 A_{gt/b}} \,, \tag{C.5}$$

The output force gain coefficient is adjusted with a delta modifier, $\Delta K_{Ft/b}$:

$$K^*_{Ft/b} = K_{Ft}\,\Delta K_{Ft/b}\,, \tag{C.6}$$

in order to fit the analytical force equation to the known disturbance force, i.e. $F_z = -\mathrm{M}g$. Thus, there are two parameters per AMB pole or four parameters in total for the axial AMB which need to be fitted. For the axial AMB, it is possible to remove the bottom axial AMB since gravity is sufficient to counteract the top AMB. In this case only two parameters need to be fitted.

A Simulink® model of the axial AMB with the two unknown parameters is used. The initial unknown parameter set is: $[z_{ot},\, \Delta K_{Ft}] = [0,\, 0,\, 1,\, 1]$. The inputs to the model are the measured position and current. The "Response optimization" toolbox is used to minimize the cost function. The optimized parameter set is given by: $[z_{ot},\, \Delta K_{Ft}]^* = [135\,\mu\mathrm{m},\, 0.679]$. The fitted force function and its inputs are as shown in Fig. C.2.

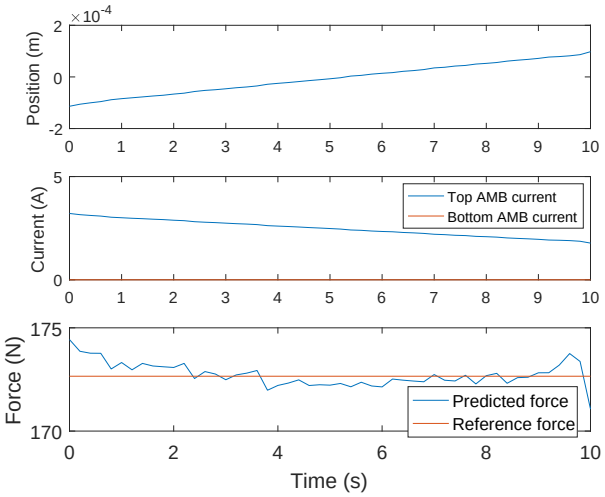

Figure C.2: Force comparison for the optimized axial AMB force parameters.

C.2 Rigid rotor parameter measurement

The rotor was removed from the Fly-UPS machine and the mass was accurately measured on a precision scale. The transverse polar moment of inertia was accurately determined from an experimental bifilar pendulum setup. The rigid rotor parameters are summarized in table C.1. The geometric dimensions are as defined in Fig. 3.3.

Table C.1: Rigid rotor parameters.

Parameter description	Symbol	Value
Rotor weight	M	17.6 kg
Bearing displacement from COG	$[a,\ b]$	$[-164,\ 64.4] \times 10^{-3} m$
Sensor displacement from COG	$[c,\ d]$	$[-190,\ 95.4] \times 10^{-3} m$
Transverse moment of inertia	J_t	0.11575 kg.m^2

C.3 Radial AMB calibration

C.3.1 Sensor gain calibration

The radial AMB sensors are calibrated by suspending the rotor with a preliminary control and sweeping the rotor in the range $[-300,\ 300\,]\mu m$ and measuring the actual rotor deviation with a dial gauge. The initial sensor gain for the preliminary control is obtained by calibrating the sensor gain according to the back-up bearing clearance which is approximately in the range of $[-500,\ 500\,]\mu m$. With this initial gain, the control is stable and the rotor can be swept whilst pushing on the external dial gauge. The top and bottom AMB sensor rings are made of the same material and the sensor gains are thus assumed equal. The calibrated radial sensor gain is 10.31 mV/μm.

C.3.2 AMB force function parameter identification

The radial AMBs were modelled using a 3D FEM model in COMSOL® and a sweep was performed on the position and bias current level in one electromagnet[1]. The modelled force function from the FEM solution was compared to the measured force. The measured force was determined by connecting an external rod to the rotor with a cable, force gauge and cable screw. The current was measured for various external forces applied by adjusting the cable tension with the cable screw. The required current to compensate the external force was compared to that of the modelled AMB. From the comparison, it was clear that the material characteristics used for the radial AMB laminations differed significantly to that which was specified during the design. The material characteristics were obtained by characterising the B-H curve of some leftover laminations used for the construction of the radial AMB. After incorporating the measured material characteristic into the FEM model the measured force function still had a reasonable amount of deviation compared to the modelled force. Other possible causes of this deviation are construction imperfections

[1]The simulation model is included in appendix E.5.

in the air-gaps and the presence of magnetic hysteresis in the B-H characteristic [157] which is not accounted for in the FEM model.

Due to the difference of the designed radial AMB to the physically constructed radial AMB, an off-line force function characterisation was opted for instead of deriving the parameters from the FEM model. The method of identifying the force function parameters is based on exciting the rotor with a pulse force on two opposing AMBs. The remaining AMBs in the particular plane of interest is switched off, whilst the AMBs in the plane orthogonal to the excited plane is kept on. The pulse measurement is repeated with different force offsets of the two opposing AMBs. The principle of the pulse excitation is that the force may be deduced from the free acceleration during the pulse period. Hence, the AMB parameters can be fitted to match the response due to the force. The AMB parameters which are identified are the air-gap size and the output gain coefficient per AMB pole-pair.

The test could be performed by exciting all of the AMBs individually in turn, but the reason why this is not preferred is that in order to excite the full current range a relatively large force is applied near the peak current. This has two disadvantages. The first is that the bending modes of the rotor are excited by the large force. The second reason is that due to the large force at peak excitation current a large acceleration is produced such that the *period* in which the rotor is excited from rest until it reaches the desired displacement is relatively short. Thus, the rotor movement is sampled in relatively few sample periods which causes uncertainty in the force produced due to noise which is further amplified by numerical differentiation. The solution to the problem encountered caused by the two combined factors is to limit the net excitation force.

By pulsing two opposing AMBs, with an offset force between each, the net excitation force may be limited by decreasing the offset. This prevents excessive excitation of the flexible modes of the rotor, which would obscure the acceleration of the rigid component of the rotor. A smaller net differential force also results in a longer excitation period (more samples) which results in less uncertainty in the rotor acceleration. The opposing AMBs are excited at different offset currents and rotor positions in order for the function domain of interest to be excited adequately. The rotor positions are varied with the magnetic centre taken as the midpoint for the stepped rotor range.

The external force due to the permanent magnet is accounted for by two means. The first is to rotate the rotor to an angle such that the disturbance force in the excitation plane of interest is minimized and symmetrical about the rotor position midpoint. The second means is to measure the rotor response when all of the AMBs are switched off and use the resulting response data to fit an external force model. This external force model is then included in the model which is used to fit the AMB force function parameters by varying the parameters such that the model's rotor response corresponds to the measured rotor response. The rigid rotor and AMB force functions are modelled in Simulink® and the parameters are optimized using the Response Optimization® tool in Simulink®.

Fig. C.3, depicts the excitation of the AMB at incremental reference current pulses and measured rotor positions. The period required for the control to reposition the rotor after each pulsed excitation has been cut out from the measurement for post-processing in the parameter fit procedure. The current pulse references are slightly low pass filtered so that eddy current effects and high bending mode frequencies may be neglected in the model which is used to fit the AMB parameters.

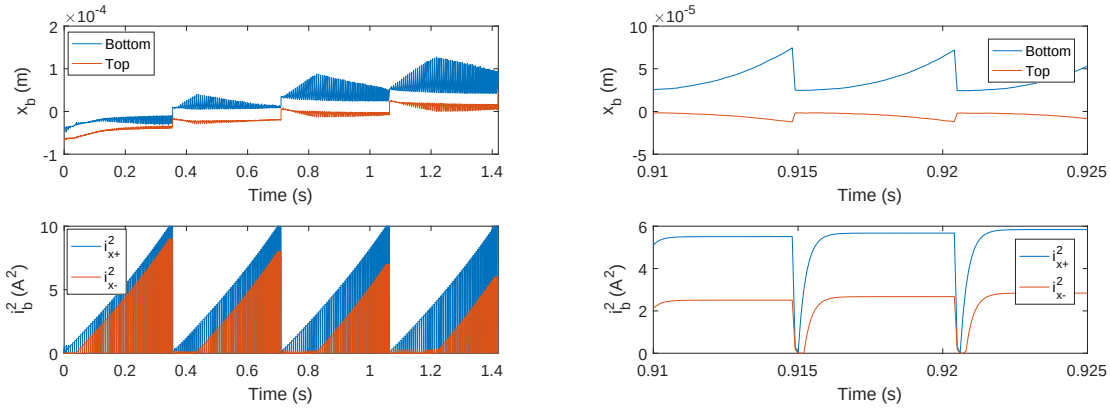

(a) Full range excitation for bottom AMB.

(b) Zoom of bottom AMB excitation.

Figure C.3: Example AMB excitation and response.

The model used for the parameter identification procedure is depicted in Fig. C.4. The reference current and measured position are inputs from which the model computes the AMB force and the resulting rotor position. The Euclidean norm is chosen as the cost function.

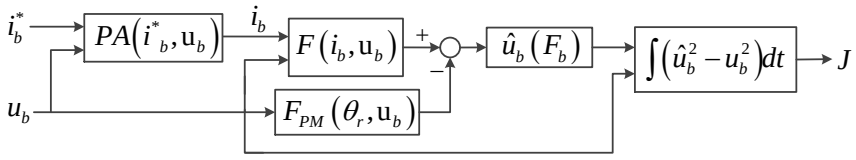

Figure C.4: AMB parameter identification model.

The numerical values of the identified AMB force function parameters are listed in table C.2.

Table C.2: Identified AMB parameters via pulsed excitation.

(a) XZ plane.

AMB parameter	Value
u_{x2+}	689.3 μm
u_{x2-}	714.6 μm
u_{x1+}	725.7 μm
u_{x1-}	748.9 μm
ΔX_2+	1.192
ΔX_2-	1.263
ΔX_1+	1.225
ΔX_1-	1.268

(b) YZ plane.

AMB parameter	Value
u_{y2+}	678.8 μm
u_{y2-}	689.2 μm
u_{y1+}	709.3 μm
u_{y1-}	712.8 μm
ΔY_2+	1.141
ΔY_2-	1.218
ΔY_1+	1.199
ΔY_1-	1.209

C.4 Flexible modes identification

C.4.1 Flexible modes of the rotor

In order to insure that the rotor control remains stable the flexible modes of the rotor needs to be accounted for. Since the application is for a flywheel and little external vibration excitation sources are expected and the operating speed is below the first bending mode, the bending mode does not require active damping via the control. In order to prevent measurement noise and control loop set point changes to excite the bending mode a notch filter is added.

Fig. C.5, depicts the frequency sweep to identify the bending mode frequencies of the rotor. A force reference of 10 N in bearing coordinates is used as an excitation source. The low-frequency disturbance response, in the $0 - 200$ Hz range, is due to the rigid modes. The first rotor bending mode is located at 737 Hz, which is close to the value predicted by rotor design verification performed in DyRoBeS® [78]. The next bending mode frequencies are located at 1336 Hz, 1478 Hz and 1970 Hz.

The higher bending mode frequency exhibit a high degree of damping and does not require further filtering. Due to the asymmetry of the rotor, the deflection due to the first bending mode of the rotor mainly resides on the bottom side of the rotor and it is only necessary to add the notch filter to the bottom sensors. Note that the measurement is performed with a notch filter already present in the control loop with a centre frequency of 737 Hz and a quality factor of 6. The position sensor signals displayed in Fig. C.5, is at the filter input and is thus unfiltered.

Fig. C.6, illustrates the mode splitting of the first bending mode which is dependent on the rotational speed. The bending frequency fit result is:

$$f_b = 742 - 0.251 f_{rot}\,\text{Hz} \tag{C.7}$$

$$f_f = 742 + 0.393 f_{rot}\,\text{Hz}\,, \tag{C.8}$$

where, f_b and f_f are the backward and forward whirling bending frequencies, respectively. At a maximum rotational speed of 330 Hz, the bending frequency resonant modes are located at 659, 871 Hz. From the frequency sweep response, a non-linear behaviour of the bending frequency may be observed. The excitation source for the frequency swept the frequency from a lower frequency to a higher frequency. Near the vicinity of the centre frequency in each case, a jump may be observed to the left-hand side of the response envelope peak and a gradual decay to the right-hand side. At higher operating speeds, the centre frequency of the split modes is too far from the centre frequency of the notch filter used. Thus, it is recommended to use two notch filters centred at the half-speed frequency of each split mode, i.e. 704, 806 Hz, with the same quality factor.

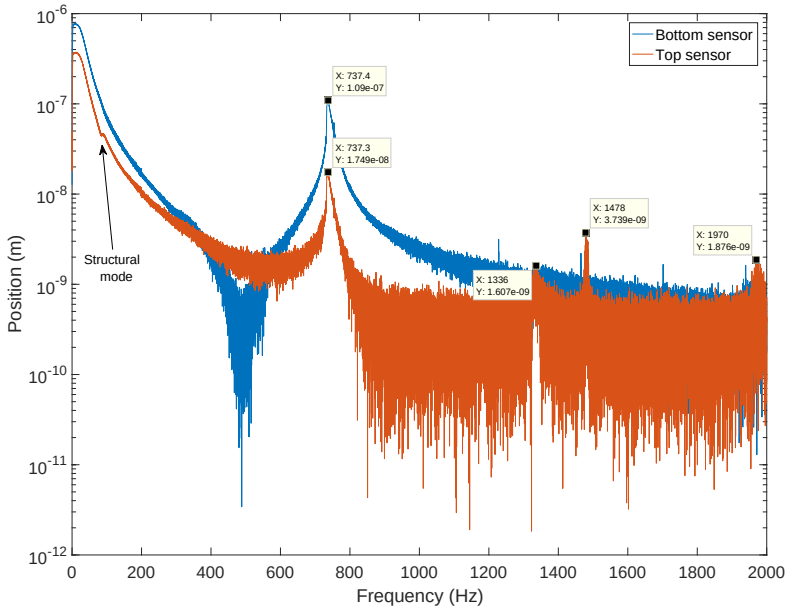

Figure C.5: Frequency sweep to identify the first bending mode.

A slight bump, with the structural mode being suspected as responsible, is apparent near 90 Hz in the top AMB sensor. This is confirmed in the following section.

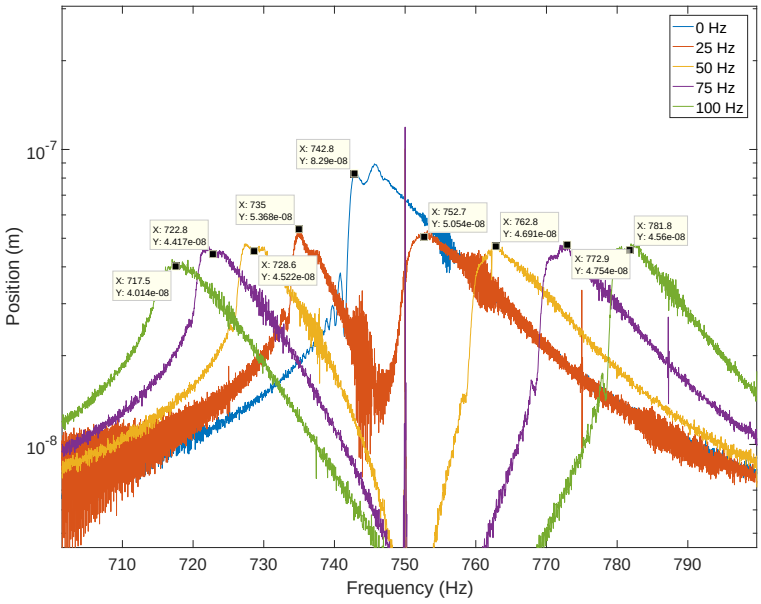

Figure C.6: Mode splitting of bending mode.

C.4.2 Flexible modes of the supporting frame

The measured sensitivity of the plant does not correspond to the system modelled with rigid rotor and rigid frame. Upon further investigation it has been observed that the support frame exhibits its own flexible mode. This has been confirmed by resting the rotor in place on the axial back-up bearing so that it does not touch the radial bearings with the aid of the control. After the rotor rests on the axial bearing the controllers are switched off by setting the controller gains to zero. A residual constant current is kept in the radial bearings to counteract the magnetic pull of the permanent magnet of the PMSM which would otherwise dislocate the rotor from the vertical standing position. An impulse force is applied to the exterior housing with a rubber mallet and the top position signal recorded as displayed in Fig. C.7. Since the rotor is assumed stationary the recorded variation of the eddy current position sensor signals are thus that of the frame's movement with respect to the stationary rotor. The base is firmly mounted and the position signals of the bottom AMB are relatively undisturbed by the impulse. Most of the signal variation is observed towards the top of the housing, which agrees with the notion that the structure of the housing can be compared to that of a cantilever beam rigidly mounted to ground. Previous authors have also noted that insufficient stiffness of the top side of the frame for a vertically mounted AMB is problematic [158]. From the signal period, the structural mode frequency is calculated as 90.9 Hz.

If the rotor is instead axially pulled towards the top AMB and the measurement is repeated the recorded vibration now has the largest variation towards the bottom AMB as shown in Fig. C.8. This is because the rotor now moves rigidly connected with the top modular

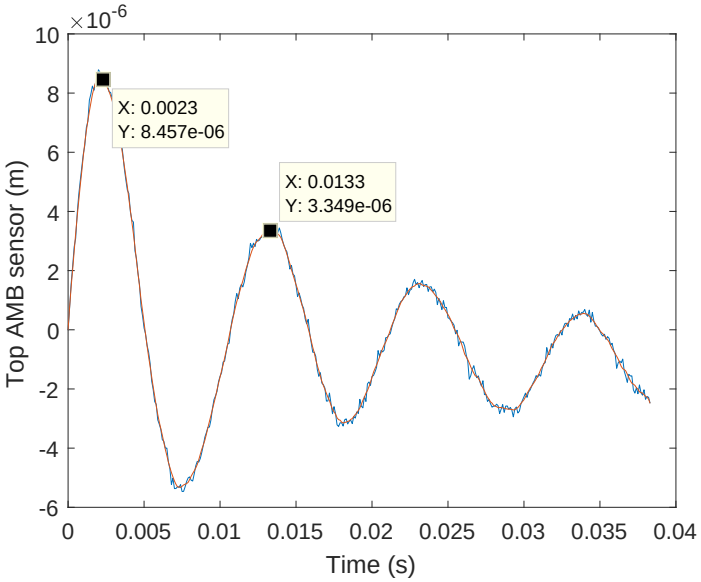

Figure C.7: Structural vibration upon impulse with rotor grounded.

section, hence it has little variation with respect to the top sensors, but the movement is now observed with respect to the bottom sensors. The structural mode frequency for the rotor pulled to the top is 75.2 Hz. Due to the contact of the rotor to the top AMB, the effective structural inertia is increased and a lower structural mode frequency results. Since in normal operation the rotor is free from the top AMB the true structural mode frequency is 90.9 Hz. This confirms that the slight bump near 90 Hz in the bending mode frequency sweep in Fig. C.5, is indeed due to the structural mode.

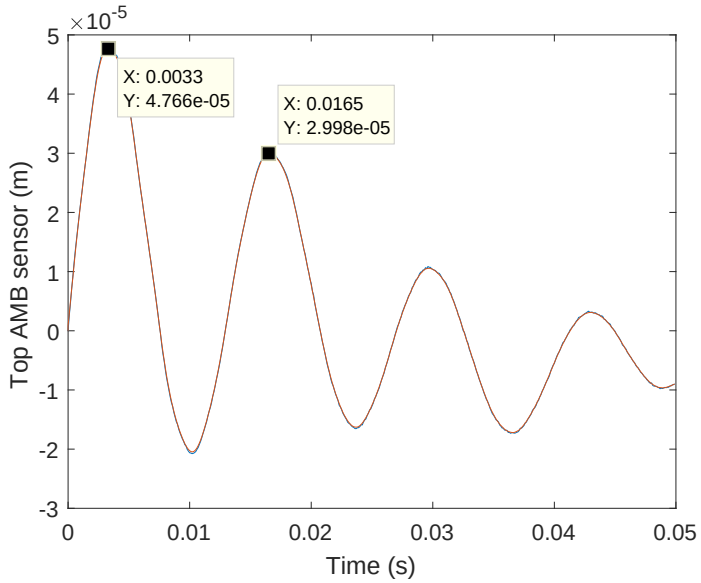

Figure C.8: Structural vibration upon impulse with rotor pulled to the top.

Appendix D

AMB power amplifier design

D.1 Power amplifier requirement

After a root cause analysis of certain problems within the flywheel system was conducted, certain flaws and shortcomings of the off-the-shelf power amplifier selected in the design[1] of the flywheel energy system were discovered. Fig. D.1, compares the current response at approximately 10 Hz and 100 Hz. The offset and magnitude difference in the current reference and measured load current is not of immediate concern since the current reference is actually an analogue voltage proportional to the reference current measured at the reference input pins of the power amplifier. The unit of the measured load current is correct. The point of concern is the large degree of distortion at higher frequencies and the larger than expected phase shift in the load current. This reveals that the power amplifier bandwidth is indeed not 2.5 kHz as were assumed by [77].

The current control bandwidth and distortion could be remedied to an extent by changing an operational amplifier gain resistor inside the power amplifier. A third shortcoming of the power amplifiers, namely that of switching noise, could not be remedied so easily. Each of the power amplifiers has its own PWM clock source of approximately, 36 kHz, which are not synchronized with each other due to the lack of a synchronization input pin to the power amplifiers. Synchronization allows to reduce the effect of switching noise by allowing the ADCs in the system, especially those of the eddy current position sensors, to sample signals within a quiet time window when no switching occurs.

The connector type to and from the power amplifier is in the form of terminal blocks. Hence, there is an inherent gap in the shielding of the power cable in order to connect to the power amplifier connectors. The cable shielding was earthed by "pig tails" which do not provide the lowest impedance path of the noisy currents redirected by the shield. Thus, the shield is no longer an optimal "ground plane" and increases radiated and conducted noise.

[1] See [77] for the design of the electrical system of the flywheel system.

Another problem of the power amplifiers was the shared common ground of the input reference signal and the power amplifier's power ground. This creates a ground loop which allows switching noise to couple with low power analogue conditioning circuitry inside the amplifier. It also poses a danger to the (costly) dSPACE controller, since in the event that a short circuit in one of the power amplifiers occurs the power amplifier is not isolated from the controller and high currents may find its way into the controller, due to the shared common ground, with possible damage which may result.

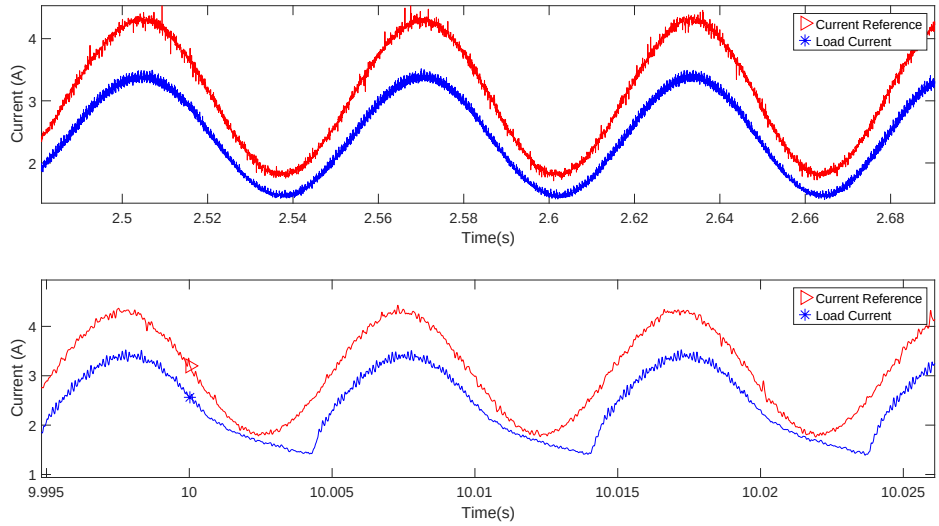

Figure D.1: Off-the-shelf DC servo drive current response.

In order to successfully exploit non-idealities within the system, it is important that the power amplifiers should not have a current distortion and that the effect of the switching noise is minimized. Thus, due to the numerous shortcomings of the power amplifier previously chosen for the system, it was decided that a new power amplifier be designed.

D.2 Power amplifiers for AMBs

Before presenting the chosen topology for the AMB power amplifier a brief literature overview of power amplifiers for AMBs are presented. The output current of the AMB is a DC current, which would lead one to conclude that the AMB power amplifier is a DC-DC converter. Due to the bandwidth requirements of the amplifier in order to track a reference in order to reject rotor disturbances, it is more appropriate to consider the AMB power amplifier as a DC-AC inverter. The inverter is considered in many applications, especially in the motor control literature. The literature considering power amplifier design for AMBs is more specialized and restricted to a large extent to ISMB conference proceedings.

The majority of the power amplifiers presented in the AMB literature are of the hard-switched type with current control. Early power amplifiers for AMBs were linear amplifiers

[159]. Switching amplifiers are preferred over linear amplifiers due to improved efficiency.

The current controlled amplifier is generally chosen due to the linearised relationship between current and force. The current control loop also facilitates implementation and commissioning due to inherent over-current protection by the current control loop. Voltage controlled power amplifiers may also incorporate other supervisory over-current protection mechanisms, but comes as an afterthought in the control loop design.

Power amplifiers which control the output voltage, in turn, has the advantage of improved rotor disturbance response since a rotor disturbance induces a current such as to dampen the disturbance. The voltage controlled amplifier receives power due to the disturbance and thus dampens the disturbance. In the case of a current controlled amplifier, the amplifier appears as a current source and thus an open circuit and no power is absorbed by the amplifier due to a disturbance.

A type of a hybrid between a current and voltage controlled amplifier is presented by Zhang *et al.* [160] and named the amplifier a synchronous three-level PWM amplifier. It performs current control at the start of a control cycle synchronous to the position controller which computed the required reference current. Upon reaching the desired reference current the duty cycle is kept constant and the current controller is essentially turned into a voltage controller. The controller thus achieves a current control characteristic with the advantage of improved position disturbance response by acting as a voltage controlled amplifier for the rest of the position control period.

Another type of amplifier which tries to further absorb the effect of disturbances such as air-gap variation and eddy currents is the transpermeance amplifier which controls the flux in the air-gap [161]. This was typically performed by means of Hall-effect sensors which senses the flux in the air-gap. Zingerli and Kolar [162] present a controller based on a flux estimator. The position and force control is greatly decoupled and a much more linear actuator result which accounts for eddy currents, magnetization, and stray flux.

Regardless of the type of state variable or signal which is controlled, e.g. current, voltage or flux, the switching amplifier may be further categorized by the type of switching law or modulation method which is employed. The switching law is typically either of the PWM or hysteresis control type. Hysteresis current controllers were of interest due to the simple control law which switches the transistor state given that a control variable is on the boundary of exiting an hysteresis window. The hysteresis current controllers have very good dynamic performance but at the cost of increased (and variable) switching frequencies. Newer research into hysteresis control aims to limit the switching frequency whilst maintaining a high dynamic response [163]. It has been found that by replacing the constant control band (hysteresis window) by a pair of parabolic control band carriers that a constant switching frequency results whilst maintaining the fast dynamic response. The type of control is known as parabolic current control (PCC) [164].

The response of PWM amplifiers are more linear and is easier to analyse. PWM amplifiers

also have the advantage that they may be synchronized, which is generally not possible in the case of hysteresis amplifiers.

D.3 Power amplifier topology justification

D.3.1 Previous approaches on reducing dv/dt

An investigation of the EMI produced by a hard-switching power amplifier in an AMB system is presented by Mo *et al.* [165]. Their analyses account for the parasitic inductance and capacitance of the PCB using a reduced number of lumped circuit elements. They compared the noise predicted from the simulation based on the lumped parameter power amplifier model with measured noise.

Hard-switching increases the amount of conducted and radiated noise. In the case of long cables, it has been shown that reflections also occur since the cable act as a transmission line. Output line filters are bulky and costly. Kumar *et al.* [166] show that a dynamic termination circuit improves the voltage overshoot whilst maintaining good efficiency. The circuit that Kumar *et al.* used is in the motor drives literature better known as a dv/dt filter [167] and is depicted in Fig. D.2 for a single half-bridge. A mirrored image of the half-bridge and filter is implied to the right-hand side of the AMB' s load inductance to complete the single-phase inverter or H-bridge.

The difference between a dv/dt and a line filter is in the relationship between the filter cut-off frequency and switching frequency. Line filters have a cut-off frequency far below the switching frequency, typically at least a decade lower. The cut-off frequency of dv/dt filters is much higher than the switching frequency. The purpose of a dv/dt filter is thus as the name implies to only limit the slope of the voltage pulse applied by the inverter and not to suppress the carrier as with a line filter. The aim of the resonant inductance, L_r, and capacitor, C_r, is to act as an LC low-pass filter. Since the cut-off frequency is much higher than the switching frequency the inductance and capacitor would resonate were it not for the addition of the clamping diodes, $D_{1,2}$, which limits the voltage overshoot that the capacitor would have experienced. This comes at the expense of circulating current in the resonant inductance and clamping diode which is damped by the addition of resistors, $R_{1,2}$. The resonant inductance and capacitor parameter values are much smaller compared to that of the line filter. Hence, the filter components are much smaller and lower in cost in comparison.

As pointed out by Habetler *et al.* [167] another means of reducing the high dv/dt is by means of soft-switching. It is noteworthy to mention that soft-switching inverters for motor drives have been given considerable attention in literate compared to only a few examples for AMBs [168, 169, 170]. Hung *et al.* presented a feedback linearisation control with a three-mode variable structure control (aka sliding mode control) which included

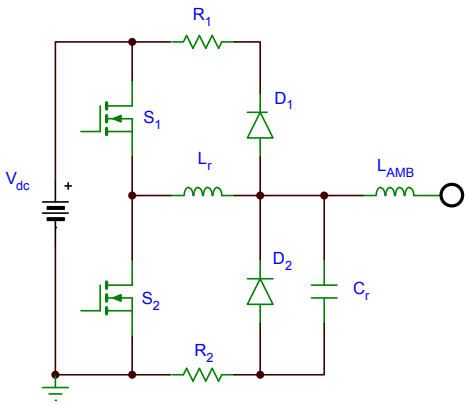

Figure D.2: Passive dv/dt filter.

the presentation of a resonant DC-link inverter as shown in Fig. D.3. The averaged output voltage is obtained by means of pulse-density modulation. The inverter achieves zero voltage switching of the H-bridge switches. The DC-link inductor gives the circuit a boost converter characteristic which allows for an increased load current slew rate when required. Hence, a higher force slew rate is possible. The disadvantage of the presented inverter is that the modulation scheme does not allow for synchronization to an external clock source due to the variable switching frequency.

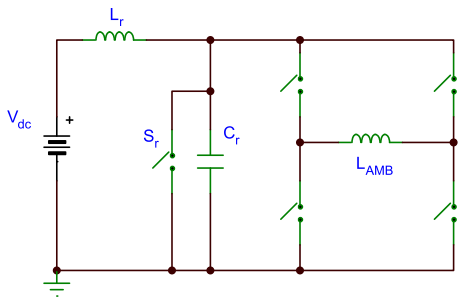

Figure D.3: Resonant DC link inverter.

It is possible to modify the resonant DC link inverter so that it achieves PWM capability as shown by Krogemann [171], which would allow synchronization. Another class of soft-switching inverters which inherently has PWM capability is that of the so-called auxiliary resonant commuted pole inverter (ARCPI) [172], which is depicted in Fig. D.4. The ARCPI achieves zero voltage turn-on of the main switch with the aid of an auxiliary switch which itself has zero current switching. Turn on of the main switch is delayed until the auxiliary switch cycle is completed. Thus, the main switch pulses are still generated with PWM. The ARCP inverter topology allows for easier stacking of the soft switching cell in order to achieve a multi-level inverter topology which has higher voltage capability.

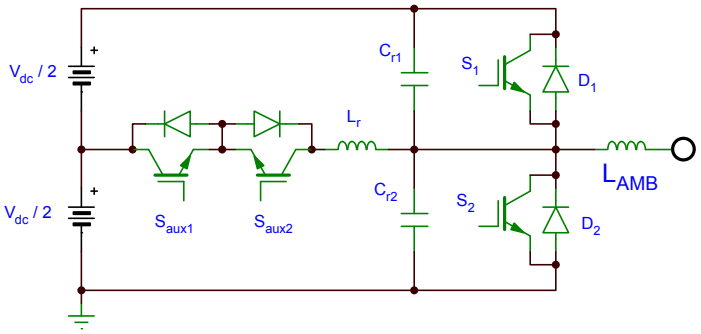

Figure D.4: Auxiliary resonant commuted pole inverter.

D.3.2 Proposed topology

The power amplifier topology proposed for the AMB is shown in Fig. D.5. Only a half-bridge is depicted and a mirrored image is implied for the right-hand side of the circuit. The operation of the inverter is related to that of the ARCP inverter. Although the circuit at first may appear complicated due to the numerous circuit elements, its operation is actually quite simple. The circuit consists of an inner H-bridge with MOSFETs, M_{1-4}, which is chosen with a low on-resistance to minimize conduction losses during the main PWM period. Auxiliary switches, M_{aux1-4}, have parameter characteristics such as to minimize the switching losses instead. The auxiliary switches are intended to carry a load current only during the dead-time period.

Considering the half-bridge, soft turn-on of the main switching transistors, $M_{1,2}$, is achieved with the aid of auxiliary switches, $M_{aux1,2}$, and resonant inductors, $L_{r1,2}$, and capacitors, $C_{r1,2}$. The resonant capacitors may not be required as explicit components, since the parasitic capacitance of the main switching transistors, $M_{1,2}$, are sufficient.

The circuit operation is explained as follows. In order to achieve zero voltage turn-on for M_1, M_2 is turned off first by means of hard-switching. After a fixed dead-time period, M_1, is turned on. The auxiliary transistor switching occurs within the dead-time period. The PWM pulse pattern for the main switches is unchanged and PWM may thus be used. The drain-source voltage of M_2 upon turn-off does not change immediately due to capacitance, $C_{r1,2}$. Two possible cases follow:

Case A: Negative load current The resonant capacitance is charged by the load current which can be approximated as a current source. That is, C_{r2}, is charged and, C_{r1}, is discharged. Were the auxiliary switches not present, the load current magnitude would determine if the dis/charging cycle of $C_{r1,2}$ is completed before the main switch, M_1, is turned on. The auxiliary circuit is thus required to guarantee that ZVS is achieved.

Case B: Positive load current The anti-parallel diode of transistor, M_2, is forward biased and the resonant capacitance voltage does not charge. Once again, the auxil-

iary circuit is required to charge the parasitic capacitance before M_1 may be turned on with ZVS.

In order to achieve zero voltage turn-on of M_1, the auxiliary switch, M_{aux1}, is turned on immediately following turn-off of M_2. The MOSFET output capacitance is charged via resonant inductor, L_{r1}. The resonant inductor is sized such that its peak current exceeds the maximum load current. At time, t_1, when the resonant inductor current exceeds the load current the body diode of switch, M_1, becomes forward biased and the surplus resonant inductor current freewheels via loop $M_{aux1} - L_{r1} - M_1$. After the dead-time period has elapsed, M_1, is turned on with essentially zero voltage turn-on, because its freewheeling diode is forward biased. After M_1 has been turned on, the auxiliary switch M_{aux1} is turned off hard. The auxiliary diode, D_{aux1}, becomes forward biased and the energy stored in the resonant inductor, L_{r1}, is returned to the DC bus, via loop $D_{aux1} - L_{r1} - M_1 - V_{dc}$.

The auxiliary switch has very little turn-on loss due to zero current switching (ZCS) and little turn-off loss since it has been selected for optimized switching characteristics. The inverter output node is shielded from the hard-switching transient of the auxiliary switches by the resonant inductors. Also, the EMI of the auxiliary switch's hard turn-off is limited because its own parasitic capacitance is charged by an inductor which essentially acts as a current source.

Hard turn-off of the body diode is one of the main sources of EMI in a hard-switching inverter, therefore the auxiliary diode has to be of a type which has no reverse recovery, such as a Schottky diode. The auxiliary diode is essentially in parallel with the body diode of the corresponding main switch, e.g. D_{aux1} is in parallel with the body diode of M_2. Thus, when the load current is positive and M_1 turns off the body diode of M_2 is forward biased and it has to be assumed that the parallel auxiliary diode is also forward biased. With the hard turn-on of the auxiliary switch, M_{aux1}, the auxiliary diode does not experience reverse recovery and the reverse recovery of the main switch, M_2, is soft due to the limited di/dt of the reverse recovery due to the resonant inductor.

D.3.2.1 Proposed topology advantages

Compared to the passive dv/dt filter, where the freewheeling current is dissipated, the resonant inverter is *more efficient*, because some of the energy in the resonant inductor is recovered. Indeed the proposed resonant inverter is obtained by reusing and rearranging the components of the passive dv/dt filter so as to make it active. A small current loop is achieved for the resonant inductor charge-discharge cycle by placing the auxiliary components in close proximity to the main switching cell.

The auxiliary switching legs are effectively in *parallel* to the power amplifier and a smaller resonant current loop is possible compared to adding a dv/dt filter in *series* to the output

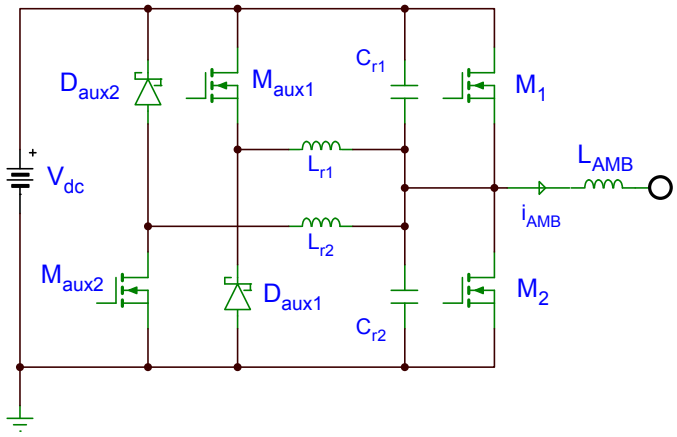

Figure D.5: Half-bridge with auxiliary switches.

of a hard-switching inverter. Thus, the proposed topology achieves lower EMI compared to the passive dv/dt filter.

In order to limit the circulating current amplitude and limit losses in the passive dv/dt filter the inductance of resonant inductor has to be increased. Since the resonant current circulates only for a limited time during the inverter dead-time, a larger current amplitude is allowed and the inductance of the resonant inductor of the active auxiliary leg is therefore smaller. Hence, the inductor of the proposed topology is smaller in size compared to the inductor for the passive dv/dt filter.

D.3.2.2 Future iteration of proposed topology

If the body diode of the switching elements in the inverter did not have reverse recovery the inverter topology may be simplified. In the case where the body diode has reverse recovery two resonant inductors have to be used so that the top and bottom switches of the auxiliary half-bridge are not directly connected. With recent developments with Silicon carbide FETs and GaN HEMTs such a topology is indeed possible. Due to the superior switching characteristics of GaN HEMTs the auxiliary switching losses may be further reduced. The GaN HEMT's on-state resistance is also not that far behind that of Silicon MOSFETs. Some GaN devices come in small packages and may be easily paralleled in the same footprint size as a counterpart Silicon MOSFET, thereby reducing the on-state resistance. A future iteration of the proposed power amplifier topology is thus depicted as in Fig. D.6. The auxiliary leg is no longer required for soft reverse recovery of the main switches since the main switches also do not have reverse recovery. The purpose of the auxiliary leg is now solely for limiting dv/dt of the inverter output node. The Schottky diodes in parallel with the auxiliary switches are kept because the GaN body diode has a relatively high forward voltage.

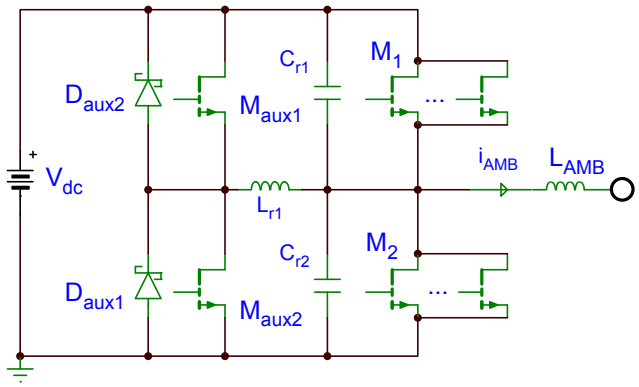

Figure D.6: GaN based half-bridge with auxiliary switches.

D.3.3 Related topology

The proposed soft-switching power amplifier topology, presented in section D.3.2, is related to another power amplifier topology known as the "Opposed Current Converter" (OCC) [173] or "Opposed Current Amplifier" (OCA) [174]. The OCC is obtained by splitting the conventional inverter leg with filter into interleaved buck and boost legs, as shown in Fig. D.7[2]. The top and bottom switches are thus no longer directly connected and are separated by the filter inductors, $L_{f1,2}$. Hence, a diode with zero reverse recovery may be chosen which reduces EMI and switching losses. Since no shoot-through is possible between the top and bottom switch the OCC may operate with no, or at least much less, dead-time between the top and bottom switch. The resulting high-quality output sine wave of the OCC is desirable in high precision power amplifiers used in high-performance positioning systems [173].

The proposed topology may be arrived at by adding half-bridge switches to the final output node of the OCC. The resulting similarity in structure is striking, but also very misleading, since there is a very important difference between the OCC and the proposed topology. The OCC *filter* cut-off frequency is below the switching frequency (thus no clamping diode at the output), whilst the cut-off frequency of the *resonant* auxiliary leg is above the switching frequency. This difference is so important, that although the topology structures are very similar and one might think that the origin of the proposed topology is from the OCC by just adding switches to the output node, such a conclusion would be incorrect. The correct way of obtaining the proposed topology is by considering it as the active form of a dv/dt filter as presented in the previous section.

[2]The "Opposed Current Converter" name originates when two such half-bridges are placed opposite each other to form an H-bridge.

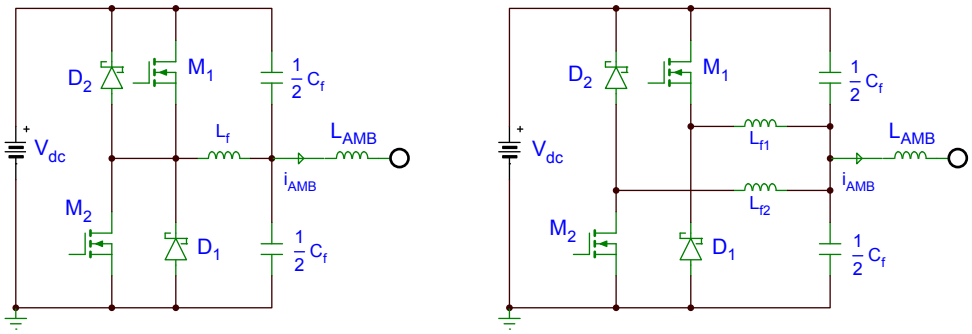

(a) Half-bridge with LC filter.

(b) Split half-bridge legs.

Figure D.7: Opposed current converter origin.

D.4 Current control design

The power amplifier utilizes a PI current controller. The current control design is quite similar to that of the current control of the drive presented in section 4.2.4. The load in both cases is an RL-load, hence the control design equations are not repeated here. The cross-over frequency, ω_c, is chosen one decade above the maximum operating frequency of 330 Hz ($\approx$ 20 krpm), thus 3.3 kHz. The original maximum flywheel speed was designed as 30 krpm. Balancing procedures were performed which compromised the rotor structure and there is an uncertainty in the tensioning of the carbon fiber sleeve. For these reasons, the maximum flywheel speed was lowered to 19 krpm.

Even though the drive and AMB loads are both inductive, the resulting proportional and integral gains are quite different. The AMB's inductance is much higher, resulting in a higher proportional gain. The proportional gain for the radial AMBs, with a nominal inductance of 8.8 mH is $K_p \approx 160$ (see (4.6)). The designed integral gain is: $K_i \approx 1.8 \times 10^3$, but since the only DC disturbance is that of the load resistance, the integral gain is lowered to $K_i \approx 100$. A lower integral gain reduces peaking near the cross-over frequency.

The axial AMB inductance has severe saturation in case that the rotor is pulled against the top AMB. This causes the current control to easily become unstable. Eddy currents in the axial AMB also excited a limit cycle even when the AMB was suspended in the centre of the air-gap which increased audible noise. Fortunately, the dynamic requirements of the axial AMB position control are much lower since it effectively low pass filtered by the full inertia of the rotor. Hence, the current control gain is tuned by hand and substantially lower than the analytically calculated value. The current control gains for the axial AMB are: $K_p \approx 30$, $K_i \approx 100$.

The current control is calculated twice per PWM period because double PWM sampling is used. The PWM frequency is 40 kHz. Hence, the reference duty cycle is calculated every 12.5 μs. The microcontroller is configured to apply immediate updates of the duty cycle, i.e. the duty cycle register update is not delayed until the next PWM period. It is due to

this relatively short sampling delay that the controller gains may be set relatively high. Due to the short sampling period, high current control gain and relatively short dead-time (2 % of the duty cycle), the power amplifier non-idealities are not compensated by other means.

A simulation model of the power amplifier, which was used to verify the controller design, is included in appendix E.3.

D.5 Digital PLL for synchronization

Electromagnetic compatibility analysis of the HTR-10GT (Helium blower supported by AMBs) is presented by Zhou *et al.* [175]. They state that: "reliability of the electronic system is the weakest link in AMB". The authors distinguish between hardware and software methods of increasing anti-interference. The main hardware improvement suggestion is in breaking ground loops. Software methods were used for monitoring.

An important approach in reducing the EMI susceptibility of the position sensors is to synchronize all the PWM clock generators of the power amplifiers and drive. Such a method may be described as a software method of increasing anti-interference.

Synchronization of the power amplifiers was presented by Jansen van Rensburg in which it appears that a high-frequency clock (51.2 MHz) generated by the main controller is shared amongst the power amplifier which is used as the clock source for the PWM counter [176]. The embedded controller for an active magnetic bearing system presented by le Roux [177] utilized the power amplifiers presented by Jansen van Rensburg, in which a 20 KHz synchronization signal is reported. The exact mechanism by which synchronization is achieved is not reported. A separate Siemens® drive was used in the project presented by le Roux. Thus, not all of the potential switching noise sources were synchronised.

The synchronization method developed for the power amplifiers in this work utilizes a digital phase-locked loop (DPLL). The PWM generation card (DS5101) which generates the PWM signals for the motor controller acts as the master clock source. The PWM generators of the power amplifiers have their own local oscillators which are synchronized to the master clock source by means of the DPLL.

Synchronizing the PWM generators of the AMB amplifiers and motor inverter facilitates the aim of cooperative control. By means of synchronisation, the EMI generated by the AMB power amplifiers do not interfere with the drive's current sensors and the drive's switching do not cause interference with the position sensor signals for the AMB control. The simultaneous benefiting of both systems due to the synchronization may also be viewed as cooperation in itself. The reduced interference improves the sensorless drive operation, which in turn causes the speed and angle estimates to be usable by the AMB unbalance control from a lower speed. The reduced interference in the AMB position sensor signals

enables the inference of the rotor angular position from relatively small variations in the radial disturbance due to the rotor's permanent magnets.

The microcontrollers[3] used to implement the current control loop have a synchronisation input pin. Unfortunately, the synchronization input pin is only applicable for edge aligned PWM. Centre-aligned PWM is preferred for current control because the mean current is sampled at the PWM carrier peaks. Therefore, another means of synchronising the PWM generators when operating in centre-aligned PWM mode had to be implemented. Such a method is possible by a DPLL.

The DPLL operates by the principle that the PWM carrier can be synchronised to an external clock source by modulating the PWM period. Its operation is explained by referring to Fig. D.8. PMTR represents the count value of the PWM counter. The digital up/down counter acts as the triangle carrier. The PMTR register cannot be accessed directly. PHASEx is the register responsible for setting the PWM period. PMTR counts up to the value in the PHASEx register and reverses the count direction. Upon reaching the carrier peak an interrupt is generated to service the PWM generator. It is within this interrupt that the current value sampled by the ADC is read. The REF pulse represents the master clock for synchronisation. The VAR pulse represents a fictitious pulse which is aligned with the triangle carrier peaks. Synchronization is achieved if the VAR and REF pulses align. The external REF pulse is connected to a special purpose pin known as the "Input capture" (IC) unit of the microcontroller. In case of a rising or falling edge on the IC pin, the timer value at that instant is recorded in the IC buffer. Upon reaching the triangle carrier peak when the PWM interrupt occurs the same timer used for the IC unit is read and the phase difference (PD) is calculated by subtracting the timer values from each other. The PWM period is updated by using the phase difference as a feedback variable:

$$\mathrm{PHASEx\,(k)} \quad = \quad \mathrm{PHASEx\,}(k-1) + K_p \mathrm{PD\,}(k-1) + K_i \int PD\,(k-1)\,dt\,, \quad \text{(D.1)}$$

where K_p, and K_i, are proportional and integral gains used for the DPLL. In the implementation $K_p = \frac{1}{16}$, and $K_i = \frac{1}{64}$. The small DPLL gains allow the period value of the PWM generator to undergo only small changes upon each update. This gives the DPLL a low pass characteristic and helps to reject jitter and noise and produces a stable PWM period.

In Fig. D.8, the scenario where the VAR pulse leads the REF pulse is illustrated. By increasing the PWM period temporarily the phase of the REF pulse catches up to that of the VAR pulse. The PWM period returns back to nominal after the phase difference is cancelled and only small adjustments are required to keep the two pulses synchronised. This concludes the basic principle of the DPLL. The implementation, which has to transfer and match the conceptual operation to specific elements within the microcontroller, is far

[3] dsPIC33EP64MC504 from Microchip®.

more nuanced and beyond the scope of this thesis.

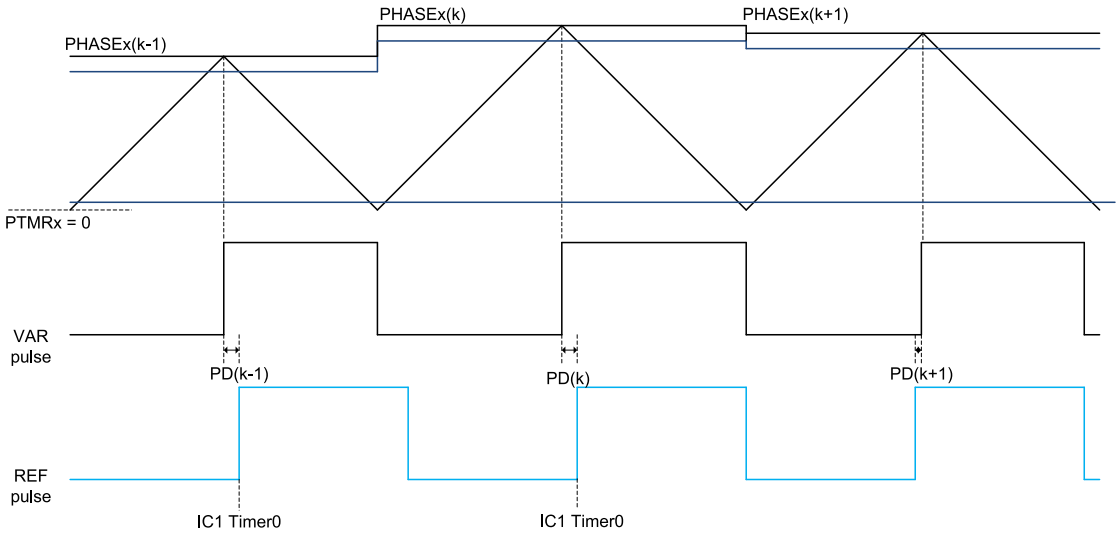

Figure D.8: PWM period modulation for synchronization.

A simulation model of the DPLL, which was used to verify the state machine design before implementation, is included in appendix E.4.

D.6 Power amplifier measurements

D.6.1 Current control measurement

The step response of the current control is shown in Fig. D.9. The control has an overshoot of only 2.5 %. The switching ripple is apparent in the unfiltered current response due to parasitic capacitance to ground in the load and cable. The actual load current ripple, which is relatively small, is visible in the smoothed current. From the result it can be concluded that the soft-switching topology does not limit the current slew rate or interfere with the control, i.e. the same response is obtained as with normal PWM control.

D.6.2 Interference comparison

The slew rate of the output voltage of the hard and soft-switching power amplifiers are presented in Figs. D.10 and D.11, respectively. The hard-switched amplifier was measured at the final output. The soft-switching amplifier was measured *before* the final output, i.e. at the output common-mode filter inputs[4]. A ringing is apparent in the turn-on of the hard-switched power amplifier. The sudden turn-on after crossing the gate-source threshold voltage causes a voltage drop in the drain-source leakage inductance which in turn causes the device to turn off. Even though the average turn-on time is on the order of

[4]The leakage inductance of the common-mode filter further reduces the output voltage slope.

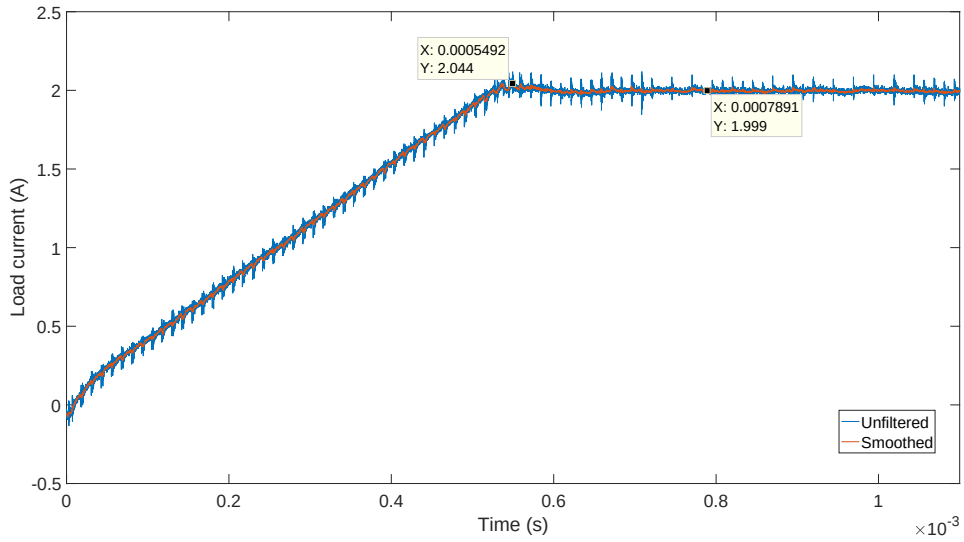

Figure D.9: Current control step response.

50 ns, the most EMI is caused by the highest slew rate in the output voltage. The highest slew rate in turn-on is in the region just before the ringing, which has a slop of $\frac{11\,\mathrm{V}}{3.6\,\mathrm{ns}}$. The slow turn-off time of the hard switched power amplifier, which is atypical of a hard-switched amplifier, comes at the cost of increased switching loss. The soft-switching power amplifier achieves an even slope in turn-on and turn-off switching transitions, without ringing.

Another means of comparing the EMI produced by the hard- and soft-switched amplifiers is by measuring the produced common mode (CM) current, as shown in Fig. D.12. The CM current produced by the hard-switched power amplifiers has a peak-peak amplitude[5] of up to 10× the peak-peak amplitude of the soft-switched amplifier. Also of note is that the common-mode current of the soft-switched power amplifier is highly damped with little to no ringing present. This is achieved in part by the limited slew-rate due to the soft-switching topology and the use of CM filters[6]. Even if synchronized sampling was used in the case of the hard-switched amplifier, some noise would still be present in the sampled eddy current position sensors due to the long settling time of the CM current, i.e. ringing is still present in the middle of PWM period when the ADC would be sampled.

The true benefit of the soft-switching amplifier, with a common mode filter and synchronised sampling, becomes apparent in the comparison of the measured eddy current position sensor signal using the hard- and soft-switched amplifiers. Fig. D.13a, compare the measured axial position eddy current sensor signal. The signals were captured whilst suspending the rotor at standstill when using the two different types of amplifiers[7]. The spectrum of the signals (smoothed) is compared in Fig. D.13b. The higher amplitude in the low-frequency region is due to the control energy. The difference in noise within

[5] Measured from the positive to the negative peak within one cycle.
[6] The off-the-shelf hard-switched amplifier had no output CM filter.
[7] All of the amplifiers are active, but only the axial sensor signal is used in the comparison.

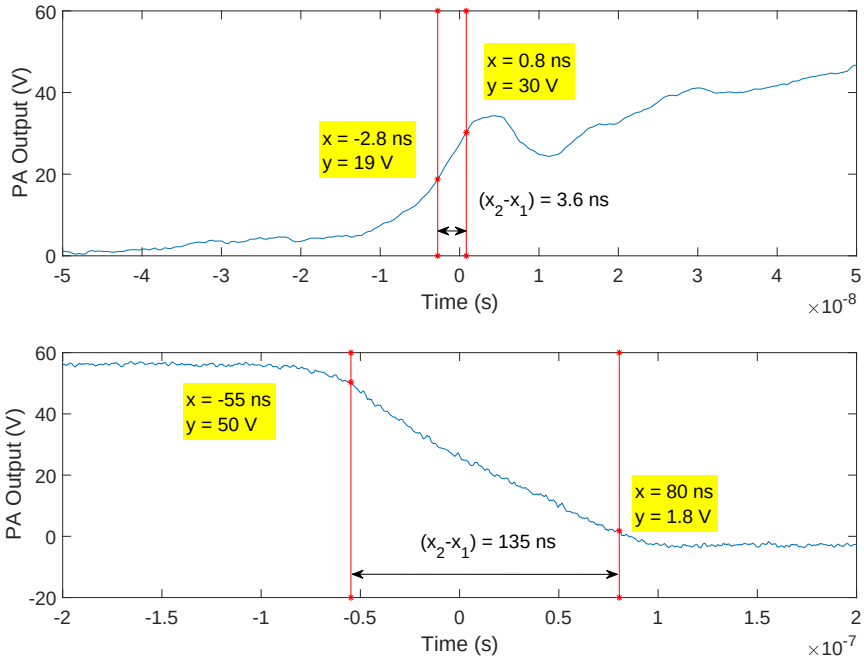

Figure D.10: dv/dt of hard-switching power amplifier.

the control region differs by up to 18 dB and at higher frequencies, the difference is up to 23 dB.

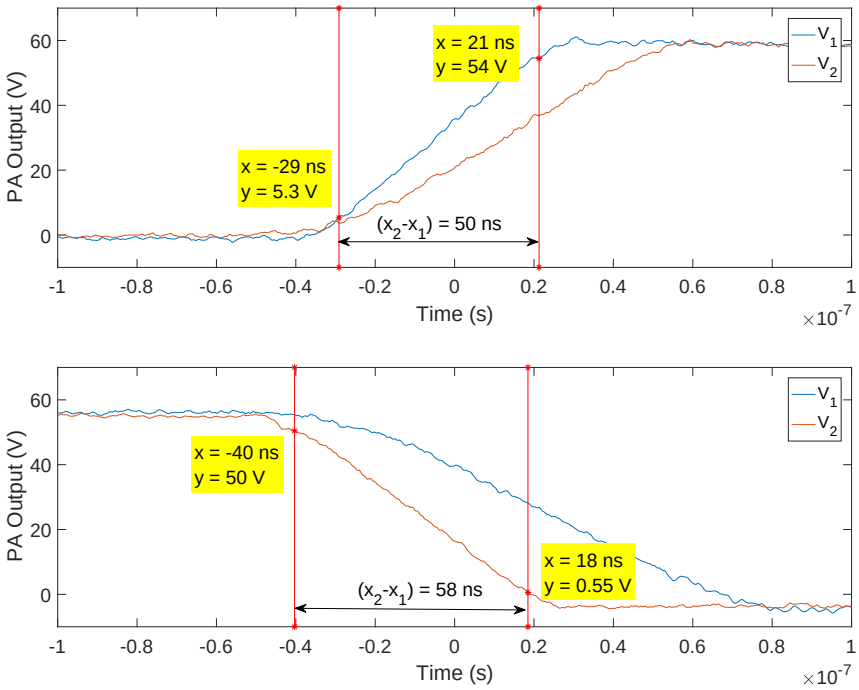

Figure D.11: dv/dt of soft-switching power amplifier.

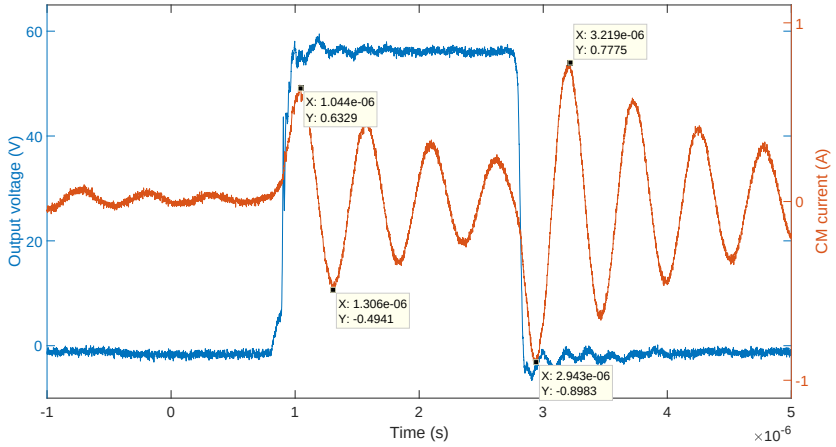

(a) Hard-switched amplifier CM current.

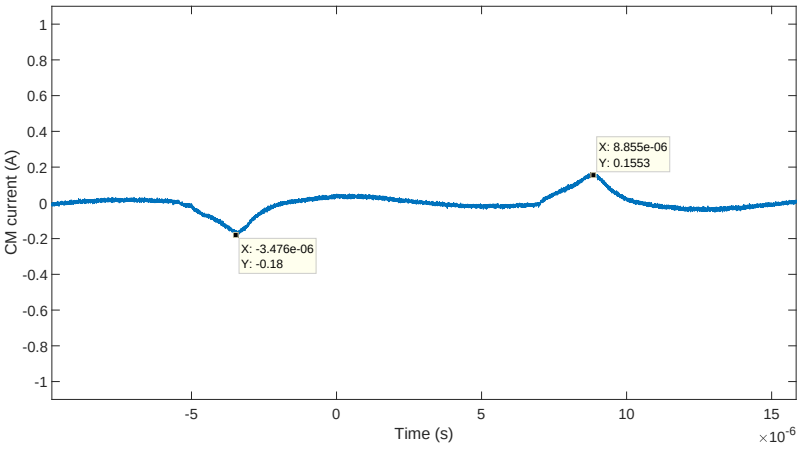

(b) Soft-switched amplifier CM current.

Figure D.12: Common mode current comparison.

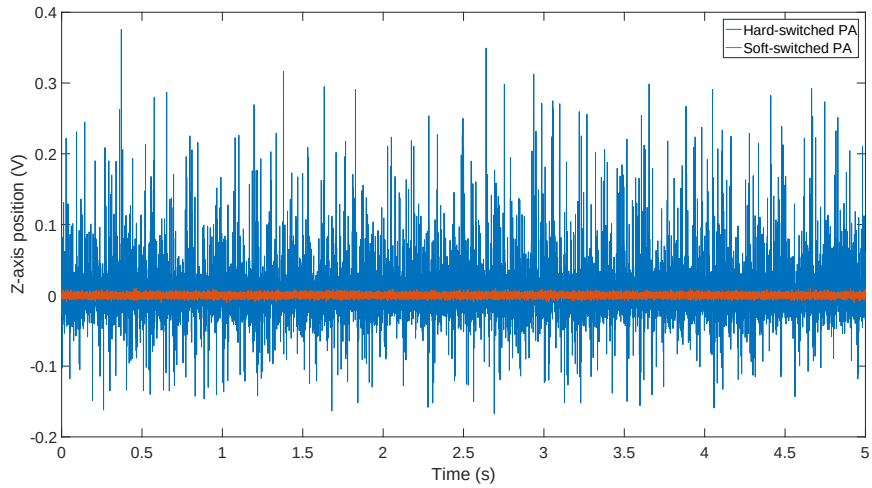

(a) Time domain signal.

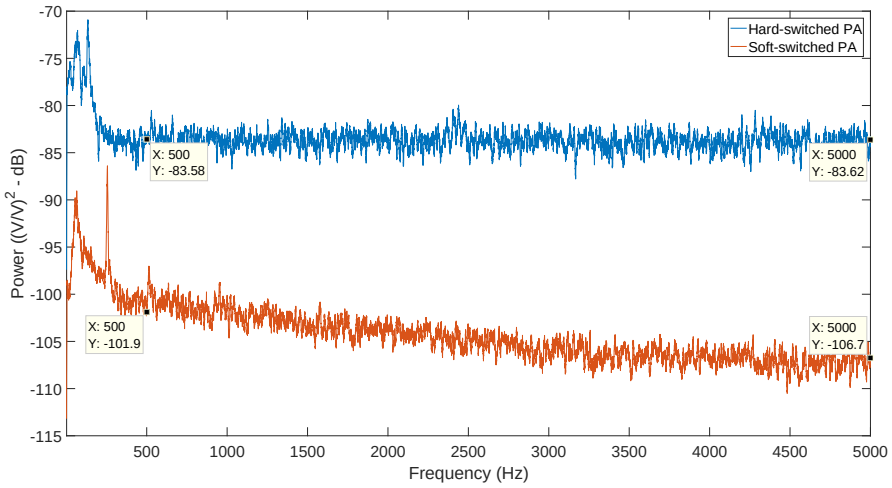

(b) Noise spectrum.

Figure D.13: Position sensor noise comparison.

D.7 Power amplifier photos

A photo of the designed power amplifier with overlaid descriptions of each section is shown in Fig. D.14. A four layer PCB layout is used. Inner layers connected to the power planes interleave the signal layers. The sandwiching structure acts as a Faraday cage and thus reduces EMI and crosstalk with sensitive signal tracks. Each amplifier is placed in its own aluminium enclosure which further reduces EMI coupling to the outside environment and reduces susceptibility to the EMI generated by outside sources (especially that of the PMSM drive which uses hard switching).

The power amplifiers are mounted on a heat sink inside a larger control enclosure, as depicted in the photo of Fig. D.15. Also shown in the photo is the synchronisation driver board responsible for fan-out of the synchronisation driver signal using high-speed, differential line drivers to each power amplifier's input optocoupler.

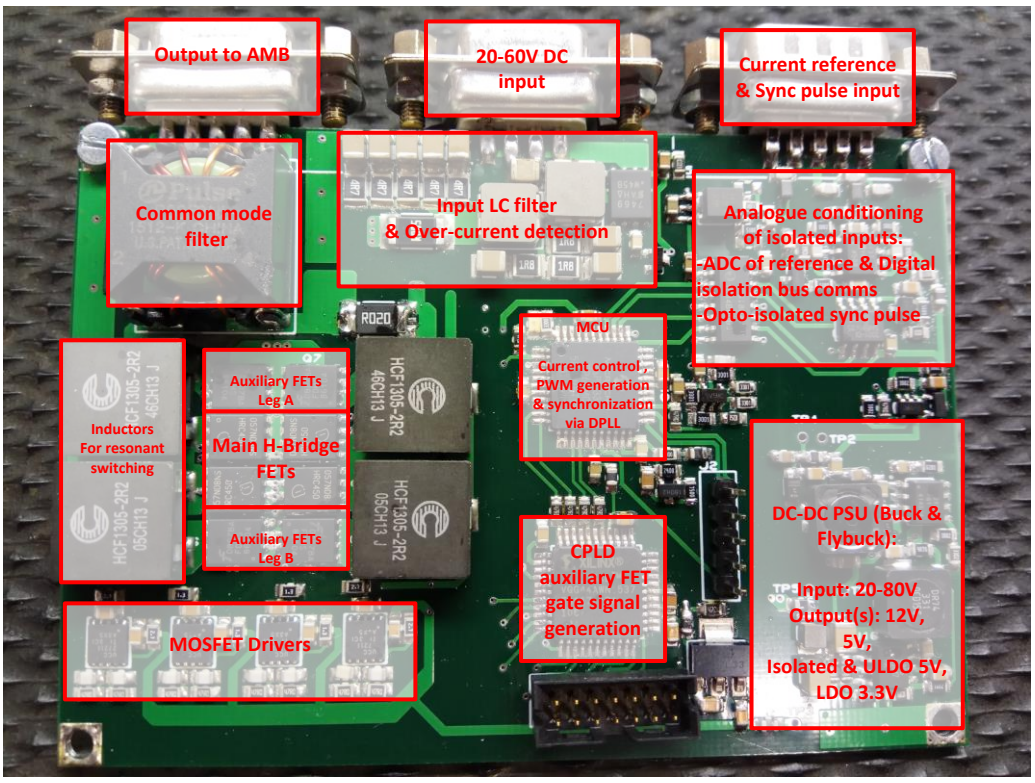

Figure D.14: Power amplifier PCB photo.

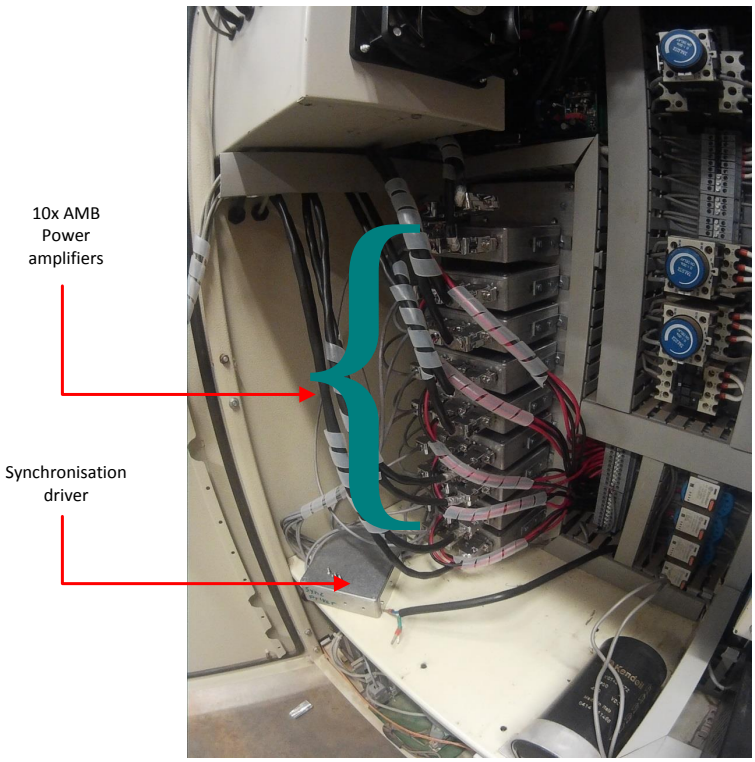

Figure D.15: Power amplifiers mounted inside enclosure.

Appendix E

Digital supplement

[E.1] Simulation and post processing files for algebraic recovery of zero component.

[E.2] Example on-line simplex search.

[E.3] Power amplifier current control design.

[E.4] Digital phase-locked loop state machine verification.

[E.5] COMSOL® simulation model of AMB.

[E.6] AMB control simulation.

[E.7] PMSM control simulation.

[E.8] Rotor angle estimation based on UMP disturbance.

[E.9] Power amplifier LTspice loss simulation.